Charge Photogeneration in Organic Donor/Acceptor Blends

SAFA SHOAEE

Imperial College London

Department of Chemistry

This thesis is submitted to Imperial College London for degree of *Doctor of Philosophy*.

ABSTRACT

Polymer-small molecule blend films are of increasing interest in the field of organic solar cells. This thesis employs transient absorption spectroscopy as a mean to study charge photogeneration in these blend films. These studies allow identifying and addressing the charge photogeneration efficiency-limiting processes in polymer:perylene diimide organic solar cells.

We approach the question by considering the influence of nanomorphology and phase segregation on charge photogeneration and recombination dynamics. We further report on yield of charge separated species in polythiophene / perylene diimide blend films as a function of electron acceptor's energy levels. We find that, compared to polythiophene / PCBM blend films, charge photogeneration is significantly enhanced. Correlations between free energy for charge dissociation and charge photogeneration yield within different polymer:acceptor series are observed and indicate the generality of this relationship. Furthermore, the energetic model proposed to account for these results is consistent with the well-established Onsager and Marcus theories. It can therefore be concluded that the yield of photogenerated charges in polymer/acceptor systems is likely to be dependent upon the excess vibrational energy of the bound radical pair, such that the key kinetic competition in the photogeneration process is between vibrational relaxation and dissociation of this species

Simultaneously, we investigate photoinduced charge separation in solid films of two perylene diimides and a donor-bridge-acceptor (D-B-A)molecule, exTTF-pcp-C_{60} relative to solution. First we find Intramolecular charge separation and recombination is correlated with a reduction in the yield of long-lived, intermolecular charge-separated species in the perylene diimide dyad. In the D-B-A system we observe the exTTF-pcp-C_{60} motif in this case leads to more charges than the reference compounds or a mixture of them but that the excited state of the electron acceptor, the fullerene, suffers from concentration self-quenching which severely affect the charge yield in solid films.

Table of contents

1. Introduction 1

1. 1 Motivation and overview 2

1.2 Historical Context 3

1.3 Organic solar cells 5

1.3.1 Dye-sensitised solar cells 9

1.3.2 Heterojunction organic solar cells 10

1.3.2.1 All molecular semiconductor and pure conducing polymer solar cells 12

1.3.2.2 Polymer/small molecule solar cells 12

1.4 Theory of organic photovoltaic cells 15

1.4.1 Properties of excitons 17

1.4.2 Exciton dissociation 18

1.4.3 Charge transfer state 19

1.4.4 Mechanism of charge recombination 23

1.4.5 Onsager theory 24

15 Device operation 26

1.6 Parameters affecting charge photogeneration in organic bulk heterojunction films 28

1.7 project objectives 33

2. Experimental methods 44

2.1 Overview 45

2.2 Materials and film preparation 46

2.2.2 Device architecture 48

2.3 Techniques: 49

2.3.1Steady state photoluminescence spectroscopy 49

2.3.2 Transient absorption spectroscopy 50

2.3.2.1 Microsecond 51

2.3.2.2 Nanosecond 52

2.3.3 Time resolved photoluminescence spectroscopy 53

2.3.4 Polarised light microscopy 54

2.3.4.1 Liquid crystals 54

2.3.5 Atomic force microscopy 57

2.3.5.1 Contact and Close-contact modes 59

2.3.6 Transmission electron microscopy 60

2.3.7 Admittance spectroscopy 61

2.3.8 Solar simulator 62

3. Influence of nanoscale phase separation on geminate versus bimolecular recombination in P3HT:fullerene blend films 65

3.1 Introduction 66

3.2 Sample preparation 69

3.3 Results and discussion 70

3.4 Conclusion 80

4. Photophysics of solutions vs. films in donor-acceptor system 84

4.1 Introduction 85

4.2 Sample preparation 88

4.3 Results and discussion: Inter versus intra-molecular photoinduced charge separation in solid films of triphenylamine/PDI system molecules 89

4.4 Conclusion 97

5. Photophysics of Charge photogeneration in polythiophene/ perylene diimide blend film 102

5.1 Introduction 104

5.1.1 Perylene diimide 104

5.1.2 Morphological aspects 107

5.2 Sample preparation 112

Results and discussion

5..3 Steady state film photophysics 113

5.3.1 Absorption 114

5.3.2 Emission 117

5.4 Characterisation of non-annealed films 118

5.4.1 Solvent, 118

5.4.2 spin-coating conditions 123

5.5 Thermal Annealing 126

5.5.1 Steady state photophysics 127

5.5.2 Morphology 128

5.5.2.1 Polarising Light Microscope 128

5.5.2.2 Atomic Force Microscope 131

5.6 Transient Absorption - Charge generation 133

5.7 Charge photogeneration in PDI2 blend films vs. PCBM blend films 138

5.8 Conclusion 146

6. free energy for charge separation in P3HT/ PDI blend films 154

6.1 Acceptor energy level control of charge photogeneration in organic donor:acceptor blends.

6.1.1 Introduction 155

6.1.2 Sample preparation 160

6.1.3 Results and discussion 161

6.1.4 Conclusion 172

6.2 PDI_X Device characterisation 174

6.2.1 Introduction 174

6.2.2 Materials and methods 177

6.2.3 Results and discussion 178

6.2.4 Conclusion 188

7. **Conclusion** 194

7.1 Charge generation 196

7.2 Future work 199

Appendix 202

LIST OF PUBLICATIONS

1) Shoaee, S.; Eng, M. P.; An, Z.; Zhang, X.; Barlow, S.; Marder, S. R.; Durrant, J. R. *Chemical Communications* **2008**, 4915-4917.

2) Shoaee, S.; An, Z.; Zhang, X.; Barlow, S.; Marder, S. R.; Duffy, W.; Heeney, M.; McCulloch, I.; Durrant, J. R. *Chemical Communications* **2009**, 5445 - 5447.

3) Shoaee, S.; Eng, M. P.; Espíldora, E.; Delgado, J. L.; Campo, B.; Martín, N.; Vanderzande, D.; Durrant, J. R. *Nano Letters* **2009**, *submitted for publication*.

4) Shoaee, S.; Clarke, M.T.; Huang, C.; Barlow, S.; Marder, R. S.; Heeney, M.; McCulloch, I.; Durrant, J. *JACS*, **2010,** *submitted for publication.*

5) Eng, P. M.; Shoaee, S.; Gouloumis, A.; Martin, N.; Durrant, J. R. *in preparation.*

6) Clarke, T.; Ballantyne, A.; Shoaee, S.; Soona, Y.; McCulloch, I.; Nelson, J.; Durrant, J. *Advanced Materials*, **2010**, *submitted for publication.*

LIST OF FIGURES

Figure 1.1 Visual representation of excitons in (a) inorganic and (b) excitonic (organic) materials.

Figure 1.2 Exciton generation. Absorption of photons with energies equal or greater than the band gap energy, Eg, forms an electron, e^-,in the lowest unoccupied molecular orbit, LUMO and a hole, h^+ in the highest occupied molecular orbital, HOMO. The strong Coulomb interaction between the hole and the electron forms a strongly bound electron-hole pair, termed exciton.

Figure 1.3 a) heterojunction bilayer where most of the polymer phase is further from the interface than the exciton diffusion length. b) bulk heterojunction: providing better understanding for bicontinuous donor and acceptor phase. A much higher percentage of the polymer phase is less than a distance of exciton diffusion length from the interface.

Figure 1.4 Schematic of charge dissociation at the polymer / acceptor interface. The polymer singlet exciton diffuses to the interface, where electron transfer to the PCBM occurs to generate the charge transfer (CT) state. The CT state has an initial electron-hole separation distance of *a* (the thermalisation length). Onsager Theory would predict that the probability of full dissociation into the free charge carriers depends upon the ratio between *a* and the Coulomb capture radius, r_c. For simplicity, the Coulomb capture radius is drawn as spherical. (see section 1.6 for more.)

Figure 1.5 top: Consecutive steps in organic donor/acceptor photovoltaics. Optical absorption and exciton formation; (ii) exciton migration to the donor-acceptor interface; (iii) exciton dissociation into charge carriers, resulting in the appearance of holes in the donor and electrons in the acceptor and; (iv) charge collection at the electrodes. Figure taken from.[100] bottom: The correlation between ΔOD measured by TAS on thin blend films and the Jsc measured in complete devices, for a series of polymer:PCBM blend systems of varying PCBM composition (most with 50 wt% PCBM). Taken from.[105].

Figure 1.7: A heterojunction interface consisting of two different semiconductors an electron donor (D) and an electron acceptor (A). Charge carrier generation can occur by splitting the exciton or energy transfer occurs where the exciton is transferred from the donor to the acceptor.

Figure 1.6 The diagram shows the electronic basis of the phenomenon of fluorescence.

Figure 1.8 The energy of this state depends upon the Coulomb attraction of the electron and hole and therefore their spatial separation, as illustrated by the dotted curve. Figure also illustrates typical binding energies for the exciton and CT states (E_B^{exc} and E_B^{CT} respectively). Adapted from reference[126].

Figure 1.9 Energetic representation of charge dissociation. The excitation leads to the promotion of an electron from S_0 to S_1, which can be dissociate into a D^+A^- pair where the electron and hole still attract each other. After which it can either dissociate into free carrier charges or geminately recombination. k_{sep}, k_{diss} and k_{rec} are the rates for the separation of exciton into charge transfer state, dissociation of charge carriers and recombination, respectively.

Figure 1.10 The potential energy surfaces for a D/A system, where photoexcitation generates $^1D^*/A$ and subsequent electron transfer generates D^+/A^-. D refers to the electron donor and A the electron acceptor.

Figure 1.11 Potential energy diagram summarising Onsager theory for autoionisation. The red curve illustrates the potential energy resulting from Coulomb attraction as a function of electron-hole (*e-h*) separation. Photoexcitation results in generation of a hot, mobile electron. This electron subsequently thermalises at a particular distance from the hole (the thermalisation length, *a*). If *a* is less than the Coulomb capture radius, r_c (as is typical for organic systems), then the charge transfer state can either undergo geminate recombination or dissociate into free charges.

Figure 1.12 current voltage characteristic of a typical solar. Taken from ref 56

Figure 1.13 Energy level diagram summarising the main processes involved in charge photogeneration. **1**: Photoexcitation to singlet exciton (S_1). **2**: Exciton dissociation to form the hot charge transfer (CT) state. **3**: Thermal relaxation of CT state. **4**: Spin mixing of the ^{1}CT and ^{3}CT states. **5**: Geminate recombination of the ^{3}CT to the triplet exciton, T_1. **6**: Geminate recombination of the ^{1}CT state back to the ground state, S_0. **7**: Dissociation of the hot CT state into a fully charge-separated (CS) state. **8**: Dissociation of thermally relaxed CT state into CS state. **9**: Bimolecular recombination of the CS state. This diffusion limited bimolecular process may result from either direct recombination or, more probably, via reformation of interfacial charge transfer states (shown as reversible arrows in processes **7** and **8**) and subsequent geminate recombination (**6**).[137] Figure taken from.[96]

Figure 2.1 ITO glass substrate.

Figure 2.2 representation of a device. The red presents the active layer and gray areas are the electrodes deposited through a mask. Silver paste is added to the device in order to get contact with ITO.

Figure 2.3 Transient absorption spectroscopy (TAS) schematic. The system consists of a pump source, either a nitrogen-dye laser or Nd-YAG laser, a probe source: Xenon lamp or laser diode. The incoming pump source excites the film and the probe source probes the decay as a function of time to study the decay dynamics of the charge species.

Figure 2.4 Schematic representations of (a) a columnar mesophase, (b) a 2D lattice arrangement of hexagonal columnar (Col_h) mesophases.

Figure 2.5 Ideal homeotropic alignment of discotic stacks in a PV device.

Figure 2.6 Flow schematic of atomic force microscope (AFM).

Figure 2.7 Schematic diagram (right) and a photo of transmission electron microscope (TEM).

Figure 3.1 Ground state UV-visible spectra of as-prepared film of pristine (top) and blend (bottom) films from o-DCB; films were spun on untreated glass substrates at 1500 rpm for 60 s.

Figure 3.2 top: Optical microscopy images of P3HT:C_{60}-1 (left), P3HT:C_{60}-2 (centre) and P3HT:PCBM (right), bottom: TM-AFM images of P3HT: C_{60}-1 (left), P3HT:C_{60}-2 (centre) and P3HT:PCBM (right) blend films.

Figure 3.3 Photoluminescence quenching of blends of C_{60}-1, C_{60}-2, and PCBM together with 50 wt % of P3HT or P3HT-OH, excited at 550 nm.

Figure 3.5 Transient decay on log/log plot: blends of C_{60}-1 (red) and C_{60}-2 (blue) obeying monoexponential and PCBM blend (black) as control film exhibiting a straight light with power law characteristics. Inset: same blend film data on log- linear plot with monoexponential fits. Excited at 533 nm, probed at 970 nm at 60 μJ.cm^{-2}. N_2 atmosphere.

Figure 3.4 Transient absorption data collected for a 1:1 P3HT:C_{60}-1 (red) and P3HT:C_{60}-2 (blue) blend films under N_2 atmosphere, spun coated from o-DCB at 700 rpm for 60s. Excited at 532 nm and measured at 50 ns, using an excitation density of 50 μJ cm^{-2}.

Figure 3.6 Excitation intensity dependence of Excitation intensity dependence of top: P3HT: C_{60}-1 blend film, bottom: P3HT:PCBM blend film under N_2 atmosphere, excited at 532 nm and probed at 970 nm. Excitation energy 70- 7 μJ cm^{-2}. Inset: normalised signal size measured at 50 ns as a function of laser excitation density.

Figure 3.7 Cyclic Voltammetry of the three fullerenes. Measurements done by Juan Luis Degado at Universidad Complutense.

Figure 4.1 UV-visible spectra of as-prepared films of **1** (black), **2** (red) and **2** in chloroform (blue). Films were spin- coated on untreated glass substrates at 500 rpm for 60 s.

Figure 4.2 Time-resolved single-photon-counting data for films of **1** (black), **2** (red) and instrument response (gray). Data were collected using 467 nm excitation and 670 nm detection, with a 250 ps instrument response and data collection times corresponding to matched densities of absorbed photons. For purpose of comparison, the time scale for instrument response and signal **2** have been shifted.

Figure 4.3 a) Transient absorption spectra of **1** and **2** films measured 1 μs after excitation. b) The decay dynamics of the corresponding transient absorption spectra monitored at 740 nm. Data taken at 20 μJ cm^{-2} energy at an excitation of 540 nm.

Figure 4.4. (a) Normalized absorption spectra of **3** in dilute toluene solutions (black line), dichloromethane (blue line) and film (red line). (B) Ground state absorption of 3, 4 and 5 in toluene.

Figure 4.5 Emission of **3** (dashed lines) and **5** (solid lines) in toluene (a) and benzonitrile (b) recorded after 450 nm excitation. (c) Emission spectra in toluene from the reference compound **4** (solid line) and the donor-bridge-acceptor molecule **3** (dashed line) compared to the emission of **3** in dichloromethane (dash-dotted line) and benzonitrile (dotted line). (d) Normalized emission spectra of **3** (solid line) and **4** (dashed line) in dichloromethane after 337 nm excitation.

Figure 4.6 (left) Normalized transient absorption spectra of pristine **3** film (solid circles) and a 2.5:97.5 w:w **4:PS** film at 1μs. Excited at 337 nm. (right) Transient absorption spectra of **3** and **4** in solution.

Figure 4.7 Transient absorption decays of **3** fitted curves (black lines) recorded as a pristine film (blue) and as a dilute (1:9 **3:PS** w:w) film (red).

Figure 4.8 The transient absorption decays of **3** in solutions that are either nitrogen purged (solid lines) or exposed to atmospheric oxygen (dashed lines) recorded after 337 nm excitation in toluene (a), DCM (b), and benzonitrile (c).

Figure 4.9 Mass-weighted absorption (top) of **3:PS** and emission (bottom) spectra (excited at 337 nm) of **3:PS** (left) and **4:PS** (right) films with 10:90 (solid line), 20:80 (dashed line), 50:50 (dotted line), and 80:20 (dash-dotted line) w:w ratios.

Figure 4.10 The energy diagram and kinetic scheme for the DBA molecule (**3**) after generating the C_{60} excited singlet state. From this state the fullerene triplet is formed with rate constant k_{ISC}, the singlet may also decay to the ground state, either by internal conversion, k_{IC}, or fluorescence, k_F. In the DBA construct the additional pathway of charge separation is added with a rate constant k_{CS}. In the solid state these formed charges may dissociate with a rate constant k_{DISS}. In the solid state an additional decay pathway from the singlet state to the ground state is added through concentration self-quenching, k_Q.

Figure 4.11. Fits to Eq. 1 of the mass-weighted TAS decays for 10:90 (solid line), 20:80 (dashed line), 50:50 (dotted line), 80:20 (dash dotted line), and 100:0 (dash dot dotted line) **3:PS** w:w films.

Figure 4.12 Mass-weighted TAS signal corresponding to C_{60} triplets (circles) and exTTF cation radicals (squares) for **3:PS** films.

Figure 5.1 Polymeric solar cell bulk heterojunction.

Figure 5.2 steady state absorption of PDI_2 in chloroform at different concentrations.

Figure 5.3 a): Absorption spectra of PDI_2 in chloroform solution (black) and in thin film prepared by spin coating (red). b): spectra of pristine PDI_2, P3HT and blend P3HT:PDI_2 spun from chloroform at 500 rpm for 90 seconds.

Figure 5.4 Emission of pristine P3HT, PDI_2 and blend P3HT:PDI_2 films spun on glass substrate from chloroform. Excited at 510 nm.

Figure 5.5 (top) UV-visible spectra of P3HT:PDI_2 films as a function of solvents: chloroform (CF), xylene, chlorobenzene (CB) and cyclohexanone. (bottom) normalised emission spectra of P3HT and P3HT:PDI_2 films in CF (red) and CB (blue). Films spun under same conditions on glass substrate (as-prepared).

Figure 5.6 5 μm × 5 μm AFM images recorded in tapping mode of films of P3HT:PDI_2 (w/w, 1:1) from: (a) chloroform (b) chlorobenzene.

Figure 5.7 (top) Absorption, (below) emission of pristine PDI_2 (blue) and P3HT:PDI_2 blend (red) spin coated at 3000 rpm for 60 seconds (solid lines) and at 500 rpm for 60 seconds (dotted lines). Inset: the absorption spectra of films spun at 3000 rpm.

Figure 5.8 AFM images along with RMS roughness of P3HT:PDI_2 films A (top) and B (bottom) prepared at 3000 rpm and 500 rpm spin rates respectively. Scan area: 5 μm×5 μm.

Figure 5.9 Pristine PDI_2 film spun from CF: (a) as-prepared at room temperature (20×), (b) heating the film to isotropic phase 100 ^{o}C (20×), (c) near Isotropic temperature 200 ^{o}C and d) cooling from isotropic phase, 180 ^{o}C (20×).

Figure 5.10 Phase-contrast AFM images of as-prepared (a) compared to annealed (b) (150 ^{o}C, 60 min) P3HT:PDI_2 films.

Figure 5.11 The transient absorption spectrum of a P3HT:PDI_2 (1:1) blend film obtained at 1μs after 40 μJ.cm^{-2} excitation at 500 nm before (black) and after (re) annealing at 150°C for 20 minutes (a) and the transient

Figure 5.12 Typical photoluminescence data for pristine P($T_{10}T_{10}TT_0$), P($T_{10}T_{10}TT_0$):PDI2 and P($T_{10}T_{10}TT_0$):PCBM 1:1 blend films.

Figure 5.13 (A) Transient absorption data collected for a 1:1 PDI2:PCBM blend film spin coated from $CHCl_3$ at 1100 rpm for 40s. Excited at 447 nm and measured at 1μs, using an excitation density of 50 μJ cm^{-2}. (B) P3HT:PDI2 (open blue square) and P3HT:PCBM (filled red squares) spun from $CHCl_3$ at 1100 rpm for 40s and chlorobenzene at 1500 rpm for 90s respectively. Both were excited at 520 nm and measured at 1 μs using an excitation density of 50 μJ cm^{-2}.

Figure 5.14 Typical transient absorption data for (red) $P(T_{10}T_{10}TT_0)$:PDI2 (red) and (blue) $P(T_{10}T_{10}TT_0)$:$PC_{60}BM$ (blue) 1:1 blend films in a N_2 environment, monitored at 850 and 960 nm respectively. Also shown for is data collected under O_2 (black) and a power law fit (gray) to the data ($\Delta OD \propto t^{-a}$).

Figure 5.15 Plot of the relative yield of long-lived, dissociated polarons in polythiophene/PDI2 (filled squares) and polythiophene/PCBM (open squares) blend films, as measured by the amplitude of the transient absorption at 850 and 1000 nm respectively, at 1μs, against estimated driving force for charge separation, $-\Delta G_{CS}^{rel}$.

Figure 6.1 Energy level diagram of a donor/acceptor interface showing a simplified viewpoint of photoexcitation of an electron into the donor LUMO (with efficiency η_{ABS}), followed by exciton dissociation via electron transfer into the acceptor LUMO ($\eta_{DISS(EX)}$) and migration of the separated charges away from the interface (η_{COLL}). Also illustrated is the potential for the electron transfer initially to generate a Coulombically bound charge transfer (CT) state that also requires dissociation ($\eta_{DISS(CT)}$) before the free charge carriers can be collected.

Figure 6.2 Absorption and photoluminescence spectra measured for the following pristine and blend films: PDI_D, P3HT and P3HT:PDI_D. The PL spectra were measured using 500 nm excitation.

Figure 6.3. TEM micrographs of P3HT:PDI_D (left) film (expanded region, centre: crystallisation of PDI_D lattice) and P3HT:PDI2 (right).

Figure 6.4 Typical transient absorption data for P3HT:PDI_D (1:1) blend film in a N_2 environment, monitored at 700 nm, with λ_{exc} = 520 nm at 50 μJcm^{-2}. Inset: spectrum of P3HT:PDI_E at 1 μs under N_2 using λ_{exc} = 520 nm at 50 μJcm^{-2}.

Figure 6.5 Transient absorbance signal measured at 1 μs of various P3HT:PDI_x (1:1) blend films with P3HT plotted against $-\Delta G_{CS}^{eff}$, estimated as $E_s - (IP_D - EA_A)$. The transient signal has been corrected for variation in the optical absorbance at the excitation wavelength (500 nm) and the PL quenching. λ_{prb} = 700 nm at 50 μJcm^{-2}.

Figure 6.6 Transient absorbance signal measured at 1 μs of various polythiophene : PCBM and polythiophene : PDI_X blend films plotted against $-\Delta G_{CS}$, using a probe wavelength of 970 nm.

Figure 6.7 Energy level diagram detailing the relevant energy levels of P3HT and PCBM along with back electrodes: calcium (Ca), aluminium (Al), silver (Ag) and gold (Au).

Figure 6.8 J-V curves for devices of (top) P3HT:PDI_2 and (bottom) P3HT:PDI_D 1:1 blends measured under constant illumination with 100 mW.cm^{-2} AM1.5 simulated light at room temperature.

Figure 6.9 The J-V curves for devices of annealed P3HT:PDI_D and P3HT:PDI2 1:1 blends measured under constant illumination with 50 mW.cm^{-2} AM1.5 simulated light at room temperature.

Figure 6.10 J-V of annealed (red) at 150 ^{o}C and non-annealed (black) P3HT:PDI_D (1:1) devices.

Figure 6.11 a) Emission spectra of P3HT:PDI_D before (black) and after (red) annealing at 150°C for 20 minutes. b) TEM images of P3HT:PDI_D film before and after thermal annealing at 150°C for 20 minutes.

Figure 6.12 TAS of annealed (red) at 150 ^{o}C and non-annealed (black) P3HT:PDI_D (1:1) films.

Figure 6.13 Transient absorption decays of P3HT:PDI_D (black), P3HT:PDI_D (blue) and SP220:PDI_D (red) measured under 40 μJcm^{-2} energy at 500 nm. and corresponding J-V curves (bottom) for devices of P3HT:PDI_D (black), P3HT:PDI_D (blue) and SP220:PDI_D (red) 1:1 blends measured under constant illumination with 100 $mW.cm^{-2}$ AM1.5 simulated light at room temperature.

Figure 6.14 (A) The J-V curves for devices of P3HT:PDI_D blend at different composition ratios measured under constant illumination with 100 $mW.cm^{-2}$ AM1.5 simulated light at room temperature. (B) Corresponding transient absorption decays excited at 500 nm with excitation energy of 40 μJcm^{-2} and probed at 700 nm.

Figure 7.1 charge photogeneration and recombination in polythiophene:perylene diimide (PDI) films. The orange arrow is the excitation process, green arrows are recombination loss mechanisms and red arrows present internal changes.

LIST OF TABLES

Table 2.1 Characterisation of Polythiophenes.

Table 5.1 Summary of donor / acceptor material properties

Table 5.2 As-prepared and annealed photophysical properties of pristine PDI2 and P3HT:electron acceptors

Table 5.3 Photophysical Properties of 1:1 Polythiophene:PDI2 and Polythiophene:PCBM blend films

Table 6.1 Properties of the P3HT:PDI_x blends

Table 6.2 Workfunction of some common back electrodes

Table 6.3 Active layer, component ratio, back electrode and annealing treatment used for each device

List of charts and schemes

Chart 1.1 Renewable Energy capital cost. (NREL)

Scheme 1: chemical structures of perylene diimide (PDI) and PCBM

Scheme 2: chemical structure of the pyrazolinofullerene derivatives **1** and **2** shown together with the **PCBM** and P3HT.

Scheme 3 Donor- Acceptor structures of PDI-TPA (2) with its PDI control (1) and exTTF-pcp-C60 (3) with its two controls: pcp-c60 (4) and exTTF-pcp (5)

Scheme 4: The calculated LUMOs (top) and HOMOs (bottom) for 1 and 2 molecules**.**

Scheme 5 Molecular structure of electron accepting small molecules PCBM (blue), PDI_2 (red) and polythiophenes with different ionisation potentials used as electron donors.

Scheme 6. Molecular structure of $\mathbf{PDI_X}$ derivatives. X = A - F starting from left, and PDI_2 at the far right.

DECLARAION

The work described in this thesis was conducted under the supervision Professor James Durrant at Imperial College London in the Nanomaterial Device section division.

No portion of the work referred to in this thesis has been submitted in support of an application for another degree or qualification of this or any other university or other institute of learning.

All the materials figures and data presented in this work are my own original work, except where specifically stated and acknowledged.

Safa Shoaee

London

2010

Dedicated to those who made it possible …..

Acknowledgements

I would like to thank everyone for making this work possible.

All of this work was made possible thanks to the guidance and training that I received from many people affiliated with James Durrant's group in Chemistry and Physics Departments.

In addition to scientific work, I would like to thank all of those who made my time at Imperial fun and memorable.

Most of all I would like to sincerely thank my supervisor, Prof. James Durrant, for his guidance over the past years. For his patience, enthusiasm, leadership, and friendship, I am grateful. By sharing his knowledge, experience and advice, he has helped me to grow both professionally and personally. None of the opportunities I have had to present my work and collaborate internationally would have been possible to the degree they were achieved without James as a supervisor.

Finally, I would like to thank my family for their constant encouragement and support. Thank you for always believing in me more than I believe in myself.

ABBREVIATIONS

E_g bandgap

E_B^{exc} exciton binding energy

E_B^{CT} charge transfer state binding energy

FF fill factor

HOMO highest occupied molecular orbital

ITO indium tin oxide

Jsc short circuit current

J-V current-voltage

LUMO lowest unoccupied molecular orbital

MEH-PPV poly(2-methoxy-5-(2'-ethyl-hexyloxy)-1,4-phenylene vinylene

Nd:YAG neodymium-doped yttrium aluminium garnet; Nd:Y3Al5O1

FET field effect transistor

P3HT poly(3-hexylthiophene)

$PC_{60}BM$ [6,6]-phenyl-C61 butyric acid methyl ester

PCPDTBT poly[2,6-(4,4-bis-(2-ethylhexyl)-4H-cyclopenta[2,1-b;3,4-b']-dithiophene)-alt-4,7-bis(2-thienyl)-2,1,3-benzothiadiazole)]

PEDOT:PSS poly(3,4-ethylenedioxythiophene) poly(styrenesulfonate)

PDI perylene diimide

PV photovoltaic

TAS transient absorption spectroscopy

UV-vis ultraviolet-visible

Abs absorption

PL photoluminescence

PLM polarising light microscope

TEM transmission electron microscope

AFM atomic force microscope

Voc open circuit voltage

CT charge transfer state

CG charge generation

CC charge collection

EXC exciton

ΔG free energy for charge dissociation

ΔOD change in optical density

D donor

A acceptor

D-A donor-acceptor molecules

D:A donor acceptor blends

SCLC space-charge limited current

DSCC dye-sensitised solar cells

EQE external quantum efficiency

CF chloroform

CB chlorobenzene

DCM dichlorobenzene

rpm revolution per minute

IP ionization potential

EA electron affinity

E_S singlet exciton energy

RMS root mean square

k_B Boltzmann constant

I. Introduction

1.1 Motivation and overview

Efficient, environmentally friendly energy production is one of mankind's biggest long term challenges. Anthropogenic climate change and limited fossil fuel resources coupled with a simultaneous rise in energy demand underline the necessity for the development and subsequent use of renewable energy. These drivers, along with the need to diversify energy sources, have resulted in the importance of renewable energy sources increasing in recent years. The most plentiful renewable energy source available to mankind is solar energy; the development of efficient and low cost technologies to utilise this resource could substantially address our future energy needs. For the above reasons, a photovoltaic (PV) solar energy conversion has moved increasingly to the forefront in the world energy dialogue over the last three decades. Substantial endeavour has been dedicated to the development of PV cells to utilise solar energy. For example, Germany is aiming to increase its share of renewable energies for electricity to be 25% - 30% by 2020, with photovoltaics intended to be a major contributor.[1] The same trend is present worldwide, resulting in typical growth of the photovoltaic market of 30-40% per annum over recent years.[2]

Currently, photovoltaic energy is one of the most expensive sources of energy (Chart 1.1). To establish the widespread use of PV cells as a source of clean and renewable energy, the cost per watt (CPW) of solar energy needs to be significantly reduced. Currently, the main photovoltaic technology is based on crystalline silicon, which entails high manufacturing costs. Alternative inorganic thin film technologies are gaining momentum, but have so far only obtained a small market share. Despite the drop of CPW of crystalline silicon PV cells over the last decade,[3] they are still generally too expensive to compete with conventional grid electricity without the benefit of government subsidies.[4] Furthermore, crystalline silicon PV modules are typically fragile, heavy and have an energy payback time of about 4 years.

In recent years, increasing attention has been given to solar cells based on organic semiconductors utilising π-conjugated polymers, the primary focus of this thesis. These polymers are promising in terms of their electronic characteristics and ease of processing. In

addition, they offer the prospect of low-cost production and applications on flexible substrates, resulting in a weight of only ~ 500 g/m^2.[5] Such materials allow the use of printing technologies and thin plastic films for roll-to-roll processing, potentially attractive for low cost and large area applications.

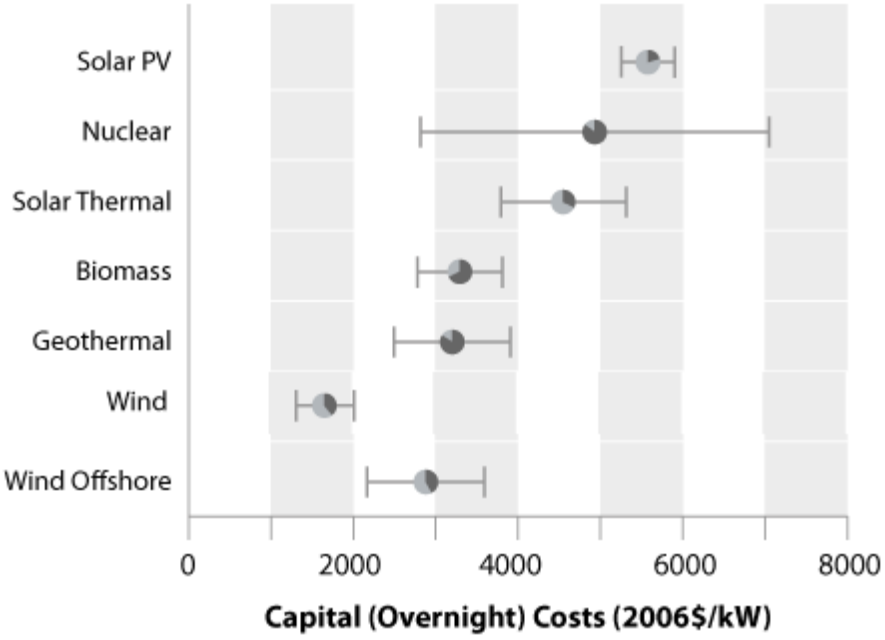


Chart 1.1 This chart indicates the range of recent cost estimates for renewable energies. The estimates are shown in dollars per installed kilowatts of generating capacity, (**www.NREL.gov**). Capital overnight cost does not consider variation in inflation and interest rates.

1.2 Historical Context

The French physicist Alexandre Edmond Becquerel discovered the photoelectric effect in 1839, when he examined the effect of light on an electrode immersed in a conductive liquid. [6] Photoconductivity was then reported in selenium by Smith in 1873.[7] In 1954 the first silicon solar cell was developed at Bell Laboratories by Chapin *et al.*,[8] with an efficiency of 6%. Since then solar to electric power conversion efficiencies have reached 24.4% for crystalline Si PV cells[9] and 19.2% for Copper indium gallium diselenide thin film devices.[10] Silicon based photovoltaic cells accounted for 85% of world production of all solar cells in 2009.[11]

However, even though the price of these cells has been dramatically reduced over the last 50 years, PV energy production remains relatively expensive and photovoltaic energy supply accounts for less than 0.1% of the total world energy production.

One potential means to reduce the high costs of inorganic solar cells is the employment of organic materials. The first observation of photoconductivity in an organic compound (anthracene) was reported in 1906 by Pochettino.[12] During the 1970 and 1980's extensive research was undertaken on organic small molecule semiconductors.[13-16] The first efforts to fabricate organic photovoltaic devices, using small molecule light absorbers, date back to 1975; however efficiencies at this time did not exceed 0.001%.[17]. For most of their history polymers had attracted interest as another electrical insulator. Photoconductivity in the poly(N-vinyl-carbazole) (PVK) polymers was first reported in 1957.[18] However interest in the electrical properties of polymers only seriously took off in the 1970s, when the Japanese scientist Hideki Shirakawa combined with efforts of American scientist, Alan Heeger and Alan MacDiarmid from New Zealand, to discover that doped polyacetylene could achieve metallic conductivity. This triggered intense research on conjugated polymers.[19] The surprising discovery of these three pioneers was later honoured with the Nobel Prize in Chemistry in 2000 and lead to a revolution in the semiconductor research field.[20-22] However, it was not until late 1990s that highly purified, soluble conjugated polymers became widely available. Since then, conjugated polymers have been extensively investigated for applications in a wide range of semiconductor devices including light emitting diodes (LEDs),[23,24] solar cells and thin film transistors (TFTs).[25]

Over the past decade, research in the field of organic solar cells has grown steeply worldwide and has lead to encouraging breakthroughs, with power conversion efficiencies increasing from 1% [26] to over 7%.[27] The report by Tang et al.,[26] using a small molecular donor- acceptor bilayer structure to achieve PV efficiencies approaching 1%, marked the first success. Bilayer devices fabricated from conjugated electron donor polymers with a small molecule fullerene as electron acceptor initially only yielded power conversion efficiencies of 0.1%,[28] due to limited interfacial contact area between the donor and acceptor layers. (For details of

donor/acceptor structures see section 1.6). These achievements were then followed by the new concept of a bulk heterojunction (BHJ) [29,30] – based upon intimate mixing of donor and acceptor material on nano-meter scale. Polymer-fullerene solar cells demonstrated by Heeger *et. al.* [29] were the first materials to utilise this bulk-heterojunction principle. Further studies showed that the employment of exciton blocking layers improved device efficiencies.[31,32] In parallel with these studies, Shaheen and co-workers realised a breakthrough to power conversion efficiencies exceeding 2.5% by tuning the morphology of bulk heterojunction solar cells based on poly[2-methoxy-5-(3',7'-dimethyloctyloxy)-*p*-phenylene vinylene] (MDMO-PPV) and 3'-phenyl-3'*H*-cyclopropa[1,9](C_{60}-I_h)[5,6]fullerene-3'-butanoic acid methyl ester (PCBM).[33] Following these contributions, a range of PV, materials and device configurations centred on the concept of heterojunction structures are the subject of wide spread research.

While the solar energy industry has continued to grow steadily over the past decade, it is necessary for solar cell technologies to become more cost effective and versatile before photovoltaics can significantly impact global energy consumption. One means to this end may lie in the rapidly developing field of organic photovoltaics. Before the potential benefits of organic solar cells can be realised, significant advantages must be taken to better understand the fundamental material properties of organic semiconductors which will enable further development of this technology.

1.3 Organic Solar cells

Most solar energy conversion systems are based on the utilisation of incident solar energy to generate dissociated charges. These charges can subsequently be used for electrical power generation (photovoltaics). Efficient devices require separation of these photogenerated electron-hole pairs into long-lived dissociated charges with a high quantum yield and minimal loss of free energy (this is discussed in section 1.5 in detail).

It is possible to separate existing solar cells into two distinct categories on the basis of their charge generation mechanisms: conventional (most inorganic) solar cells and excitonic solar cells.[23,31, 26,30,33-50]

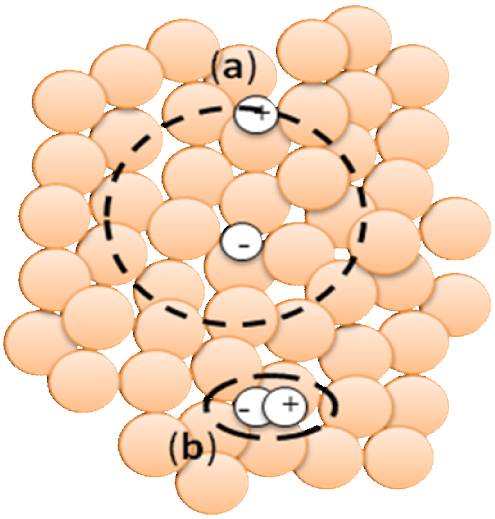


Figure 1.1 Visual representation of excitons in (a) inorganic and (b) excitonic (organic) materials.

The function of the organic solar cells is fundamentally different from inorganic counterparts. The primary difference lies in the type of states that are generated when sunlight is absorbed (Figure 1.1). The process of photon absorption gives rise to a transition between electronic states, corresponding to the excitation of an electron from the material's highest occupied molecular orbit, HOMO (valence band), to its lowest unoccupied molecular orbital, LUMO (conduction band), leaving a hole in the HOMO orbital. In organic materials, these electrons and holes are not free charge carriers but rather they are tightly bound by a strong Coulomb attraction; this state is termed an (singlet, S_1) exciton. The Coulomb attraction is given by the electric charge e, permittivity of vacuum ε_0, dielectric constant of the surrounding medium ε_r and the distance between the electron-hole pair separation r:

$$V = \frac{e^2}{4\pi\varepsilon_0\varepsilon_r r} \quad (1)$$

The Coulomb interaction causes a large binding energy for the exciton (E_B^{exc}). The nature of the exciton depends on its binding energy. In three-dimensional inorganic semiconductors the exciton binding energy is small (<0.1 eV) due to the high dielectric constant of silicon (ε_r ~ 12) and the more delocalised electronic states and so the excited electron and its corresponding hole are immediately separated as overcoming the Coulomb attraction is relatively easy. However, binding energies in organic semiconductors are usually large (0.1 eV to 1 eV)[51,52] in comparison to thermal energy k_BT (0.025 eV). As such, overcoming their larger Coulomb attraction is more difficult. This is due to their smaller dielectric constant, ε_r ~ 3-4, and the weak, non-covalent, van der Waals interactions between molecules; this results in a low intermolecular orbital overlap and more localised electronic states, resulting in the formation of Coulombically bound excitons. This relatively large binding energy means that unlike inorganic semiconductors, e^--h^+ pair exists as natural, bound states, which do not show significant thermal dissociation. Efficient device performance relies upon the photogenerated exciton moving to a donor / acceptor interface (in devices requiring film thickness less than the optical absorption depth) so that an exciton can overcome its binding energy in order for dissociation to occur. In the absence of mechanisms to dissociate the excitons into free charge carriers, the exciton will undergo radiative and non-radiative decay, with a typical exciton lifetime in the range 100 ps – 1 ns. This results in relatively small exciton diffusion lengths (L_{ex} ≈ 3–10 nm) where L_{ex} is the average length over which an exciton can diffuse within the polymer before relaxation of the electron to its ground state.[53]

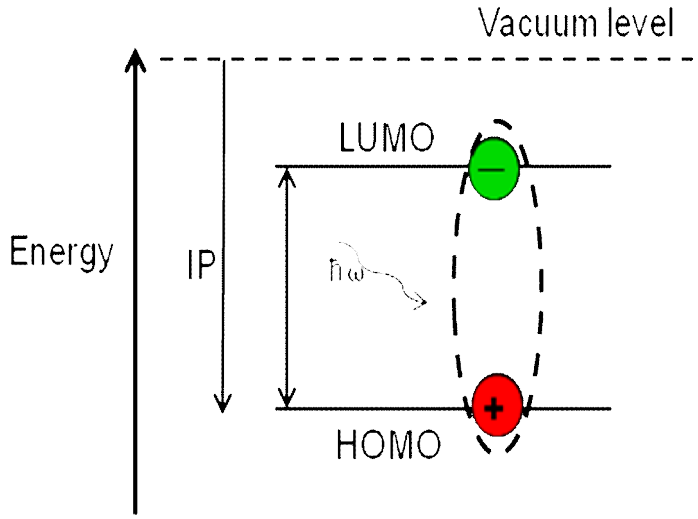


Figure 1.2 Exciton generation. Absorption of photons with energies equal or greater than the band gap energy, Eg, forms an electron, e^-,in the lowest unoccupied molecular orbit, LUMO and a hole, h^+ in the highest occupied molecular orbital, HOMO. The strong Coulomb interaction between the hole and the electron forms a strongly bound electron-hole pair, termed exciton.

Several analyses have concluded that organic solar cells, although currently producing relatively low power conversion efficiencies (~ 5 – 7 %)[54-56] compared to inorganic solar cells, have the potential to compete effectively with alternative solar cell technologies. However, in order for this to be feasible, the efficiencies of organic solar cells need further improvement; this is the focus of extensive studies worldwide. The electronic properties of organic semiconductors, including macromolecules, dyes, dendrimers, oligomers and polymers are based upon conjugated π electrons. A conjugated system is based on an alternation between single and double bonds. The backbone of conjugated polymers comprises a linear series of overlapping p_z orbitals that have formed via sp^2-hybridisation, thereby creating a cloud of delocalised electrons. In many conjugated polymers, the delocalisation of these electrons is divided into many segments by structural disorder. The interaction of the π electrons dictate the polymer's electronic structure and optical qualities.[57] In general, the π and π* orbitals, corresponding to the highest occupied molecular orbital and

lowest unoccupied molecular orbital respectively, enable the movement of the electrons by hopping from segment to segment. In this way, organic semiconductors can support an electric current and so can be used to fabricate PV devices.

All solar cells have the function of taking the energy inherent in sunlight and converting it to electricity. The electrons and holes generated by sunlight travel from where they are formed to electrodes, creating an electric current. Due to the differences between organic and inorganic cells, the architectures of organic PV cells need to be intrinsically different from the design employed for inorganic materials.[49] Organic solar cells can be grouped into two main classes according to their underlying working principle: dye sensitized solar cells (DSSCs)[58] and organic heterojunctions (HJs).[59,60]

What will follow in the next two subsections are short descriptions of the main different types of organic solar cells. As the work done on this thesis is concerned with bulk heterojunctions (BHJ), we will then focus our concentration only on BHJ solar cells.

1.3.1 Dye-sensitised Solar Cell (DSCS)

DSCS, also known as **Grätzel cells,** were invented in 1991[61] by Michael Grätzel and co-workers and have since then reached externally verified efficiencies of 11%. DSSC's consist of two semiconducting glass electrodes, one coated with an inorganic nanoporous film, usually titanium dioxide (TiO_2) that is then coated with a layer of light absorbing dye which, upon illumination, injects an electron into the surface of the inorganic material. Continuous pathways to the electrode then allow for electron collection while the hole charge is carried to the anode by an electrolyte, usually based on a iodine/tri-iodide redox couple.

These cells exhibit a high dielectric constant for the electron accepting TiO_2 (ε_r~80) and the electrolyte and thus overcoming the electron-hole Coulomb attraction is facile (as seen from equation 1). As a result, after the initial electron injection step from the molecular excited state, the Coulomb attraction of electrons and holes is effectively screened and becomes

negligible.[62] However, for all organic polymeric and molecular films, overcoming this Coulomb attraction is significantly more challenging.

1.3.2 Heterojunction organic solar cells

Within the class of HJ organic solar cells, two main methodologies have been explored to develop a viable device: the donor acceptor bilayer,[39,63,64] mostly achieved through vacuum deposition,[65] and the BHJ (Figure 1.3) – an interpenetrating network of donor and acceptor materials which is widely known as a bulk heterojunction (BHJ) -[66-68] more readily suitable for solution processable materials.[30,69] Typical materials for BHJs are currently π-conjugated polymers as the electron donor (such as polythiophenes) in combination with small molecule fullerene derivatives as the electron acceptor.[59] The employment of small organic molecules as electronic components integrated on nanometre scale with conjugated polymers is proved to be a good active layer for photovoltaic blends. A major prerequisite for the acquirement of high values of external quantum efficiencies from BHJ based devices are the appropriate matching of the HOMO and LUMO energetics between the blend components that will allow for efficient charge photogeneration on the electron-transporting (n-type) and hole-transporting (p-type) components of the blend.

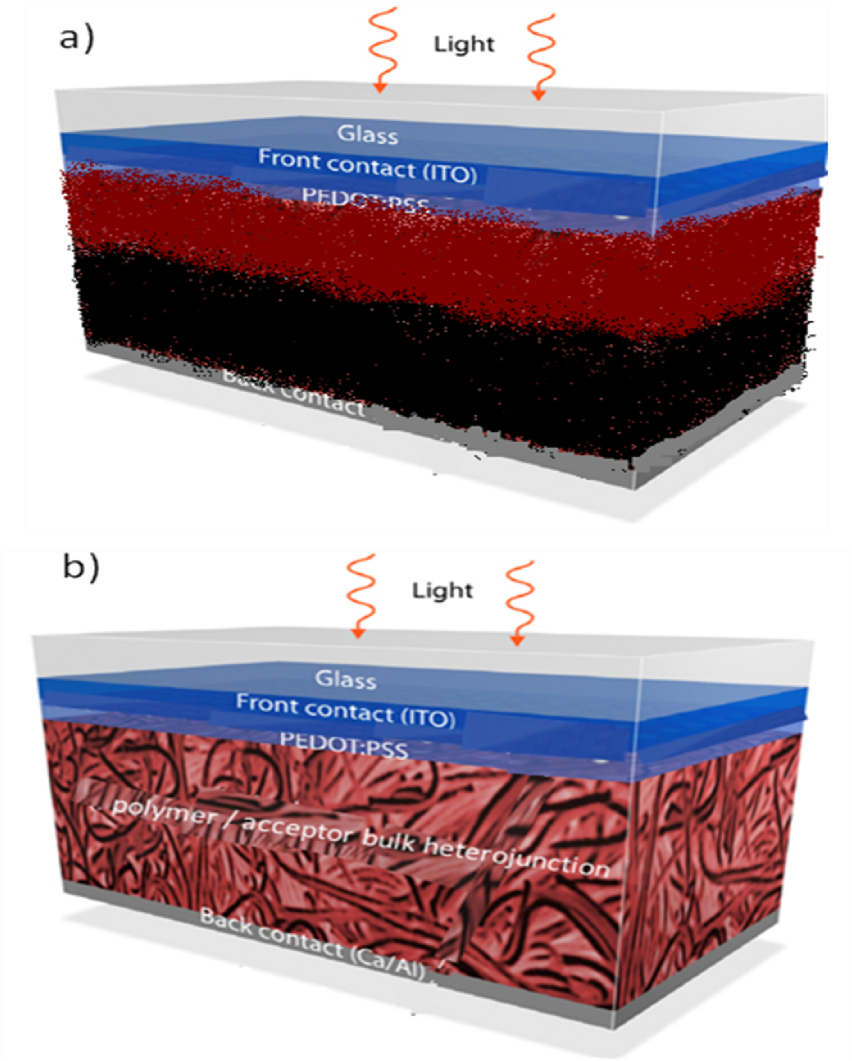


Figure 1.3 Schematics of a) a heterojunction bilayer where most of the polymer phase is further from the interface than the exciton diffusion length and b) a bulk heterojunction based device, which enables a much higher percentage of the polymer phase to be less than exciton diffusion length from the interface.

1.3.2.1 All molecular semiconductor and pure conducing polymer solar cells

Small molecular based solar cells are typically fabricated by molecular beam deposition, where thin layers of blends or multi-layers of small molecules can be deposited onto a substrate by sublimation. Beam deposition has advantages in having fine control over the growth of the materials on the substrate and that both the blend and electrode can be deposited in sequence using the same equipment under high vacuum. Device architectures can be either bilayer or bulk heterojunction (mixing of donor and acceptor).

Polymer-polymer solar cells are made from a mixture of two conjugated polymers, one more electronegative than the other. The ease of solution processability of polymers is very attractive, favouring their commercialisation. However, to date polymer- polymer solar cells have shown lower device efficiencies than polymer / fullerene blends. Despite the devices achieving high open circuit voltages (Voc > 1V), low fill factors (see section 1.4) and poor current collection badly limit their efficiencies.[70-72] This has been assigned partly to lack of optimum phase segregation.

1.3.2.2 Polymer/small molecule solar cells

For photovoltaic cells made from pristine conjugated polymers, energy conversion efficiencies were typically in the range of 10^{-3}-10^{-2} %,[73-75] too low to be used in practical applications. The discovery of fast photoinduced electron transfer at the interface between a semiconductor polymer and buckminsterfullerene, C_{60} and its derivatives,[73,76] provided a molecular approach to improve carrier generation and collection efficiency.

Efficient charge photogeneration has long been recognised as a key challenge for molecular based solar cells. In order to overcome the dissociation challenges set by the properties of organic small molecules and polymers, it is necessary to optimise HOMO-LUMO energetics of the donor and acceptor components in the blend, and also create a morphology which aids charge photogeneration and collection.[5,33,77-79] By controlling the morphology of the phase separation into an interpenetrating bi-continuous network of donor (D) and acceptor (A)

phases, one can achieve a high interfacial area within a bulk heterojunction film.[47,69] Moreover, a bi-continuous network can provide the needed pathways for collecting the separated carriers at the external electrodes: holes from the donor phase and electrons from the acceptor phase. Thus, thin film sandwich devices with a bi-continuous BHJ as the active material can potentially function as efficient photovoltaic cells and efficient photodetectors with high carrier collection efficiency.[69,80] The efficient and balanced extraction of the photoinduced charge carriers via the electrodes of the device demands the formation of sufficient percolation pathways[81] that will minimize charge carrier recombination events and thickness limitations.[82,83]

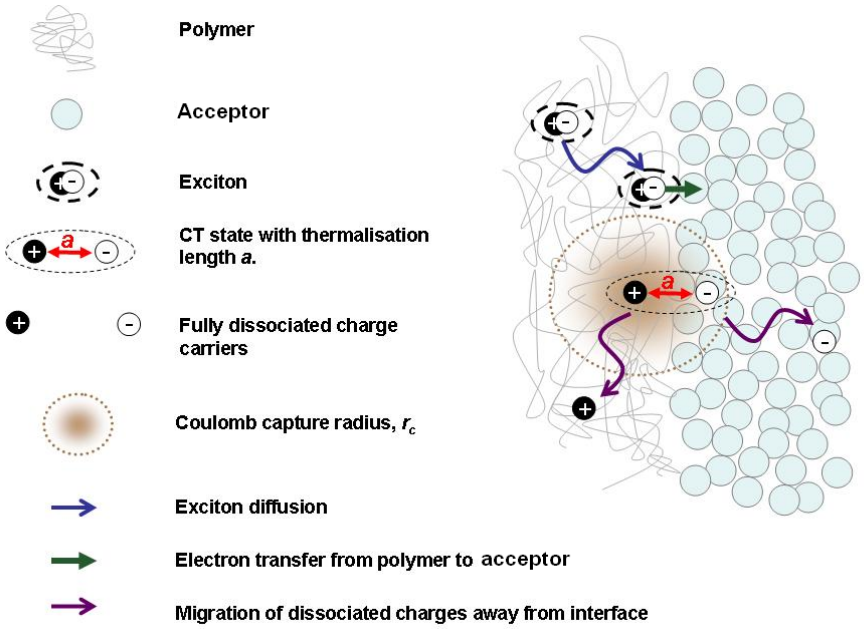


Figure 1.4 Schematic of charge dissociation at the polymer / acceptor interface. The polymer singlet exciton diffuses to the interface, where electron transfer to the PCBM occurs to generate the charge transfer (CT) state. The CT state has an initial electron-hole separation distance of *a* (the thermalisation length). Onsager Theory would predict that the probability of full dissociation into the free charge carriers depends upon the ratio between *a* and the Coulomb capture radius, r_c. For simplicity, the Coulomb capture radius is drawn as spherical. (see section 1.6 for more details.)

The process of charge generation in a bulk heterojunction, as described in equation 2, can be summarised as the following cascade: Absorption of a photon generates an exciton. The exciton subsequently diffuses until it reaches an interface. At this interface, the exciton may be dissociated if an electron is transferred from the donor material to the acceptor material - creating a moderately separated bound electron-hole pair or 'charge transfer' state (we discuss this state more in detail in section 1.4.4). Dissociation of these generated bound electron-hole pairs creates free charge carriers which can then be transported and collected by the device electrodes. The process of charge photogeneration at an organic donor / acceptor interface is illustrated in Figure 1.4.

Simple single layer organic solar cells, based on pristine polymer and two electrodes of different work function, resulted in poor photocurrent efficiency.[84] Since the seminal work of Tang,[26] however, organic solar cells have undergone a gradual evolution that has led to energy conversion efficiencies of over 6%.[85] Keeping pace with this increase in device efficiency is the number of refereed journal publications related to organic PV materials and devices, which has increased exponentially for approximately the past three decades. The benchmark materials for polymer/small molecule photovoltaics are based on thiophene derivative donor-acceptor molecules with the fullerene 6,6-phenyl C_{61}-butyric acid methyl ester (PCBM see scheme 1 for chemical structure) as the electron acceptor.[85] Other material classes commonly used as acceptors are perylene derivatives and oligothiophenes.[86-88]

Current organic solar cells have reached power conversion efficiencies (PCE) of up to 8% and lifetimes above 1000 hours under continuous illumination (although not with the same materials), which are values close to those required for entering the market, at least in niches.[89,90] Consequently, companies have just started production[91] or are preparing to make them commercially available soon[92-95] to offer an inexpensive renewable energy resource. However, to reach a broad market share, in particular in large-scale energy generation, the efficiencies and lifetimes have to be increased substantially. The benchmark here is crystalline silicon with more than 20% module efficiency and lifetimes larger than 25 years.[96]

Device photocurrent generation efficiency is believed to depend strongly on charge photogeneration (Figure 1.5). Previous studies have demonstrated changes in external quantum efficiencies/short circuit current can be directly linked to changes in charge photogeneration yield for a variety of thiophene-based polymers.[97,98] As such, monitoring the optical absorption of photogenerated charges can be exploited as a tool to approximate the short circuit current of a device. There are many examples of organic donor/acceptor heterojunctions that achieve efficient exciton quenching at the donor/acceptor interface but do not achieve efficient photocurrent generation. This has been related to the efficiency of charge photogeneration at the donor/acceptor interface. Indeed, many reports have related sub-unity photocurrent quantum yields to charge photogeneration limitations.[97,99-102] It is thus apparent that understanding the mechanism of charge photogeneration at donor/acceptor is of great importance for the development of efficient organic photovoltaic devices.

Our understanding of the mechanism of charge photogeneration in organic solar cells remains incomplete. However, significant progress has been made over the last few years, in particular in understanding the roles of interfacial energetics and nanomorphology in determining the efficiency of this process. In this thesis, we will be focussing in particular upon the role of interfacial charge transfer states in influencing the efficiency of charge generation and subsequently photocurrent generation in organic solar cells. The following section starts off with some fundamental theories relevant to charge separation or organic materials at donor / acceptor interfaces.

1.4 Theory of Charge Photogeneration

In this section we provide an overview of the theories relative to charge photogeneration by identifying and discussing the states that play a role in the efficiency of charge photogeneration.

The process of charge generation and transport within organic PV cells is believed to occur in consecutive steps, namely, exciton generation and dissociation, charge dissociation and

charge collection (depicted in Figure 1.5a). Each step has an efficiency, which their product determines the external quantum efficiency, EQE. [103]

$$EQE = \eta_{ABS}\,\eta_{DISS(EXC)}\,\eta_{DISS(CT)}\,\eta_{COLL} \qquad (2)$$

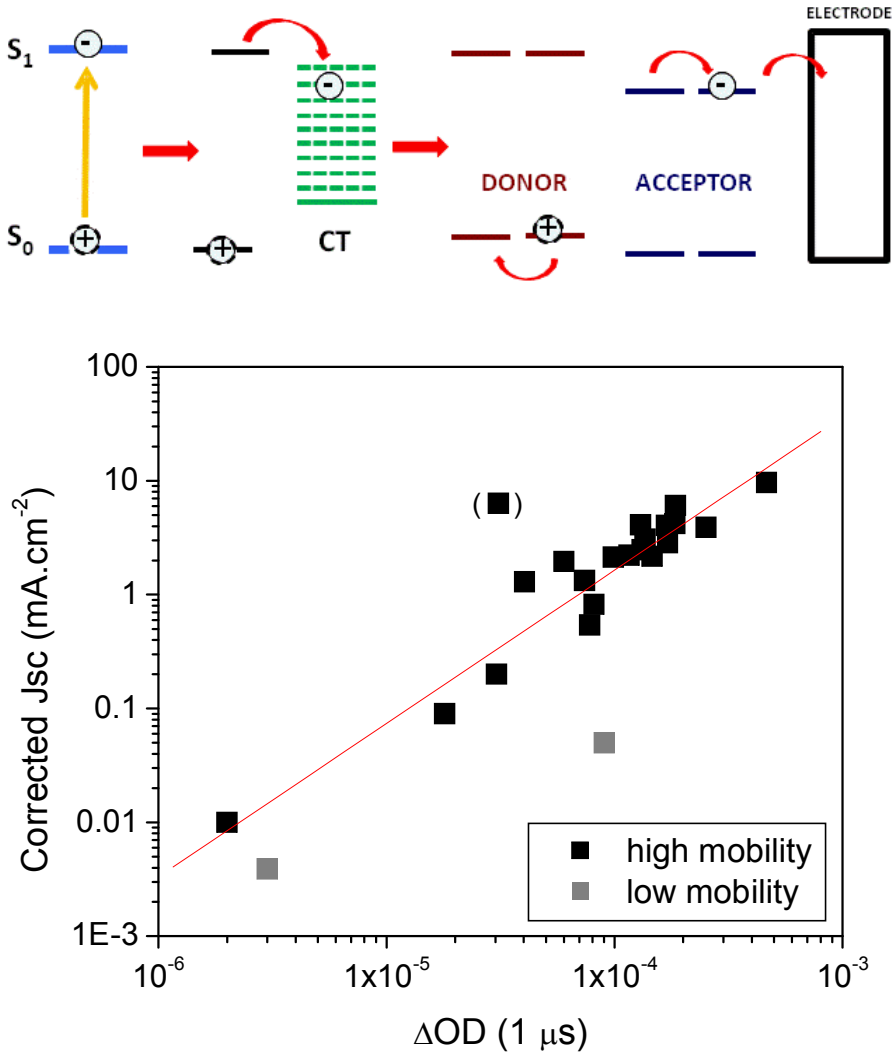


Figure 1.5 top: Consecutive steps in organic donor/acceptor photovoltaics. Optical absorption and exciton formation; (ii) exciton migration to the donor-acceptor interface; (iii) exciton dissociation into charge carriers, resulting in the appearance of holes in the donor and electrons in the acceptor and; (iv) charge collection at the electrodes. Figure taken from.[99] bottom: The correlation between ΔOD measured by TAS on thin blend films and the Jsc measured in complete devices, for a series of polymer:PCBM blend systems of varying PCBM composition (most with 50 wt% PCBM). Taken from[104].

Our objective in this thesis is the overall efficiency of charge dissociation ($\eta_{DISS(CT)}$) (and subsequently determination of steps limiting charge photogeneration). Thus, we consider the exciton dissociation and charge separation steps.

1.4.1 Properties of excitons

The properties of excitons in polymer materials have been studied extensively. Some of these properties, such as exciton diffusion length, are important parameters for organic solar cells as they strongly influence the probability of exciton dissociation and thus charge photogeneration.[105-112] The exciton diffusion length is the average distance an exciton can travel before relaxing back to the ground state. Dissociation of the exciton must therefore occur within this distance. Clearly, this will limit the extent of the donor/acceptor interfacial area and domain sizes (collectively referred to as phase segregation) possible in a bulk heterojunction blend for efficient device performance. (Chapter 3 clearly demonstrates this.) In general, phase segregation on the order of the exciton diffusion length is desired. A typical method of estimating this parameter is to assess the photoluminescence quenching of pristine polymer as a function of layer thickness. Measurements [109,110,113] have yielded exciton diffusion lengths of 5 – 14 nm for poly(*p*-phenylene vinylene) (PPV) derivatives and 3 – 9 nm for poly(3-hexylthiophene) (P3HT).[114,115]

Efficient device performance relies upon the photogenerated excitons diffusing to an interface so that exciton dissociation can occur before exciton relaxation to the ground state.[116] The optical transition from S_0 (ground state) to S_1 can lead to an excited vibronic level, depending on incident photon energy. If the initially generated exciton is vibrationally excited, i.e. higher-lying singlet excitons are created, the exciton diffusion process allows time for intramolecular vibrational relaxation from $S_1(\nu = n)$ to $S_1(\nu = 0)$ to take place non-radiatively on a timescale sub-100 fs.[111] The speed of this internal conversion therefore implies emission only occurs from the lowest lying vibronic energy level, $S_1(\nu = 0)$.The internal conversion of $S_1 \rightarrow S_0$, however, occurs on a timescale several orders of magnitude

slower (100's picoseconds to nanoseconds). This is illustrated by Jablonski diagram in Figure 1.6.

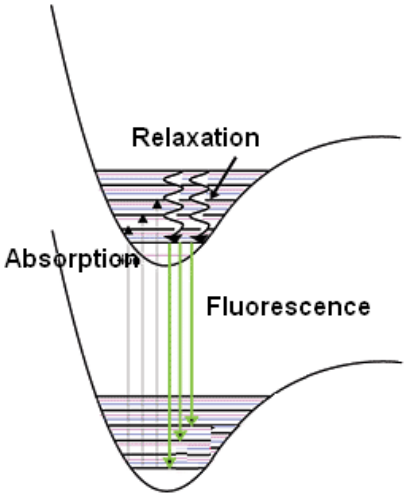


Figure 1.6 The diagram shows the electronic basis of the phenomenon of fluorescence.

1.4.2 Exciton dissociation

In Eq. (2) the parameter $\eta_{DISS(EXC)}$ is the exciton dissociation yield, which represents the ability of photogenerated exciton to diffuse through the polymer without relaxation back to ground state.

The inability to efficiently dissociate excitons in pristine single layer materials has led to the employment of blends of electron donating and electron accepting materials to produce driving force for electron transfer and energetically stabilise the charge transfer state in organic solar cells. In 1995 it was first realised that by fabricating the light absorbing semiconductor with a second component having a lower LUMO energy level, it was possible to increase the yield of exciton dissociation.[30,69] The difference in electron affinities creates a driving force at the interface between the two materials that can be strong enough to separate the photogenerated excitons.[73,117-119] The LUMO and HOMO of the electron acceptor should be lower than those of the donor, otherwise there maybe some possibility for energy transfer

rather than charge transfer (Figure 1.7). It is necessary to incorporate materials with an energy offset greater than the Coulomb binding energy of the exciton, E_B^{exc}, allowing the primary electron transfer step to be energetically downhill. However, this electron transfer does not necessarily directly generate dissociated charge carriers as we discuss further below.

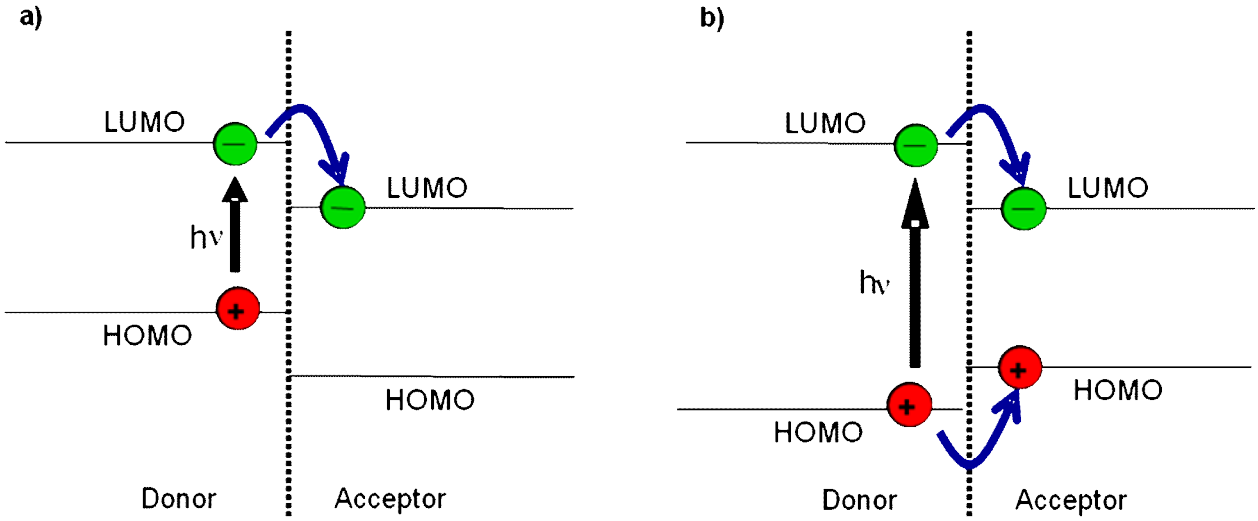


Figure 1.7: A heterojunction interface consisting of two different semiconductors, an electron donor (D) and an electron acceptor (A). Charge carrier generation can occur by splitting the exciton or energy transfer occurs where the exciton is transferred from the donor to the acceptor.

1.4.3 Charge transfer state

Once the exciton diffuses to a donor / acceptor interface and is quenched by electron transfer, bound electron-hole pair states with partial spatial separation may be generated. These states consist of the hole localised on the HOMO of the donor orbital and the electron on the acceptor LUMO. Despite the charges located on adjacent species, the separation between the electron and the hole is still moderate, typically of the same order of magnitude as the size of the molecules (or molecular orbitals) concerned: 0.5 – 1 nm. Therefore the charges are still

Coulombly attracted to each other such that the charges cannot be identified as two independent freely moving entities. Rather, we can consider this state as a charge transfer (CT) state. The conversion of excitons to charge transfer states depends on the time it takes for an exciton to travel to the nearest interface which is clearly dictated by the morphology of the blend film. This CT state may have a lifetime considerably greater than the lifetime of the exciton. The charge transfer state may play a crucial role in charge generation and recombination and thus be of key importance in organic solar cells. It should be noted that literature uses a range of nomenclature for such interfacial charge transfer states, including geminate pairs, bound radical pairs and exciplexes.[102,120-127]

It is generally agreed that the charge transfer state can be achieved by utilising a suitable energy offset between the donor and acceptor LUMO levels, as illustrated in Figure 1.7a. This requires that the energy offset is greater than the Coulomb binding energy of the exciton, E_B^{exc}. As mentioned above, this initial electron transfer step results in only a modest spatial separation of the electron and hole. At this spatial separation, the electron and hole still exhibit a significant Coulomb attraction. Employing a simple point charge approximation, the magnitude of this Coulomb attraction, which we will refer to as the charge transfer state binding energy E_B^{CT}, can be estimated to be in the range 0.1 – 0.5 eV,[113,121,128] as illustrated in Figure 1.8. The magnitude of this Coulomb attraction is usually estimated to be lower than the Coulomb attraction of the singlet exciton (Figure 1.8) due to the increased electron-hole separation distance, however, it is still clearly sizeable compared to the thermal energy (0.025 eV) and, in principle, presents a large energetic barrier to charge photogeneration at donor/acceptor organic interfaces.

The exciton binding energy, E_B^{exc}, is usually defined as the potential energy difference between the neutral singlet exciton and the two fully dissociated, structurally relaxed charge carriers in the same material. Similarly we define the charge transfer state binding energy, E_B^{CT}, as being the potential energy difference between the thermally relaxed, nearest neighbour charge transfer state at the donor/acceptor interface and the two fully dissociated, structurally relaxed charge carriers in the donor and acceptor materials.

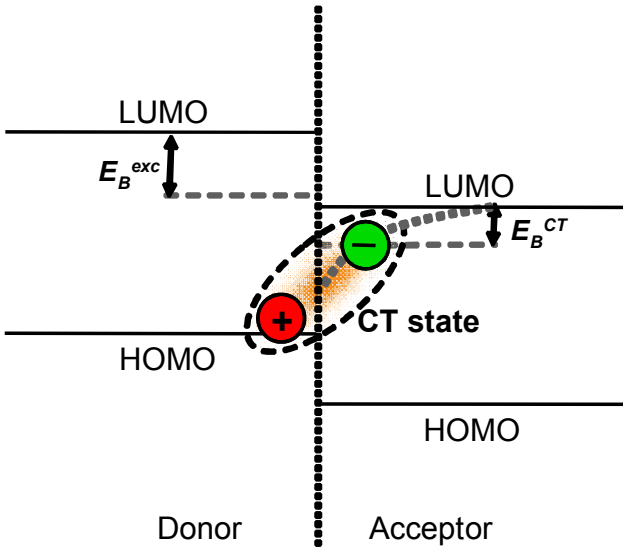


Figure 1.8 The energy of the exciton and CT state depends upon the Coulomb attraction of the electron and hole and therefore their spatial separation, as illustrated by the dotted curve. Figure also illustrates typical binding energies for the exciton and CT states (E_B^{exc} and E_B^{CT} respectively). Adapted from reference[129].

From the CT state two competing pathways exist; the CT states can either undergo geminate recombination (of the initially formed bounded electron-hole pairs) to either the ground state, S_0, dictated by its rate of recombination (k_{rec}), or a triplet exciton, T_1, depending on the spin state of the CT state. Alternatively, this CT state can undergo full charge separation to form dissociated charge carriers to escape their mutual attraction (where rate of separation, $k_{diss} > k_{rec}$). A schematic of charge dissociation is depicted in Figure 1.9. The effect of such CT states on the efficiency of charge photogeneration yields and subsequently photocurrent yields is further discussed in Chapter 5 and 6.

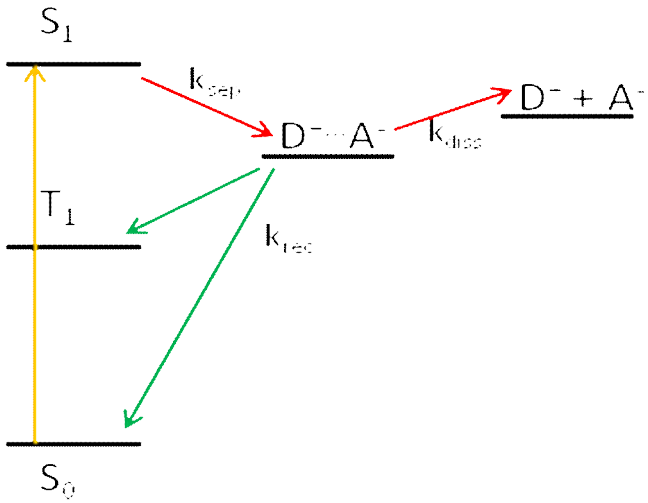


Figure 1.9 Energetic representation of charge dissociation. Optical excitation leads to the promotion of an electron from S_0 to S_1, which can be dissociate into a bound D^+….A^- pair (or 'CT' state) where the electron and hole still attract each other. Subsequently this state can either dissociate into free carrier charges or geminately recombination. k_{sep}, k_{diss} and k_{rec} are the rates for the separation of exciton into charge transfer state, dissociation of charge carriers and recombination, respectively. We note that most considerations of charge photogeneration do not include consideration of the change in entropy associated with changing from a single species (the exciton) to two separated charges with random positions relative to each other. It is apparent that entropy contribution serves to stabilize the CS states relative to the CT state (see Figure 1.13).

Charge generation may either occur from CT states formed from highly excited singlet states, hot excitons, or cold excitons via thermal activation. In terms of exciton quenching, it may be relevant to consider the energy difference between the exciton and thermally relaxed charge transfer state, (indicated as ΔG_{CT} in Figure 1.13). A study by Janssen *et al*,[130] on polymer/PCBM blends concluded that only a minimal driving force is required to generate the CT state, $\Delta G_{CT} < 0.1$ eV; as such, the principal energy loss required for charge separation occurs after the initial creation of the CT state, and is associated with overcoming the Coulomb binding energy of the CT state. This conclusion is consistent with the report by Ohkita *et al*[131] and suggests that the majority of free energy required for driving the

generation of free charge carriers is associated with the dissociation of the CT states into free charges, as we discuss further in chapters 5 and 6.

Considering parameter $\eta_{DISS(CT)}$ in Equation 2; this is the charge generation yield. Figure 1.13 emphasizes the potential importance of charge transfer states in the charge photogeneration mechanism. In particular, within this viewpoint the dissociation of CT state and subsequently the yield of fully dissociated charges is likely to depend on the kinetic competition between the relevant processes. We discuss this in more detail in section 1.6.

1.4.4 Mechanism of charge recombination

Bimolecular recombination involves the recombination of fully dissociated charge carriers that did not previously belong to the same charge transfer state. Geminate (monomolecular) recombination, in contrast, involves recombination of bound charge carriers that were generated from the same exciton. There are two possibilities for this type of recombination. Firstly, geminate recombination could occur between the two charges while coulombically bound in the CT state. Secondly, if after escaping their Coulombic attraction, both charges remain confined by the physical sizes of their respective domains, such that each electron can only recombine with its original hole, then recombination remains a monomolecular process. The parameters affecting the efficiency of this recombination are discussed in chapter 3.

Bimolecular recombination differs from monomolecular (or geminate) recombination in that the charges have diffused away from each other before recombination where the diffusion process significantly slows the overall kinetics. Thus, in general, geminate recombination dynamics are expected to be faster than bimolecular recombination. Typical timescales reported for geminate recombination in organic donor/acceptor films range from 100's of picoseconds up to ~ 100 ns. Bimolecular recombination dynamics have been observed extending out to the millisecond timescale. Apart from distinguishing these recombination processes on the basis of their timescale, it is possible to distinguish them in terms of their kinetic and excitation density behaviour. In general, the dynamics of geminate recombination should be independent of excitation density (except at very high excitation densities such that

different CT states interact with each other) and exhibit monoexponential decay dynamics. In contrast, bimolecular recombination involves the recombination of two fully dissociated charge carriers, and thus follows second order kinetics. This results in the recombination dynamics exhibiting power law type decay dynamics which accelerate as the excitation density is increased. In practice, the bimolecular recombination dynamics of organic donor / acceptor films have been shown to be strongly influenced by the presence of charge trapping.

In a blend of a polymer and a small molecule, such as the well studied polythiphene:PCBM blend,[97,126,132] a model has been described for charge photogeneration and the timescales of initial charge-transfer state generation, its geminate recombination and its spatial separation.

1.4.5 Onsager Theory

Onsager theory was originally developed to describe the probability that a photogenerated electron-hole pair in a weak electrolyte would escape its Coulomb attraction and dissociate into generate free charges.[133],[133] Specifically, the theory proposed that photon absorption generates a localised hole and a hot electron; the latter, due to its excess thermal energy then undergoes rapid motion until it thermalises at distance a (the thermalisation length) from the localised hole. The resultant electron-hole pair is analogous to the interfacial CT states referred to herein. The competition between dissociation of this electron / hole pair and its geminate recombination back to the ground state depends upon the magnitude of the Coulombic interaction felt by this species. Onsager proposed a definition for a coulomb capture radius (also called the Onsager radius), r_c: the distance at which the Coulomb attraction energy equals the thermal energy k_BT.

$$r_c = \frac{e^2}{4\pi\varepsilon\varepsilon_0 k_B T} \qquad (3)$$

where e is the charge of an electron, ε is the dielectric constant of the surrounding medium, ε_0 is the permittivity of vacuum, k_B is Boltzmann's constant and T is temperature. If the thermalisation length a is greater than the coulomb capture radius, the charge carriers are

considered to be fully dissociated. If, however, the thermalisation length is smaller than r_c, then the dissociation of the CT state into free charges occurs with an escape probability of *P(E)* while geminate recombination to reform the ground state occurs with a probability of 1 – *P(E)*. This is illustrated in Figure 1.11

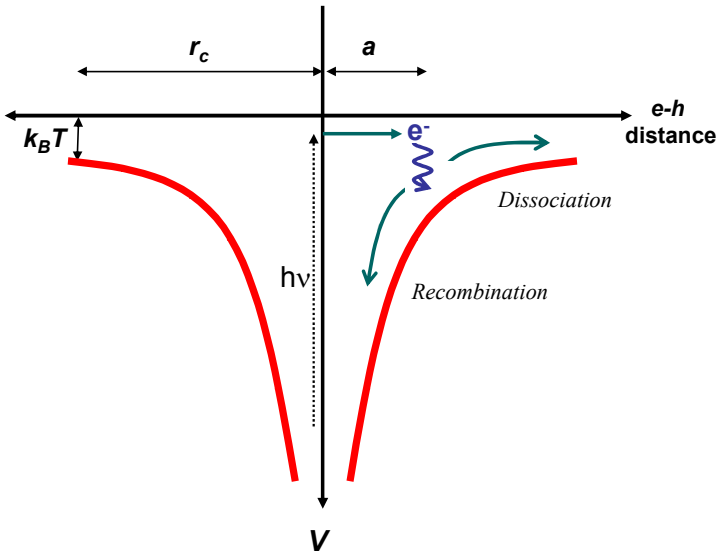


Figure 1.11 Potential energy diagram summarising Onsager theory for autoionisation. The red curve illustrates the potential energy resulting from Coulomb attraction as a function of electron-hole (*e-h*) separation. Photoexcitation results in generation of a hot, mobile electron. This electron subsequently thermalises at a particular distance from the hole (the thermalisation length, *a*). If *a* is less than the Coulomb capture radius, r_c (as is typical for organic systems), then the charge transfer state can either undergo geminate recombination or dissociate into free charges.

Whilst Onsager theory has proved very effective in predicting experimental observed variations in charge photogeneration for homogeneous systems, there remain significant challenges in the application of this theory to predict absolute yields of charge photogeneration at organic donor/acceptor heterojunctions.

1.5 Device operation

The operation of photovoltaic devices is based on conversion of sun's light energy into electricity.

Solar cell performance is characterised by steady state electrical properties of the device and are studied in the form of current voltage (J-V) curves which gives information on the parameters described below. A typical J-V curve is depicted in Figure 1.12.

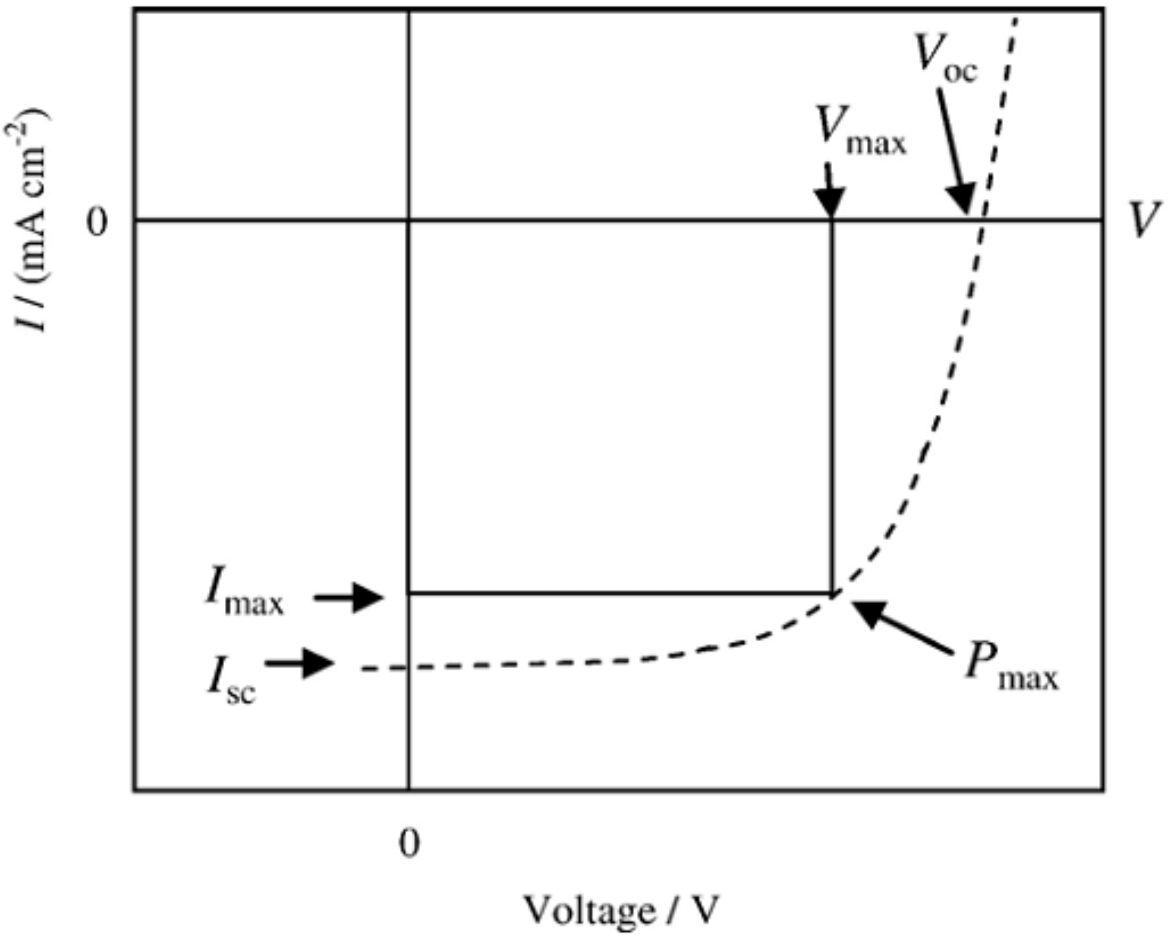


Figure 1.12 Current voltage characteristic of a typical solar. Taken from ref 56

The characterisation of photovoltaic cells is performed under AM1.5 conditions by a solar simulator. Air mass (AM) is a gauge for the length of the path which the light of the sun relative to the shortest way from the zenith to the ground takes.[66] Thus, AM1.5 conditions mean an angle of 48.2°, a global irradiance of 1000 W/m^2 and 25 °C.[134]

The key parameter characterising the PV cell performance is the power conversion efficiency, PCE, η.[135] The PCE is the ratio of the maximum power output (Pmax) to incident light power (P_{ill}):

$$\eta = \frac{P_{max}}{P_{ill}} = \frac{FF V_{OC} J_{SC}}{P_{ill}} \quad (4)$$

where FF is the fill factor, V_{OC} the open circuit and J_{SC} the short circuit current density.

The point where the electrical power reaches the maximum value represents the condition where the solar cell can deliver its maximum power to an external load. The ratio of this maximum power output to the product of short circuit current and open circuit voltage is termed the fill factor:

$$FF = \frac{P_{max}}{I_{SC} V_{OC}} \quad (5)$$

Another important parameter is the external quantum efficiency or EQE. The EQE is defined as the ratio of the number of photogenerated electrons collected under short-circuit conditions to the number of incident photons. The EQE (or IPCE) is usually measured using monochromatic light. The PCE for a cell generally increases with the EQE, although a high EQE does not necessarily guarantee a high PCE.

1.6 Parameters affecting charge photogeneration in organic bulk heterojunction films

The efficiency of organic solar cells partly depends on efficiency of charge photogeneration. Several factors have been shown to influence charge photogeneration. Experimental studies have addressed the role of charge transfer states,[97,100,121,126,136] excess thermal energy,[97,98,102,120,126,137] thermal annealing[97,100,138] and nanomorphology[132,139-143] in driving the charge photogeneration. However, other considerations suggest that more factors are also likely to play a role in determining the efficiency of charge photogeneration. The polarization (reorganization) energies of the states involved, the magnitudes of the electronic coupling, the thermalisation distance and timescale and the mobilities of the charge carriers are some of the additional factors likely to be involved. In this thesis we will be concentrating in particular upon nanomorphology and the free energy required for driving the charge photogeneration.

Figure 1.13 illustrates the state energy level diagram for sequential steps in charge photogeneration at an organic donor/acceptor interface with an emphasis on the potential importance of CT states in the charge photogeneration mechanism. This CT state will, in general, initially form with excess thermal energy, but will subsequently thermally relax. Where charge photogeneration occurs primarily from the hot CT state, the main kinetic competition will be between thermalisation and dissociation (processes **3** and **7** in Figure 1.13). However, when charge photogeneration occurs primarily from the relaxed CT state, the key kinetic competition will be between geminate recombination and dissociation (processes **5/6** and **8** in Figure 1.13). With the generation of CT state, the separation distance between the electron and hole increases and the charges therefore experience less coulombic attraction. If the separation distance between the electron and hole increases to greater than the coulomb capture radius, and the charges avoid geminate recombination, then the free fully dissociated charge carriers have formed. Due to the energy offset of the donor and acceptor energy levels, the electron injected into the acceptor will initially be thermally hot (corresponding to the 'crossing point' in Marcus electron transfer theory).

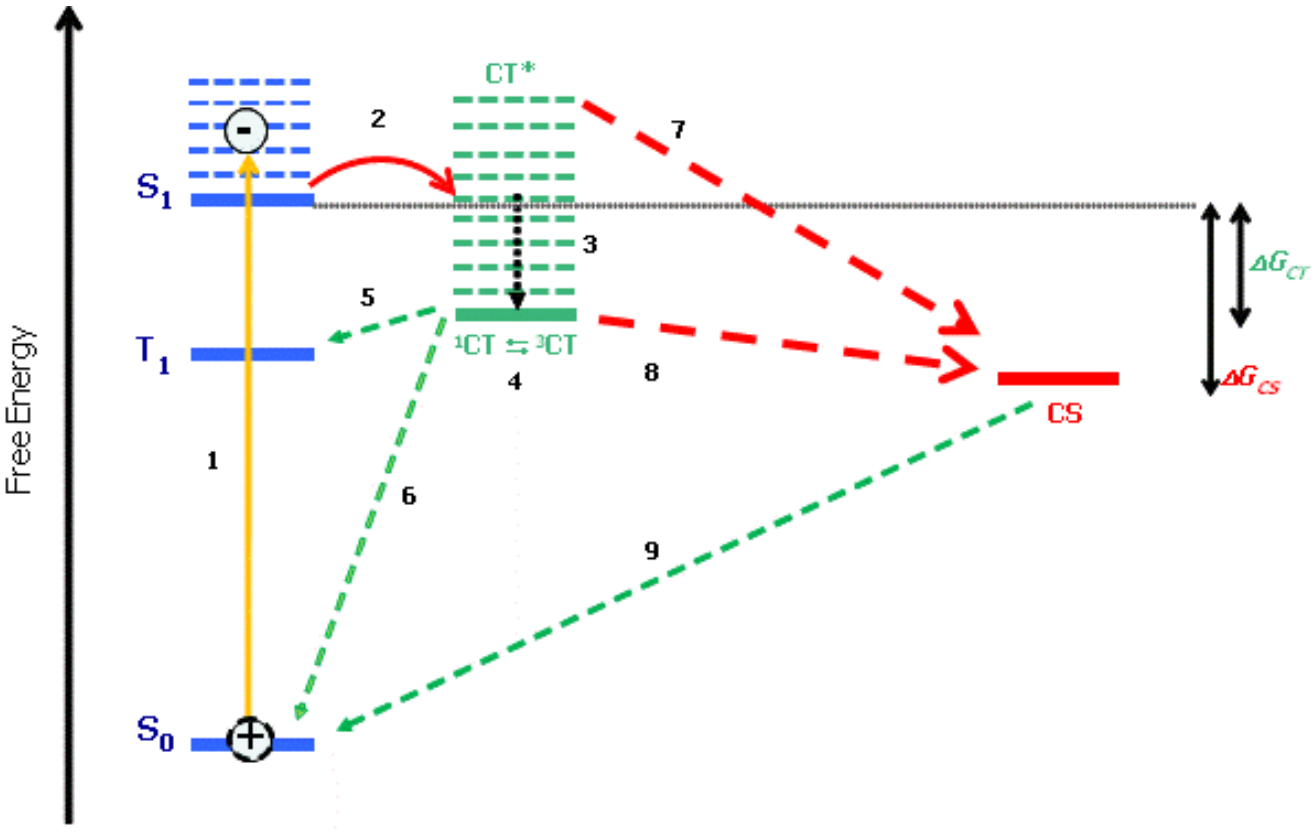


Figure 1.13 Energy diagram for charge formation in a donor/acceptor (D/A) system via a bound ($D^{+}\cdots A^{-}$) CT state, summarising the main processes involved in charge photogeneration. **1**: Photoexcitation to singlet exciton (S_1). **2**: Exciton dissociation to form the hot charge transfer (CT) state. **3**: Thermal relaxation of CT state. **4**: Spin mixing of the ^{1}CT and ^{3}CT states. **5**: Geminate recombination of the ^{3}CT to the triplet exciton, T_1. **6**: Geminate recombination of the ^{1}CT state back to the ground state, S_0. **7**: Dissociation of the hot CT state into a fully charge-separated (CS) state. **8**: Dissociation of thermally relaxed CT state into CS state. **9**: Bimolecular recombination of the CS state. This diffusion limited bimolecular process may result from either direct recombination or, more probably, via reformation of interfacial charge transfer states (shown as reversible arrows in processes **7** and **8**) and subsequent geminate recombination (**6**).[136] Figure taken from.[99]

The overall free energy loss associated with charge photogeneration is illustrated in Figure 1.13 as ΔG_{CS}. This parameter has been defined as the difference in energy between the charge separated state (estimated as the difference between the electron affinity of the acceptor, EA_A, and the ionisation potential of the donor, IP_D) and the singlet exciton, Es, of the polymer. $\Delta G_{CS} = Es - (IP_D - EA_A)$. The ΔG_{CS} is correlated with the LUMO level offset between the donor and acceptor, but it also includes the effect of the Coulomb binding energy of the exciton, E_B^{exc}. Efficient charge photogeneration and device performance requires a minimization of the free energy required to drive the charge-separation ΔG_{CS}, which is a key challenge for optimum conversion of the incident solar irradiation into electrical power

The idea that photoexcitation initially generates a hot electron (and/or hole) is used to study the influence of excess thermal energy in charge photogeneration. Following Onsager theory, in this picture the electron (or hole) is thought to thermalize at a particular distance from the hole (or electron). This distance is known as the thermalisation length. The thermalisation length compared to the Coulomb capture radius determines the efficiency of charge photogeneration. When charge photogeneration occurs at the donor/acceptor interface, it is plausible to use the same idea to determine the efficiency of charge dissociation. Generally, the electron injected into the acceptor (or hole into the donor) will be thermally hot relative to the acceptor LUMO level (donor HOMO). Thus using the idea of thermalisation length versus Coulomb attraction distance, it is possible to determine the yield of charge photogeneration at donor/acceptor interfaces.

A limited number of experimental studies have provided evidence indicating that hot CT states may be critical to achieving efficient charge photogeneration at donor/acceptor interfaces, which have been supported by theoretical calculations. For example, Peumans and Forrest[144] employed Monte Carlo calculations to simulate the dissociation of charges at a donor/acceptor interface based upon Onsager theory. The model assumed that the electron was injected with an excess thermal energy corresponding to the free energy difference between the exciton and the dissociated charges, ΔG_{CS} (see Figure 1.13). These calculations

were observed to be in agreement with photocurrent generation efficiencies for small molecule bilayer organic solar cells. Another paper by paper, by Morteani *et al.*,[102] focused upon electric-field dependent photoluminescence measurements of emissive CT states in (poly[9,9'-dioctyfluorene-co-bis-N,N0-(4-butylphenyl)-bis-N,N-phenyl-1,4-phenylenediamine]) : poly(9,9'-dioctylfluorene-alt-benzothiadiazole) (PFB:F8BT) and (poly[9,9'-dioctylfluorene-co-N-(4-butylphenyl)diphenylamine]) (TFB):F8BT blend films. It was concluded that thermal relaxation of the CT state leads to an emissive state with a shorter spatial separation compared to the initially generated, vibrationally hot, CT state; this relaxed CT state was termed an exciplex. The Coulomb binding energy of this 'exciplex', by virtue of its shorter electron-hole separation distance, was proposed to be too great to allow dissociation into the free charge carriers. Instead, this state decayed by radiative and non-radiative geminate recombination (or by thermal excitation to re-form the exciton). Dissociation into free charge carriers therefore must take place from the thermally excited CT state prior to thermal relaxation to the 'exciplex'. Both of these studies addressed the role of excess thermal energy in overcoming the Coulomb attraction of interfacial CT states. This concept was further addressed by Ohkita *et al*. In their work, they employed transient absorption spectroscopy to monitor the yields of dissociated polarons for a series of polythiophenes blended with 5 % PCBM. A clear correlation was observed between the yield of dissociated polarons and the free energy of charge separation, ΔG_{CS}, with the yield varying by over two orders of magnitude for a 0.3 eV change in ΔG_{CS}. PL quenching was observed to be over 70 % for the films studied, indicating that the 100 fold change in yield of dissociated polarons could not be assigned to a change in exciton separation at the interface. Rather, the change in polaron yield was assigned to variations in the efficiency of dissociation of interfacial CT states. The correlation between polaron yield and ΔG_{CS} is particularly striking as it implies that the efficiency of dissociation is dependent upon the energy of the starting exciton (ΔG_{CS}).

In photovoltaic devices, the requirement for excess thermal energy to drive charge separation has important implications to its efficiency. A large ΔG_{CS} corresponding to a large initial

thermal energy of the CT state limits the energy available to be output as electrical power. However, studies demonstrating a clear correlation between charge photogeneration and ΔG_{CS} are very limited to date.

Many studies have addressed the influence of nanomorphology in donor/acceptor blends on the properties of the CT state and subsequently charge photogeneration in such blends. Controlled morphology and optimal phase segregation (the collection of donor/acceptor interfacial area and domain sizes), having substantial effect on charge photogeneration[139] must exist to balance both exciton dissociation and charge transport requirements by minimising recombination whilst optimising charge photogeneration. For instance, if the domain sizes are too fine, this may lead to an enhanced geminate recombination. In fact, it has been noted that if the domain size is smaller than the Coulomb capture radius, geminate recombination may result[140] as the charges will not be able to escape one another efficiently not because they are confined by their Coulomb attraction, but rather by the physical size of the domains. Conversely, if the phase segregation is too large, the limited diffusion length of the photoinduced excitons means that some excitons will not reach an interface within their lifetime. Control over donor/acceptor blend morphology on nanometer scale by vertically separating the two materials to provide different paths for electrons and holes to the electrodes, with an optimised interfacial area for efficient exciton dissociation and with the scale of phase separation on the order of the exciton diffusion length and greater than the Coulomb capture radius, engineers an ideal morphology. Achievement of these conditions may not be simple, with estimates of the Coulomb capture radius typically being of similar magnitude or exceeding estimates of the exciton diffusion length.

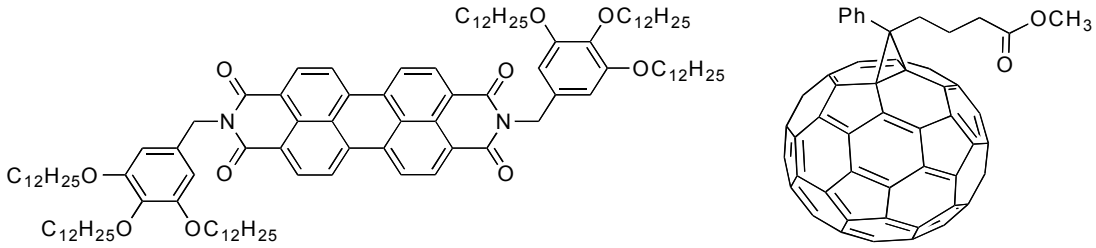
Achieving a favourable nanomorphology using new materials possessing energy levels compatible with higher device efficiencies (e.g. lower ΔG_{CS}, lower optical bandgap, etc) is a key challenge for the development further advances in device efficiency.

The nanomorphology studies have also revealed that thermal annealing can have an influence on charge photogeneration. These observations have been correlated with an increase in

material's crystallinity, usually enhancing the phase segregation in a blend film.[97] Several studies indicate that the enhanced phase segregation can favour the dissociation of interfacial CT states, thus reducing geminate recombination and enhancing the overall yield of charge photogeneration.[100,145]

1.7 Project Objectives

Selecting the appropriate materials for bulk heterojunction organic solar cells is essential to produce efficient devices. Here, we concentrate on electron accepting materials. The range of electron acceptors that work well with common electron donors namely, polythiophenes and PPVs, is surprisingly limited. The soluble C60 derivative, PCBM, has been studied extensively as an electron acceptor and has produced some of the most efficient PV devices to date. In this study, we investigate the efficiency of charge photogeneration by changing the electron transporter material from PCBM to perylene diimide (PDI) derivatives. The chemical structures of two materials are given in scheme 1.



PDI_2 **PCBM**

Scheme 1: chemical structures of perylene diimide (PDI_2) and PCBM

This thesis focuses on the investigation of photogenerated charges and the subsequent effect of energetics and nanomorphology in donor / acceptor blend films comprising of polythiophene:perylene diimides and P3HT:fullerene as well as covalently linked donor-acceptor molecules, which influence the obtained efficiency of photocurrent in devices. One of the central issues in the development of efficient organic photovoltaic devices is to develop

an understanding of the relationship between molecular structure and photovoltaic device performance. The molecular structures of all small molecules, polymers and donor-acceptor molecules examined in this thesis are displayed in each chapter. This thesis primarily focuses on specific aspects of the materials structure / efficiency of charge photogeneration at the donor/acceptor interface and the subsequent morphology in such solid films. Solid films potentially allow the formation of percolation pathways required for more efficient charge collection of the photogenerated charges at the donor/acceptor interface to external device electrodes.

In order to address the mechanism by which such devices can overcome the Coulomb attraction of the photogenerated electron-hole pair, and in particular achieve this with a high quantum and energy efficiency, we employ several spectroscopic methods, namely steady state absorption and emission spectroscopy, transient absorption and time resolved emission spectroscopy to study the photophysics of the blends, correlating these studies with analyses of blend morphology using polarising light microscopy, atomic force microscopy and transmission electron microscopy. Finally, the device performance is investigated. The details of all the techniques used for this thesis is given in chapter 2.

Chapter 3 will present the effect of nanomorphology on charge generation. Here we look at films of two modified fullerenes blended with P3HT, with PCBM blend film as control. Using steady and transient spectroscopy, coupled with electrochemical data, we address the direct transition between bimolecular and geminate recombination as a function of molecular structure. We compare the nanomorphology in such films by means of atomic force and transmission electron microscopy. Conclusions are drawn concerning the influence of blending and phase segregation on the efficiency of dissociation of charge transfer states into free charges.

Chapter 4 looks at charge photogeneration in solid films fabricated from covalently linked donor-acceptor molecules. In order to overcome the challenge of random phase segregation observed in blends, dyads are employed to control and confine the domain size and interfacial

area of donor and acceptor materials. The photophysics of solution versus films of covalently linked donor-acceptor molecules is studied to elucidate what makes such a molecule function well for the generation of long-lived charges in solid state, and to what extent the results of solution studies can be extrapolated to performance in solid state. For these studies we investigated the photophysics by means of transient absorption and time resolved photoluminescence spectroscopy.

In chapter 5 and 6, the emphasis is on the photophysics of polythiophene / perylene blend films. Various microscopies (PLM, AFM and TEM) are used to probe the morphology of the films. Transient absorption spectroscopy is employed to monitor charge photogeneration in polythiophene / perylene diimide blend films. It is observed in these blend films, relative to PCBM blend films, more efficient charge generation is achieved. In chapter 6, we focus in particular upon the correlation between charge generation efficiency and acceptor LUMO level, and role of nanomorphology in determining device photocurrents.

Finally, Chapter 7 summarises this work's findings about charge photogeneration in organic donor / acceptor blend films. General conclusions about charge generation are discussed. Suggestions are offered for future work in this field.

References:

(1) Bundesministerium fur Wirtschaft und Technologie, Eckpunkte fur ein integriertes Energie- und Klimaprogramm, **2007**.

(2) Fawer, M. *Sustainable Investment: Nachhaltigkeitsstudie (Basel: Bank Sarasin & Cie Ag)* **2007**.

(3) Shah, A.; Torres, P.; Tscharner, R.; Wyrsch, N.; Keppner, H. *Science* **1999**, *285*, 692.

(4) Johnson, J. C. *Chem. Eng. News* **2004**, *82*, 25.

(5) Arias, A. C.; MacKenzie, J. D.; Stevenson, R.; Halls, J. J. M.; Inbasekaran, M.; Woo, E. P.; Richards, D.; Friend, R. H. *Macromolecules* **2001**, *34*, 6005.

(6) Becquerel, A. E.; Acad, C. R. *Science.* **1839**, *9*, 561.

(7) Smith, W. *Nature* **1873**, *303*.

(8) Chaplin, D. M.; Fuller, C. S.; Pearson. G. L.; *J. Appl. Phys.* **1954**, *25*, 676.

(9) Zao, J.; Wang, A.; Green, M.; Forrazza, F. N.; *App. Phys. Lett* **1998**, *73*, 1991.

(10) Ramanathan, K.; Contreras, M. A.; Perkins, C. L.; Asher, S.; Hasoon, F. S.; Keane, J.; Young, D.; Romero, M.; Metzer, W.; Noufi, R.; Ward, J.; Duda, A. *Prog. Photovolt.: Res. Appl.* **2003**, *11*, 225.

(11) Goetzberger, A., Hebling, C.; Chock, Mater. H.W.; *Sci. Eng. R* **2003**, *40*, 1.

(12) Pochettino, A. *Acad. Lincei Rend.* **1906**, *15*, 355.

(13) Revcroft, P. S.; Ulal. H. *Sol. Ener. Mater.* **1979/1980**, *2*, 217.

(14) Minami, N.; Sasaki, K.; Tsuda, K.; *J. Appl. Phys.* **1983**, *54*, 6764.

(15) Sasabe, H.; Furuno, T.; Takimoto. K.; *Synthetic Metals* **1989**, *28*, c 787.

(16) Horowitz, G. *Adv. Mater.* **1990**, *2*, 287.

(17) Tang, C. W.; Albrecht, A. C. *The Journal of Chemical Physics* **1975**, *62*, 2139.

(18) Hoegel., H. *J. Phys. Chem.* **1965**, *69*, 755.

(19) Chiang, C. K. *Physical Review Letters* **1977**, *30*, 1097.

(20) Heeger, A. J. *Reviews of Modern Physics* **2001**, *73*, 681.

(21) MacDiarmid, A. G. *Reviews of Modern Physics,* **2001**, *73*, 701.

(22) Shirakawa, H. *Reviews of Modern Physics,* **2001**, *73*, 713.

(23) Burroughes, J. H. *Nature* **1990**, *347*, 539-.

(24) Braun, D.; Heeger, A. J. *Appl. Phys. Lett.* **1991**, *58*, 1982.

(25) Sirringhaus, H. *Nature* **1999**, *401*, 685.

(26) Tang, C. W. *Appl. Phys. Lett.* **1986**, *48*, 183.

(27) Liang, Y.; Xu, Z.; Xia, J.; Tsai, S-t.; Wu, Y.; Li, G.; Ray, C.; Yu, L.; *Advanced Materials* **2010**, *22*, 1-4.

(28) Halls, J. J. M.; Pickler, K.; Friend, R. H.; Moratti, S. C.; Holmes. A. B.; *Appl. Phys. Lett.* **1996**, *68*, 3120.

(29) Yu, G.; Gao, J.; Hummelen, J. C.; Wudl, F.; Heeger, A. J. *Science* **1995**, *270*, 1789

(30) Halls, J. J. M.; Walsh, C. A.; Greenham, N. C.; Marseglia, E. A.; Friend, R. H.; Moratti, S. C.; Holmes, A. B. *Nature* **1995**, *376*, 498.

(31) Suzuti, T.; Shirota, Y.; Rostalski, J.; Meissner, D.; *Solar Energy Mater. Solar Cells* **2000**, *61*, 1.

(32) Peumans, P.; Forrest, S. R. *App. Phys. Lett.* **2001**, *79*, 126.

(33) Shaheen, S. E.; Brabec, C. J.; Sariciftci, N. S.; Padinger, F.; Fromherz, J.; Hummelen, J. C. *Appl. Phys. Lett* **2001**, *78*, 841.

(34) Simon, J.; Andre, J-J. *Molecular Semiconductors* **1985**, *Springer-Verlag: Berlin,*.

(35) Sodergren, A.; Hagfeldt, A.; Olsson, J.; Lindquist, S.-E. *J. Phys. Chem.* **1994**, *98*, 5552.

(36) Yu, G.; Gao, J.; Hummelen, J. C.; Wudl, F.; Heeger, A. J. *Science* **1995**, 270.

(37) Gregg, B. A. *Chem. Phys. Lett.* **1996**, *258*, 376.

(38) Schlichthorl, G.; Huang, S. Y.; Sprague, J.; Frank, A. J. *J. Phys. Chem. B* **1997**, *101*, 8141.

(39) Granström, M.; Petritsch, K.; Arias, A. C.; Lux, A.; Andersson, M. R.; Friend, R. H. *Nature* **1998**, *395*, 257.

(40) Kalyanasundaram, K.; Gratzel, M. Coord. *Chem. Rev.* **1998**, *77*, 347.

(41) Malliaras, G. G.; Salem, J. R.; Brock, P. J.; Scott, J. C. *J. Appl. Phys.* **1998**, *84*, 1583.

(42) Arango, A. C.; Johnson, L. R.; Bliznyuk, V. N.; Schlesinger, Z.; Carter, S. A.; Horhold, H.-H. *Adv. Mater.* **2000**, *12*, 1689.

(43) Jenekhe, S. A.; Yi, S. *Appl. Phys. Lett.* **2000**, *77*, 2635.

(44) Peumans, P.; Bulovic, V.; Forrest, S. R. *Appl. Phys. Lett.* **2000**, *76*, 2650.

(45) Hagfeldt, A.; Gratzel, M. *Acc. Chem. Res* **2000,**, *33*, 269.

(46) Heeger, A. J. *J. Phys. Chem. B* **2001**, *105*, 8475-8491.

(47) Brabec, C. J.; Cravino, A.; Meissner, D.; Sariciftci, N. S.; Fromherz, T.; Rispens, M. T.; Sanchez, L.; Hummelen, J. C. *Adv. Funct. Mater.* **2001** *11*, 374.

(48) Huynh, W. U.; Dittmer, J. J.; Alivisatos, A. P. *Science* **2002**, *295*, 2425.

(49) Gregg, B. A.; Hanna, M. C. *J. Appl. Phys.* **2003**, *93* 3605.

(50) Nazeeruddin, M. K.; Kay, A.; Rodicio, I.; Humphry-Baker, R.; Muller, E.; Liska, P.; Vlachopoulos, N.; Gratzel, M. *J. Am. Chem. Soc.* **1993**, *115*, 6382.

(51) Lee, C. H.; Yu, G.; Moses, D.; Heeger, A. J. *Physical Rev. B* **1994**, *49*, 2396.

(52) Moses, D.; Wang, J.; Heeger, A. J.; Kirova, N.; Brazovski, S. *Proceedings of the National Academy of Sciences* **2001**, *98*, 13496.

(53) Sirringhaus, H. *Adv. Mater.* **2005**, *17*, 2411.

(54) Kim, J. Y.; Lee, K.; Coates, N. E.; Moses, D.; Nguyen, T.-Q.; Dante, M.; Heeger, A. J. *Science* **2007**, *317*, 222.

(55) Park, S. H.; Roy, A.; Beaupre, S.; Cho, S.; Coates, N.; Moon, J. S.; Moses, D.; Leclerc, M.; Lee, K.; Heeger, A. J. *Nature Photonics* **2009**, *3*, 297.

(56) Peet, J.; Kim, J. Y.; Coates, N. E.; Ma, W. L.; Moses, D.; Heeger, A. J.; Bazan, G. C. *Nature Materials* **2007**, *6*, 497.

(57) Colsmann, A. *Lichtemission und Transistoreffekt in organischen Halbleitern,* **2003**, *Diplomarbeit, Ludwig-Maximilian-Universität München*.

(58) Li, B.; Wang, L. D.; Kang, B. N.; Wang, P.; Qiu, Y. *Energy Mater. Sol. Cells* **2006**, *90*, 549.

(59) Gunes, S.; Neugebauer, H.; Sariciftci, N. S.; *Chem. Rev.* **2007** *107* 1324.

(60) Rand, B. P.; Genoe, J.; Heremans, P.; Poortmans, J.; *Prog. Photovolt.,* **2007,** *15,* 659.

(61) O'Regan, B. Gratzel, M. *Nature* **1991**, *353* 737.

(62) Durrant, J. R. Haque., S. A.; Palomares, E. *Chem. Comm.* **2006**, 3279.

(63) Sariciftci, N. S. *Appl. Phys. Lett.* **1993**, *62*, 585.

(64) Xue, J.; Uchida, S.; **2004**, *84*, 3013.

(65) Peumans, P.; Forrest, S. R.; Yakimov, A *J. Appl. Phys.* **2003**, *93*, 3693.

(66) Li, G.; Shrotriya, V.; Huang, J.; Yao, Y.; Moriarty, T.; Emery, K.; Yang, Y. *Nat. Mater* **2005**, *4*, 864.

(67) Kim, Y.; Cook, S.; Tuladhar, S. M.; Choulis, S. A.; Nelson, J.; Durrant, J. R.; Bradley, D. D. C.; Giles, M.; McCulloch, I.; Ha, C.-S.; Ree, M.; *Nat. Mater.* **2006**, *5*, 197.

(68) Peet, J.; Kim, J. Y.; Coates, N. E.; Ma, W. L.; Moses, D.; Heeger, A. J.; Bazan, G. C., *Nat. Mater.* **2007**, *6*, 497.

(69) Yu, G.; Heeger, A. J. *Appl. Phys. Lett* **1995**, *78*, 4510.

(70) Kim, Y., Cook, S.; Choulis, S. A.; Nelson, J.; Durrant, J, R.; Bradley, D. D. C.; . *Chemistry of Materials* **2004**, *16*, 4812.

(71) Kietzke, T.; Hans-Heinrich, H.; Neher, D.; *Chemistry of Materials* **2005**, *17* 6532.

(72) Koetse, M.; Santos, M.; J.; Hoekerd, K. T.; Schoo, H. F. M.; Veenstra, S. C.; Kroon, J. M.; Yang, X. N.; Loos, J.; *Appl. Phys. Lett.* **2006**, *88*.

(73) Sariciftci, N. S.; Smilowitz, L.; Heeger, A. J.; and Wudl, F.; *Science* **1992**, *258*, 1474.

(74) Kanicki, J. I. **1986**, *Marcel Dekker: New York,*, 543.

(75) Antoniadis, H.; Hsieh, B. R.; Abkowitz, M. A.; Jenekhe, S. A.; Stolka, M. *Synthetic Metals* **1994**, *62*, 265.

(76) Sariciftci, N. S.; Braun, D.; Zhang, C.; Srdanov, V. I.; Heeger, A. J.; Stucky, G.; Wudl, F.; *Applied Physics Letters,* **1993**, *62*, 585.

(77) Halls, J. J. M.; Arias, A. C.; MacKenzie, J. D.; Wu, W.; Inbasekaran, M.; Woo, E. P.; Friend, R. H. *Adv. Mater.* **2000**, *12*, 498.

(78) Vogel, M.; Strotmann, J.; Johnev, B.; Lux-Steiner, M. Ch.; Fostiropoulos, K. *Thin Solid Films* **2006**, *367*, 511.

(79) Campoy-Quiles, M.; Ferenczi, T.; Agostinelli, T.; Etchegoin, P. G.; Kim, Y.; Anthopoulos, T. D.; Stavrinou, P. N.; Bradley, D. D. C.; Nelson, J. *Nat. Mater* **2008**, *7*, 158.

(80) Yu, G.; Geo, J.; Yang, C. Y.; Heeger, A. J. *Proceedings of SPIE Photodetectors* **1997**, *2999*, 306.

(81) Arias, A. C.; Corcoran, N.; Banach, M.; Friend, R. H.; MacKenzie, J. D.; Huck, W. T. S. *App. Phys. Lett* **2002**, *80*, 1695.

(82) Dittmer, J. J.; Marseglia, E. A.; Friend, R. H. *Adv. Mater.* **2000**, *12*, 1270.

(83) Offermans, T.; Meskers, S. C. J.; Janssen, R. A. *J. Org. Electron* **2006**, *7*, 213.

(84) Hoppe, H. S.; Sariciftci, N.; *J. Mater. Res.* **2004**, *19*, 1924.

(85) Irwin, M. D.; Buchholz, D. B.; Hains, A. W.; Chang, R. P.; Marks, T. J.; *PNAS* **2008**, *105*, 2783.

(86) Peumans, P. U., S.; Forrest, S. R.; *Nature* **2003**, *425*, 158.

(87) Yoo, S.; Domercq, B.; Kippelen, B. *Appl. Phys. Lett.* **2004**, *85* 5427.

(88) Schulze, K.; Uhrich, C.; Schuppel, R.; Leo, K.; Pfeiffer, M.; Brier, E.; Reinold, E.; Baeuerle, P.; *Adv. Mater.* **2006** *18*, 2872.

(89) Lungenschmied, C.; Dennler, G.; Neugebauer, H.; Sariciftci, S. N.; Glatthaar, M.; Meyer, T.; Meyer, A.; *Sol. Energy Mater. Sol. Cells* **2007** *91*, 379.

(90) Green, M. A.; Emery, K.; King, D. L.; Hisikawa, Y.; Warta, W. *Prog. Photovolt.* **2007**, *15* 35.

(91) Tierney, S.; Heeney, M.; McCulloch, I. *Synth. Met.* **2005**, *148*, 195.

(92) Langhals, H.; Demmig, S.; Huber, H. *Spectrochim. Acta* **1998**, *44A*, 1189.

(93) Gvishi, R.; Reisfeld, R.; Burshtein, Z. *Chem. Phys. Lett.* **1993**, *213*, 338.

(94) Shi, M.; Chen, H.; Sun, J.; Ye, J.; Wang, M. *Chem. Comm.* **2003**, 1710.

(95) van Herrikhuyzen, J.; Syamakumari, A.; Schenning, A. P. H. J.; Meijer, E. W. *J. Am. Chem. Soc.* **2004**, *126*, 10021.

(96) Davydov, A. S. *Theory of Molecular Excitons* **1971**, *Plenum new York*.

(97) Clarke, T. M.; Ballantyne, A. M.; Nelson, J.; Bradley, D. D. C.; Durrant, J. R. *Advanced Functional Materials* **2008**, *18*, 4029.

(98) Clarke, T.; Ballantyne, A.; Jamieson, F.; Brabec, C.; Nelson, J.; Durrant, J. *Chemical Communications* **2009**, 89-91.

(99) Brédas, J.-L.; Norton, J. E.; Cornil, J.; Coropceanu, V. *Accounts of Chemical Research* **2009**, *accepted for publication*.

(100) Mandoc, M. M.; Veurman, W.; Sweelssen, J.; Koetse, M. M. *Applied Physics Letters* **2007**, *91*, 073518.

(101) Veldman, D.; Opek, O.; Meskers, S. C. J.; Sweelssen, J.; Koetse, M. M.; Veenstra, S. C.; Kroon, J. M.; Bavel, S. S. v.; Loos, J.; Janssen, R. A. J. *Journal of the American Chemical Society* **2008**, *130*, 7721.

(102) Morteani, A. C.; Sreearunothai, P.; Herz, L. M.; Friend, R. H.; Silva, C. *Phys. Rev. Lett.* **2004**, *92*, 247402.

(103) Moliton, A. N., J-M.; *Polym. Int.* **2006**, *55*, 58.

(104) Clarke, T.; Ballantyne, A.; Shoaee, S.; Soona, Y.; McCulloch, I.; Nelson, J. Durrant, J. *In prepration,* **2010**.

(105) Brédas, J.-L.; Cornil, J.; Heeger, A. J. *Advanced Materials* **1996**, *8*, 447.

(106) McBranch, D. W.; Kraabel, B.; Xu, S.; Kohlman, R. S.; Klimov, V. I.; Bradley, D. D. C.; Hsieh, B. R.; Rubner, M. *Synthetic Metals* **1999**, *101*, 291.

(107) Stubinger, T.; Brutting, W. *Journal of Applied Physics* **2001**, *90*, 3632.

(108) Österbacka, R.; Wohlgenannt, M.; Shkunov, M.; Chinn, D.; Vardeny, Z. V. *The Journal of Chemical Physics* **2003**, *118*, 8905.

(109) Markov, D. E.; Amsterdam, E.; Blom, P. W. M.; Sieval, A. B.; Hummelen, J. C. *The Journal of Physical Chemistry A* **2005**, *109*, 5266.

(110) Scully, S. R.; McGehee, M. D. *Journal of Applied Physics* **2006**, *100*, 034907.

(111) Scheblykin, I. G.; Yartsev, A.; Pullerits, T.; Gulbinas, V.; Sundstrom, V. *The Journal of Physical Chemistry B* **2007**, *111*, 6303.

(112) Wang, Z.; Mazumdar, S.; Shukla, A. *Physical Review B (Condensed Matter and Materials Physics)* **2008**, *78*, 235109.

(113) Blom, P. W. M.; Mihailetchi, V. D.; Koster, L. J. A.; Markov, D. E. *Advanced Materials* **2007**, *19*, 1551.

(114) Kroeze, J. E.; Savenije, T. J.; Vermeulen, M. J. W.; Warman, J. M. *The Journal of Physical Chemistry B* **2003**, *107*, 7696.

(115) Lüer, L.; Egelhaaf, H. J.; Oelkrug, D.; Cerullo, G.; Lanzani, G.; Huisman, B. H.; de Leeuw, D. *Organic Electronics* **2004**, *5*, 83.

(116) Chasteen, S. V.; Harter, J. O.; Rumbles, G.; Scott, J. C.; Nakazawa, Y.; Jones, M.; Horhold, H. H.; Tillman, H.; Carter, S. A. *Journal of Applied Physics* **2006**, *99*, 033709.

(117) Feng, W.; Cao, M.; Wei, W.; Wu, H. C.; Wan, M. X.; and Yoshino, K.; *Acta Phys. Sin.* **2001**, *50*, 1157.

(118) Schmidt-Mende, L.; Fechtenkotter, A.; Mullen, K.; Moons, E.; Friend, R. H.; and MacKenzie, J. D.; *Science* **2001**, *293*, 1119.

(119) Tian, R. Y.; Yang, R. Q.; Peng, J. B.; and Cao, Y.; *Chin. Phys.* **2005**, *14*, 1032

(120) Peumans, P.; Forrest, S. R. *Chem. Phys. Lett.* **2004**, *398*, 27.

(121) Offermans, T.; Hal, P. A. v.; Meskers, S. C. J.; Koetse, M. M.; Janssen, R. A. *J. Physical Review B (Condensed Matter and Materials Physics)* **2005**, *72*, 045213.

(122) Benson-Smith, J. J.; Goris, L.; Vandewal, K.; Haenen, K.; Manca, J. V.; Vanderzande, D.; Bradley, D. D. C.; Nelson, *J. Adv. Func. Mater.* **2007**, *17*, 451.

(123) Loi, M. A.; Toffanin, S.; Muccini, M.; Forster, M.; Scherf, U.; Scharber, M. *Adv. Func. Mater.* **2007**, *17*, 2111.

(124) McNeill, C. R. Westenhoff, S.; Groves, C.; Friend, R. H.; Greenham, N. C. *J. Phys. Chem. C* **2007**, *111*, 19153.

(125) Yin, C.; Kietzke, T.; Neher, D.; Horhold, H.-H. *Appl. Phys. Lett.* **2007**, *90*, 092117.

(126) Ohkita, H.; Cook, S.; Astuti, Y.; Duffy, W.; Tierney, S.; Zhang, W.; Heeney, M.; McCulloch, I.; Nelson, J.; Bradley, D. D. C.; Durrant, J. R. *J. Am. Chem. Soc.* **2008**, *130*, 3030.

(127) Veldman, D.; Meskers, S. C. J.; Janssen, R. A. J. *Adv. Func. Mater.* **2009**, *19*, 1939.

(128) Hallermann, M.; Haneder, S.; Como, E. D. *Applied Physics Letters* **2008**, *93*, 053307.

(129) Muntwiler, M.; Yang, Q.; Tisdale, W. A.; Zhu, X. Y. *Physical Review Letters* **2008**, *101*, 196403.

(130) Veldman, D.; Meskers, S. C. J.; Janssen, R. A. J. *Advanced Functional Materials* **2009**, *19*, 1939.

(131) Ohkita, H.; Cook, S.; Astuti, Y.; Duffy, W.; Tierney, S.; Zhang, W.; Heeney, M.; McCulloch, I.; Nelson, J.; Bradley, D. D. C.; Durrant, J. R. *J. Am. Chem. Soc.* **2008**, *130*, 3030.

(132) Veldman, D.; Ipek, O.; Meskers, S. C. J.; Sweelssen, J.; Koetse, M. M.; Veenstra, S. C.; Kroon, J. M.; van Bavel, S. S.; Loos, J.; Janssen, R. A. J. *Journal of the American Chemical Society* **2008**, *130*, 7721.

(133) Onsager, L. *Physical Review* **1938**, *54*, 554.

(134) *IEC* **1989**, 904.

(135) Nelson, J. *The physics of solar cells, London: Imperial College Press,* **2003**.

(136) Tvingstedt, K.; Vandewal, K.; Gadisa, A.; Zhang, F.; Manca, J.; InganaÌs, O. *J. Am. Chem. Soc.* **2009**, *131*, 11819.

(137) Shoaee, S.; An, Z.; Zhang, X.; Barlow, S.; Marder, S. R.; Duffy, W.; Heeney, M.; McCulloch, I.; Durrant, J. R. *Chemical Communications* **2009**, 5445 - 5447.

(138) Reyes-Reyes, M.; Kim, K.; Carroll, D. L. *Applied Physics Letters* **2005**, *87*, 083506.

(139) Chasteen, S. V.; Sholin, V.; Carter, S. A.; Rumbles, G. *Solar Energy Materials and solar cells* **2008**, *92*, 651.

(140) Ruseckas, A.; Shaw, P. E.; Samuel, I. D. W. *Dalton Transactions* **2009**, *accepted for publication*.

(141) Lindner, S. M.; Hüttner, S.; Chiche, A.; Thelakkat, M.; Krausch, G. *Angewandte Chemie International Edition* **2006**, *45*, 3364.

(142) Sommer, M.; Hüttner, S.; Wunder, S.; Thelakkat, M. *Advanced Materials* **2008**, *20*, 2523-2527.

(143) Zhang, F.; Jespersen, K. G.; Björström, C.; Svensson, M.; Andersson, M. R.; Sundström, V.; Magnusson, K.; Moons, E.; Yartsev, A.; Inganäs, O. *Advanced Functional Materials* **2006**, *16*, 667.

(144) Peumans, P.; Forrest, S. R. *Chemical Physics Letters* **2004**, *398*, 27.

(145) Erb, T.; Zhokhavets, U.; Gobsch, G.; Raleva, S.; Stühn, B.; Schilinsky, P.; Waldauf, C.; Brabec, C. J. *Advanced Functional Materials* **2005**, *15*, 1193.

II. Experimental methods

2.1 Overview

This chapter details the experimental methods and devices fabrication techniques that were used in this work to study charge photogeneration.

2.2 Materials and fabrication

2.2.1 Sample and film preparation

2.2.2 Device fabrication

2.3 Techniques:

2.3.1Steady state photoluminescence spectroscopy: study the ground state emissive excited state.

2.3.2 Transient absorption spectroscopy: probe the charge generation yields

2.3.2.1 Microsecond

2.3.2.2 Nanosecond

2.3.3 Time resolved photoluminescence spectroscopy: probe the lifetime of excited states in donor-acceptor molecules

Various microscopes were used to observe the morphology of the films

2.3.4 Polarised light microscopy

2.3.4.1 Liquid crystals

2.3.5 Atomic force microscopy

2.3.5.1 Contact and Close-contact modes

2.3.6 Transmission electron microscopy

2.3.7 Solar simulator: allow characterisation of devices.

2.2 Materials and fabrication

2.2.1 Materials and film preparation

All the materials were used as received and underwent no further purification. The modified C_{60} small molecules studies in chapter 3 were supplied by Nazario Marttin in departamento de Quimica Organica, Universidad Complutense, Spain and polythiophene; P3HT employed in chapter 3 was kindly supplied by Dirk Vanderzande in Universiteit Hasselt, Institute for Materials Research, division Chemistry, Belgium. All other polythiothenes studied in chapters 3, 5 and 6 were synthesized as reported by Merck. In addition to Merck P3HT (regioregularity >94.4%) another P3HT (highly regioregular 98.5 %) was purchased from Rieke Metals (Sigma Aldrich) (specifically stated if used). Polymer details are given in Table 2.1. The small molecule perylene derivatives used in chapter 5 and 6 and perylene dyad (chapter 4) synthesized as reported elsewhere, were supplied by Seth Marder at Georgia Institute of Technology and 1-(3-Methoxycarbonyl)propyl-1-phenyl-[6,6]-C61 (PCBM) utilised in chapters 3, 5 and 6 was purchased from Solenne. (All materials' synthesis is given in appendix.)

Table 2.1 Characterisation of Polythiophenes

	M_W	M_n	M_W/M_n
P3HT (Merck)	20700	12400	1.67
P3HT (Rieki)	50000	-	-
$P(T_{12}NpT_{12})$	22000	9000	2.44
$P(T_{10}T_{10}TT_0)$	51400	27900	1.84
$P(T_{12}SeT_{12})$	46400	23800	1.95
$P(T_0TT_{16})$	47600	22900	2.08
$P(T_{16}T_{16}TT_0)$	51400	27900	1.84

Indium tin oxide glass substrates with sheet resistance 15 Ω/sq were purchased from PsioTec Ltd, UK. PEDOT:PSS was purchased from H.C. Starck (Bayer AG). The solvents: chloroform, chlorobenzene, dichloromethane, toluene and benzonitrile were all purchased from Aldrich. Electrodes for deposition were purchased from Aldrich.

The substrates were cleaned by sonication for 15 minutes in acetone and isopropanol successively before drying under a stream of gaseous nitrogen. Thin films were then prepared by spin coating the sample (pristine and the blend solutions) solutions onto glass substrates.

Spin coating was done under nitrogen atmosphere. Sample preparation and spin coating conditions are individually reported for each set of materials in the following chapters.

2.2.2 Device fabrication

The organic photovoltaic cells studied in this thesis consist of a nanometer scaled layer of active layer, which is enclosed by two electrodes. Indium tin oxide (ITO) is used as the transparent conducting oxide electrode and the top electrode consists of a low workfunction electrode usually aluminium (Al) or calcium (Ca). The absorber layer in this project is based on conjugated polymer/small molecule consisting of a blend of polythiophenes and perylene diimides (PDI). The specific details of the active layer used are given in chapter 6. Unless specifically stated otherwise, all devices were prepared according to the following procedure:

As substrates, glass sheets of 12 mm x 12 mm covered with 8 mm x 12 mm ITO, 110 nm thick, were used.

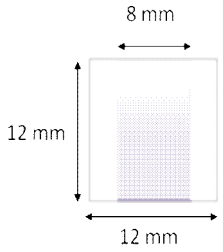


Figure 2.1 ITO glass substrate

The ITO substrate was first cleaned as described for film. The substrate was then coated with approximately 20 nm thick layer of PEDOT:PSS by spin-coating at 6100 rpm for 80 seconds. Afterwards the substrate is heated to 140 °C for an hour, to remove any remaining H_2O present in the PEDOT:PSS. The absorber layer is then spun at 1100 rpm for 90 seconds. On top of these films a 120 nm metal electrode is evaporated ($p < 5\times10^{-6}$ mbar) where evaporation is done in a deposition form. All processes before electrode evaporation were performed in air. Once the electrodes were deposited, the devices were kept under nitrogen

atmosphere at all times. In order to achieve contact with ITO, silver paste is painted on the top central coordinate of the device. If contact needs to be further improved, silver paste is also added on the electrodes.

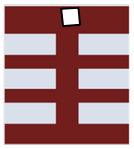


Figure 2.2 representation of a device. The red presents the active layer and gray areas are the electrodes deposited through a mask. Silver paste is added to the device in order to get contact with ITO.

2.2 Techniques

2.2.1 Steady state photoluminescence

Photoluminescence (PL) measurements allow characterization of emissive excited states formed. Comparative studies of the PL intensities in blend with respect to pristine material can be used to determine the fraction of emissive donor states that decay non-radiatively. This is referred to as PL quenching. For PL studies, location and orientation of the sample were fixed to minimize differences in PL due to variation in measurement geometry between samples in the series. The percentage PL quenching (PLQ) is defined as

$$PLQ = 1- [PL_{blend} / PL_{pristine}] \qquad (1)$$

The quantity is either defined at the maximum wavelength of emission or integrated intensity. If there is significant PL quenching, it indicates a reduction in exciton - either via charge separation or significant energy transfer to another state/ground state via a non-radiative decay mechanism.

2.2.2 Transient absorption spectroscopy

The apparatus is best described as an optical technique designed to probe the short-lived transient species that are formed as a result of photoexcitation. This technique is used in conjunction with solid-state absorption and photoluminescence as TAS probes the recombination dynamics as well as the initial charge generation and has been widely employed.[1,2] The technique involves irradiation of a sample with a short intense pulse of light (pump / excitation pulse) and observing the consequent change in the sample's optical density (Figure 2.3). The change in optical density is determined by monitoring the transmission of a second less intense beam of light that passes through the sample known as the probe. This technique yields information from a single excitation wavelength at a single probe wavelength, but over a broad range of timescales to provide kinetic data on the decay of transient species.

Figure 2.3 is a schematic detailing the set-up for TAS.

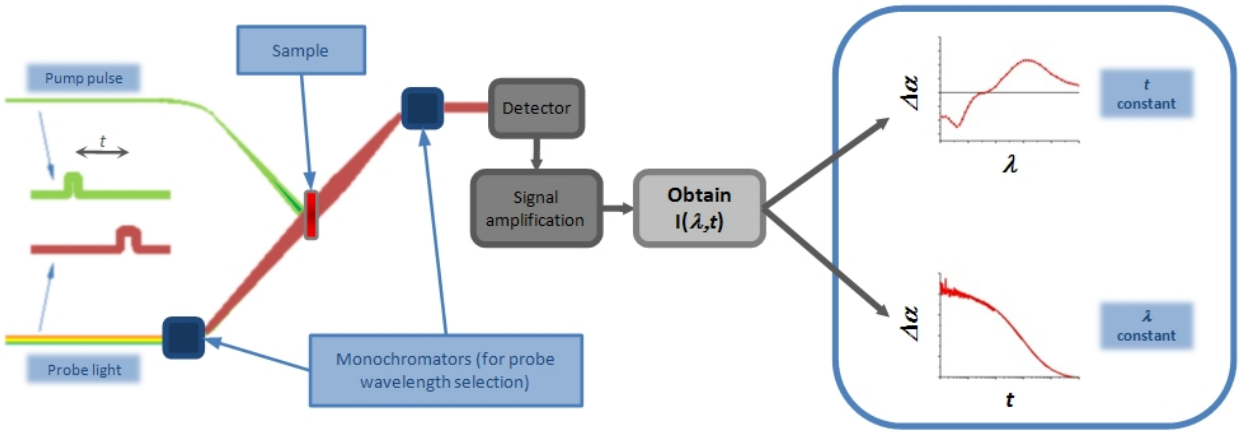


Figure 2.3 Transient absorption spectroscopy (TAS) schematic. The system consists of a pump source, either a nitrogen-dye laser or Nd-YAG laser, a probe source: Xenon lamp or laser diode. The incoming pump source excites the film and the probe source probes the decay as a function of time to study the decay dynamics of the charge species.

The technique arises from manipulation of voltage. The voltage signal measured at the photodetector relates to the fractional change in the optical density (OD) of the sample by

$$\frac{V(t)-V(0)}{V(0)} = \frac{10^{-OD(t)} - 10^{-OD(0)}}{10^{-OD(0)}} = 10^{-OD(t)+OD(0)} - 1 \quad (2)$$

Since we know that for small values of x, $10^{-x} \approx 1 - x\ln 10$, then

$$\frac{\Delta V(t)}{V(0)} = 1 - \Delta OD\ln 10 - 1 = \Delta OD\ln 10 \quad (3)$$

Or, equally, we can say that

$$\Delta OD = \frac{1}{2.303}\frac{\Delta V(t)}{V(0)} \quad (4)$$

So the change in voltage is linearly proportional to ΔOD for small changes in optical density.

The two main modes of TAS employed in this study were microsecond and nanosecond TAS systems.

2.2.2.1 Microsecond TAS system

This system is capable of monitoring kinetics from 10^{-7} to $>10^{-3}$ second timescale. Due to scatter and emission noise from the pump excitation source, however, the system resolution is typically from a microsecond onwards. The PTI GL-3300 nitrogen laser produced 600 ps laser pulses at a wavelength of 337 nm with pulse energy of around 1 mJ at a variable repetition rate chosen using a frequency generator. A GL-301 PTI dye laser module was used in conjunction with the nitrogen laser to provide a variable wavelength source of excitation (400–750 nm). The energy of the pulse at different wavelengths was found to be dependent on the type of dye employed in the dye laser. A part of the light from the dye module was used as a trigger signal to start the oscilloscope, but the majority was focused into a light guide pipe and then on to the sample. The power of the laser beam was modified by a series

of neutral density filters. A 100-W tungsten lamp was used as the probe light source. An advantage of having a tungsten lamp is that transient signals over a wide wavelength range can be observed (400–1050 nm). The monitoring wavelength from the lamp was selected by using a monochromator. Long pass filters (Comar Instruments) were placed in front of the monochromator aperture in order to block the second harmonics of the second wavelength leaving the monochromator. A second monochromator was used after the sample to minimise any emission or pump scatter from the sample from reaching the photodiode. The detection system comprised an oscilloscope and a silicon photodetector. Tekave 1.43 software (Costronics Electronics) was used for data acquisition.

2.2.2.2 Nanosecond TAS system

This system consists of a nanosecond response silicon photodiode (Fast optical transient pre-amplifier, ~5MW, Costronics Electronics), a Nd-YAG laser (Ultra Nd:YAG BigSkyLaser Company) as the excitation source (532nm FWHM <6ns) and a 75W Xenon arc lamp (200-2000nm) or laser diode (Thorlabs TLCDM9, controlled by ITC502 laser diode combi controller) as the probe source coupled to a single PTI model 101 monochromator after the sample.

A photodetector with a quicker response photodiode was used in order to obtain earlier time resolution transient decays (~50ns). The use of a laser photodiode allowed for an increase in the distance between the sample and photodiode so that scatter and emission noise were reduced. This required the use of a probe beam that was more coherent over long distances and so a laser diode was used with a probe wavelength of 980nm (~50mW, 24°C, 106mA). The system response was typically 50ns with a threshold RC high pass coupling of 10 microseconds. Long pass filters between 680 - 1000nm were used throughout the system to reduce the laser scatter and noise. The signal was collected using an oscilloscope (Techtronics, TDS220) and the data collected on to the computer using Tekave acquisition software (Costronics Electronics).

2.2.3 Emissive state lifetime measurements

Time correlated single photon counting (TCSPC) depends on the concept that the relationship of emission intensity versus time is given by the probability distribution for the emission of a single photon after an excitation event. This distribution is obtained by sampling the emission of single photons following a large number of low intensity excitation events. The technique is suitable to both strongly and weakly emitting materials.

Sample excitation is provided by the pulse from an electrically driven laser diode system (IBH NanoLED) 404 nm. The system provides a 1-MHz pulse train, with each pulse having a FWHM of 200 ps. The subsequent emission photon is detected perpendicular to the excitation beam by a photomultiplier tube (Hamamatsu R3809U). Emission wavelength selection was provided by means of interference filters, providing a bandpass FWHM of 15 nm. An analogue electronic pulse is generated by the detector, which is routed through a wideband amplifier (Research Communications Model 9009) followed by a constant fraction timing discriminator, CFTD (EG&G Ortec Model 584), to the start input of the time-to-amplitude converter, TAC (Tennelec TC864). This initiates charging of a fast linear voltage ramp, which is used to time the delay between the excitation and the emission. At the same time as the optical pulse is generated, a logical sync pulse is produced, which is routed through a delay line to stop input of the TAC to halt the voltage ramp. The TAC produces an electronic pulse, whose amplitude is proportional to the voltage generated, and therefore the time between the start and stop triggers. An analogue-to-digital converter, ADC, which is built into the multichannel analyser, MCA (EG&G/Perkin Elmer Ortec Trump Card), digitises the pulse. A count is then stored in the address (MCA channel) of a data storage device corresponding to that number (time). A histogram representative of the fluorescence decay is formed in the MCA memory by repetition of the whole process.

2.2.4 Polarised light microscope

The polarized light microscope is designed to observe and photograph specimens that are visible primarily due to their optically anisotropic character, for instance liquid crystals. The microscope is equipped with both a polarizer, positioned in the light path somewhere before the specimen, and an analyzer**,** placed in the optical pathway between the objective rear aperture and the camera port.

A polarised microscope differs from a conventional light microscope in a number of ways. A polarizing microscope has a pair of polars (polarizing devices) in the optical train. The first polar (polarizer) defines the initial plane of polarization for light entering the microscope and is located between the illuminator and the condenser. The other polar (analyzer) is usually placed between the objective and the ocular tube and defines the plane of polarization of the light reaching the ocular. One or both must be accurately rotatable about the optical axis of the instrument. Usually the analyzer is also removable from the optical path.

2.2.4.1 Liquid crystals

Liquid crystals (LC) are a state of matter that lie between solid crystals and conventional (isotropic) liquids.[3] Liquid crystals are generally characterized by the type of ordering they exhibit. One can distinguish positional order (whether molecules are arranged in any sort of ordered lattice) and orientational order (whether molecules are mostly pointing in the same direction). Moreover, order can be either short-range (only between molecules close to each other: nematic) or long-range (extending to larger, sometimes macroscopic, dimensions: smectic). The ordering of liquid crystalline phases is extensive on the molecular scale. Some techniques, such as an applied electric field, can be used to enforce a single ordered domain in a macroscopic liquid crystal sample.

According to the conditions under which liquid crystals can be formed, liquid crystals can be identified as either lyotropic or thermotropic.[3] In lyotropic liquid crystals, formation of liquid crystalline phases and phase properties are dependent on the solvent used and the concentration of the solution. On the other hand, in thermotropic liquid crystals, the phase

transitions and phase properties are dependent on the temperature. According to the shape of the mesogenic (LC molecule) units, thermotropic liquid crystals can be divided into two types: calamitic (rod-like) and discotic (disc-like).[3]

In the discotic phase, LC molecules can orient themselves in a layer-like fashion. If the disks pack into stacks, the phase is called a discotic columnar. The columns themselves may be organized into rectangular or hexagonal arrays. Discotic liquid crystals can self-assemble into one-dimensional columns through π-orbital interaction and phase segregation, between the usually flat rigid aromatic cores and the flexible side chains. The stacks of the aromatic cores can provide efficient channels for the charge carriers to transport along the columns, but the intercolumnar charge transport process is negligible due to the insulating effect of the side chains surrounding the columns. Discotic liquid crystals can form either nematic (N_D) or columnar (Col) mesophases.[3] There are only a few discotic liquid crystals that form nematic phases; whilst most discotic liquid crystals form columnar mesophases.[4] Nematic phases only have an orientational order with the normal of the discs aligned along the director; columnar phases have higher orders with the discs organised into columns, which then arrange themselves into 2 dimensional lattices (Figure 2.4).[3] The columnar hexagonal phase is characterized by a hexagonal packing of the molecular columns. Hexagonal mesophases are often denoted as Col_{ho} or Col_{hd} where h stands for hexagonal and o and d for ordered or disordered stacking of the molecules, according to the regularity of the discs within the same column.[5] When the separation between two neighbouring discs is in a random fashion within the same column, the corresponding columnar mesophase is a disordered one; on the other hand, a relatively long-range order is expected when the intracolumnar distance is constant, which defines the columnar mesophase as an ordered columnar mesophase (Figure 2.4).

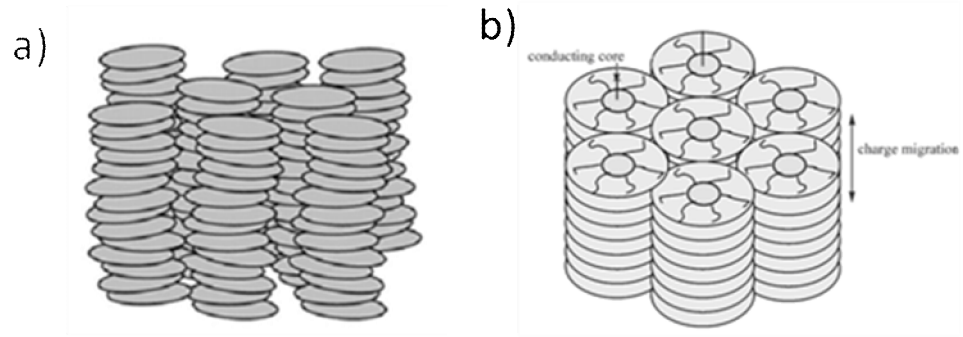


Figure 2.4 Schematic representations of (a) a columnar mesophase, (b) a 2D lattice arrangement of hexagonal columnar (Col_h) mesophases.

There are two types of alignments of discotic liquid crystals that can be beneficial for electronics and optoelectronics. When an axis of the column structure, which is formed by disc-like liquid crystalline molecules, aligns perpendicularly to the plane of the substrate, the alignment is called *homeotropic* alignment where the discs take the "face-on" orientation.[3] On the other hand, when the director (axis) of the discs is parallel to the plane of the substrate, the alignment is called *homogeneous/ planar* alignment where the discs take the "edge-on" orientation.[3] Ideally, if all the columns that are formed in the columnar liquid crystalline phases can be aligned parallel to each other and perpendicular to the electrodes (Figure 2.5) when used in PV devices, the charge carriers would travel the shortest distance through the materials and the charge carrier mobilities would have the largest component (100%) along the direction normal to the electrodes, thus providing the devices with the best possible performance if other parameters are optimal at the same time. Moreover, in uniformly aligned columnar phases, the charge carriers will experience a minimum number of boundaries between otherwise randomly distributed columns. Therefore, alignment of discotic liquid crystals is important to improve the charge-transport process in columnar liquid crystalline materials and the performance of the devices using discotic liquid crystals as charge-transport materials. However, it has unfortunately been found that most discotic liquid crystals do not form these two types of alignment spontaneously.[6] Thereby, surface

treatments of the substrate, or external driving forces has to be applied when attempting to align discotic liquid crystals.

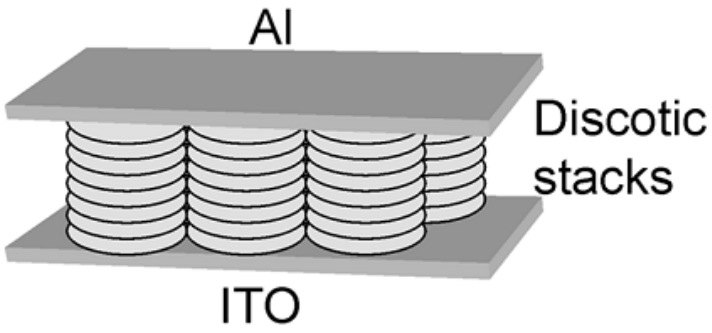


Figure 2.5 Ideal homeotropic alignment of discotic stacks in a PV device.

2.2.5 Atomic force microscope (AFM)

Atomic force microscopy (AFM) is a subset of scanning force microscopy (SFM) which is one of the most notable tools for imaging matter at the nanoscale. The information is gathered by probing the surface with a mechanical probe. This is facilitated by the presence of a piezoelectric crystal that allows for the detection of miniscule changes in attractive and repulsive forces. A schematic of AFM is shown in Figure 2.6.

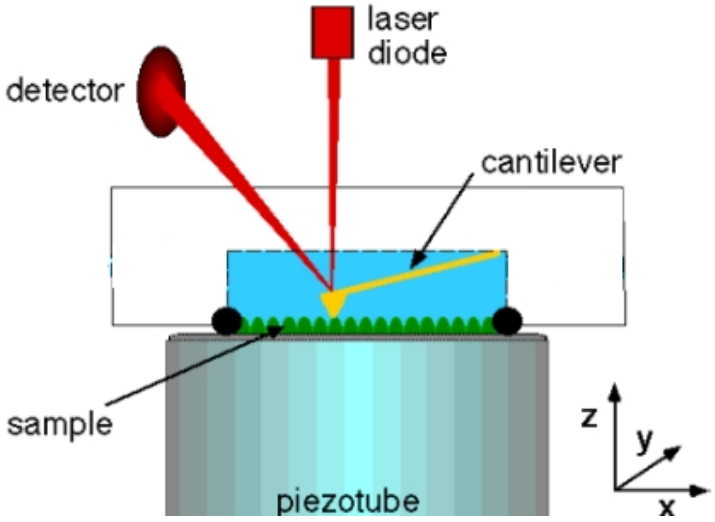


Figure 2.6 Flow schematic of atomic force microscope (AFM).[7]

The AFM operates by allowing an extremely sharp tip to either come in contact or in very close proximity to the sample that is being imaged. The tip is located at the free end of a cantilever that is 100 to 200μm long and typically made of silicon or silicon nitride. The sample is then scanned beneath the tip. Different forces either attract or repel the tip.

AFM monitors the interactive forces between the sample and the tip. The force most commonly associated with AFM is the inter-atomic van der Waals force. AFM can be applied to non-conducting surfaces where a constant attractive/repulsive force between sample and the tip is maintained. This will result in deflection of the cantilever as it scans the surface of the solid, which will be monitored by the reflection of a laser beam off the cantilever.

AFM is based on the fact that two given bodies (here, the tip and the substrate) will experience attractive and repulsive forces. These forces can be as small as a few nano-Newtons and will differ in magnitude depending on the distance, between them. Usually the forces exerted are in the range 0.1-0.5 nN. When the tip and the surface are far apart, the magnitude of force is negligible and thus there is no cantilever deflection. As the tip and the sample get closer a variety of attractive and repulsive forces deflect the cantilever. This region is the non-contact region. Once the tip and the sample get very close, then an

attractive force is experienced between the two bodies. This force is at its highest when the tip is in contact with the surface giving rise to contact mode AFM.

The force is detected by placing the tip on a flexible cantilever which deflects proportionally to the force exerted on the tip. The deflection of this tip is monitored by means of an electrical feedback loop which controls the piezoelectric crystal inside the AFM's scanner, in order to maintain a constant force. The exact mechanism, by which an AFM operates, is dependent on the mode of operation and the made of the AFM.

2.2.5.1 Contact and close contact modes

In contact mode the surface is scanned at a constant force with one of the cantilevers on the contact mode substrate. In contact mode the tip and the sample maintain contact. When the tip experiences a change in feature such that the feature threatens either the constant force applied to the surface, or the constant contact of the tip and the sample, the piezoelectric crystal responds in order to revert back to the original position and force. This is achieved through the monitoring of the deflection of the tip which caused the reflected laser signal to fall on a different section of the photodetector than that of the standard point of incidence. An electrical feedback loop forces the piezoelectric crystal to either contract or expand in order to re-align the laser position. The different voltages applied to the piezoelectric crystal in order to maintain the constant force and contact are displayed in the form of a topographical image.

Close contact tip is a rigid tip which can oscillate with high frequencies (≈300 kHz). The concept of close contact mode is similar to that of contact mode. The difference in the two modes is that in close contact mode the tip is oscillating at high frequencies and only ever lightly touches the surface of the sample. This minimises surface damage which is often associated with contact mode AFM. Close contact mode operates by maintaining constant resonance amplitude for the tip. When the tip experiences a feature which would cause the amplitude to decrease or increase above the standard resonance amplitude an electrical

feedback loop forces the piezoelectric crystal to contract (to move the sample down) or expand (to move the sample up) such that the tip can oscillate with its natural amplitude. The response of the piezoelectric crystal is then mapped in terms of voltage applied to it in order to maintain a constant amplitude, and thus a topographical image is produced.

2.2.6 Transmission Electron Microscope (TEM)

Transmission electron microscopy allows one to visualize objects that are as small as 1 nm. Here the specimen is not illuminated with light but bombarded by electrons as a source for image formation. Globally, TEM is used to study the inner structure of objects. TEM operates on the same basic principles as the light microscope but rather than light, it uses beam of electrons that is transmitted through an ultra thin specimen, interacting with the specimen as it passes through. An image is formed from the interaction of the electrons transmitted through the specimen; the image is magnified and focused onto an imaging device.

From the top down, the TEM consists of an emission source. The ray of electrons is produced by a pin-shaped cathode heated up by current. The electrons are vacuumed up by a high voltage at the anode. By connecting the emission source gun to an HV source (Typically ~120 kV for many applications) the gun will, given sufficient current, begin to emit electrons into the vacuum. Once extracted, the upper lenses of the TEM allow for the formation of the electron probe to the desired size and location for later interaction with the sample (Figure 2.7).

The lens-systems consist of electronic coils generating an electromagnetic field. The ray is first focused by a condenser, and then passes through the object, where it is partially deflected. The degree of deflection depends on the electron density of the object. The greater the mass of the atoms, the greater is the degree of deflection. Biological objects have only weak contrasts since they consist mainly of atoms with low atomic numbers (C, H, N, O). Consequently it is necessary to treat the preparations with special contrast enhancing chemicals (heavy metals) to get at least some contrast.

After passing the object the scattered electrons are collected by an objective. Thereby an image is formed, that is subsequently enlarged by an additional lens-system (called projective with electron microscopes). The formed image is made visible on a fluorescent screen. Photos taken with electron microscopes are always black and white.

For TEM examination, solutions were spun onto PEDOT:PSS coated substrates (10 nm), retrieved on carbon-coated copper grids. The sample film thickness was controlled by the solution concentration, typically around 30 nm. The samples were then selectively stained by RuO_4 vapour.

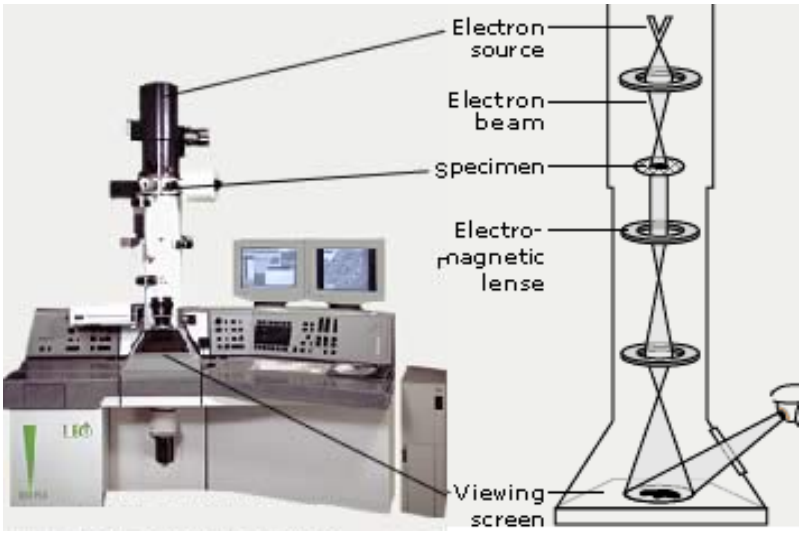


Figure 2.7 Schematic diagram (right) and a photo of transmission electron microscope (TEM).

2.2.8 Steady State J-V

Probably the simplest and most widely used technique in studying semiconductor devices is the steady-state Current density-voltage (J-V) curve that measures the electrical characteristics of PV devices. In this measurement, the current density through the device is measured as a function of bias applied between electrodes bounding a device structure.

In order to understand the current-voltage characteristics of solar cell devices, it is necessary to model the electrical circuit of the device. The circuit consists of a current source, a series resistance (R_S) and a shunt resistance (R_{SH}). For ideal solar cells, series resistance must be zero and shunt resistance = ∞.

In practice, organic solar cells do not function as ideal diodes and are affected by series and shunt resistance effects. Shunt and series resistances can be recognised in the J-V curves. A large series resistance results in a linear curve at high forward bias where the current should be increasing exponentially with voltage. The effect of shunting can be seen when there is a non-zero slope of the J-V curve near zero voltage since shunting results in a larger current in reverse bias. Shunt resistance is caused by leakage pathways for the current through the device which may be due to poor choice of electrodes or to short circuits where one material forms a percolation pathway such that it is in contact with both electrodes.

To measure device efficiencies between -1V to +1V, a Sciencetech Solar Simulator with an externally applied voltage (Keithley 2400 source meter) and a 300W Xenon lamp (Oriel Instruments) was used. The devices were connected up via the ITO and Al contacts to the Keithley source meter.

The solar simulator consists of:

an arc lamp housing that must be water cooled

an arc lamp power supply, which is current regulated DC power supply. The current is adjustable to provide 75-160 watts of power to the arc lamp

a beam conditioner

a feedback/computer control unit.

The devices were placed into a sample chamber with a glass cover lid. To create conditions close to the solar constant (0.136 Wcm^{-2}) the sample is placed approximately 25 inches away from the exit of the beam conditioner with the AM1.5 filter. The measurements were made by exciting the samples using the Xenon arc lamp. All the device measurements were investigated using white light to determine the power conversion efficiencies. Current-voltage measurements were taken using a Keithley high voltage source measurement unit.

Calibration was performed by employment of a photodiode (Newport UV-818) to measure the light intensity (typically at 1 sun) approximately at the same distance and height that the device would experience.

References

(1) Montanari, I.; Nogueira, A. F.; Nelson, J.; Durrant, J. R.; Winder, C.; Loi, M. A.; Sariciftci, N. S.; Brabec., C. *App. Phys. Lett.* **2002**, *81*, 3001.

(2) Nogueira, A. F.; Montanari, I.; Nelson, J.; Durrant, J. R.; Winder, C.; Sariciftci, N. S.; Brabec, C. *J. Phys. Chem. B* **2003**, *107*, 1567.

(3) Demus, D. G., J.; Gray, G. W.; Spiess, H. W.; Vill, V. **1998**.

(4) Hoger, S. E., V. ; Bonrad, K.; Tschierske, C. *Angew. Chem. Int. Ed.* **2000**, *39*, 2268.

(5) Maeda, F. H., K.; Ohta, K. Kimura, M. *J. Mater. Chem.* **2003**, *13*, 243.

(6) Hatsusaka, K. O., K.; Yamamoto, I.; Shirai, H. **2001**, *11*, 423.

(7) http://www.mih.unibas.ch/Booklet/Booklet96/Chapter3/Fig3-1.jpg.

III. Influence of nanoscale phase separation on geminate versus bimolecular recombination in P3HT:fullerene blend films

Numerous studies provide general evidence indicating the importance of charge transfer states in determining the yield of charge photogeneration. The majority of the studies have focused upon comparative studies as a function of nanomorphology. We therefore turn now to considering this issue.

In this chapter, we compare the charge recombination dynamics observed in films comprising of poly(3-hexylthiophene) blended with three C60 derivatives: PCBM and two alternative pyrazolinofullerenes. Transient absorption data indicate that replacement of PCBM with either pyrazolinofullerene derivative results in a transition from bimolecular to monomolecular (geminate) recombination dynamics. We show that this transition cannot be explained by a difference in interfacial energetics. However, this transition does correlate with nanomorphology data which indicate that both pyrazolinofullerenes yield a much finer phase segregation, with smaller domain sizes, than that observed with PCBM. Our results therefore provide evidence of the role of nanomorphology in determining the nature of recombination dynamics in such donor/acceptor blends.

3.1 Introduction

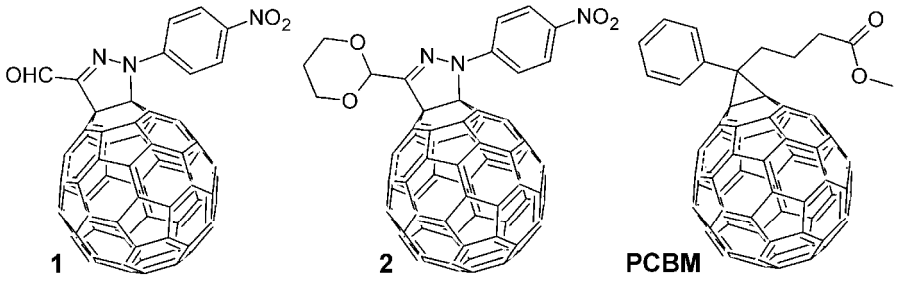
The observation of efficient photoinduced electron transfer from a semiconducting polymer to a fullerene in blend films has motivated extensive studies of the application of such films for photovoltaic solar energy conversion.[1-3] For such blend films, the formation of an interpenetrating donor/acceptor network, with nanoscale phase separation (the 'bulk heterojunction approach'), is essential to enable efficient separation of photogenerated excitons at the polymer / fullerene interface.[2] Following this charge photogeneration, two alternative recombination pathways can compete with charge collection and photocurrent generation – geminate recombination of the initially generated charges at the polymer / fullerene interface[4-9] and bimolecular recombination of dissociated charges during their transport to the device electrodes,[10,11] As was discussed in chapter 1, we have previously shown that the extent of geminate recombination losses can be strongly dependent upon the charge separation energetics at the donor / acceptor interface.[12] Furthermore, several studies have addressed the potential importance of nanomorphology, and in particular domain size, in influencing the importance of geminate versus bimolecular recombination losses[13-15] although such studies have not typically included direct studies of recombination dynamics. In particular, the donor / acceptor interfacial area and domain sizes are key parameters that have been suggested to have substantial effect on charge transfer (CT) state and, therefore, charge photogeneration.[16] Such studies have identified that optimal phase segregation must exist to minimise geminate recombination and thus maximise charge photogeneration, whilst at the same time balancing exciton dissociation and charge transport requirements. For example, if the phase separation is too fine, the large interfacial area may enhance geminate recombination. In this case the charges will not be able to escape one another efficiently and geminate recombination may result. We note in such a morphology the charges may not be confined by their Coulomb attraction (see section1.4), but rather by the physical size of the domains. An ideal blend morphology will involve both an optimised interfacial area for efficient exciton dissociation and phase separation on the order of the exciton diffusion length, with a bicontinuous interpenetrating network of donor and acceptor components. The achievement of such an appropriate morphology has therefore been the focus of numerous studies: the two blend systems that have been studied most extensively in this context are (poly[2-methoxy-5-(3′,7′-dimethyloctyloxy)-1,4-phenylenevinylene) : methanofullerene,

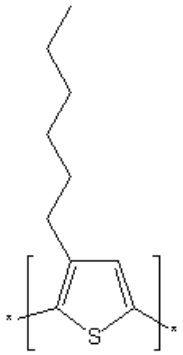
[6,6]-phenyl C_{61}-butyric acid methyl ester (MDMO-PPV:PCBM) and poly-3-hexylthiophene : methanofullerene, [6,6]-phenyl C_{61}-butyric acid methyl ester (P3HT:PCBM).[14,17-22]

The effect of morphology upon interfacial dynamics has been noted in a study by Müller et al,[4] investigating the presence of CT states in two polymer:PCBM blends (MDMO-PPV and MeLPPP). The studies revealed evidence of CT states in MeLPPP:PCBM but not MDMO-PPV:PCBM. This was attributed to the different blend film morphologies formed for each polymer. This study reported MDMO-PPV shows a tendency towards aggregation into domains whereas MeLPPP does not. Another study used Monte Carlo modeling to address the issue of geminate recombination as a function of domain size.[13] This modeling suggested that increasing the domain size from 4 to 16 nm progressively improved the CT state dissociation efficiency, after which the efficiency begins to saturate. This was attributed to the ease with which the geminate charges can move away from one another, which is greater in large domains.

In this study we focus upon the correlation between blend nanomorphology and recombination dynamics and show, for the first time, a transition between geminate and bimolecular recombination of photogenerated charges that is correlated with a change in blend nanomorphology.

For the study reported herein we employ films of polythiophenes blended with three different **C_{60}** derivatives. Our control films are based upon films of the methanofullerene, [6,6]-phenyl C_{61}-butyric acid methyl ester (PCBM) blended with poly-3-hexylthiophene (P3HT). Annealed 1:1 blend films of these materials have been shown to achieve photovoltaic device efficiencies exceeding 4%.[23,24] In such blend films, we have previously shown that charge recombination losses are dominated by bimolecular rather than geminate recombination, consistent with the favourable interfacial energetics and high degree of phase segregation. This phase segregation, resulting in domain sizes of the order of 10 nm, has been attributed to the tendency of both P3HT and PCBM to form aggregates during film deposition and annealing. For the study reported herein, data for these control films are compared to films employing two alternative pyrazolinofullerenes, blended with P3HT and a derivative of P3HT which incorporates hydroxyl group, illustrated in Scheme 2.





P3HT

Scheme 2: chemical structure of the pyrazolinofullerene derivatives **1** and **2** shown together with the **PCBM** and P3HT.

3.2 Materials and methods

All films employed for these experiments were fabricated as described in chapter 2. The solution samples were prepared by dissolving 20 mg of P3HT (Rieke Metal) and 20 mg of either fullerene, in 1 ml of o-dichlorobenzene solvent. Solutions were spun at 1500 rpm for 60 seconds.

All measurements were performed on non-annealed spin coated films of polymer:fullerene blends in a 1:1 ratio by weight. The resultant films were optically smooth (RMS roughness of < 1 nm), approximately 60 nm thick, as measured by AFM.

3.3 Results and discussion

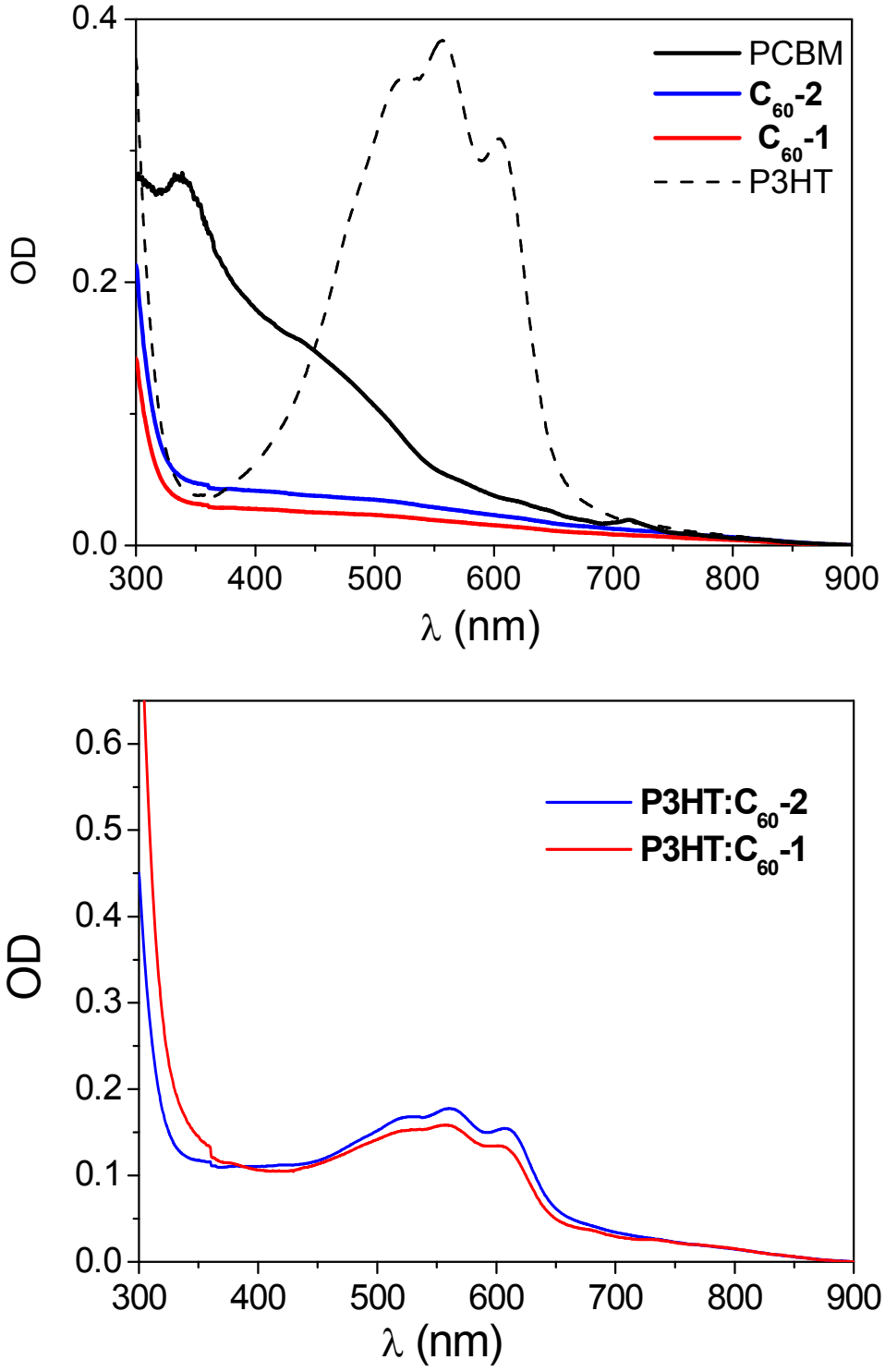


Figure 3.1 Ground state UV-visible spectra of as-prepared film of pristine (top) and blend (bottom) films from o-DCB; films were spun on untreated glass substrates at 1500 rpm for 60 s.

Figure 3.1 displays the UV/visible absorption spectra of pristine and blend spin-coated films. It is noticeable the pristine film of PCBM shows the appearance of strong visible absorption bands not observed in dilute solution, assigned to aggregation of PCBM in the solid film.[25] In contrast, pristine films of both C_{60}-1 and C_{60}-2 show only relatively weak visible light absorption, indicative of a lower tendency to form aggregates. This reduced tendency to form aggregates may be assigned to reduced flexibility (and absence of an ester) in the chemical groups attached to the fullerene core. The P3HT spectrum, however, indicates crystallisation of P3HT, consistent with the spectrum of annealed P3HT film. (It should be noted: the crytallinity of P3HT, both in pristine and blend films, results from employment of Rieke P3HT rather than Merck's P3HT with very crystalline features.) The ground state absorption spectrum of a pristine film of P3HT shows a maximum absorbance at 560 nm and a lowest energy band at 600 nm, as displayed in Figure 3.1. The addition of either C_{60}'s or PCBM to create a 1:1 blend film causes changes to the spectra, inducing a blue-shift of the absorption maximum from 560 nm to ~ 550 nm. The magnitude of the blue-shift is dependent upon the film fabrication conditions and hence the crystallinity of the resulting film. PCBM is known to disrupt the crystallinity of P3HT in a blend film: the PCBM molecules can disperse between P3HT chains and consequently prevent the formation of polymer crystallite domains.[26] Thus a greater blue-shift in the absorption spectrum is indicative of decreasing P3HT crystallinity. However, the absorption spectra of the blend films are quite similar to that of linear superposition of the two components, indicating that the modified C_{60}'s do not have an appreciable detrimental effect on the P3HT crystallinity, as had been expected.[27] In fact, the blend film spectra, all show features typical of crystalline P3HT.

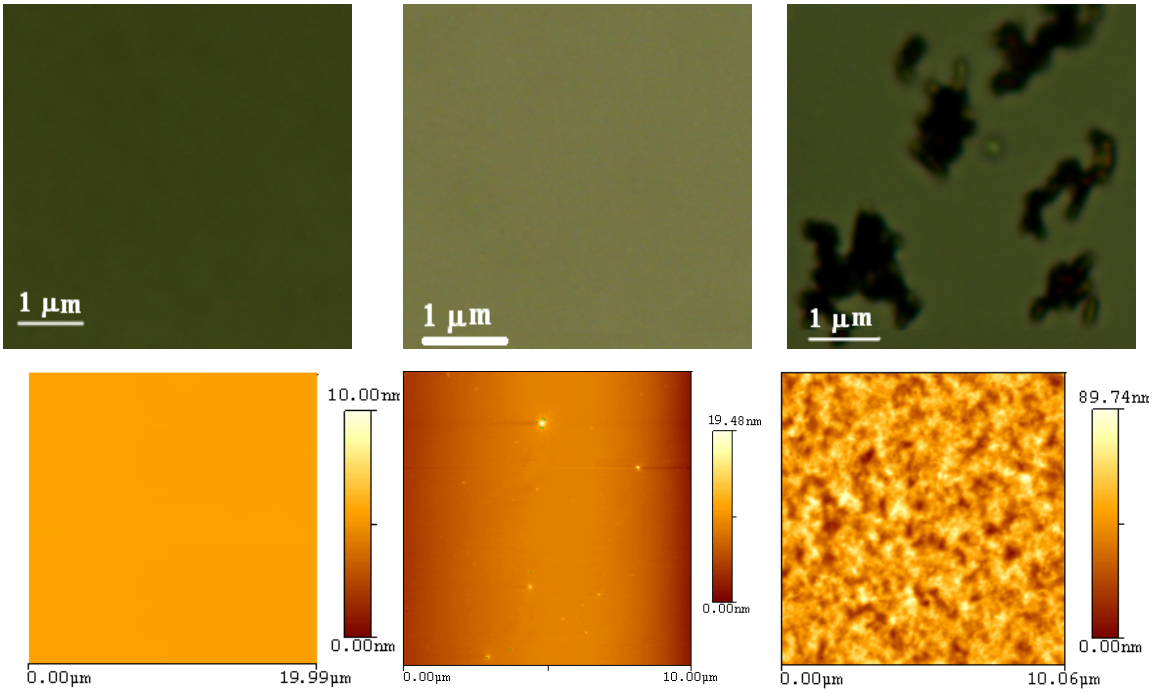


Figure 3.2 top: Optical microscopy images of P3HT:C_{60}-1 (left), P3HT:C_{60}-2 (centre) and P3HT:PCBM (right), bottom: TM-AFM images of P3HT: C_{60}-1 (left), P3HT:C_{60}-2 (centre) and P3HT:PCBM (right) blend films.

Figure 3.2 depicts optical microscope and atomic force microscopy images of the blend films, for P3HT:C_{60}-1, P3HT:C_{60}-2 and P3HT:PCBM. The larger crystallites observable in the P3HT:PCBM optical images have previously been assigned to PCBM crystals. The absence of such crystallites in the P3HT:C_{60}-1 and P3HT:C_{60}-2 is consistent with these fullerenes' reduced tendency to crystallise. Furthermore, the remarkably smooth AFM image for this blend film indicates a high degree of blending and interpenetration of P3HT and C_{60}-1 in this blend film. This contrasts with the rougher AFM image indicative of significant phase segregation for the P3HT:PCBM control. Previous studies have identified PCBM crystallisation as a key driver for P3HT:PCBM phase segregation.[28-30]

In order to address the affect of different phase segregation on the photophysics of these films, we start off by investigating exciton quenching. Photoluminescence (PL) data was collected to evaluate the efficiency of exciton quenching for the blend films. As shown in Figure 3.3, for all the blend films studied herein we observe quenching of the P3HT polymer PL by inclusion of 50 wt % of the fullerene to be > 90 %, indicative of efficient exciton diffusion to, and separation at, the polymer/fullerene interface. However, as we have shown

previously, PL quenching alone is not a reliable indicator of the generation of fully dissociated charges, due to the potential for geminate recombination of initially formed CT state prior to dissociation into separated charges.[12]

To address this issue we employed transient absorption spectroscopy (TAS) to monitor the charge separation yields and recombination dynamics. TA spectra of all the blend films showed an absorption peak around 950-1000 nm. Typical spectra, observed at 50 ns, for P3HT:C_{60}-1, P3HT:C_{60}-2, blend films are shown in Figure 3.4, consistent with previous literature. This band can be assigned to localised P3HT positive polarons ($P3HT^{\bullet+}$) due to its similarity with other results in the literature.[31-33] Altering the electron acceptor from C_{60}-1 to C_{60}-2 has only trivial effect on the maximum peak position. Thus the P3HT polaron absorption dominates the spectrum.

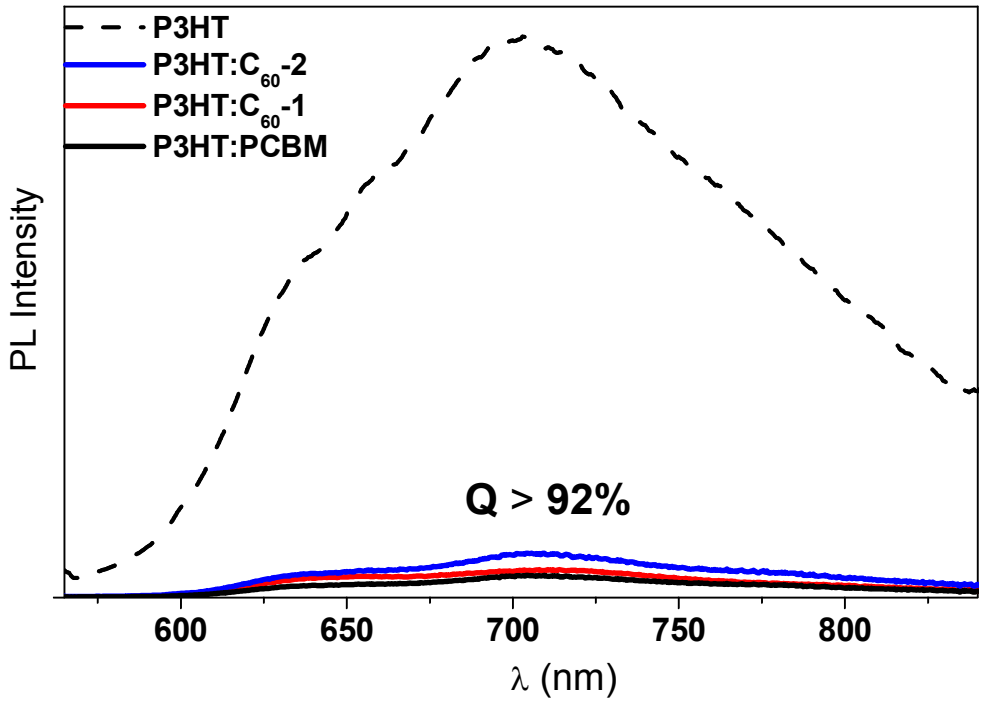


Figure 3.3 Photoluminescence quenching of blends of C_{60}-1, C_{60}-2, and PCBM together with 50 wt % of P3HT or P3HT-OH, excited at 550 nm.

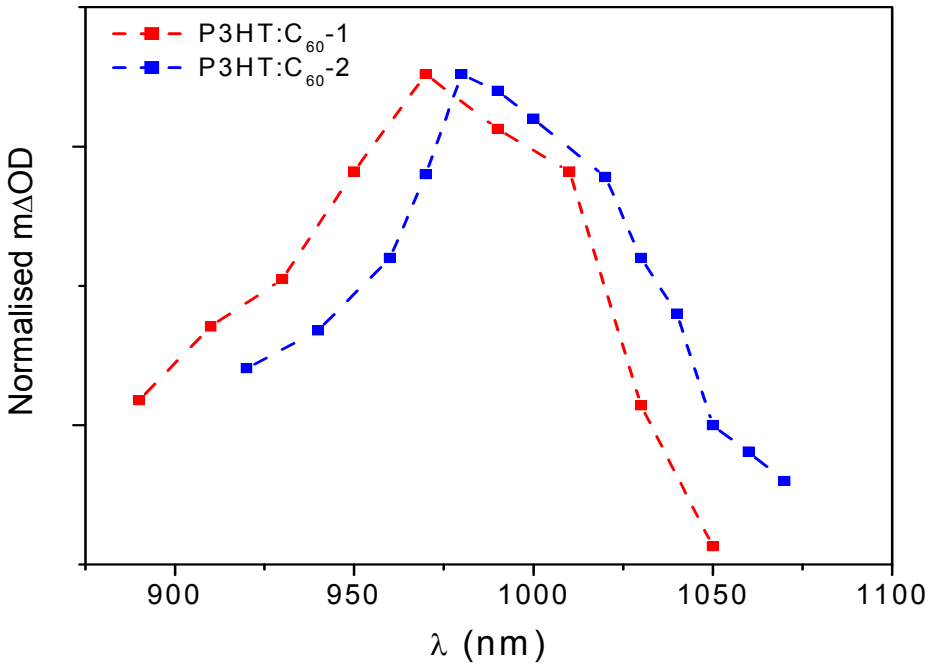


Figure 3.4 Transient absorption data collected for a 1:1 P3HT:C_{60}-1 (red) and P3HT:C_{60}-2 (blue) blend films under N_2 atmosphere, spun coated from o-DCB at 700 rpm for 60s. Excited at 532 nm and measured at 50 ns, using an excitation density of 50 μJ cm^{-2}.

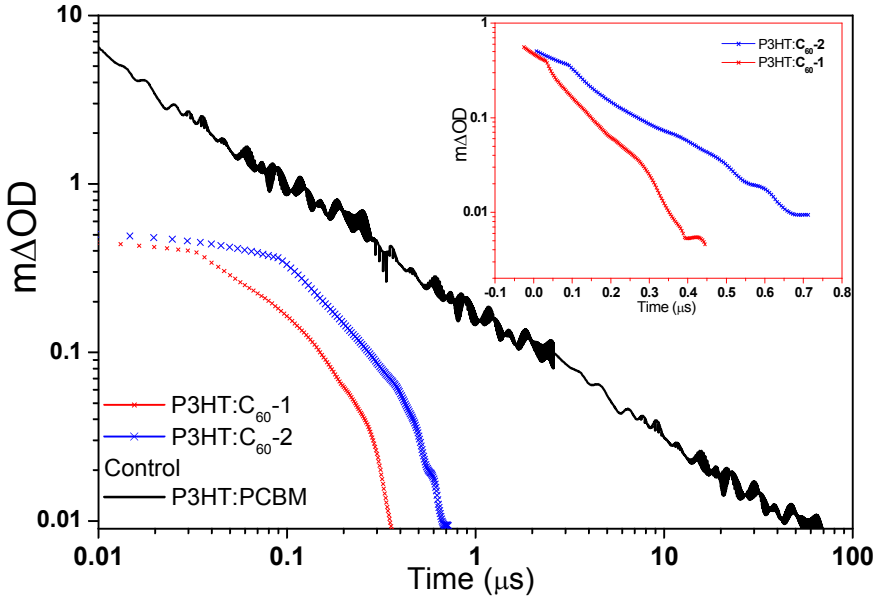


Figure 3.5 Transient decay on log/log plot: blends of C_{60}-1 (red) and C_{60}-2 (blue) obeying monoexponential and PCBM blend (black) as control film exhibiting a straight line with power law characteristics. Inset: same blend film data on log- linear plot with monoexponential fits. Excited at 533 nm, probed at 970 nm at 60 μJ.cm^{-2}. N_2 atmosphere.

The transient absorption decays of the various polymer:acceptor blends can now be examined. Figure 3.5 shows typical decay dynamics of the photoinduced absorption, monitored at the $P3HT^+$ absorption maximum (970 nm). These decay dynamics were all oxygen independent, consistent with their assignment to polaron rather than triplet absorption. The control P3HT:PCBM film exhibited a strong, long-lived ΔOD signal, obeying a power law ($\Delta OD \propto t^{-0.7}$, corresponding to a straight line on the log/log plot shown), typical of those we have reported previously, and assigned to bimolecular recombination. In contrast both the C_{60}-1 and C_{60}-2 blend films with either P3HT exhibit a relatively weak, much shorter-lived transient signal. Moreover, these faster decay dynamics are not power laws, but rather monoexponentials as evidenced by the straight line on the log/lin insert plot. These monoexponential (first order) behaviours, and much faster decay dynamics, are clear evidence that the decay dynamics of C_{60}-1 and C_{60}-2 blend films are dominated by monomolecular (geminate) rather than bimolecular recombination.

In order to identify the origin of the recombination dynamics of the blend films, it is helpful to employ a laser excitation density-dependent TAS study. Typical data for a P3HT:C_{60}-1 blend film is shown in Figure 3.6 a. All the other modified C_{60} blend films follow the same trend (data not shown). As expected for a first order process, the signal amplitude increases linearly with excitation density, whilst the decay lifetime is invariant. In contrast, the absorption transients for the P3HT:PCBM films (Fig 3.6 b), showed a sub-linear increase in amplitude, and faster decay dynamics, with increasing excitation density, consistent with their assignment to bimolecular recombination. Indeed, the same dynamics behaviour is observed in other P3HT:PCBM films.[34]

It should be pointed out that our control P3HT:PCBM blend film does not have the biphasic characteristic of typical P3HT:PCBM films. The charge generation yield and recombination kinetics of a polymer:PCBM blend film, as monitored by TAS, are dependent upon a number of factors such as their crystallinities. Altered crystallinity of the film is reflected in the transient absorption data. For instance, P3HT:PCBM recombination decays generally possess a slow phase that can be fitted to a power law and a fast phase. The lack of two phases in our control film decay may be attributed to the highly crystalline P3HT in the blend film. This is consistent with studies showing for more crystallised films, generally a faster power law decay with a more pronounced slow phase is observed.

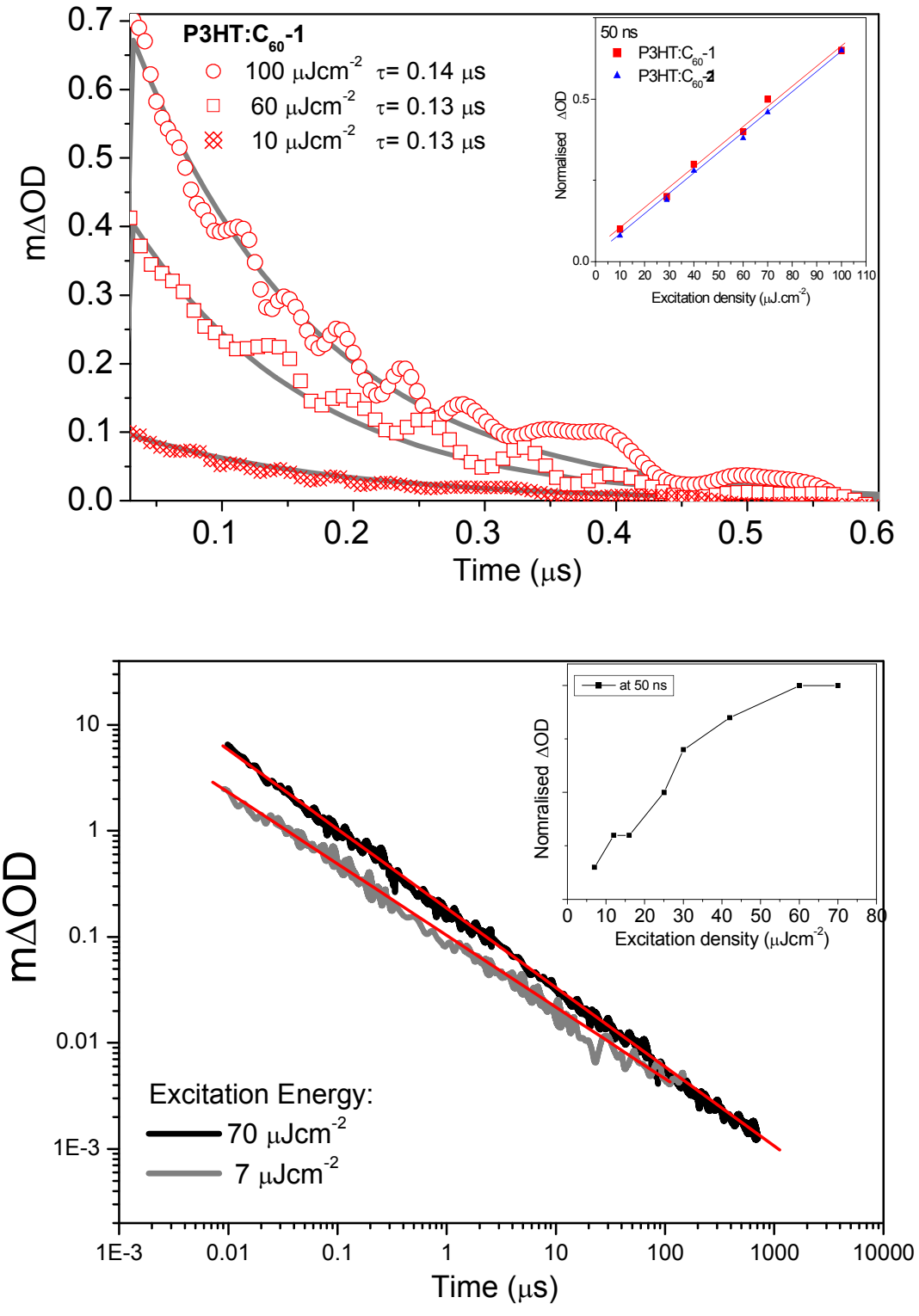


Figure 3.6 Excitation intensity dependence of: (top) P3HT: C_{60}-1 blend film and (bottom) P3HT:PCBM blend film under N_2 atmosphere, excited at 532 nm and probed at 970 nm. Excitation energy 70- 7 μJ cm^{-2}. Inset: normalised signal size measured at 50 ns as a function of laser excitation density.

To investigate the electron acceptor strength of the modified fullerenes against PCBM, we turn to cyclic voltammetry. These data were collected by Juan Luis Degado at Universidad Complutense. Electrochemical data presented in Figure 3.2 show, C_{60}-1 and C_{60}-2 are both stronger electron acceptors (less negative reduction potentials) than PCBM, due to the presence of the electron withdrawing nitrogen atoms in the heterocyclic ring fused to the C_{60} core. As a consequence, the energetic driving force for charge separation will be larger for C_{60}-1 and C_{60}-2 compared to PCBM. Following our ΔG_{CS} studies,[12] we therefore expect, in terms of energetic considerations alone, replacement of PCBM with either C_{60}-1 or C_{60}-2 to allow the CT state to have more thermal energy available to overcome the Coulomb barrier and thus lower geminate recombination losses. Thus, following from our previous studies,[12] on energetic grounds alone, we might expect more dissociated charges (less geminate recombination) when using C_{60}-1 and C_{60}-2 as electron acceptor rather than PCBM.

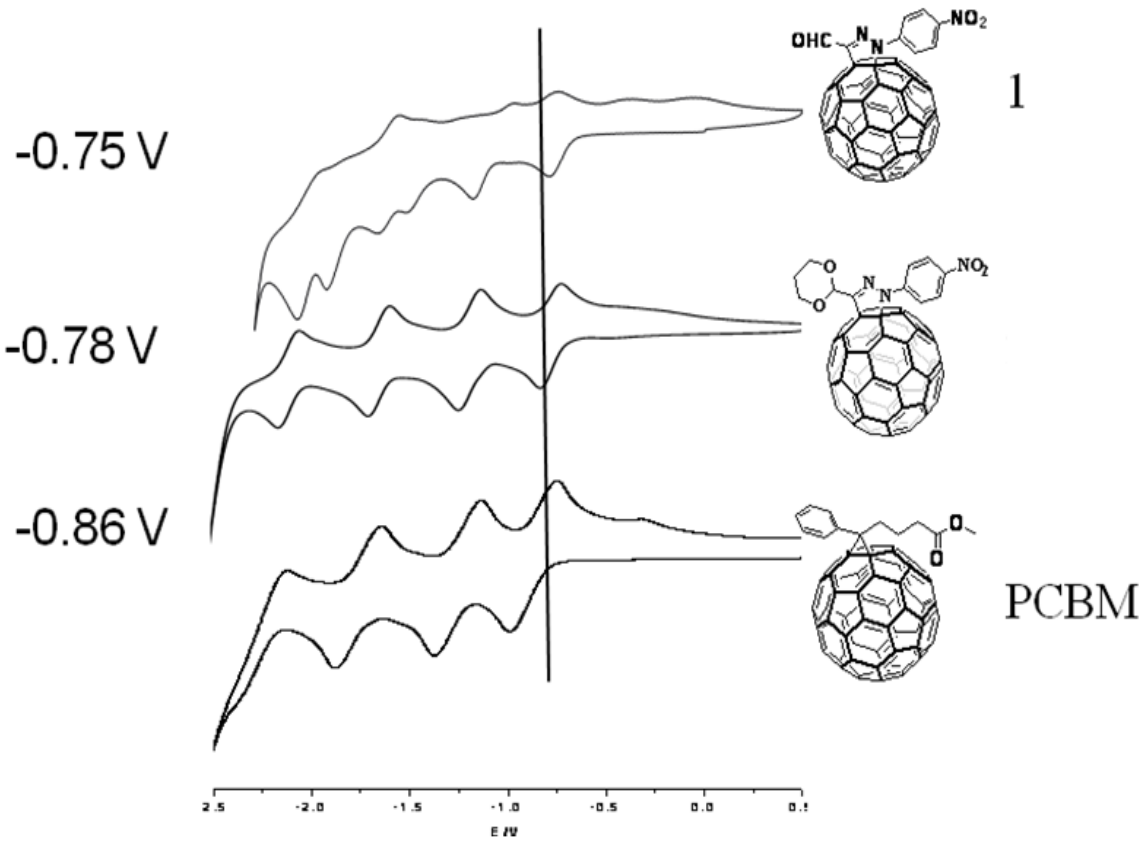


Figure 3.7 Cyclic Voltammetry of the three fullerenes. Measurements done by Juan Luis Degado at Universidad Complutense.

We have concluded that replacing PCBM in P3HT:PCBM blend films with either C_{60}-1 or C_{60}-2 results in a transition from bimolecular to geminate recombination dynamics. As we have argued above, electrochemical data strongly suggests that this transition cannot be assigned to a change in interfacial energetics (which would tend to favour reduced geminate recombination losses for C_{60}-1 and C_{60}-2). Rather, it appears more likely that this transition results from the pronounced change in nanomorphology between the blend films. More specifically, P3HT:C_{60}-1 and P3HT:C_{60}-2 blend films exhibit much smoother blend films indicative of a finer blend nanomorphology, which is likely to result in a reduced blend domain size and thus impede the dissociation of the initially generated polaron pairs into spatially uncorrelated charges.

Several theoretical modelling and device performance analyses have previously proposed a correlation between nanomorphology and geminate recombination in polymer / PCBM blend films.[15,35,36] For example, studies as a function of annealing and PCBM composition have been interpreted in terms of changes in domain size influencing the efficiency of dissociation of the initially generated geminate polarons pairs.[13,14,37] This rationale has been invoked in a number of studies of CT state dissociation. A comprehensive study exploring the influence of morphology was reported by Janssen *et al*,[38] where the composition dependence of the CT emission in PF10TBT:PCBM films was examined. Photoexcitation of the PF10TBT blends revealed not only the expected efficient PL quenching with addition of PCBM, but also a broad red-shifted emission band attributed to the CT state. As the PCBM concentration was increased, the CT state emission red-shifted. The dissociation of the CT state into free charge carriers was observed to improve in efficiency with increasing PCBM concentration. The concentration of these polarons increased with increasing PCBM concentration, thereby supporting the theory that higher PCBM concentrations enhance the dissociation of the CT state. The charge photogeneration yield improves as a result, consistent with the higher short-circuit currents measured for higher PCBM concentrations. These results reflect the changes in morphology as the PF10TBT:PCBM blend composition is varied.[38] High concentrations of PCBM produced phase segregation and the formation of large PCBM domains; this was not observed at lower PCBM concentrations. Only the sample with 80% PCBM revealed nanocrystalline PCBM domains of 50 – 100 nm in diameter and this was correlated with the highest device efficiency. The potentially higher electron mobility in these domains, larger effective dielectric constant of the blend, and greater electron-hole separation distances were

all suggested to facilitate the dissociation of the CT state at the donor/acceptor interface. Geminate recombination is thereby reduced, increasing the charge photogeneration yield and consequently enhancing the photocurrent and device efficiency.

The data we report herein is, we believe, the first direct observation of a transition in the observed decay dynamics from monomolecular to bimolecular induced by such a change in nanomorphology. At present it is unclear whether the geminate recombination we observe herein on a 100 ns timescale corresponds to the recombination of Coulombically bound polaron pairs or, rather, the recombination of polaron pairs that have escaped their Coulomb attraction but remain physically confined by the physical size of their respective domains. In this regard we note that the initial amplitude of the polaron signals (measured at ~ 10 ns) is significantly smaller for the P3HT:C_{60}-1 and P3HT:C_{60}-2 blends relative to P3HT:PCBM, indicative of the presence of an additional, faster decay phase for the P3HT:C_{60}-1 and P3HT:C_{60}-2 blends. We note that picosecond timescale geminate recombination has been previously reported in non-annealed P3HT:PCBM blend films.[39] On the other hand, geminate recombination dynamics of Coulombically bound, emissive charge transfer states in polymer / polymer blends (sometimes referred to as 'exciplexes') have been reported to occur on the ~ 50 ns timescale.[13,40,41] Notwithstanding these uncertainties, it is clear from the data shown herein that blend nanomorphology can have a substantial role in minimizing geminate recombination in the organic polymer / fullerene blend films.

This study therefore clearly demonstrates that nanomorphology is key not only to determining the efficiency of exciton quenching and charge transport in organic bulk heterojunction solar cells, but it is furthermore important in enabling the dissociation of the CT state. If phase segregation is too large, the limited diffusion length of the photoinduced excitons reduces charge photogeneration, while blends that are too intimately mixed may suffer from geminate recombination and poor charge carrier yields. Furthermore, many studies have concluded that a minimum PCBM domain size is necessary to facilitate the dissociation of the CT state at the donor/acceptor interface. This decreases the probability of geminate recombination, thereby enhancing the charge photogeneration yield and device efficiency. It appears likely that an important factor behind the efficiency of P3HT:PCBM solar cells is the achievement of relatively optimum nanomorphology. Achieving such a favourable morphology using new materials possessing energy levels compatible with higher device efficiencies is a key challenge for further advances in device efficiency.

3.4 Conclusion

Replacing PCBM with either of C_{60}-1 and C_{60}-2 appears to greatly increase geminate recombination losses. As we have argued above, electrochemical data strongly suggests that this transition cannot be assigned to a change in interfacial energetics (which would tend to favour reduced geminate recombination losses for 1 and 2). Rather, it appears more likely that this transition results from the pronounced change in nanomorphology between the blend films. More specifically, P3HT: C_{60}-1 and P3HT: C_{60}-2 blend films exhibit much smoother blend films indicative of a finer blend nanomorphology, reducing the blend domain size, and thus impeding the dissociation of the initially generated polaron pairs to dissociate into spatially uncorrelated charges. Thus, for the first time we directly observe a switch from bimolecular to geminate recombination that appears to be driven by the morphology of the blend. Whilst clearly this is not promising for device studies, it is interesting in terms of photophysics and highlights the importance of the domain size in the bulk heterojunction on achieving efficient charge dissociation.

References:

(1) Brabec, C. J.; Sariciftci, N. S.; Hummelen, J. C. *Adv. Funct. Mater.* **2001**, *11*, 15.

(2) Yu, G. Geo, J.; Hummelen, J. C.; Wudl, F.; Heeger, A. J. *Science* **1995**, *270*, 1789

(3) Halls, J. J. M; Walsh, C. A.; Greenham, N. C.; Marseglia, E. A.; Friend, R. H.; Moratti, S. C.; Holmes, A. B. *Nature* **1995**, *376*, 498.

(4) Müller, J. G.; Lupton, J. M.; Feldmann, J.; Lemmer, U.; Scharber, M. C.; Sariciftci, N. S.; Brabec, C. J.; Scherf, U. *Physical Rev. B* **2005**, *72*, 195208.

(5) Arias, A. C.; MacKenzie, J. D.; Stevenson, R.; Halls, J. J. M.; Inbasekaran, M.; Woo, E. P.; Richards, D.; Friend, R. H. *Macromolecules* **2001**, *34*, 6005.

(6) Halls, J. J. M.; Arias, A. C.; J. D. MacKenzie, W. Wu, M. Inbasekaran, E. P. Woo, R. H. Friend, *Adv. Mater.* **2000**, *12*, 498.

(7) Snaith, H. J.; Arias, A. C.; Morteani, A. C.; Silva, C.; Friend, R. H. *Nano Lett.* **2002**, *2*, 1353.

(8) Martens, T.; Munters, T.; Goris, L.; D'Haen, J.; Schouteden, K.; D'Olieslaeger, M.; Lutsen, L.; Vanderzande, D.; Geens, W.; Poortmans, J.; De Schepper, L.; Manca, J. V. *Applied Physics a-Materials Science & Processing* **2004**, *79*, 27.

(9) van Duren, J. K. J.; Yang, X.; Loos, J.; Bulle-Lieuwma, C. W. T.; Sieval, A. B.; Hummelen, J. C.; Janssen, R. A. J. *Adv. Funct. Mater.* **2004**, *14*, 425.

(10) Nelson, J. *Physical Rev. B* **2003**, *67*, 155209.

(11) Forrest, S. R. *MRS Bulletin* **2005**, *30*, 28.

(12) Ohkita, H.; Cook, S.; Astuti, Y.; Duffy, W.; Tierney, S.; Zhang, W.; Heeney, M.; McCulloch, I.; Nelson, J.; Bradley, D. D. C.; Durrant, J. R. *J. Am. Chem. Soc.* **2008**, *130*, 3030.

(13) Groves, C.; Marsh, R. A.; Greenham, N. C. *J. Chem. Phys.* **2008**, *129*, 114903.

(14) Müller, C.; Ferenczi, T. A. M.; Campoy-Quiles, M.; Frost, J. M.; Bradley, D. D. C.; Smith, P.; Stingelin-Stutzmann, N.; Nelson, J. *Adv. Mater.* **2008**, *20*, 3510.

(15) Mihailetchi, V. D.; Koster, L. J. A.; Blom, P. W. M.; Melzer, C.; de Boer, B.; van Duren, J. K. J.; Janssen, R. A. J. *Adv. Funct. Mater.* **2005**, *15*, 795.

(16) Chasteen, S. V.; Sholin, V.; Carter, S. A.; Rumbles, G. *Solar Energy Materials and Solar Cells* **2008**, *92*, 651.

(17) Hoppe, H.; Glatzel, T.; Niggemann, M.; Schwinger, W.; Schaeffler, F.; Hinsch, A.; Lux-Steiner, M. C.; Sariciftci, N. S. *Thin Solid Films* **2006**, *511-512*, 587.

(18) Quist, P. A. C.; Martens, T.; Manca, J. V.; Savenije, T. J.; Siebbeles, L. D. A. *Solar Energy Materials and Solar Cells* **2006**, *90*, 362.

(19) Clarke, T. M.; Ballantyne, A. M.; Nelson, J.; Bradley, D. D. C.; Durrant, J. R. *Adv. Funct. Mater.* **2008**, *18*, 4029.

(20) Erb, T. T. *Thin Solid Films* **2006**, *511*, 483.

(21) Kim, Y.; Choulis, S. A.; Nelson, J.; Bradley, D. D. C.; Cook, S.; Durrant, J. R. *App. Phys. Lett.* **2005**, *86*, 063502.

(22) Li, B.; Wang, L. D.; Kang, B. N.; Wang, P.; Qiu, Y. *Energy Mater. Sol. Cells* **2006**, *90*, 549.

(23) Reyes-Reyes, M.; Kim, K.; Carroll, D. L. *App. Phys. Lett.* **2005**, *87*, 083506.

(24) Ma, W. W.; Yang, C.; Gong, X.; Lee, K.; Heeger, A. J. *Adv. funct. mater.* **2005**, *15*, 1617.

(25) Cook, S.; Ohkita, H.; Kim, Y.; Benson-Smith, J. J.; Bradley, D. D. C.; Durrant, J. R. *Chem. Phys. Lett.* **2007**, *445*, 276.

(26) Erb, T.; Zhokhavets, U.; Gobsch, G.; Raleva, S.; Stühn, B.; Schilinsky, P.; Waldauf, C.; Brabec, C. J. *Adv. Funct. Mater.* **2005**, *15*, 1193.

(27) Moule, A. J.; Allard, S.; Kronenberg, N. M.; Tsami, A.; Scherf, U.; Meerholz, K. *J. Phys. Chem. C* **2008**, *112*, 12583.

(28) Campoy-Quiles, M.; Ferenczi, A. T.; Etchegoin, P. B.; Kim, Y.; Anthopoulos, T. D.; Stavrinou, P. N.; Bradley, D. D. C. *Nat. Mater* **2008**, *7*, 158.

(29) Klimov, E.; Li, W.; Yang, X.; Hoffmann, G. G.; Loos, J. *Macromolecules* **2006**, *39*, 4493.

(30) Écija, D.; Otero, R.; Sánchez, L.; Gallego, J. M.; Wang, Y.; Alcamiz, M.; Martín, F.; Martín, N.; Miranda, R. *Angew. Chem. Int. Ed* **2007**, *46*.

(31) Korovyanko, O. J.; Österbacka, R.; Jiang, X. M.; Vardeny, Z. V.; Janssen, R. A. J. *Physical Rev. B* **2001**, *64*, 235122.

(32) Österbacka, R.; An, C. P.; Jiang, X. M.; Vardeny, Z. V. *Science* **2000**, *287*, 839.

(33) Westerling, M.; Österbacka, R.; Stubb, H. *Physical Rev. B* **2002**, *66*, 165220.

(34) Clarke, T.; Jamieson, F. C.; Durrant, J. R., *J. Phys. Chem. C.* **2009**, *113*, 20934.

(35) Chirvase, D.; Parisi, J.; Hummelen, J. C.; Dyakonov, V. *Nanotechnology* **2004**, *15*, 1317.

(36) Mihailetchi, V. D.; Xie, H. X.; de Boer, B.; Koster, L. J. A.; Blom, P. W. M. *Adv. Funct. Mater.* **2006**, *16*, 699.

(37) Yang, X.; Loos, J.; Veenstra, S. C.; Verhees, W. J. H.; Wienk, M. M.; Kroon, J. M.; Michels, M. A. J.; Janssen, R. A. J. *Nano Lett.* **2005**, *5*, 579.

(38) Veldman, D.; Opek, O.; Meskers, S. C. J.; Sweelssen, J.; Koetse, M. M.; Veenstra, S. C.; Kroon, J. M.; Bavel, S. S. v.; Loos, J.; Janssen, R. A. J. *J. Am. Chem. Soc.* **2008**, *130*, 7721.

(39) Hwang, I. W.; Moses, D.; Heeger, A. J. *Journal of Physical Chemistry C* **2008**, *112*, 4350.

(40) Morteani, A. C.; Paiboon, S.; Herz, L. M.; Friend, R. H.; Silva, C. *Phys. Rev. Lett.* **2004**, *92*, 247402.

(41) Ford, T. A.; Ohkita, H.; Cook, S.; Durrant, J. R.; Greenham, N. C. *Chem. Phys. Lett.* **2008**, *454*, 237.

IV. Photophysics of solutions vs. films in donor-acceptor system

The concept of studying photophysical kinetics in covalently bond donor-acceptor molecules designed to mimic the heterojunctions found in donor / acceptor blends may be a fruitful approach in gaining insight into, and control over, the interfacial nanomorphology that may limit efficient charge photogeneration and transport in devices – the covalent linkage of many donor and acceptor moities places a limit on the domain size and phase segregation in the solid state. Such studies complement and may resolve the blend morphology limitations that we observed in previous chapter, which lead to enhanced geminate recombination.

In this chapter we report on photoinduced charge separation in solid films of two perylene diimides one of which incorporates an electron donor group. Intramolecular charge separation and recombination is correlated with a reduction in the yield of long-lived, intermolecular charge-separated species.

4.1 Introduction

Recently, a new class of photofunctional nanomaterials based on electron donor (D)-acceptor (A) ensembles has been extensively studied, arising from the possibility of mimicking the photochemical processes in photosynthetic reaction centres and, in part, due to the potential use of such molecules in applications ranging from solar energy conversion to non-linear optical absorption.[1,2,3]As an alternative to blends, covalently linking a π-electron donating and a π-electron accepting moiety with a molecular bridge is a possible approach to control and obtain nanoscale phase segregation in thin multicomponent films.[4] These molecular π-assemblies can be designed to have small electron transfer reorganization energies between D and A, which results in fast charge separation.[5,6]

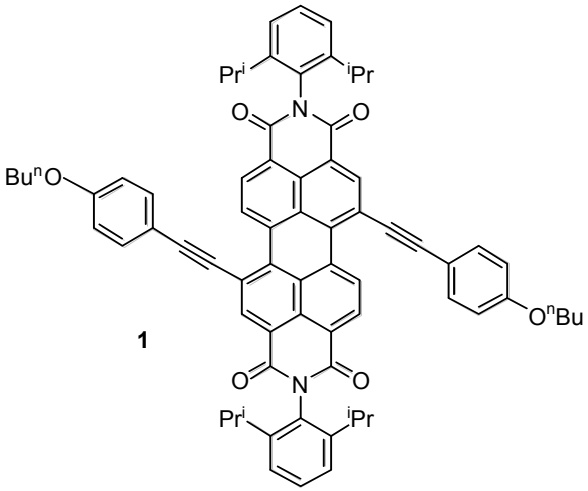
Supramolecular donor–acceptor structures have been widely studied in solution as simple model systems for photoinduced electron transfer dynamics.[7-9] The structure / function relationships that determine the solution photophysics and photochemistry of such molecules have now been elucidated in considerable detail.[5,6,10-13] Careful design of D–A linked molecules that have led to the development of artificial photosynthetic systems aimed towards the realisation of efficient solar energy conversions.[5] Such studies have demonstrated charge separation yields near unity, with lifetimes of the long-lived charge separated state of up to tens of microseconds in solutions.[14] However, relatively few studies have addressed the question of whether this understanding of solution photochemistry can be extended to the function of such donor / acceptor structures in solid films.[1] This is a significant barrier for communication between the fields of general and applied research and has sparked our interest in studying the effects on the now rather well known solution photophysics when going to the solid state. This issue is of particular importance for technological applications, which will typically be based upon solid-state, rather than solution systems.[15-17]

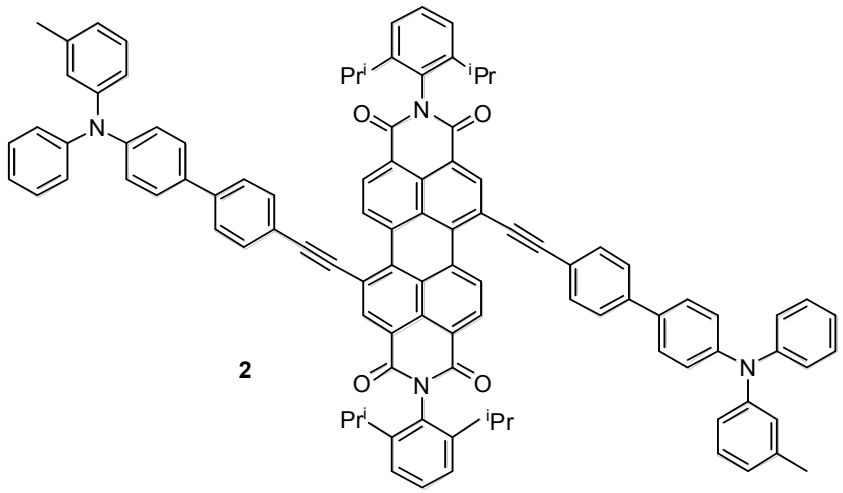
Supramolecular systems based on the donor-acceptor approach have previously been used as the sole component in active layers for PV energy conversion with some success.[18-31] Perylene diimides and their derivatives have been widely used in multifunctional supramolecular arrays that employ photoinduced charge transfer[32-37] or energy transfer processes, [38] owing to their relatively low reduction potentials, outstanding thermal, chemical and optical stabilities, and tuneable absorption and emission properties. [39-42] For example, Thelakkat *et al*. synthesized a novel donor-bridge-acceptor (D-B-A) dyad illustrating both

energy- and electron-transfer processes. This D-B-A consisted of tetraphenylbenzidine (TPD) and PDI linked by a dodecyl spacer.[43] The selective excitation of the TPD donor leads to a highly efficient, energy transfer to the PDI. The assigned intramolecular energy transfer was four times more efficient in the dyad than in the blend of the constituent materials. Conversely, direct excitation of the PDI acceptor in the dyad exhibited reduced fluorescence emission of the acceptor, indicating efficient electron transfer. π-Conjugated oligothiophenes, as substituents at the bay position of a perylene core[44] demonstrate another D-A system with intramolecular electron transfer. The thiophene-substituted perylene D–A structure, relative to the original PDI, experiences a bathochromic shift along with considerable band broadening and a less pronounced vibronic fine structure. The oxidation potential of this D-A structure can be tuned by varying the number of thiophene groups. Such characteristics, along with well-controlled self-assembly properties, are used to mimic photosynthetic processes for potential applications in molecular electronics, such as molecular switches, wires and solar cells.[45,46]

The highest total power conversion efficiency reported for the D–A approach in solid state is, to our knowledge, 0.37 %.[24] The low efficiencies may be primarily limited by inefficient charge photogeneration and transport issues as well as high series resistance. Although not very impressive, the efficiencies still give promise for the approach as a potential new method for achieving cheap energy production. It also highlights the importance of a more in-depth study of the photophysics of this type of compounds in the solid state since this will be imperative for improving efficiency.

We commence our studies on photoinduced electron-transfer processes occurring in films of a bis(4-(diarylamino)biphenylethynyl)-substituted perylene diimide dyad (**2**), and compare these, to films of a bis(4- alkoxyphenylethynyl)-substituted perylene diimide control (**1**), (Scheme 3). In this study, we address the charge photogeneration properties of thin solid films of these molecules, focusing upon the generation of the long-lived charge-separated species which are essential for applications such as solar energy conversion. In particular, we consider whether the donor / acceptor structural motif that is found in solution to favour intramolecular charge separation in many donor / acceptor molecules such as dyad **2**, also results in enhanced intermolecular charge generation in solid films.





Scheme 3 Donor- Acceptor structures of PDI-TPA (**2**) with its PDI control (**1**)

4.2 Materials and method

Films were prepared as described in chapter 2.

Compounds 1 and 2 were synthesized by Georgia Institute of Technology as described in the literature. The materials were dissolved in chloroform at a concentration of 20 mg/ml. Solutions were spun on glass substrates at a 500 rpm for 60 seconds.

Solution absorption and emission was measured in 1 cm quartz cuvettes and transient absorption in quartz cuvettes with septa to isolate the film from oxygen in the atmosphere. Oxygen was removed from the solutions by leaving the cuvette open in a glove-box for more than 30 minutes. In solution the concentration of the studied compound was kept below 4 μM.

All film measurements were performed as described in chapter 2.

4.3 Inter versus intra-molecular photoinduced charge separation in solid films of triphenylamine/PDI molecular dyads

Solid films of both **1** and **2** were approximately 120 nm thick and optically non scattering; AFM data indicating root mean squared (RMS) roughness of ~5 nm for both films. Typical spin-coated film absorption and emission spectra are shown in Figure 4.1. The film absorption spectrum of **2** is essentially indistinguishable from the corresponding solution spectrum, indicating TPA π orbitals involved in the electronic transition are not strongly perturbed in the film relative to their solution state and thus indicative of only modest intermolecular interactions. Compared to parent perylene diimides, **1** has a similar absorption maximum around 490 nm with less vibronic features of the perylene core. However, this typical PDI absorption feature is not apparent in **2**. The loss of fine vibronic structures for **2** may be a result of twisting of the two naphthalene units of the perylene skeleton upon substitution at the 1, 7 perylene diimide bay position.[47,48] Furthermore the lowest energy band of **2** is red-shifted relative to **1**, assigned to the expected donor-acceptor charge-transfer character of the lowest excited state of **2**.

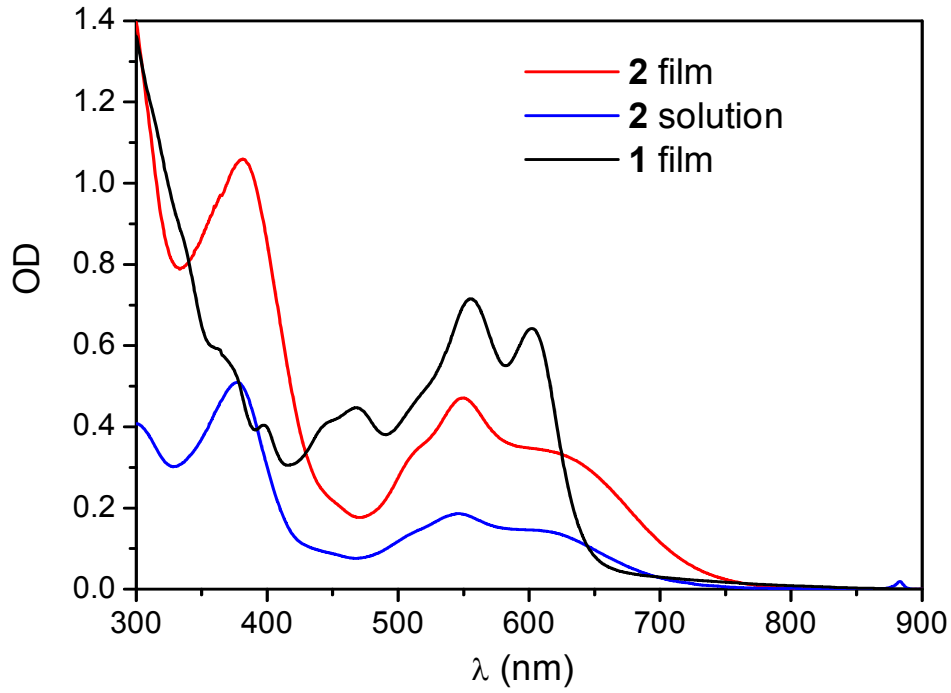
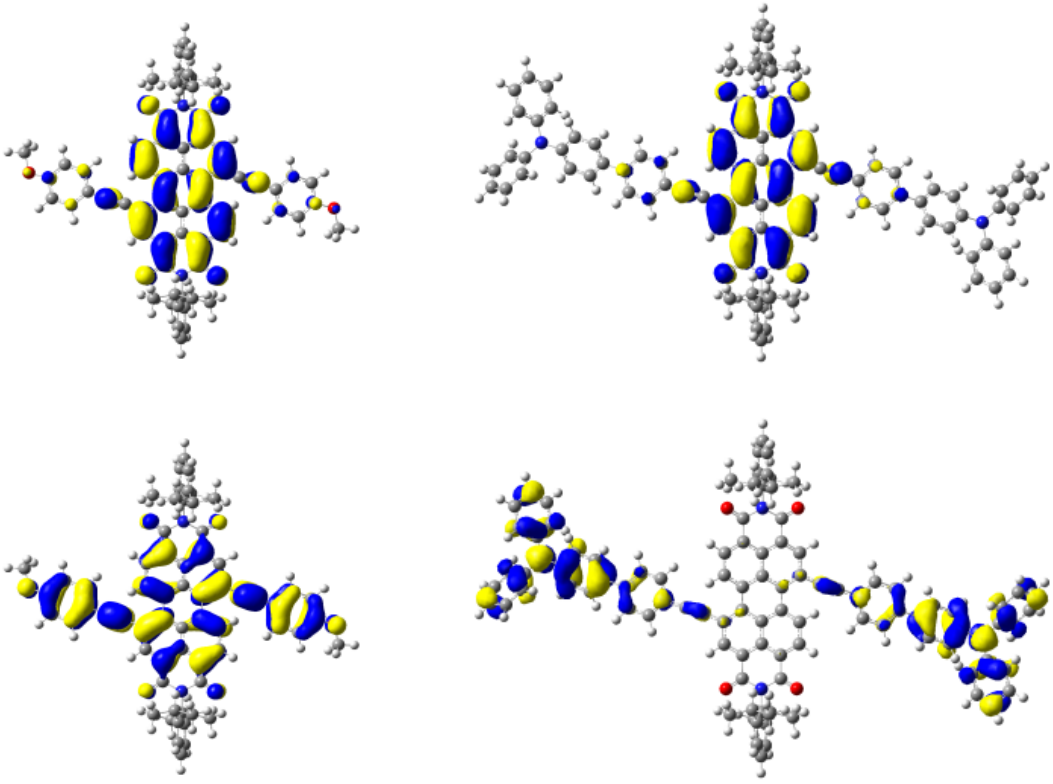


Figure 4.1 UV-visible spectra of as-prepared films of **1** (black), **2** (red) and **2** in chloroform (blue). Films were spin- coated on untreated glass substrates at 500 rpm for 60 s.



Scheme 4: The calculated LUMOs (top) and HOMOs (bottom) for 1 and 2 molecules**.**

These experimental data were complemented by DFT and TD-DFT calculations (details given in the Appendix). The calculated HOMOs and LUMOs of the geometry optimized structures are shown in Scheme 4 and indicate qualitatively different electronic structures for the two compounds. In contrast to molecule **1**, molecule **2** shows a clear spatial separation of its HOMO and LUMO, consistent with optical excitation resulting in the formation of an intramolecular charge transfer state.

Figure 4.2 shows time-resolved fluorescence decays for the two molecular films. The control film of **1** shows a monoexponential decay with a lifetime of 4.1 ns, indicative of formation of a long-lived singlet excited state. In contrast, the fluorescence quantum yield for the film of **2** is strongly reduced, showing only a low-amplitude instrument response limited transient signal indicative of a singlet excited-state decay time of < 250 ps. These emission dynamics are similar to those observed in solution. The fluorescence quenching for the film of **2** is consistent with the observation of ultrafast (~ 10 ps) intramolecular charge separation for this molecule in dilute solution;[49] this emission quenching can, therefore, be attributed to intramolecular photoinduced charge separation in the film.

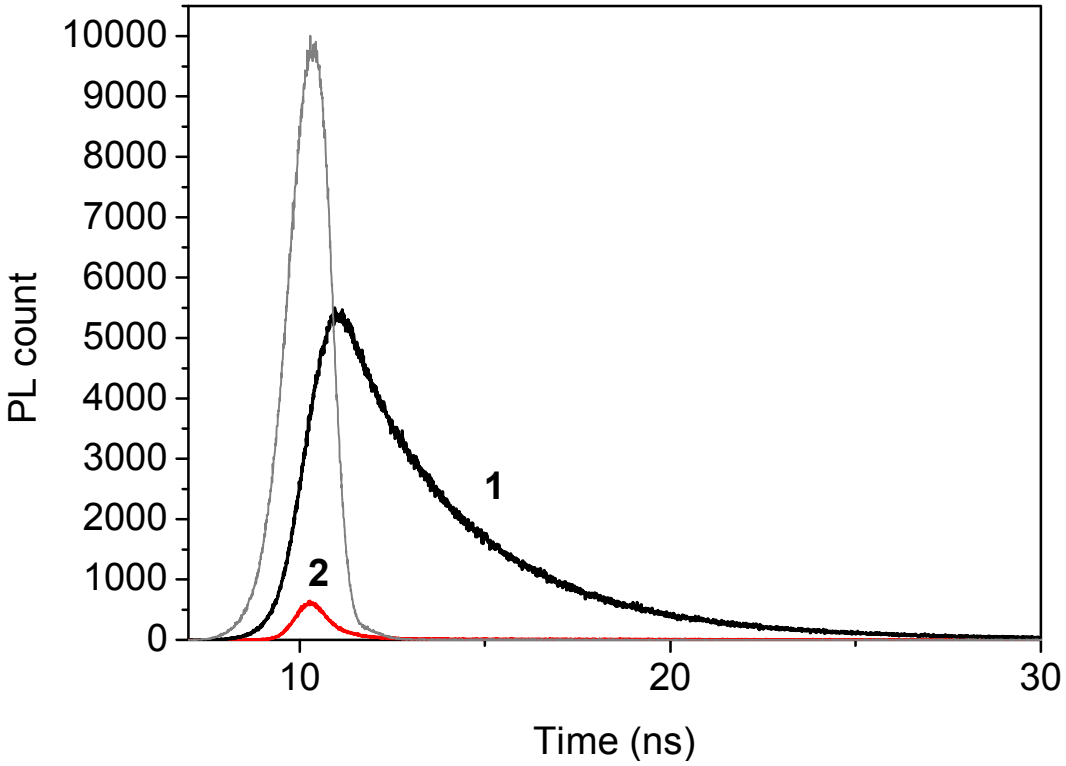


Figure 4.1 Time-resolved single-photon-counting data for films of **1** (black), **2** (red) and instrument response (gray). Data were collected using 467 nm excitation and 670 nm detection, with a 250 ps instrument response and data collection times corresponding to matched densities of absorbed photons. For purpose of comparison, the time scale for instrument response and signal **2** have been shifted.

These emission data were complemented by transient absorption studies of photo-induced charge generation, as shown in Figure 4.3. Previous solution transient absorption studies have revealed that the intramolecular charge separated state formed in **2** exhibits a decay time of 750 ps, which is assigned to intramolecular charge recombination.[49] Herein, however, we focus on the possibility of molecular films of this species generating long-lived, intermolecular charge separated species observable on the microsecond timescale. Control data in dilute solution showed no measurable signals on this timescale, consistent with ultrafast intramolecular charge recombination to the ground state. In contrast, a solid film of **2** shows a clear transient absorption signal, as illustrated in Figure 4.3. The absorption difference spectrum (Figure 4.3a) shows a photoinduced absorption maximum at 740 nm, consistent with previous reports of the absorption of radical anions of PDI derivatives[50,51] and

distinguishable from the PDI triplet absorption at 480 nm and TPA cations at 660 nm.[52] This transient spectrum is, therefore, assigned to a charge-separated state in which hole and electron are localised on triarylamine and PDI moieties, respectively. Figure 4.3b shows the corresponding decay dynamics of this transient absorption signal, monitored under low excitation densities (20 μJ/cm^2). It is apparent that this absorbance is long-lived, exhibiting dispersive (approximately power law) decay dynamics, with a decay extending to 100's of microseconds. These decay dynamics were observed to be independent of the presence of oxygen, confirming they cannot be assigned to triplet states (in agreement with the transient spectrum discussed above). Moreover, this decay lifetime is four orders of magnitude longer than the intramolecular charge recombination timescale observed in solution, and therefore, cannot be assigned to the same intramolecular charge-separated species. Rather, this long-lived transient signal is assignable to the formation of dissociated, intermolecular charge-separated states, i.e. $\mathbf{2}^{\bullet+}$ / $\mathbf{2}^{\bullet-}$. The observed recombination lifetime and dispersive power law behaviour of the recombination dynamics are typical of those previously reported for intermolecular bimolecular recombination of dissociated charges in polymer / fullerene blend films.[53]

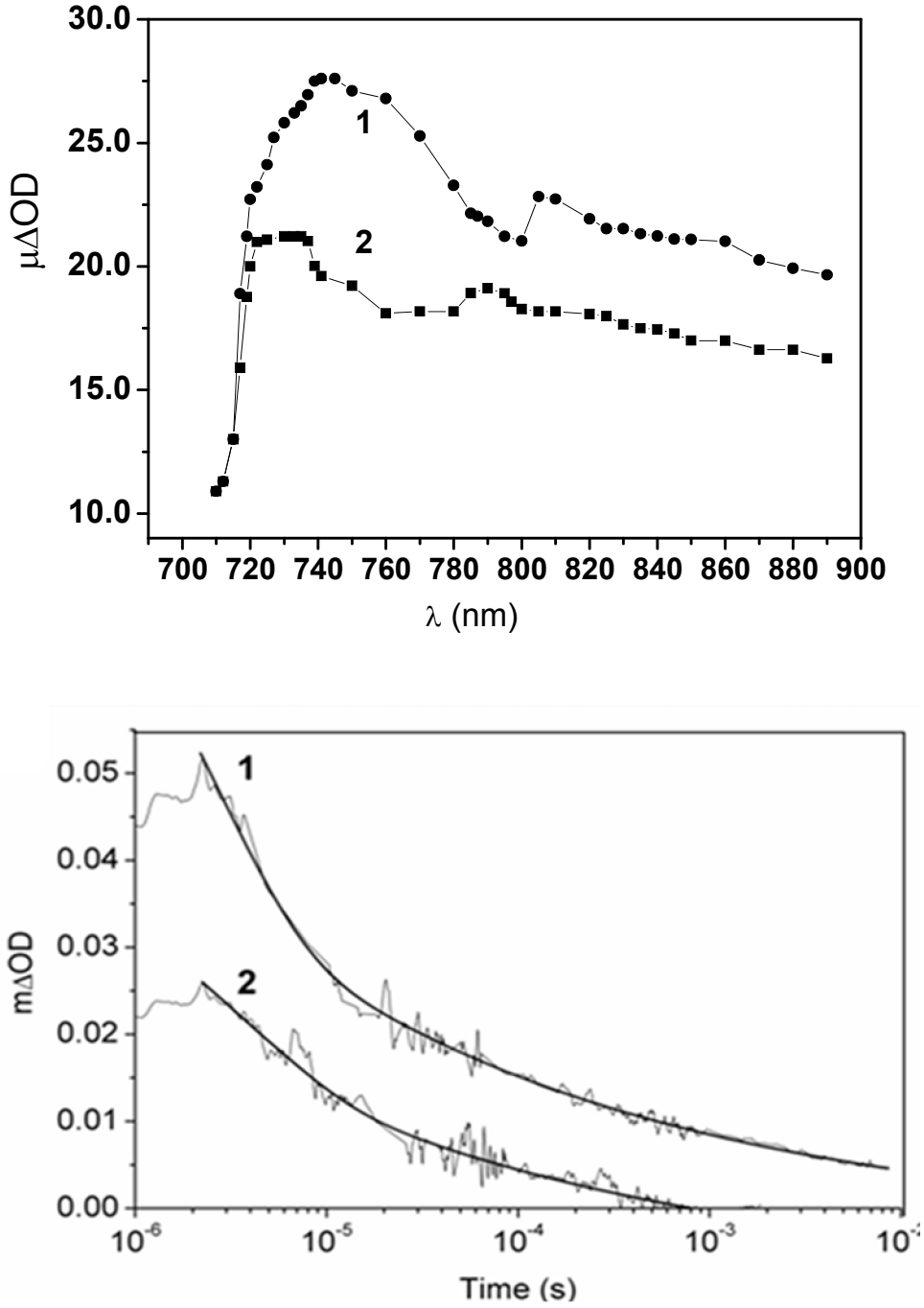


Figure 4.2 a) Transient absorption spectra of **1** and **2** films measured 1 μs after excitation. b) The decay dynamics of the corresponding transient absorption spectra monitored at 740 nm. Data taken at 20 μJ cm^{-2} energy at an excitation of 540 nm.

We now turn to our control molecule, **1**. Studies in solution did not reveal any significant charge photogeneration, even on ultrafast timescales, consistent with the absence of a charge-transfer type feature in the absorption spectrum and with the weaker electron-donor properties of the alkoxyphenyl moiety.[49] However, it is apparent from Figure 4.2 that solid films of 1 yield a transient absorption signal that is both larger and longer lived than that observed for **2**. The transient spectrum for film **1** again exhibited an absorption maximum at ~ 740 nm indicative of the formation of PDI anions and exhibited oxygen-independent, dispersive decay dynamics. This transient signal is, therefore, also assigned to intermolecular charge-separated states, in this case corresponding to the formation of $\mathbf{1}^{\bullet+}$ and $\mathbf{1}^{\bullet-}$. The transient signal for the film of **1** is larger than for the **2** film (normalised to equal densities of absorbed photons) for all probe wavelengths measured. As PDI radical cations are reported to show a sharp absorption maximum at longer wavelengths (900 nm for isolated PDIs[38] and presumably expected at still longer wavelengths for extended species such as $\mathbf{1}^{\bullet+}$) the larger amplitude signal for the film of **1** is unlikely to be due to contributions from $PDI^{\bullet+}$ absorption alone, but rather to an ~ two fold increase in the yield of charge-separated species. We, thus, conclude that the film of **1** exhibits a ~ two-fold enhancement of long-lived charge photogeneration relative to the **2** film.

It is clear from the above data that, at least for the molecules studied here; the ability of a molecule to achieve efficient intramolecular charge separation in solution is not in itself an indicator of the ability of that molecule to achieve efficient intermolecular charge separation in solid films. Clearly this is only a limited study covering two such molecules, and further studies are required to confirm its general applicability. Notwithstanding this caveat, this conclusion may have important implications for the relevance of solution studies of intramolecular electron transfer to the application of molecular donor / acceptor systems to solid-state solar energy conversion systems.

In general, it might be expected that the ability of a molecular structure to achieve an intramolecular charge-separated state should favour intermolecular charge separation in the solid state. This intramolecular charge separation should reduce the coulombic attraction (or 'binding energy') of the electron and hole, thereby facilitating subsequent intermolecular charge dissociation. Indeed charge-transfer molecules are employed to achieve efficient charge separation in both dye-sensitised and polymer / fullerene solar cells.[13,14] It is, therefore, striking that, for the molecules studied in this paper, intramolecular charge separation appears to correlate with a reduction in the yield of long-lived, intermolecular charge dissocation. The origin of this reduction in yield can be understood in terms of the relative lifetimes of the intramolecular photogenerated states for the two molecules studied. The lifetime of the intramolecular charge-separated state for the **2** dyad in solution, 750 ps, is, in fact, shorter than the lifetime of the singlet excited state of the control **1** (4.5 ns). In this context, the addition of the triarylamine moiety, enabling intramolecular charge separation, can be regarded as accelerating the decay of photogenerated states to the ground state. This acceleration can be understood in terms of an increase in vibronic coupling resulting from the generation of charged species. This accelerated decay to the ground state can be expected to compete with intermolecular charge dissociation, consistent with the observed lower charge generation yield. It is also possible that this reduction in yield may be associated with a reduction in intermolecular electronic coupling for the film of **2**, resulting perhaps from the triarylamine substituent disrupting the molecular packing. This will act in favour of an intramolecular charge recombination as opposed to charge dissociation. Indeed, we have previously reported an enhanced yield of intermolecular charge separation in solid films of planar TTF:fullerene dyads relative to their twisted analogues, and have attributed this to enhanced intermolecular coupling for the planar molecule.[54] In either case, it is apparent that whilst solution studies are essential for our understanding of the intramolecular photochemistry of molecular donor / acceptor systems, the application of such structures to solid-state solar energy conversion requires careful consideration of the film rather than solution photochemistry.

4.5 Conclusion

It can be concluded from the studies reported here that long-lived charges observed in the film is due to intermolecular charge separation. However, in **2**, the intramolecular charge separation functions to accelerate non-radiative decay to ground. As a result, **2** is shorter lived with a lower yield than **1**.

The solution studies of supramolecular donor-acceptor structures, is used as simple model systems for studies of photoinduced electron-transfer dynamics, neglecting intermolecular process and concentrating on fast intra processes not observable in solid films.

Reference:

(1) Wasielewski, M. R. *J. Org. Chem.* **2006**, *71*, 5051.

(2) Fukuzumi, S. K., T. *J. Mater. Chem* **2008**, *18*, 1427.

(3) Imahori, H.; Fukuzumi, S. *Adv. Funct. Mater.* **2004**, *14*, 525.

(4) Peeters, E.; van Hal, P. A.; Knol, J.; Brabec, C. J.; Sariciftci, N. S.; Hummelen, J. C.; Janssen, R. A. J. *J. Phys. Chem. B.* **2000**, *104*, 10174.

(5) Thomas, K. G., Bijiu, V., Kamat, P. V., George, M. V., Guldi, D. M., *Chem. Phys. Chem.* **2003**, *4*, 1299.

(6) Martini, I. B., Ma, B., Da Rose, T., Hegelson, R., Wudl, F., Schwartz. B. *J., Chem. Phys. Lett.* **2000**, *327*, 253.

(7) Marcus, R. A. *J. Chem. Phys.* **1965**, *43*, 679.

(8) Marcus, R. A. *Angew. Chem. Int. Ed. Engl.* **1993**, *32*, 1111.

(9) Weller, A. Z. *Phys. Chem. Neue Floge* **1982**, *133*, 93.

(10) Giacalone, F.; Segura, J. L.; Martín N.; Guldi, D. M.; *J. Am. Chem. Soc.* **2004**, *126*, 5340.

(11) De la Torre, G.; Giacalone, F.; Segura, J. L.; Martín N.; Guldi, D. M.; *Chem. Eur. J.,* **2005**, *11*, 1267.

(12) Imahori H.; Sakata, Y. *Eur. J. Org. Chem.* **1999**, 2445.

(13) Curiel, D.; Ohkubo, K.; Reimers, J.R.; Fukuzumi S.; Crossley, M.J.; *Phys. Chem. Chem. Phys.* **2007**, *9*, 5260.

(14) Förster, T. *Discuss. Faraday Soc.* **1959**, *27*, 7.

(15) van Hal, P. A.; Meskers, S. C. J.; Janssen, R. A. J.; *Appl. Phys. A,* **2004**, *79*, 41.

(16) Lehtivuori, H.; Efimov, A.; Lemmetyinen, H.; Tkachenko, N. V. *Chem. Phys. Lett.* **2007**, *437*, 238.

(17) Chukharev, V.; Vuorinen, T.; Efimov, A.; Tkachenko, N. V.; *Langmuir* **2005**, *21*, 6385.

(18) Camaioni, N.; Fabbrini, G.; Menna, E.; Maggini, M.; Ridolfi, G.; Zanelli, A. *New J. Chem.* **2006**, *30*, 335.

(19) Eckert, J. F.; Nicoud, J. F.; Nierengarten, J. F.; Liu, S. G.; Echegoyen, L.; Barigelletti, F.; Armaroli, N.; Ouali, L.; Krasnikov, V.; Hadziioannou, G. *J. Am. Chem. Soc.* **2000**, *122*, 7467.

(20) Gouloumis, A.; de la Escosura, A.; Vazquez, P.; Torres, T.; Kahnt, A.; Guldi, D. M.; Neugebauer, H.; Winder, C.; Drees, M.; Sariciftci, N. S. *Org. Lett.* **2006**, *8*, 5187.

(21) Guldi, D. M.; Luo, C. P.; Swartz, A.; Gomez, R.; Segura, J. L.; Martin, N.; Brabec, C.; Sariciftci, N. S. *J. Org. Chem.* **2002**, *67*, 1141.

(22) Hua, J. L.; Meng, F. S.; Ding, F.; Li, F. Y.; Tian, H. *J. Mat. Chem.* **2004**, *14*, 1849.

(23) Loi, M. A.; Denk, P.; Hoppe, H.; Neugebauer, H.; Winder, C.; Meissner, D.; Brabec, C.; Sariciftci, N. S.; Gouloumis, A.; Vazquez, P.; Torres, T. *J. Mat. Chem.* **2003**, *13*, 700.

(24) Maggini, M.; Possamai, G.; Menna, E.; Scorrano, G.; Camaioni, N.; Ridolfi, G.; Casalbore-Miceli, G.; Franco, L.; Ruzzi, M.; Corvaja, C. *Chem. Comm.* **2002**, 2028.

(25) Meng, F. S.; Hua, J. L.; Chen, K. C.; Tian, H.; Zuppiroli, L.; Nuesch, F. *J. Mat. Chem.* **2005**, *15*, 979.

(26) Narutaki, M.; Takimiya, K.; Otsubo, T.; Harima, Y.; Zhang, H. M.; Araki, Y.; Ito, S. *J. Org. Chem.* **2006**, *71*, 1761.

(27) Nierengarten, J. F.; Eckert, J. F.; Nicoud, J. F.; Ouali, L.; Krasnikov, V.; Hadziioannou, G. *Chem. Comm.* **1999**, 617.

(28) Peeters, E.; van Hal, P. A.; Knol, J.; Brabec, C. J.; Sariciftci, N. S.; Hummelen, J. C.; Janssen, R. A. J. *J. Phys. Chem. B* **2000**, *104*, 10174.

(29) Possamai, A.; Camaioni, N.; Ridolfi, G.; Franco, L.; Ruzzi, M.; Menna, E.; Casalbore-Miceli, G.; Fichera, A. M.; Scorrano, G.; Corvaja, C.; Maggini, M. *Synthetic Met.* **2003**, *139*, 585.

(30) Possamai, G.; Maggini, M.; Menna, E.; Scorrano, G.; Franco, L.; Ruzzi, M.; Corvaja, C.; Ridolfi, G.; Samori, P.; Geri, A.; Camaioni, N. *Appl. Phys. A - Mater.* **2004**, *79*, 51.

(31) Possamai, G.; Marcuz, S.; Maggini, M.; Menna, E.; Franco, L.; Ruzzi, M.; Ceola, S.; Corvaja, C.; Ridolfi, G.; Geri, A.; Camaioni, N.; Guldi, D. M.; Sens, R.; Gessner, T. *Chem. - Eur. J.* **2005**, *11*, 5765.

(32) Rademacher, A.; Märkle, S.; Langhals, H. *Chem. Ber.* **1982**, *115*, 2927.

(33) Feiler, L.; Langhals, H.; Polborn, K. *Liebigs Ann.* **1995**, 1229.

(34) Quante, H. ; Geerts, Y.; Müllen, K. *Chem. Mater.* **1997**, *9*, 495.

(35) Lee, S. K.; Zu, Y.; Herrmann, A.; Geerts, Y.; Müllen, K.; Bard, A. J. *J. Am. Chem. Soc* **1999**, *121*, 3513.

(36) Ahrens, M. J.; Fuller, M. J.; Wasielewski, M. R. *Chem. Mater.* **2003**, *15*, 2684.

(37) Würthner, F. *Chem. Comm.* **2004**, 1564.

(38) Shibano, Y., Umeyama, T., Matano, Y., Tkachenko, N. V., Lemmetyinen, H., Imahori, H. *Org. Lett.* **2006**, *8*, 4425.

(39) O'Neil, M. P.; Niemczyk, M. P.; Svec, W. A.; Gosztda, D.; Gaines III, G. L.; Wasielewski, M. R. *Science* **1992**, *257*, 63.

(40) Serin, J. M.; Brousmiche, D. W.; Fréchet, J. M. *Chem. Comm.* **2002**, 2605.

(41) van der Boom, T.; Hayes, R. T.; Zhao, Y.; Bushard, P. J.; Weiss, E. A.; Wasielewski, M. R. *J. Am. Chem. Soc* **2002**, *124*, 9582.

(42) Ahrens, M. J.; Sinks, L. E.; Rybtchinski, B.; Liu, W.; Jones, B. A.; Giaimo, J. M.; Gusev, A. V.; Goshe, A. J.; Tiede, D. M.; Wasielewski, M. R. *J. Am. Chem. Soc* **2004**, *126*, 8284.

(43) Bauer, P.; Wietasch, H.; Lindner, S. M.; Thelakkat, M. *Chem. Mater.* **2007**, *19*, 88.

(44) Chen, S. ; Liu, Y.; Qiu, W.; Sun, X.; Ma, Y.; Zhu, D. *Chem. Mater.* **2005**, *17*, 2208.

(45) Hua, J., Meng, F., Ding, F., Li, F., Tian, H., *J. Mater. Chem* **2004**, *14*, 1849.

(46) Liu, Y.; Xiao, S., Li, H., Li, Y., Lui, H., Lu, F., Zhuang, J., Zhu, D., J. Phys. Chem. 2004, 108, 6256 *J. Phys. Chem.* **2004**, *108*, 6256.

(47) Hofkens, J.; Vosch, T.; Maus, M.; Köhn, F.; Cotlet, M.; Weil, T.; Herrmann, A.; Müllen, K.; Schryver, F.C *Chem. Phys. Lett.* **2001**, *333*, 255.

(48) Jones, B.; Ahrens, A., M.; Yoon, M.-H.; Facchetti, A.; Marks, T. J.; Wasielewski, M. R. *Angew. Chem. Int. Ed.* **2004**, *43*, 6363.

(49) An, Z.; Huang, C.; Odom, S. A.; Zhang, X.; Barlow, S.; McCamant, D.; Lockard, J.; Cohen, B.; Kelley, R. F.; Wasielewski, M. R.; Padilha, L.A.; Hagan, D.J.; Van Stryland, E.W.; Marder, S.R **in preparation**.

(50) Fuller, M. J.; Sinks, L. E.; Rybtchinskim, B.; Giaimo, J. M.; Li, X.; Wasielewski, M.R. *J. Phys. Chem. A* **2005**, *109*, 970.

(51) Giaimo, J. M.; Gusev, A. V.; Wasielewski, M.R. *JACS* **2002**, *124*, 8530.

(52) Seo, T. E.; Nelson, F. R.; Fritsch, M. J.; Marcoux, S. lb L.; Leedy, W. D.; Adams, N. R.; *J. Am. Chem. Soc* **1966**, *88*, 3498.

(53) Koster, L. J. A.; Mihailetchi, V. A. D.; Blom, P. W. M.; *App. Phys. Lett.* **2006**, *88*, 052104.

(54) Handa, S. ; Giacalone, F.; Haque, S. A.; Palomares, E.; Martín, N.; Durrant, J. D.; *Chem. Eur. J.* **2005**, *11*, 7440.

V. Charge photogeneration of polythiophene/ perylene diimide blend films

The proceeding sections have focused upon the role of nanomorphology in donor-acceptor blends and dyad molecules in driving charge photogeneration at organic donor / acceptor interface. However, further considerations and analogies suggest that additional factors are also likely to be important in determining the efficiency of charge photogeneration. Here, we turn to study the overall reaction free energy in determining the charge separation efficiency between two electron acceptor systems.

Charge photogeneration and decay dynamics have been investigated using transient absorption spectroscopy for polythiophene / perylene diimide films. Control and optimisation of blend morphology at the microscopic scale is critical for optimising the efficiency of charge photogeneration and power conversion efficiencies of donor / acceptor solar cells. We first report on the effects of solvent, concentration and spin coating rate on the microstructure, grain size, surface roughness and thickness of poly(3-hexylthiophene): *N,N'*-bis[3,4,5-tri(*n*-dodecyloxy)benzyl]-3,4,9,10-tetracarboxylic perylene diimide, (P3HT:PDI_2)

thin films in order to optimise morphology of the films for charge photogeneration. Variable coating rates influence the microstructure of the films. All films are polycrystalline and single phase, as was found from atomic force microscopy and polarised light microscope analysis. Changing the solvents and the spin rate does influence the roughness, thickness and grain sizes of the films. All films have nanometre particle size ranging from 200 nm to 500 nm. However, roughness and thickness of the film strongly depend on the spin coating rates. The highest spin rates produce the thinnest film with the roughest surface, while the lowest spin rate produced the thickest films with the smoothest surface. Furthermore, the effect of thermal annealing is found to have an appreciable effect on both morphology and photophysics of these films. We find the desired homeotropic alignment of the hexagonal columnar mesophases is formed at certain temperatures.

Transient absorption spectroscopy is employed to monitor charge photogeneration. Data are analysed as a function of thermal annealing, analogues of P3HT donor polymers and comparison of polythiophene / perylene diimide blend films with polythiophene / PCBM. These decay dynamics are analysed on micro- millisecond timescales. Thermal annealing results in an increase in charge photogeneration. Of particular importance, we also find that, compared to polythiophene / PCBM blend films, charge photogeneration in polythiophene / PDI_2 is more efficient with smaller ΔG values.

5.1 Introduction

For commercialisation of OPV, a higher PCE than the current 8% is desired and so research is needed on understanding the parameters that limit the efficiencies of these devices. As such the search for new materials with good performance characteristics as well as the improvement in the device fabrication has been a subject of importance.

5.1.1 Perylene diimides

In addition to fullerene, perylene tetracarboxylic diimide (PDI) derivatives - fused aromatic rings in conjunction with tetracarboxylic diimide units and tails at the imide position and / or substituent on the core - have been investigated as they are an interesting group of functional materials that have attracted attention for a wide spectrum of applications. PDIs are potentially promising agents for applications in photovoltaic cells,[1] field-effect transistors,[2-4] and colour tuneable light-emitting diodes.[5] Whereas most organic conducting species can be described as p-type semiconductors, in which holes in the valence band are the majority charge carriers, PDIs are known to support electron transport through the conduction band,[6-9] and this material is thus classified as an n-type semiconductor. Such materials are potentially useful as the electron-accepting material in organic photovoltaic solar cells, as was reported in 1986 for the first solar cell based on copper phthalocyanine (CuPc) and a perylenetetracarboxylic derivative.[10] Most alternative electron acceptors for bulk heterojunction PV devices, such as fullerene derivatives and TiO_2 nanoparticles, have relatively weak molar absorption coefficients in the visible range and do not have a strong tendency for specific orientation, in particular, when blended with electron donor polymers. PDIs, however, in addition to advantages such as low cost and excellent photochemical and thermal stability,[11,12] have emerged since they combine a large molar absorption coefficient, high electron affinity (good electron accepting properties),[13] high mobilities[14] and possible generation of a highly conducting direction along the π–π stacking axis[15] all in a single molecular architecture. Furthermore, PDIs can be used as fundamental building motifs to construct supramolecular structures that can self-organise into nano/microscopic

architectures.[16,17] Due to combined planarity and electron deficiency,[18] PDIs have been focused on for their discotic liquid crystal properties with good charge transport along the one dimensional π stacks.[14,18-20] Features such as charge carrier mobilities of up to 1.3 cm^2/Vs, [14] measured by space-charge limited current (SCLC) technique under ambient conditions,[21] and the reported air stability of some PDIs make these compounds promising as n-type components in organic photovoltaic cells.

Perylenes have already received significant attention for applications in solar cells.[21] To date, most of these photovoltaic applications with perylene derivatives have been performed on dye-sensitised solar cells (DSCC)[22] or bi-layered structures through vapour deposition with insoluble PDIs in which the PDI derivatives were acting as the electron transport component.[10,23-25] The Tang cell, the first organic bilayer structure solar cell composed of CuPc and 3,4,9,10-perylene tetracarboxylic bis-benzimidazole, PTCBI,[10] achieved a power conversion efficiency of ~ 1%. Furthermore, Armstrong *et al*. reported photoelectrical studies on 3,4,9,10-perylene tetracarboxylic dianhydride, PTCDA, and a phthalocyanine derivative based on bilayer heterojunction structure.[26] In these thin films it was found that the photocurrent yield spectrum indicated that a narrow region near the donor / PTCDA interface was responsible for most of the photocurrent production. It was found that the transient photocurrent was directly proportional to the number of phthalocyanine / PTCDA interfaces. A study on evaporation of PTCDI with pentacene in a blend structure for solar cells[27] has demonstrated a power conversion efficiency of 2% under 80 $mWcm^{-2}$ AM1.5 illumination with a short circuit current of 8.6 $mAcm^{-2}$. In addition, a few other studies on polymer/PDI blends illustrate that PDI derivatives in BHJ device arrangements with p-type discotic liquid materials have exhibited EQEs close to 30%.[1,28] In this study Friend and Mullen demonstrated that a donor material exhibiting discotic liquid crystal nature, hexa-perihrxabenzocoronene (HBC-PhC_{12}), in which ordered structures can be achieved through self-organisation, combined with a PDI derivative as electron acceptor to form thin films with vertical segregation between PDI and HBC and large interfacial areas. The relatively high quantum efficiency of the devices was attributed to efficient photoinduced charge transfer between the two material components, as well as effective transport of charges through vertically segregated PDI and HBC π-systems. Further to this system, it has also been shown that devices based on blends of PDI with hole-transporting polymer hosts such as P3HT,[29,30]

MEH-PPV,[31] and poly(2,7-carbazole)[32] can give EQE values of the order of 10–15%. The limited attention on blend devices is presumably in part due to the poor resultant device efficiencies, which have been attributed to blend morphologies incompatible with efficient charge transport to the device electrodes. As such there has been research in trying to address the morphology. Gregg *et al.* examined the effect of solvent vapour annealing on the photophysics and device properties of perylene bis(phenethylimide), PPEI, films.[33] He found methylene chloride vapour evolved the amorphous PPEI film structure to a polycrystalline phase. Furthermore, the heterojunction barrier height in the CH_2Cl_2 vapour treated PPEI/titanyl phthalocyanine (TiOPc) was significantly reduced. Of great importance was the observation of highly organised bilayers and respective pristine material single layers of PPEI/titanyl phthalocyanine with localised crystalline region with further conclusion that the highly solvent-annaeled PPEI/TiOPc interface is comprised of relatively large PPEI crystals with irregular contact to small TiOPc nanocrystals. However, despite the low interfacial contact between PPEI and TiOPc, the crystalline character of both layers appears to be beneficial for long range exciton diffusion and also expected to give rise to more effective charge photogeneration and increased charge carrier mobility in both layers.[34,35] A study by Keivandidis *et al.*[36] correlated the photophysics and photovoltaic properties with the respective blend morphologies. It was concluded the composition dependence study of PDI in inert PS and annealing dependence of 60 wt% PS:PDI composition showed that PDI aggregation and excimer formation dominate the photophysical properties in the solid state. An increase in order of the PDI aggregates in blends of (poly[9,9'-dioctylfluorene-co-N-(4-butylphenyl)diphenylamine]) TFB:PDI, (poly(9,9'-dioctylfluorene-co-benzothiadiazole) F8BT:PDI and (poly[9,9'-dioctyfluorene-co-bis-N,N0-(4-butylphenyl)-bis-N,N-phenyl-1,4-phenylenediamine]) PFB:PDI upon annealing was correlated with a phase separation between the blend components. The morphology of the as-spun blends was found to dictate the magnitude of the obtained external quantum efficiencies. Consequently, the device efficiency of these systems is limited by the distance which the photogenerated holes must diffuse between the PDI-rich domain to the hole collecting electrode of the device. In addition, it was proposed that the better performance of the as-spun F8BT:PDI device is due to the ability of the F8BT matrix to solubilise efficiently the PDI derivative and to promote extensive disorder in the $\pi-\pi$ stacking within the PDI aggregates in the blend. The anticipated interpenetrating network of the two components in the F8BT:PDI blend seems to forms due to the increase in

the density of grain boundaries between the small PDI disrupted crystallites that act as interconnections for electron-transport rather than the formation of large and isolated PDI crystalline phases in the blend. Another study has demonstrated device performance through morphology of PDIs using blends of perylene substituted polyisocyanide with poly(3-hexylthiophene) and PFB.[37] The devices exhibited an order of magnitude improvement in power conversion efficiency, as compared to analogous blend using perylene monomers. It was proposed the employment of polyisocyanide suppressed the PDI aggregates whilst forming a particular orientation with respect to the plane of the device substrate; this offers a method by which the morphology and connectivity of photovoltaic blends can be modified.

Other studies show that PDIs in the solid state exhibit a plethora of morphological qualities interdependent on their photophysical and charge transport properties. As such, it is central to address morphology of PDIs in order to improve the device efficiency.

5.1.2 Morphological aspect

At present, the state of the art organic photovoltaic devices based upon bulk heterojunction structure consist of relatively random blend morphologies.[38] There are examples of organic donor / acceptor heterojunctions that do not achieve efficient photocurrent generation relative to the efficiency of their CT state dissociation. This can be attributed to the inefficient charge percolation or transport. Several works are already published relating the relationship between the nanomorphology of the organic photoactive layer (bulk heterojunction) and the performance of the polymer solar cells. For example, a study by Chasteen *et al.*[39] demonstrated that the donor/acceptor interfacial area and domain sizes are key parameters that have a substantial effect on charge photogeneration. *Nelson*[40] also demonstrated that concentration of PCBM in a P3HT:PCBM blend film had a significant effect on charge generation and morphology. It was suggested the concentration of PCBM in the blend influences both morphology and charge photogeneration, effectively influencing the device performance.[41-46] The studies of blend morphology demonstrate that in order to have a significant effect on the efficiency of polymer photovoltaic devices, [47-50] a better understanding of how to predict or even control this blend morphology is essential.

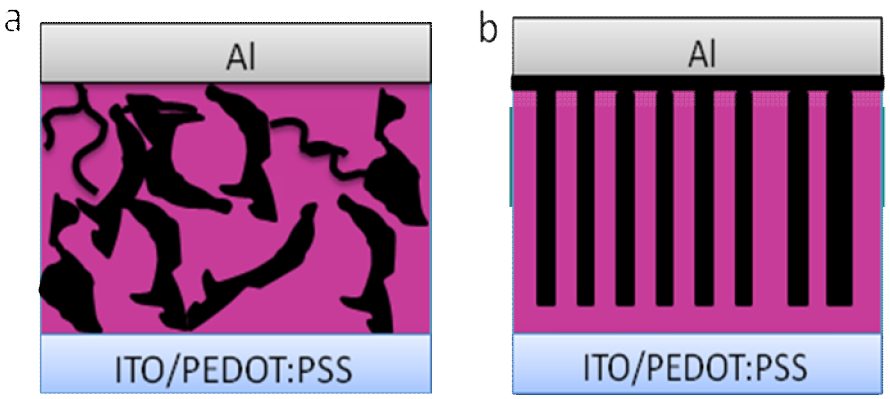


Figure 5.1 Polymeric solar cell bulk heterojunction.

Films spun from blend solutions often phase separate. The morphology and thus scale of phase segregation of this layer can be strongly affected by the processing conditions used such as the donor–acceptor composition, solvent, solubility of the materials, parameters of the spin-coating process such as speed[51] and thermal annealing of the organic layer. Shaheen *et al.* found that the power conversion efficiency of organic photovoltaic devices based on a conjugated polymer / methanofullerene blend is dramatically affected by molecular morphology. The use of toluene as solvent rather than chlorobenzene for the (poly[2-methyl,5-(3',7'' dimethyloctyloxy)]-p-phenylene vinylene), MDMO-PPV:PCBM system led to a coarser phase separation by structuring the blend to be a more intimate mixture that contains less phase segregation of methanofullerenes, whilst simultaneously increasing the degree of interactions between conjugated polymer chains.[50] If the morphology could be controlled on a molecular scale, the efficiency of charge separation and transport could be expected to be substantially higher. In the current state of the art active layer designs, heterojunctions are formed relatively randomly (Figure 5.1a) and do not guarantee a continuous pathway for charge carriers to the electrodes. One approach for controlling the morphology on the nanometer scale is vertically separating the two materials to provide different paths for electrons and holes to the electrodes (Figure 5.1b).[52] The use of discotic liquid crystalline materials, with the ability to self-organise into columnar stacks may be one potential solution in reaching this goal. For photovoltaic devices it would be ideal to have stacks of these discs perpendicular to the substrate (see chapter 2 – liquid crystals).

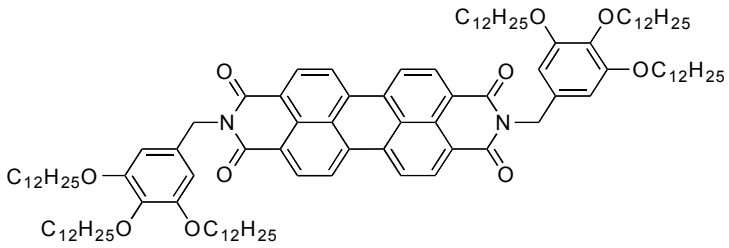
Most of the works on polymer:PDI bulk heterojunction photovoltaic devices using PDIs as the electron acceptor has been referring to the effect of material chemical structure on the photovoltaic performance.[13,29,30,32] Moreover, the interplay among film processing conditions, post-treatments, morphology and photovoltaic performance for polymer / fullerene blends has been studied extensively.[29,53,54] In order to achieve optimised charge photogeneration in blend films, we first look at the effect of processing conditions on morphology of the pristine discotic liquid crystalline small molecule: *N,N'*-bis[3,4,5-tri(*n*-dodecyloxy)benzyl]-3,4,9,10-tetracarboxylic perylene diimide, PDI_2, and its blend film with poly(3-hexylthiophene), P3HT. This particular perylene derivative is chosen due to its high electron mobility along with its liquid crystal character as well as other merits PDIs have in general. We employ different optical techniques to focus on morphology of PDI_2 film. The studies are then extended to examine the underlying photophysics of charge photogeneration at the polythiophene / PDI interface. PDI_2[9] is employed as an electron acceptor (Scheme 5). Initial studies look at charge photogeneration of P3HT:PDI_2 blend films. Further on, we make a comparison of charge photogeneration in blends of PDI_2 and PCBM employing a series of polythiophenes as electron donors (scheme 5). The polythiophenes studied in this work were chosen based on previous PCBM blend studies,[55] where despite high photoluminescence quenching, poor charge photogeneration was measured by transient absorption. Control films employed PCBM as the electron acceptor. Some properties of these materials are summarized in Table 5.1.

In Chapter 6 the overall device performance coupled with morphology and photophysics are simultaneously considered.

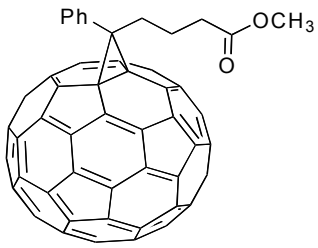
Table 5.1. Summary of donor / acceptor material properties.

	μ	IP[d]	EA[e]	E_s[f]	Function
$P(T_{10}T_{10}TT_0)$	2×10^{-1} [a]	5.1		2.0	donor
$P(T_{16}T_{16}TT_0)$	2×10^{-1} [a]	5.1		2.0	donor
$P(T_{12}SeT_{12})$	2×10^{-1} [a]	5.0		1.9	donor
P3HT	7×10^{-3} [a]	4.8		2.0	donor
$P(T_0TT_{16})$	3×10^{-1} [a]	5.0		2.1	donor
PDI_2	1.3[b]		<3.7	2.1	acceptor
PCBM	1×10^{-3} [c]		~3.7	1.8	acceptor

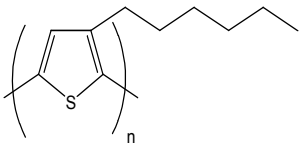
[a] Field-effect hole mobilities evaluated in the saturated regime measured in $cm^2V^{-1}s^{-1}$.[56] [b] SCLC electron mobility ($cm^2V^{-1}s^{-1}$).[14] [c] FET electron mobility in $cm^2V^{-1}s^{-1}$. [d] Film ionization potentials in eV evaluated by ambient UV photoelectron spectroscopy.[55] [e] Estimated electron affinities (eV), [f] Singlet exciton energy (eV).



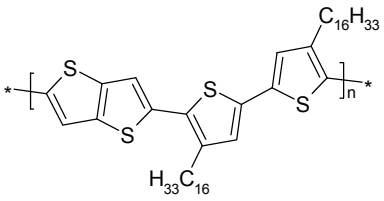
PDI_2



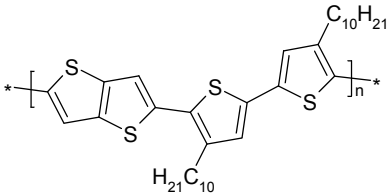
PCBM



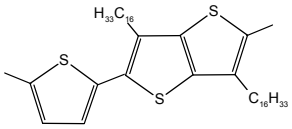
P3HT



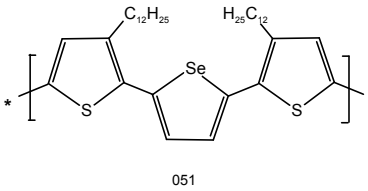
$P(T_{16}T_{16}TT_0)$



$P(T_{10}T_{10}TT_0)$



$P(T_0TT_{16})$



$P(T_{12}SeT_{12})$

Scheme 5 Molecular structure of electron accepting small molecules PCBM, PDI_2 and polythiophenes with different ionisation potentials used as electron donors.

5.2 Sample preparation

Six polythiophenes (Scheme 5) were synthesized as reported elsewhere.[57,58] All materials were received and handled as described in Chapter 2.

Chloroform and chlorobenzene were used as the solvents in PDI_2 and PCBM films respectively.

To the polythiophene solutions (~20 mg mL^{-1}), solutions of PCBM or PDI_2 were added at a concentration of ~20 mg mL^{-1}. Pristine polymer films were spun from solution onto glass substrates at a spin rate of 3000 rpm for 90 s under N_2 atmosphere. The weight concentration of PDI_2 and PCBM in the final polymer blend solutions was fixed at 50 wt %. Solid blend films of polythiophene / PDI_2 and polythiophene / PCBM were prepared by spin-coating blend solutions at 500 rpm and 1100 rpm for 60s respectively.

Films were handled as described in chapter 2.

5.3 Steady state film photophysics of PDI_2

The photophysics of perylenes in dilute solution is well studied. Optical excitation of such solutions leads to emission with mono-exponential lifetime of around 4 nanoseconds. However, as discussed in Chapter 4, for OPVs, which is based upon solid-state, it is important to extend the solution studies to solid state. In films when the PDI molecules are closely packed, sometimes generating excimers, the photophysics in general becomes more complicated. In order to successfully perform time resolved spectroscopy measurements, it is essential to have information on the ground state of the samples of interest. Thus, here we start off by looking at the steady state photophysics of perylenes in solid state to gain information on general morphology of films which affect the charge transfer states formation and charge photogeneration efficiency. These results are then altered to optimise charge photogeneration in such blend films. The steady state measurements are also employed to check the integrity of samples before and after time resolved experiment series and in general.

5.3.1 Absorption

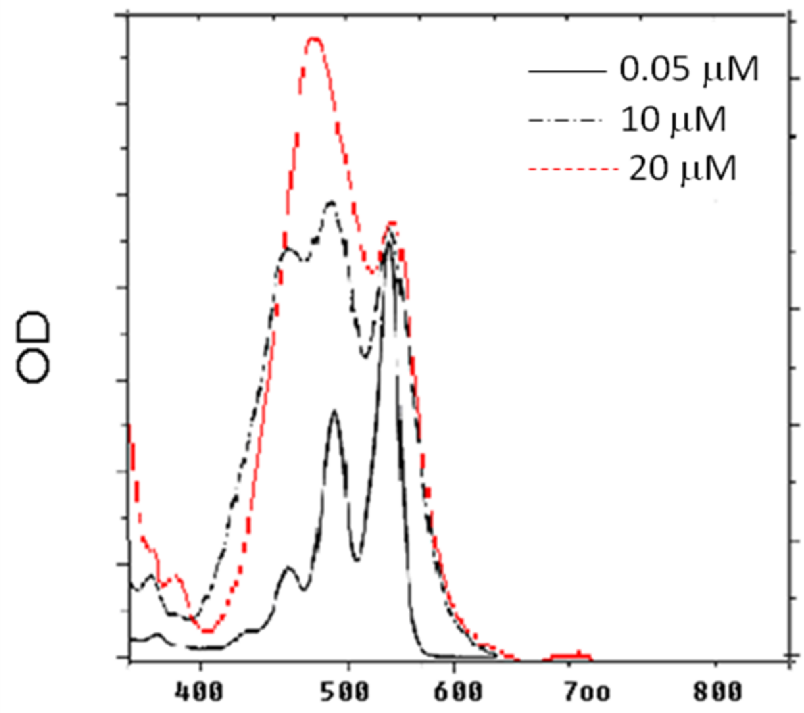


Figure 5.2 steady state absorption of PDI_2 in chloroform at different concentrations.

In order to get an understanding of the π–π stacking in PDI_2, we examine solution absorption spectra of pristine PDI_2 at different concentration as they can be used indirectly to probe the PDI stacking. It is well established that self organisation depends on the delicate balance between molecule-molecule and molecule-solvent interactions,[59] and hence solvents always play a crucial role in this system. UV/vis absorption spectra are sensitive to inter-chromophore distance and orientation[60,61] and have been widely used to study π– π stacking of perylene diimides.[19,21,62-64] Figure 5.2 presents the absorption spectra of PDI_2 as a function of its concentration. At low concentration the spectrum resembles that of monomeric perylene diimide,[65] while at higher concentration the spectrum deviates from the dilute solution. Consistent with literature, [67-69] at the higher concentration, the order of intensity for 0→0 and 0→1 vibronic transitions is reversed, which is indicative of π – π stacking in perylene diimides.[62-64,66-68]

The absorption spectrum of PDI_2 in CF has the characteristic $S_0 \rightarrow S_1$ transition with the fine vibronic structure of perylene diimides. Usually the absorption maximum of PDIs does not change significantly with different imide groups due to the presence of nodes in both HOMO and LUMO at the imide nitrogen atom.[69] The low intensity band at 365 nm is attributed to the $S_0 \rightarrow S_2$ electronic transition.[70] Consistent with high concentration spectrum, the absorption spectrum of the compound in solid state has different characteristics than that in solution. The absorption maximum is shifted from the $0 \rightarrow 0$ transition (528 nm) in solution to the $0 \rightarrow 1$ transition (507 nm) in solid state, possibly due to strong exciton-phonon coupling in solid state.[71] The $0 \rightarrow 0$ transition (550 nm) in solid state is red-shifted and broadened compared to that in solution, suggesting possible formation of *J*-aggregates.[72] The aggregation may have detrimental effects on morphology and subsequently charge photogeneration and device performance.

It should be noted that the ground state absorptions of P3HT and PDI_2 have a great spectral overlap, preventing selective excitation of either component in the blend. The resulting spectrum of blend P3HT:PDI_2 is shown in Figure 5.3 b.

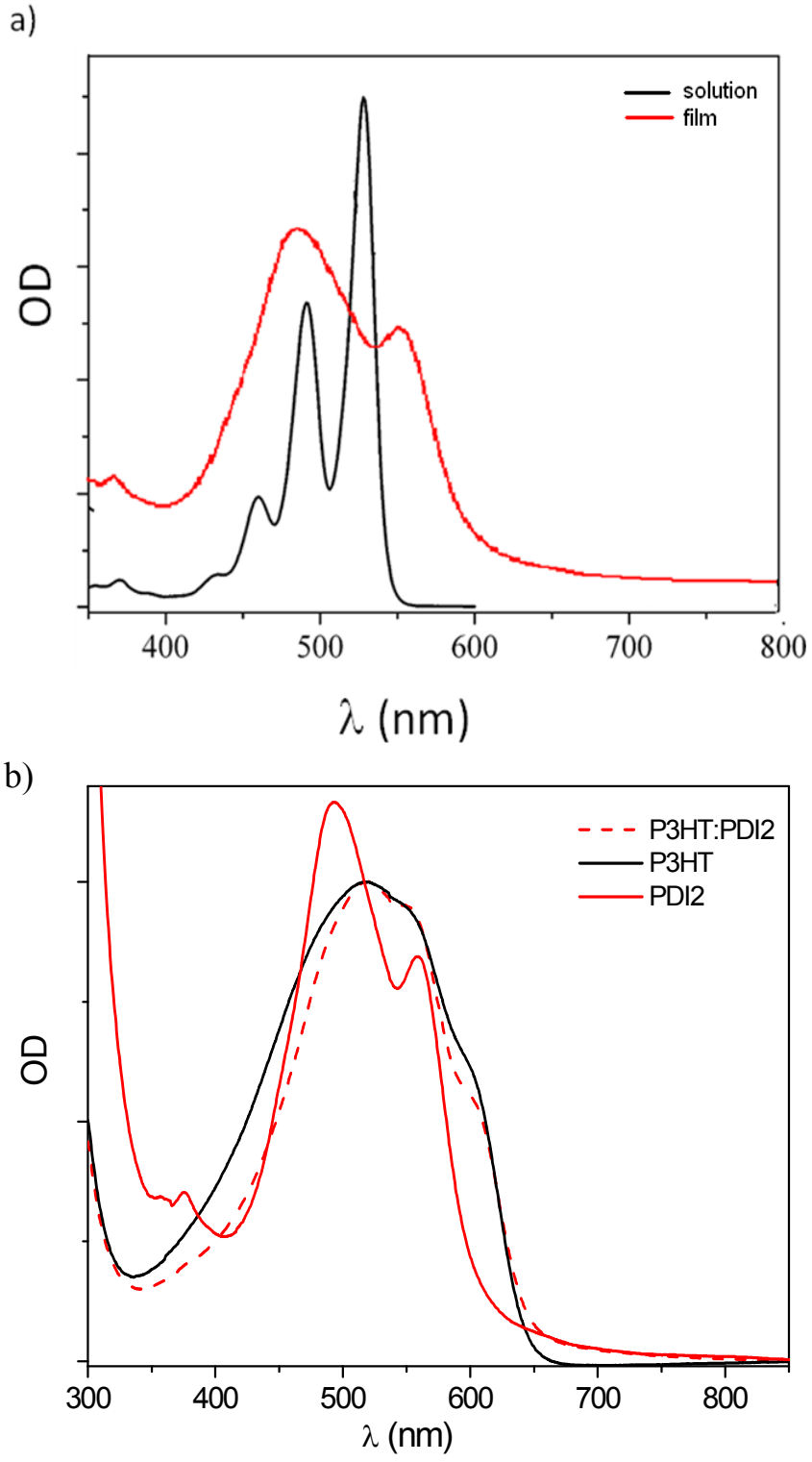


Figure 5.3 a): Absorption spectra of PDI_2 in chloroform solution (black) and in thin film prepared by spin coating (red). b): spectra of pristine PDI_2, P3HT and blend P3HT:PDI_2 spun from chloroform at 500 rpm for 90 seconds.

5.3.2 Emission

Steady state PL spectra of the polymer, PDI_2 and the blend are shown in Figure 5.4. As with the ground state absorption, consistent with the absorption spectra, the emissions of the two pristine materials also overlap - making detection of any energy transfer in the blend film difficult. From the integrated PL intensities of the pristine and blend films, we observe a poor quenching of PL for the blend film relative to either pristine films.

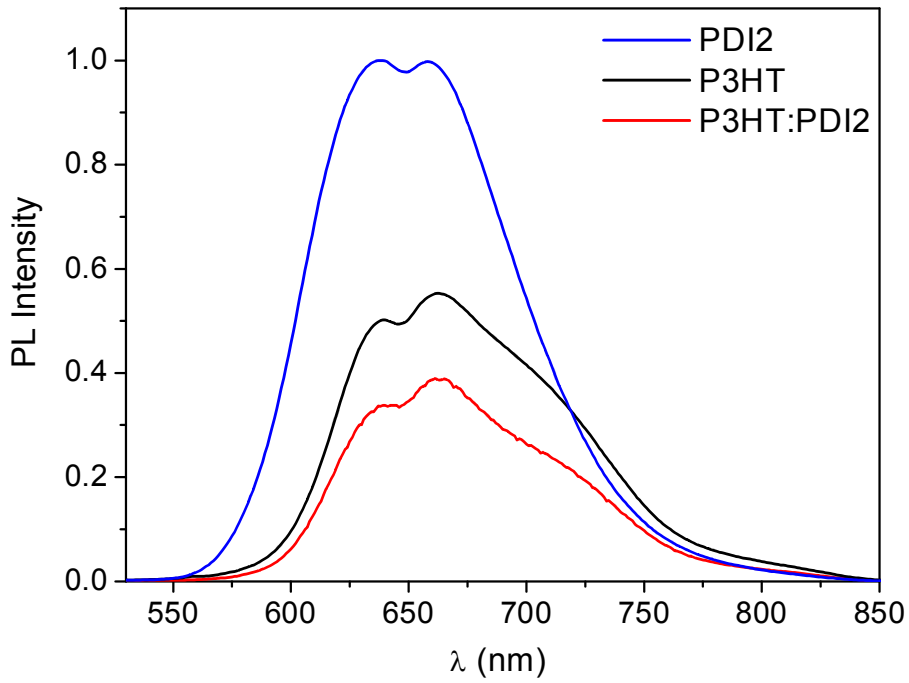


Figure 5.4 Emission of pristine P3HT, PDI_2 and blend P3HT:PDI_2 films spun on glass substrate from chloroform. Excited at 510 nm.

Emission quenching is employed as an indicator of exciton dissociation for efficient charge photogeneration. As discussed in Chapter 1, efficient charge photogeneration is dependent upon generation and subsequent dissociation of CT state (i.e. diffusion and dissociation of photogenerated excitons to and at donor / acceptor interface). One approach to achieving efficient PL quenching and subsequently efficient charge generation, is tuning of the nanomorphology of these films. As such, we probe the nanomorphology of the films in order

to understand and better control some of the parameters that affect the miscibility, domain size and phase segregation, which influence efficiency of charge photogeneration.

5.4 Characterisation of as-prepared films

Charge photogeneration (and thus device performance), is influenced by various treatments by probing the morphology of the films. A number of ways to control the blend nanomorphology have been developed. These include both deposition and post-deposition procedure, including choice of solvent, concentration and composition ratios, rate of drying, and thermal annealing. For P3HT:PCBM blends, these factors have been shown to alter the crystallinity of the polymer, which tends to promote the formation of a phase-separated morphology. It is this parameter that appears to have one of the greatest impacts on solar cell performance. In the coming sections, we therefore examine the effect of altering the blend films' crystallinity through a variety of methods to study morphology and charge generation in P3HT:PDI_2 blend films.

5.4.1 Solvent influence

It has been reported that the donor / acceptor (D/A) blend morphology can be controlled on nanometre scale by spin-coating the blend from a specific solvent preventing large-size phase separation or enhancing the polymer chain packing.[50,73] As discussed in earlier chapters, many studies have addressed the influence of blend nanomorphology on the properties of the CT state and, therefore, charge photogeneration in donor/acceptor blends. In particular, the donor/acceptor phase segregation is a key parameter that have a substantial effect on charge photogeneration.[74] Optimal phase segregation must exist to minimise geminate recombination and thus maximise charge photogeneration; moreover, both exciton dissociation and charge transport requirements need to be balanced. For example, MDMO-PPV:PCBM blends were examined by Quist *et al.*, using time-dependent microwave photoconductivity measurements to investigate films deposited from both chlorobenzene and toluene solutions as a function of PCBM concentration.[75] Initial TEM studies confirmed previous results[76,77] that both solvents produce evidence of phase segregation, but the onset of phase segregation occurs at a higher PCBM concentration for chlorobenzene-cast films, due to PCBM's greater solubility in this

solvent. Furthermore, chlorobenzene-spun samples had higher photoconductivity than toluene-spun films after the onset of phase segregation. The authors proposed that the increases in photoconductivity could be assigned to both an increase in PCBM electron mobility and, to a lesser extent, to an enhanced charge generation.

We start off by a systematic study the effect of solvent on films of P3HT:PDI_2 blend. Films spun from chlorobenzene (CB), xylene, cyclohexanone and chloroform (CF) solvents, at 40 mg/ml concentrations on glass substrate, were investigated as both PDI_2 and P3HT are readily soluble in all four solvents. Figure 5.5 depicts the absorption spectra of as-prepared P3HT:PDI_2 blend films (1:1) spun from CB, xylene, cyclohexanone and CF solutions along with emission spectra of P3HT and P3HT:PDI_2 spun from CF and CB. We observe that the pristine and blend films made from CF solution give the maximum optical density (OD) and the highest emission quenching in the blend films compared to their pristine film (Figure 5.5), the later implying efficient exciton diffusion to, and quenching at, the donor / acceptor interface.

Complementing these studies, AFM images in Figure 5.5 show the morphological changes in the blend films for solutions spun from CF and CB. The length scale is 5 μm. The film from chloroform with a root mean square (RMS) roughness of ~ 40 nm is smoother than the blend film spun from chlorobenzene with an RMS roughness of 70 nm. It can be seen that in the film from CB many large PDI_2 crystal/ needle-like domains develop, the largest one up to dimensions of 1.3 μm × 0.1μm.

The high PL quenching observed for blend film spun from CF may be due to smaller size domains of P3HT and PDI_2 formed as a result of CF's lower boiling point. Conversely during the film-forming process from CB solution the planar PDI_2 molecules have more time to form crystal-like aggregates due to the strong interaction between the molecules. Since the solvents have different boiling points (CF: 61 ^{o}C and CB: 131 ^{o}C), their evaporation rates from the blend film after spin coating are different. Figure 5.6(a, b) shows AFM height images of the P3HT: PDI_2 blends spun from CF and CB solution. It can be seen that a large scale phase separation between PDI_2 and P3HT is observed and large PDI2 crystals can be seen clearly for the CB-processed P3HT:PDI_2 blend film. The large PDI_2 crystals in P3HT:PDI_2 blend film processed from CB solution may be attributed to slow evaporation of CB from the blend film. The large PDI_2 crystals result in sizeable P3HT domains surrounding PDI_2 crystalline

particles. For the P3HT: PDI_2 blend film processed from CF solution, the growth of PDI_2 crystal can be restrained to a certain extent due to rapid evaporation of CF and therefore phase separation between PDI_2 and P3HT is small compared to the blend film processed from CB. Previous studies of polycrystalline perylene diimide films have demonstrated exciton diffusion ranges up to 2.5 μm.[78] However, the exciton diffusion length in conjugated polymers is merely few nm,[79,80] several orders of magnitude smaller than that in perylene diimide polycrystals. Therefore, the large phase separation of P3HT: PDI_2 blend in CB-processed PV films causes inefficient quenching of excitons created in P3HT due to its short diffusion ranges (lower PL quenching). This will potentially lead to a small Jsc in the blend devices.

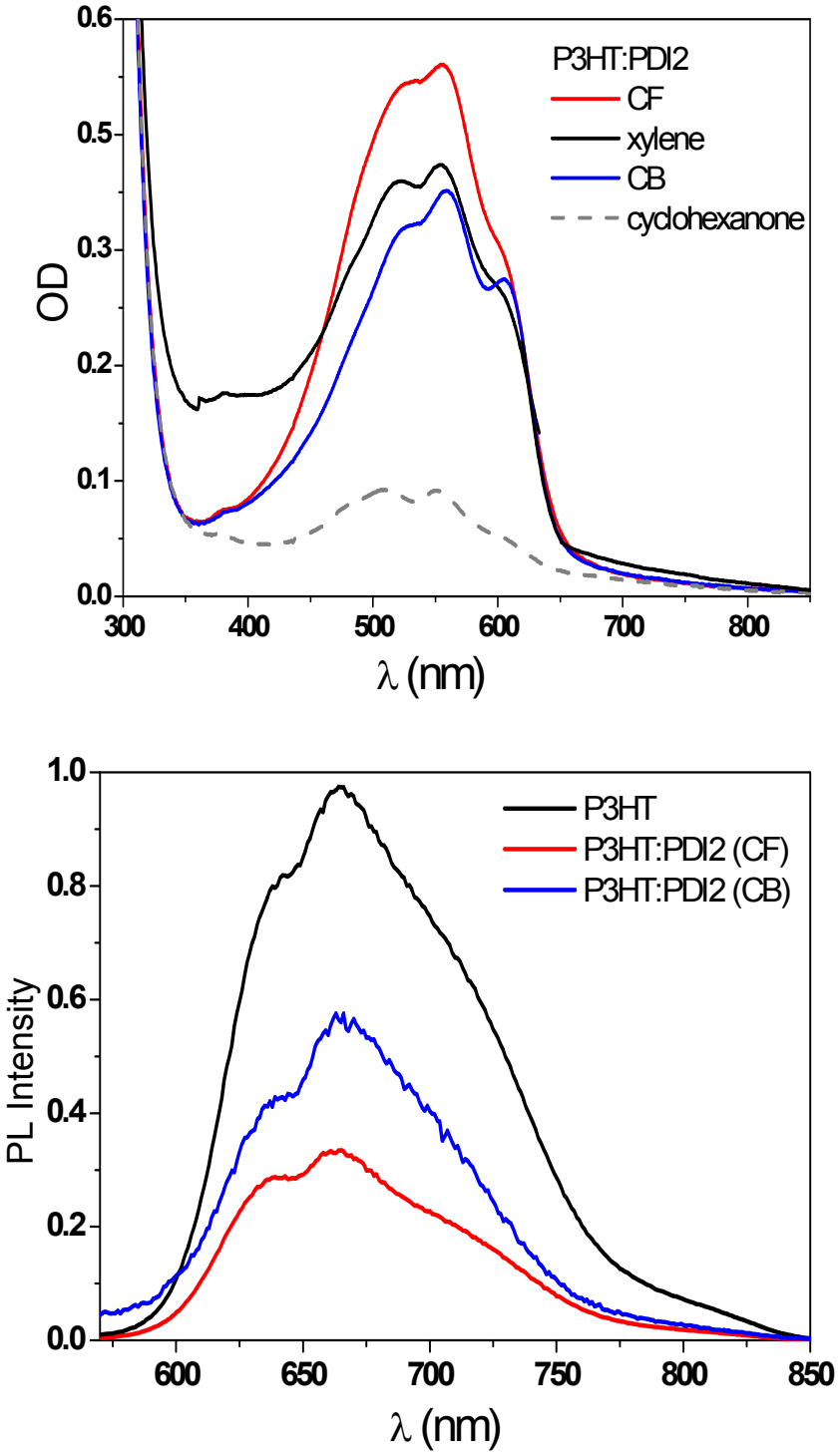


Figure 5.5 (top) UV-visible spectra of P3HT:PDI_2 films as a function of solvents: chloroform (CF), xylene, chlorobenzene (CB) and cyclohexanone. (bottom) normalised emission spectra of P3HT and P3HT:PDI_2 films in CF (red) and CB (blue). Films spun under same conditions on glass substrate (as-prepared).

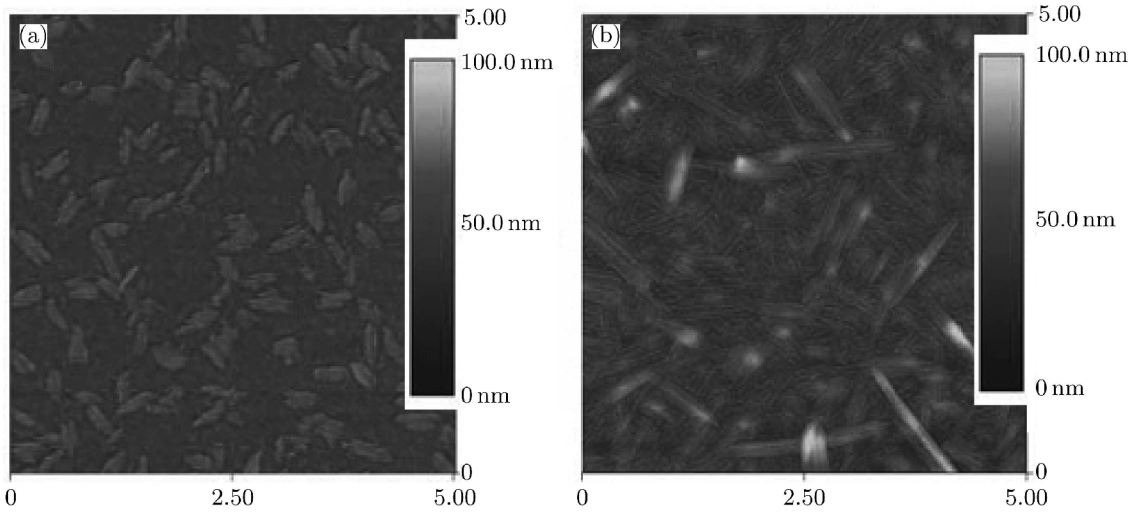


Figure 5.6 5 μm × 5 μm AFM images recorded in tapping mode of films of P3HT:PDI_2 (w/w, 1:1) from: (a) chloroform (b) chlorobenzene.

To further optimise the efficiency of charge photogeneration for such active layer in organic solar cells, we need to exploit other mechanisms which play a role on molecular rearrangement.

5.4.2 Spin coating conditions

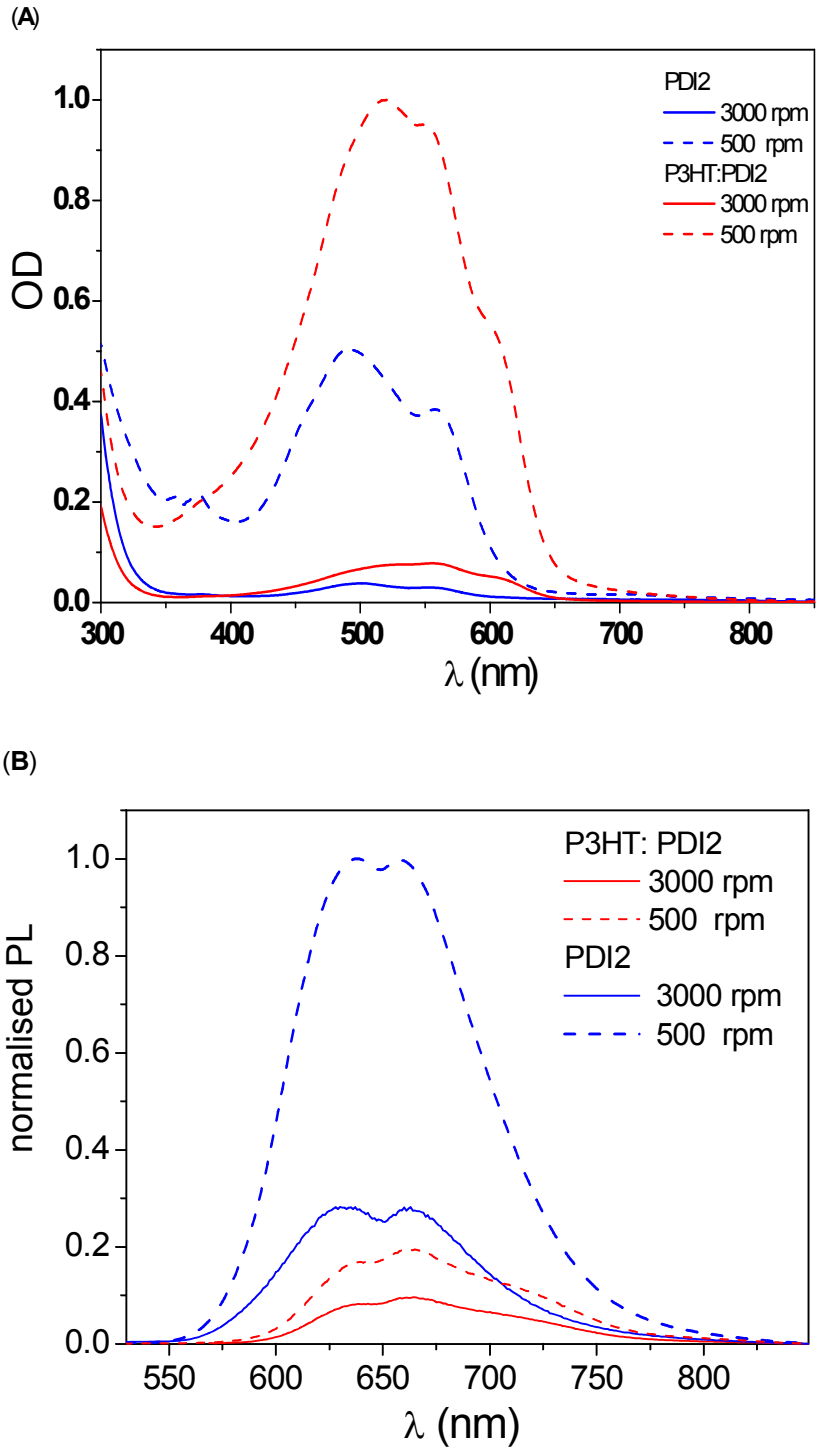


Figure 5.7 (top) Absorption, (below) emission of pristine PDI_2 (blue) and P3HT:PDI_2 blend (red) spin coated at 3000 rpm for 60 seconds (solid lines) and at 500 rpm for 60 seconds (dotted lines). Inset: the absorption spectra of films spun at 3000 rpm.

Previous studies on P3HT: fullerens have addressed the importance of crystallinity for both optimum phase segregation and charge generation (Chapter 3). For PDI films, the organisation and orientation are very much dependent on deposition method and substrate in contact [81,82] (the intermolecular forces control the orientation and crystallinity of the film, while the film-substrate interactions are comparatively weak). As such, the crystallinity, thickness and other properties such as mobility vary significantly depending on the details of sample fabrication. Here we consider the effect of spinning parameters on achieving more efficient charge transfer states, the prerequisite for charge photogeneration. Figure 5.7 shows the absorption and emission of PDI spun at two different speeds: 3000 revolution per minutes (rpm) at an acceleration of 26650 rpm per seconds (ps) (film A) and also at a speed of 500 rpm with a corresponding acceleration of 498 rpmps (film B). The intensity of absorption and emission for both blend and pristine films are enhanced when spinning at the lower speed condition. Furthermore, a small red shift in the position of the maximum peak absorption is observed when switching from high speed to slower speed. The different spinning rates influence the crystallinity, thickness and roughness of the films. As observed from the absorption spectra (Figure 5.7 panel a) going from film A to B, the position of maximum absorption peak has red shifted, suggesting a greater degree of crystallinity in film B. This is particularly evident for the P3HT:PDI_2 blend film (compared to pristine PDI_2 film), implying the conjugation length of P3HT has increased, leading to a more crystallised P3HT. Simultaneously, as shown in Figure 5.7 b, the photoluminescence quenching data suggest this enhanced crystallisation favours optimum phase segregation, which results in higher PL quenching of both the polymer and PDI_2 by the other component in the blend.

In complement with the absorption and emission spectra (Figure 5.7), AFM data in Figure 5.8 further supports the above results. Figure 5.8 shows the surface morphologies of the films obtained using the AFM. The scan area was 5 μm × 5 μm. The measured data show an increase in thickness and a decrease of roughness going from film A to film B; the latter may be caused by a change in domain size between the films. The root mean square (RMS) roughness was measured as 101 nm and 51 nm for films A and B, respectively. This shows that the RMS roughness decreased as the spin coating rate decreased, perhaps suggesting when the film has better packing (more crystallised) the roughness decreases. Yang *et al*.[83] and Shim *et al*.[84] have also reported that the RMS roughness decreased as the film thickness

increased. On the contrary, more crystallised blend films of P3HT:PCBM become rougher relative to their more amorphous morphology.

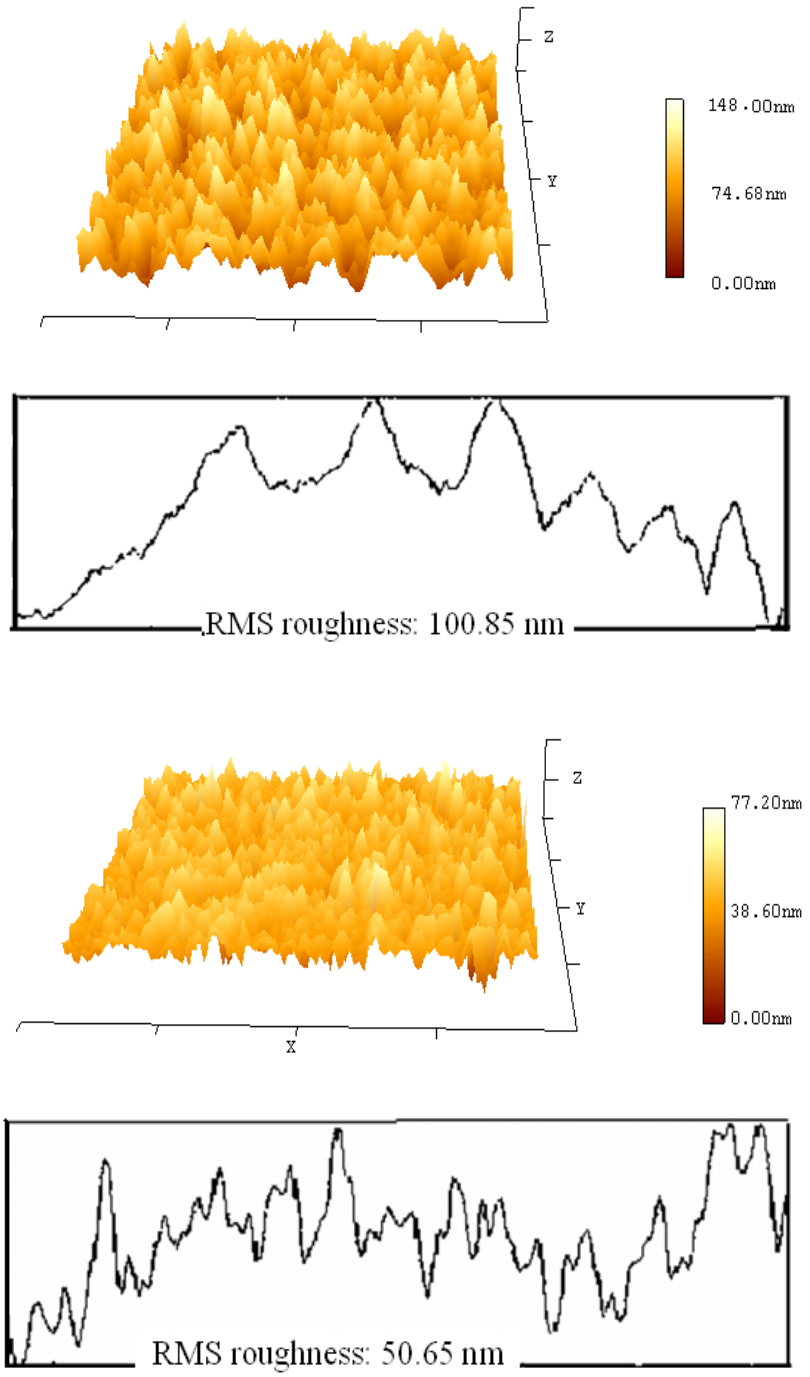


Figure 5.8 AFM images along with RMS roughness of P3HT:PDI_2 films A (top) and B (bottom) prepared at 3000 rpm and 500 rpm spin rates respectively. Scan area: 5 μm×5 μm.

On the basis of these results, unless stated otherwise all further films produced are fabricated from chloroform, in a 1:1 weight ratio for blends and spun at low spin speeds i.e. 500 rpm, in order to achieve smoother films with optimum thickness and crystallisation.

In addition to above morphology aspects, many studies have addressed the influence of thermal annealing on crystallinity and blend nanomorphology, which subsequently has impact on the properties of the CT state and, therefore, charge photogeneration in donor/acceptor blends. For example, it has been established that the rates of geminate and bimolecular recombination depend upon the crystallinity of the (P3HT:PCBM) blend system. We now turn to examine the impact of this parameter on both morphology of the films and charge dissociation.

5.5 Thermal Annealing

The role of thermal annealing of organic donor/acceptor blend films has been extensively studied. In P3HT:PCBM blend films the observations of changes have been assigned to an increase in the material's crystallinity. The crystallisation process has been suggested to facilitate and enhance the formation of distinct P3HT phases and PCBM aggregates in the blend film due to the more ordered packing of the polymer chains.[85-89] Thus, phase segregation is enhanced upon thermal treatment. In devices, the higher photocurrents measured as a result of the altered morphology upon thermal annealing have most often been attributed to the observed increase in charge carrier mobility.[90-94] An alternative possibility for the increase in photocurrent is a reduction in geminate recombination losses, thereby increasing the efficiency of CT state dissociation into the free charge carriers.[95]

McNeill *et al.*[96] utilised a number of experimental techniques to study the effect of annealing on PFB:F8BT blend films. He concludes that geminate recombination was the limiting factor for device efficiency. Thermal annealing increased device EQE, however, photoluminescence measurements showed the PL quenching progressively decreasing with increasing annealing temperature, consistent with the growing domain sizes observed by AFM. On the basis of the enhanced device performance despite a decrease in exciton dissociation efficiency upon annealing; it was concluded that geminate recombination limits the efficiency of PFB:F8BT

solar cells. It was proposed that as phase segregation increased, geminate recombination is reduced and the overall yield of charge photogeneration thus improves.

In a study by Clarke *et al* thermal annealing of P3HT:PCBM blend films resulted in an almost two-fold increase in the yield of dissociated P3HT polarons. The magnitude of this enhancement in charge photogeneration upon annealing – on a timescale relevant to device performance[97] – was sufficient for it to be a significant contributor to the improvement in photocurrent. The authors attributed this enhancement to a reduction in geminate recombination losses, thereby increasing the yield of dissociated polarons. In addition, the authors suggested that the enhanced crystallinity of the P3HT phase lowers the ionisation potential of the P3HT and thus increases the free energy of charge separation.

5.5.1 Steady state photophysics

The effect of thermal annealing on the films of P3HT, PDI_2 and P3HT:PDI_2 is first studied using steady state absorption and emission spectroscopy. Table 5.2 presents optical absorption and emission data of the films as-prepared and after thermal annealing at 150 ^{o}C for 20 minutes. The annealing temperature is chosen to be around P3HT's glass transition temperature[98,99] and is consistent with P3HT:PCBM annealing temperature studies.[100,101]

It is observed, after thermal annealing at 150°C for 20 minutes, that the optical density (OD) of pristine PDI_2 and blend P3HT:PDI_2 films increase along with an increase in the PL of the blend, which subsequently reduces PL quenching of P3HT:PDI_2 blend film. The increase in OD of the blend film is most likely to be as a consequence of phase separation and crystallisation of separate domains of PDI_2 and P3HT. In the blend P3HT:PDI_2, P3HT chains self-assemble to form crystallites; this is reflected in absorption spectra through a slight increase in the absorption band at 450- 650 nm, characteristic peak due to the π–π^* transition of the P3HT backbone.[102] There are also better resolved vibronic sidebands, and particularly through the more pronounced shoulder centered at ~615 nm, which has been assigned to a highly delocalized inter-chain excitation.[103,104] The intensity of this shoulder has previously been correlated with the degree of P3HT crystallinity as deduced from X-ray diffraction data.[105] The above observations are consistent with previous studies.[106,107] The decrease in emission of P3HT:PDI_2 blend film may be attributed to an increase in domain sizes of P3HT

and PDI_2, causing larger phase segregation. This increase in phase segregation will reduce the percentage of excitons diffusing to the interface (within their lifetime) to dissociate and hence a reduction in PL quenching is observed. This observation is in agreement with blend films of P3HT:PCBM where annealing of the film increases the photoluminescence of P3HT:PCBM, thus a reduction in quenching of P3HT.[108]

Table 5.2: As-prepared and annealed photophysical properties of pristine PDI2 and P3HT:electron acceptors.

Film	As-prepared		Annealed	
	Abs	PL*10^7	Abs	PL*10^7
PDI_2 (λ_{max} at 490 nm)	0.4	1.1	0.5	1.2
P3HT:PDI_2 (λ_{max} at 510 nm)	0.6	0.3	0.7	0.4
P3HT (λ_{max} at 510 nm)	0.7	0.8	0.7	0.8
P3HT:PCBM (λ_{max} at 510 nm)	0.58	0.05	0.65	0.3

Absorption and emission data of as-prepared and annealed films of PDI_2 (excited at 490 nm), P3HT:PDI_2 (excited at 522 nm), and P3HT:PCBM (excited at 500 nm) thin films. PDI_2 and P3HT:PDI_2 films annealed at 150°C for 20 minutes and spun at 500 rpm for 60 seconds. P3HT:PCBM annealed at 150°C spun at 1500 rpm for 60 seconds.

5.5.2 Morphology

5.5.2.1 Polarising Light Microscope

The effect of annealing is further investigated with the use of polarising light microscope (PLM). The growths of PDI_2 crystallites was monitored optically, by imaging the surface of pristine and blend films, spun on glass substrate, during continuous heating. Figure 5.9 shows

PLM micrographs of the same (~ 300 × 220 μm^2) region of a PDI_2 pristine film at increasing temperatures (25, 100, 200 and 180 $^{\circ}C$, with a ramp rate of 5 $^{\circ}C\ min^{-1}$). It can be seen at room temperature the as-prepared films show no characteristics of ordered liquid crystals. However, upon thermally annealing the films from room temperature to PDI_2's isotropic temperature (T ~200 ^{o}C), fan shaped domains, typical of columnar discotic liquid crystals phase (Figure 5.9b and c), appear. Upon approaching the isotropic temperature, all the structures eventually disappear to form a completely black field of view. Thereafter, as the temperature begins to cool down within the mesophase, a competition between homeotropic alignment and planar alignment (characterised by the birefringent textures as the orientation is anisotropic - directionally dependent) is observed. The isotropic dark field of view is distinguished from homeotropic (also viewed as dark regions under PLM) alignment through the application of a stress force which changes the alignment from homeotropic to planar. By going to the isotropic phase and cooling down slowly, the desired homeotropic alignment is achieved. The results are in agreement with expectation. During the process of heating the film from room temperature to isotropic phase, the film enters the columnar hexagonal mesophase (c) and by slowly lowering the temperature from isotropic phase, homeotropic alignment remains (d). As the temperature continues to decrease, however, planar alignment becomes more involved and eventually the morphology becomes combination of homeotropic and planar alignment- oblique arrangement. These alignments are observed to be a function of cooling rate, thickness and time, and thus these factors influence the competition between homeotropic and planar configuration.

Comparison of the 100 $^{\circ}C$ and 200 $^{\circ}C$ images shows a one-to-one correspondence in crystallite locations with an uneven growth in crystallite size, strongly suggesting that there is an initial nucleation followed by an irregular growth. Panel c also shows that the regions around the crystallites become depleted of PDI_2. In particular, there is a lighter colouration evident within a halo-like region around each of the crystallites.

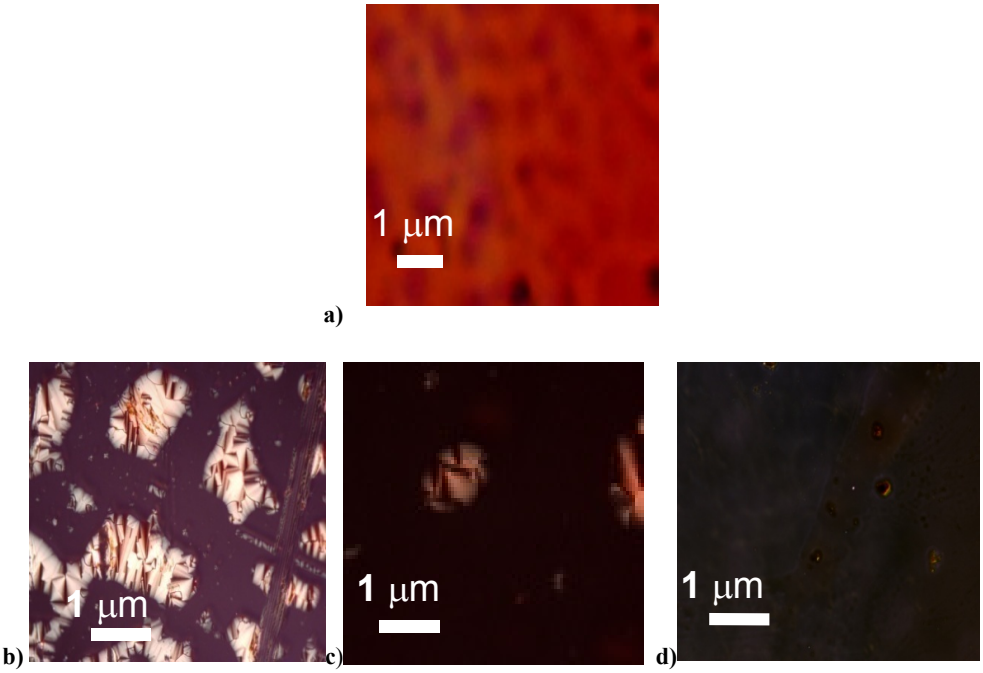


Figure 5.9 Pristine PDI_2 film spun from CF: (a) as-prepared at room temperature (20×), (b) heating the film to isotropic phase 100 ^oC (20×), (c) near Isotropic temperature 200 ^oC and d) cooling from isotropic phase, 180 ^oC (20×).

Similar behaviour was observed for the investigation of P3HT:PDI_2 (1:1) blend film under continuous heating as observed by PLM. Consistent with pristine PDI_2 film, the as-prepared blend film at room temperature shows no texture whilst the annealed films display the columnar hexagonal mesophase upon cooling from isotropic temperature. These characteristics are assigned to PDI_2. However, in the blend, PDI_2's homeotropic alignment is further disturbed due to the P3HT.

The absence of a textured structure for an as-prepared (pristine or blend) film is due to the spin coated films having insufficient time to allow chains to reorganise into a well ordered crystal or liquid crystalline structure. By thermally annealing the films, the viscosity of the sample is reduced and a process known as coarsening takes place; the chains and domains begin to reorganise and the very small domains that cannot be resolved by the light microscope become larger with temperature, which is observed as a development of texture.

This process is hastened as the clearing (isotropic) temperature is approached. The observation of a dark field of view in the LC mesophase, assigned to homeotropic alignment, is characterised by the optic axis being along the direction of light propagation.

The substrate–LC interactions are phenomenologically described by the ratio of the surface tensions of the surface (γ_s) and the LC (γ_{LC}). If $\gamma_s > \gamma_{LC}$, then the intermolecular LC forces are larger than the surface–LC forces and homeotropic alignment results. Planar alignment is achieved when the surface anchoring forces are dominant. The nature of the LC–surface interaction is complex and includes dispersive (Van der Waals), polar and steric terms as well as ionic terms. Topological factors should also be included.

5.5.2.2 Atomic force microscope

The morphology of the P3HT:PDI_2 (1:1) blend film is further studied by AFM. Figure 5.10 depicts AFM images of a P3HT:PDI_2 blend film spun on glass substrate before and after annealing. The data reveal a much rougher surface for annealed films than the as-prepared films (80 nm and 50 nm respectively). The increased roughness rules out any contribution from the P3HT component as studies show annealing of P3HT helps the self-organization of each P3HT component [89,109] and thus the roughness is reduced (12.8 – 4.5 nm). Thus the result suggests the increased roughness can be solely attributed to PDI_2 moieties due to the dewetting that occurs on approaching PDI_2's isotropic phase. Also, phase contrast AFM measurements of the blend film show an increase in domain size of both P3HT and PDI_2 moieties upon annealing. At the annealed temperature (150 ^oC), which is above P3HT's glass transition temperature, increased planar stacking of P3HT chains occurs, thereby increasing the P3HT crystallite size but not affecting the cluster size of the PDI_2 molecules. At 150 ^oC, the PDI_2 molecules diffused to form larger aggregates; therefore, phase separation of P3HT and PDI_2 occurs providing improved continuous pathways for the holes and electrons.

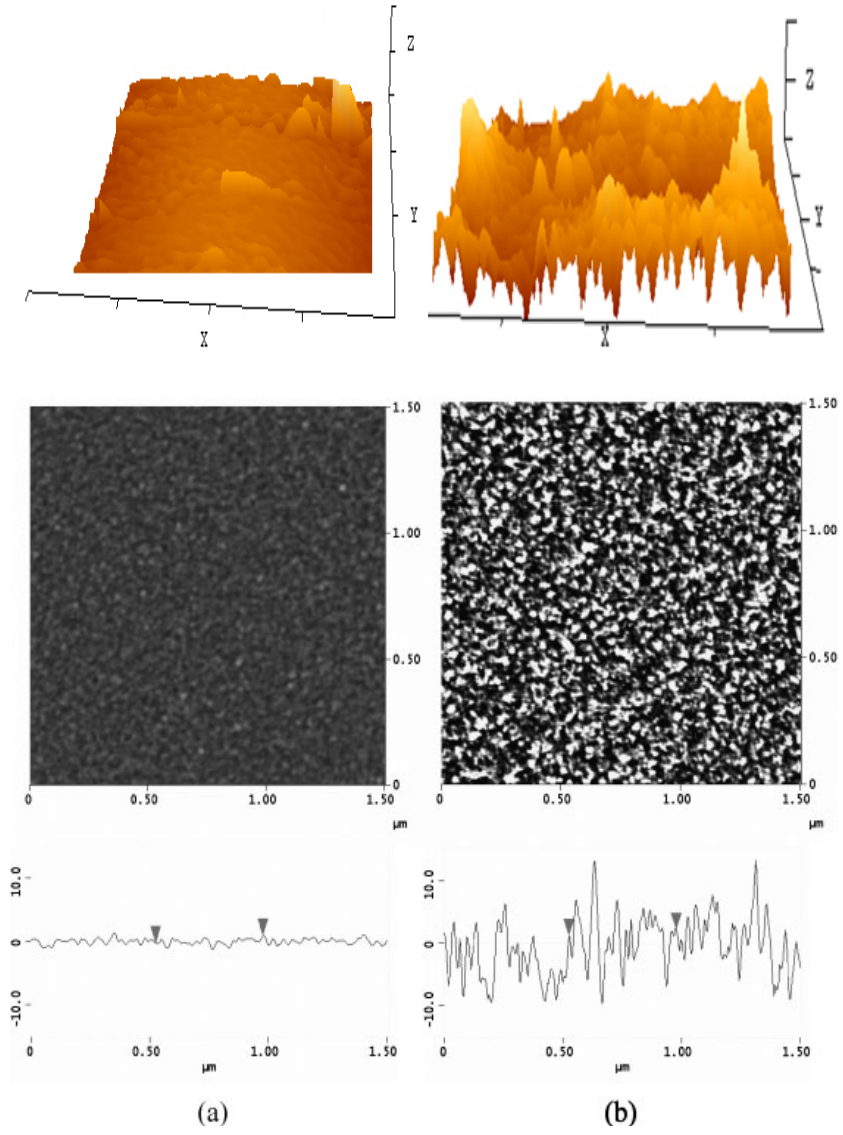


Figure 5.10 Phase-contrast AFM images of as-prepared (a) compared to annealed (b) (150 ^{o}C, 60 min) P3HT:PDI_2 films.

This observation is in agreement with those for P3HT:PCBM blend films. AFM images of P3HT:PCBM films reveal that after thermal annealing the morphology of interpenetrating P3HT:PCBM networks and phase separation becomes apparent – with typical domain sizes ranging from between 10 to 30nm – for the sample that had experienced annealing at 150 ^{o}C

for 20 minutes relative to that of the as-spun film, consistent with other studies.[89,110,111] Thermal annealing enables the PCBM molecules to diffuse through the film to form aggregates. The size of these domains varies from 10 to 100nm on annealing for 5 min at 100 ^{o}C (ref.[112]), up to tens of μm [46,87,113] on annealing for longer periods (typically >30 min) and at higher temperatures (>130 ^{o}C).[86]

The high temperature also improves the crystallinity of P3HT within the phase separated networks and thereby facilitates charge transport to the electrodes. The increased crystallinity of P3HT upon annealing has been observed by many groups.[110] This nanoscale control of the morphology of the donor-acceptor interpenetrating networks result in optimized and stable phase separation for efficient charge separation and transport and thereby leads to thermally stable, high efficiency solar cells.

Efficiencies of light absorption, charge collection and charge pair generation are three aspects of PV device function that significantly influence the performance. The charge generation yield and recombination kinetics of polymer:PCBM blend films, as monitored by TAS, are dependent on a number of factors but their crytallinity and the overall morphology are primary concerns. Charge generation (polaron) yields are measured using transient absorption spectroscopy (TAS), which directly monitors the optical absorption, and therefore yield, of photogenerated charges on the microsecond timescale.

5.6 Charge generation in P3HT:PDI_2 blend films

Transient absorption spectroscopy (TAS), monitors the transient optical absorption of photogenerated charge carriers on the microsecond time scale, providing a powerful probe of this charge generation yield.[55] In addition, TAS also provides information on the recombination dynamics of these photogenerated charges. Both geminate recombination (from the CT state (Coulombically-bound radical ion pairs) before full charge separation into free charge carriers) and bimolecular recombination (from the fully charge separated species) represent significant loss pathways in photovoltaic cells; as such, it is important to investigate their contributions to a particular system.

Charge generation can be divided into two separate issues: the efficiency of exciton quenching at the donor / acceptor interface and the efficiency of dissociation of the resultant polaron pairs into free charges. The first issue can be investigated using fluorescence spectroscopy. The extent of emission quenching of the pristine polymer compared to the polymer / acceptor blend film is a useful indicator of acceptor's effectiveness in quenching polymer excitons, however, this technique is unable to assay whether the initially generated charges at the donor / acceptor interface dissociate into free charges or undergo geminate (monomolecular) recombination (as observed in Chapter 3). TAS is then employed as it can assay the efficiency of polaron pairs as the technique examines the overall efficiency of charge photogeneration (η_{CG} in equation 2, chapter 1) in such blend films – i.e. the product exciton dissociation and charge transfer state dissociation.

Pristine and blend film were fabricated using optimum conditions as recognised by above morphology studies (as detailed in experimental methods, 5.2). Photoluminescence emission of non-annealed and annealed (150°C for 20 minutes) P3HT:PDI_2 blend film exhibits ~ 70% and ~ 60% PL quenching relative to PDI_2 respectively (see Table 5.2), indicative of charge transfer state formation. Transient absorption is thus employed to monitor the efficiency of dissociation of these CT states into free charges.

Transient absorption spectrum is taken to identify the species present in the blend. The spectrum of a non-annealed P3HT:PDI_2 film, displayed in Figure 5.11.a, shows two peaks centred at ~ 700 nm and 980 nm assigned to PDI_2 anions and P3HT cations respectively. TAS data measured in ambient air conditions were identical to those measured under nitrogen, confirming our assignment of the TAS signal to polaron rather than triplet states. It is apparent that thermal annealing at 150 ^{0}C for 20 minutes induces very little change in the transient absorption spectrum of $PDI_2^{\bullet-}$ and $P3HT^{\bullet+}$ in terms of band shape and λ_{max}; only the signal size increases. This lack of change in the transient spectrum strongly indicates that the $PDI_2^{\bullet-}$ and $P3HT^{\bullet+}$ absorption spectral shape and molar extinction coefficient are unchanged with annealing and that any change in signal magnitude will therefore primarily originate from a change in polaron concentration. Figure 5.11b shows the corresponding decay dynamics of the photoinduced absorption signals for the non-annealed and annealed films, monitored at 700 nm (the $PDI_2^{\bullet-}$ absorption maximum).

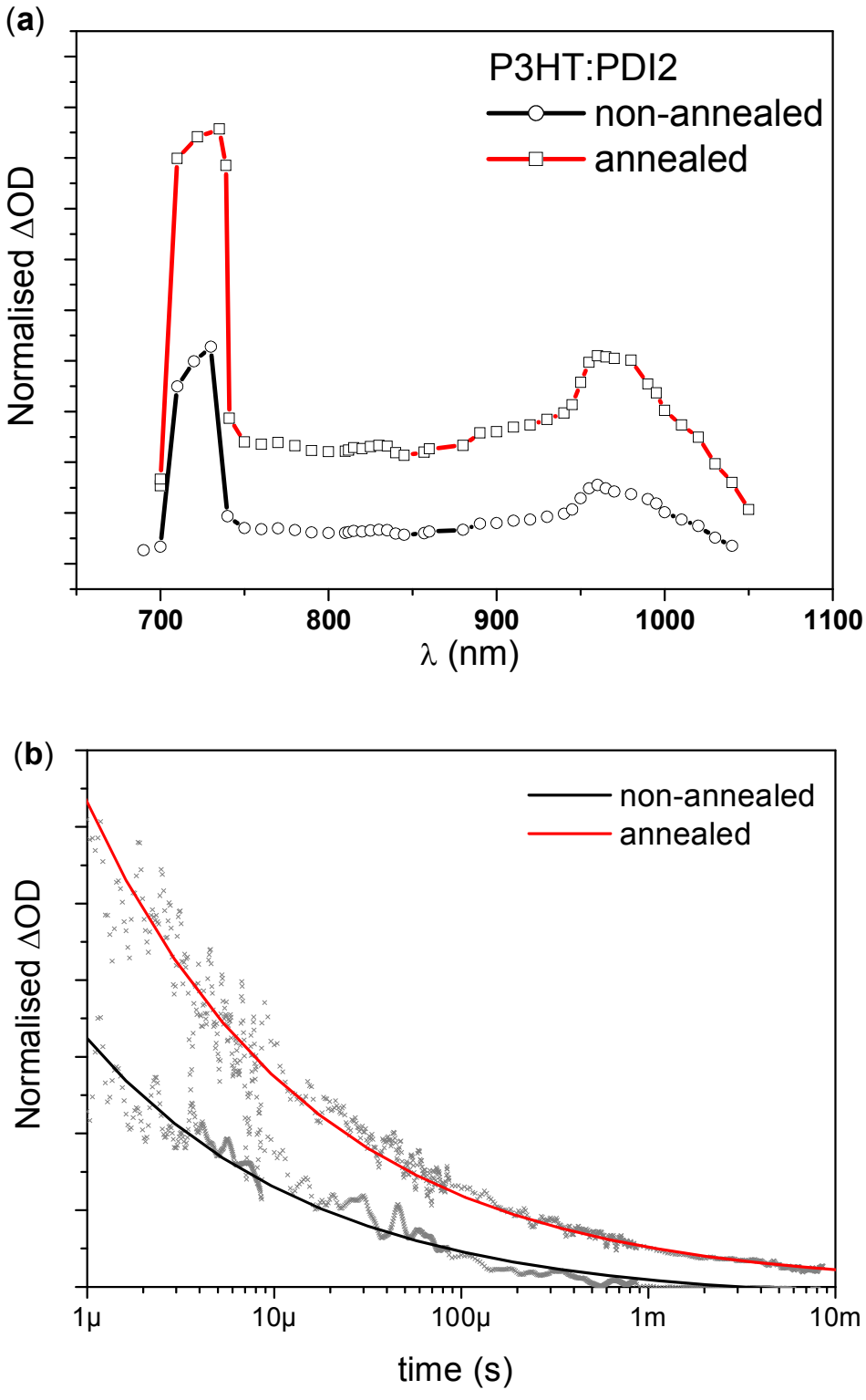


Figure 5.11 The transient absorption spectrum of a P3HT:PDI_2 (1:1) blend film obtained at 1μs after 40 μJ.cm^{-2} excitation at 500 nm before (black) and after (re) annealing at 150°C for 20 minutes (a) and the transient absorption decay kinetics of a P3HT:PDI_2 (1:1) blend film obtained using 20 μJ.cm^{-2} excitation at 500 nm and a probe wavelength of 720 nm before (black) and after (red) annealing at 150°C for 20 minutes (b).

The most striking effect of annealing observed in the TAS data is the significant increase in the ΔOD signal amplitude. This increase was observed at all probe wavelengths studied and over a wide range of time delays (1 μs – 100 μs). This increase in amplitude was also observed over a wide range of excitation densities (0.7 – 40 $\mu J.cm^{-2}$). The magnitude of this signal increase was observed to depend upon the relative crystallinities of the film before and after annealing, with the largest changes in ground state absorption spectrum upon annealing correlating with the largest relative increase in ΔOD signal amplitude. The data shown herein, corresponding to an increase in amplitude by a factor of two, is typical behaviour. We note that the signal amplitude has already been corrected for changes in ground-state absorbance at the excitation wavelength (which were small at the 500 nm pump wavelength employed). We therefore conclude that the observed increase in ΔOD signal amplitude derives from an enhancement in charge generation yield: the yield of dissociated polarons observed on the microsecond timescale has approximately doubled as a result of annealing.

As discussed above, the cause of increase in charge photogeneration cannot be attributed to an enhanced efficiency of exciton splitting at the P3HT:PDI_2 interface. An alternative possibility for the increase in charge generation is a reduction in geminate recombination losses, thereby increasing the net efficiency of bound radical pair dissociation into the free charge carriers. This observation is also apprent in P3HT:PCBM blend films and is supported by a recent ultra-fast time-resolved spectroscopic study by Moses *et al*, which found that thermal annealing of P3HT:PCBM films resulted in a shorter lifetime of the bound radical pair state, also attributed to an enhanced efficiency of charge generation.[37] Geminate recombination has been widely discussed as a potentially significant limiting factor in OPV devices. It results from the monomolecular recombination of a coulombically-bound radical pair, forming their respective ground state species, rather than the dissociation into free charges that can contribute to the device current.

Thermal annealing usually enhances the phase segregation and increases the crystallinity present in a blend film. There are now several studies that suggest that this can favour the dissociation of interfacial CT states, thereby reducing geminate recombination. This reduction in geminate recombination is crucial for efficient charge photogeneration and

appears to be a significant loss mechanism in current photovoltaic devices. However, it is likely that such an effect will eventually reach an optimum.

5.7 Charge photogeneration in PDI_2 blend films vs. PCBM blend films

Several recent studies have indicated this charge generation can be divided into two separate issues: the efficiency of exciton quenching at the donor / acceptor interface and the efficiency of dissociation of the resultant polaron pairs into free charges. The first issue can be investigated using fluorescence spectroscopy. The extent of emission quenching of the pristine donor (or acceptor) compared to the donor / acceptor blend film is a useful indicator of acceptor's (or donor's) effectiveness in quenching donor (or acceptor) excitons, although it is not a direct measure of charge generation.

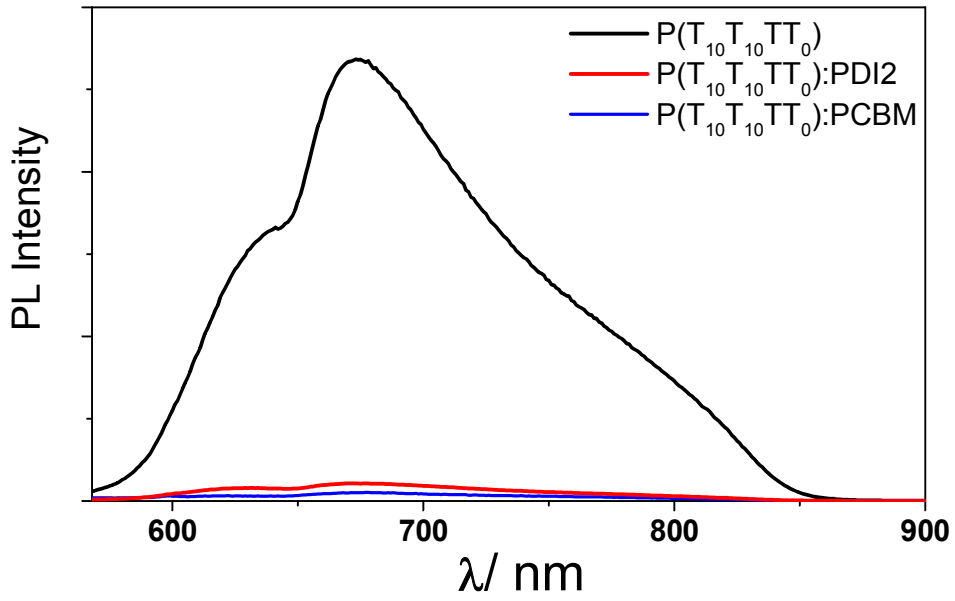


Figure 5.12 Typical photoluminescence data for pristine $P(T_{10}T_{10}TT_0)$, $P(T_{10}T_{10}TT_0)$:PDI_2 and $P(T_{10}T_{10}TT_0)$:PCBM 1:1 blend films.

Photoluminescence (PL) data were collected to evaluate the efficiency of exciton quenching for all blend films. PL data for a $P(T_{10}T_{10}TT_0)$:PDI_2 film are typical and are compared to data for the pure donor and its blend with PCBM (Figure 5.12). For all blend films studied herein, PL quenching was > 70 % for both polymer:PDI_2 and polymer:PCBM compared to the corresponding pristine films, indicative of efficient exciton diffusion to, and quenching at, the donor / acceptor interface. However, as it has been shown previously,[55] such PL quenching is

not a reliable indicator of the generation of fully dissociated charges, due to the potential for geminate recombination of initially generated electron / hole pairs prior to their dissociation into separated charges. To address this issue, we employed transient absorption spectroscopy (TAS) to monitor the yields of long-lived, dissociated charges observed on the μs timescale (which correspond to the typical time scale for charge collection in polymer:fullerene devices[114]).

Previously reported estimates of the film electron affinities (EA) of PCBM and PDI_2 as 3.7 eV and 3.3 eV, respectively,[1,115] suggest that PCBM is a stronger electron acceptor than PDI_2 but were obtained using different electrochemically-based approaches. The estimate for PCBM is supported by a recent inverse photoelectron study giving a value of 3.9±0.1 eV;[116] however, direct measurements of the EAs of PDIs have not been published. In fact, solution electrochemical data[14,117] indicate similar reduction potentials for PDI_2 and PCBM. However, due to different solvents used for each study, and due to the possibility of differing effects of intermolecular interactions in the two solids, the relative EAs of the two materials in the solid state remains unclear. In order to address further the relative electron accepting properties of PDI_2 and PCBM, we studied the photophysics of PDI_2:PCBM blend films using transient absorption spectroscopy. These data indicated that photoexcitation of a blend of PCBM and PDI_2 resulted in the formation of PDI_2^+:$PCBM^-$ (Figure 5.13), consistent with PCBM exhibiting a larger EA than the PDI_2 in films. As shown by TAS in Figure 5.13, photoexcitation of a blend of the two molecular n-type materials, PCBM and PDI_2, resulted in electron transfer from PDI_2 to PCBM. Consistent with previous reports, the transient spectrum exhibited an absorption maximum at ~850 and ~1040 nm indicative of the formation of PDI cations[118] and PCBM anions[119] respectively. These are distinguishable from PDI triplet absorption at 480 nm and PDI radical anions that have been reported to show structured absorption with a sharp absorption maximum at shorter wavelengths of 700 nm.[64,120] The ΔOD of the transient peak at ~850 nm therefore corresponds to the formation of PDI_2^+ whilst the ΔOD at ~1040 nm is assigned to $PCBM^-$. These TAS data are consistent with PCBM exhibiting a higher electron affinity than PDI_2.

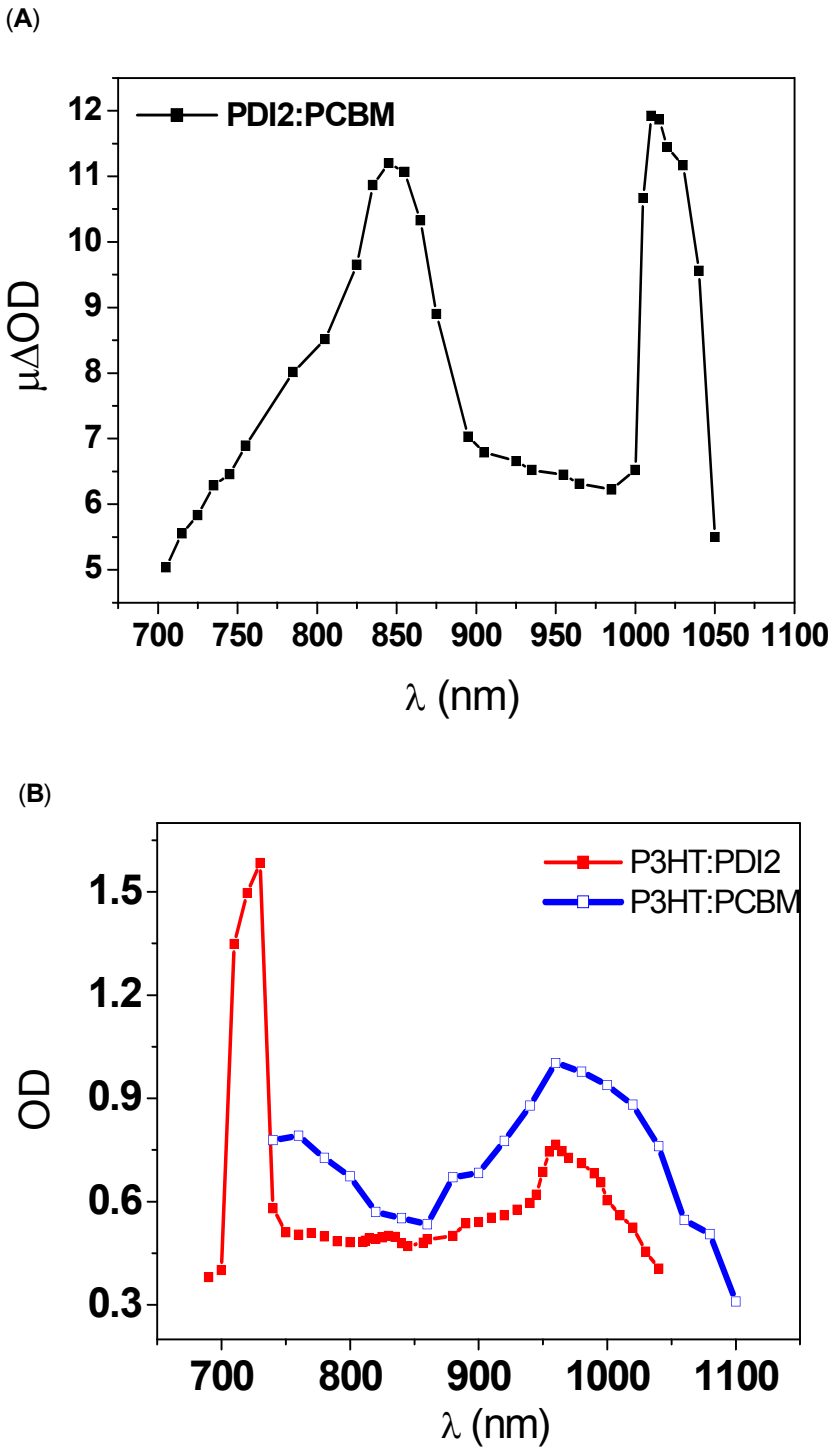


Figure 5.13 (A) Transient absorption data collected for a 1:1 PDI_2:PCBM blend film spin coated from $CHCl_3$ at 1100 rpm for 40s. Films were excited at 447 nm and measured at 1μs, using an excitation density of 50 μJ cm^{-2}. (B) P3HT:PDI_2 (open blue square) and P3HT:PCBM (filled red squares) spun from $CHCl_3$ at 1100 rpm for 40s and chlorobenzene at 1500 rpm for 90s respectively. Both were excited at 520 nm and measured at 1 μs using an excitation density of 50 μJ cm^{-2}.

On the basis of these results, higher charge photogeneration yields might be expected using PCBM rather than PDI_2 as the acceptor. Typical transient absorption spectra, observed at 1 μs, for P3HT:PDI_2 and P3HT:PCBM blend films are shown in Figure 5.13. All such spectra exhibited spectral features characteristic of radical ion formation (e.g.: $P3HT^+$ absorption maximum at ~ 960[121-123] nm and PDI_2^- absorption at 700 nm[64,120]). These transient absorption signals exhibited microsecond- to milisecond-timescale, dispersive, O_2-independent decay dynamics, confirming their assignment to long-lived, dissociated radical ions.

Whilst all the μs to ms transients observed for polymer:PDI_2 and polymer:PCBM blend films exhibited decay dynamics and transient spectra consistent with their assignments to dissociated charges, the amplitudes of these transients, and, therefore, the yields of dissociated charges varied strongly between films. Typical data illustrating this are shown in Figure 5.14 which compares the transient absorption decays observed for blend films employing the polythiophene P($T_{10}T_{10}TT_0$). For P($T_{10}T_{10}TT_0$):PCBM blend films, the signal magnitude is $\leq$ 5 μΔOD. In contrast, P($T_{10}T_{10}TT_0$):PDI_2 blend films exhibited a much stronger transient absorbance signal (~0.25 mΔOD). This difference cannot be assigned to differences in exciton quenching, with the PL in fact being more strongly quenched for the P($T_{10}T_{10}TT_0$):PCBM blend film. Rather, this increase in long-lived polarons is assigned to more efficient dissociation of initially generated polaron pairs, thereby avoiding geminate charge-recombination losses.

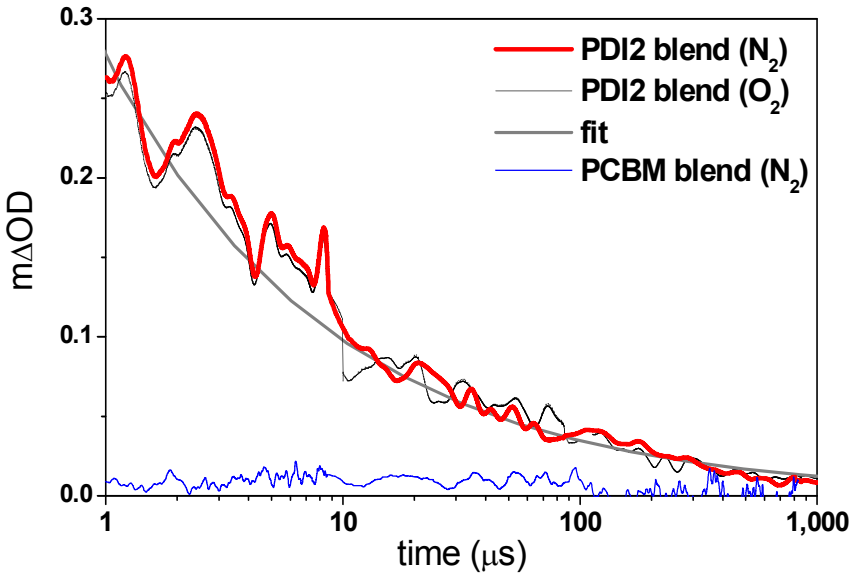


Figure 5.14 Typical transient absorption data for (red) $P(T_{10}T_{10}TT_0)$:PDI_2 (red) and (blue) $P(T_{10}T_{10}TT_0)$:$PC_{60}BM$ (blue) 1:1 blend films in a N_2 environment, monitored at 850 and 960 nm respectively. Also shown for is data collected under O_2 (black) and a power law fit (gray) to the data ($\Delta OD \propto t^{-a}$).

Table 5.3 summarises the transient absorption decays of as-prepared polythiophene:PDI_2 and polythiophene:PCBM blend films. The amplitudes have been normalized for variation in thickness and optical densities between blend films. With the exception of the P3HT:PDI_2 blend, in all cases it is observed that the polymer:PDI_2 blends give a higher yield than the PCBM counterpart blends. Due to the higher extinction coefficient of PDI_2 anions,[124] the transient decays of the PDI_2 blends are probed at 830 nm, a wavelength with partial contribution both from polymer cations and PDI_2 anions. Furthermore, this probing wavelength is chosen such that it corresponds to the lowest ΔOD on the spectra of P3HT:PDI_2 and hence emphasizing the higher yield of PDI_2 blends.

Table 5.3: Photophysical Properties of 1:1 Polythiophene:PDI_2 and Polythiophene:PCBM blend Films:

	Assignment	$\Delta G_{rel}^{CS\ a}$	$m\Delta OD^b$	PLQ^c %
P3HT				
PDI_2	$P^+/\mathbf{PDI_2}^-$	0.5	0.2	65
PCBM	$P^+/PCBM^-$	0.9	0.18	>95
$P(T_{10}T_{10}TT_0)$				
PDI_2	$P^+/\mathbf{PDI_2}^-$	0.2	0.25	95
PCBM	$P^+/PCBM^-$	0.6	0.06	>95
$P(T_{16}T_{16}TT_0)$				
PDI_2	$P^+/\mathbf{PDI_2}^-$	0.2	0.2	85
PCBM	$P^+/PCBM^-$	0.6	0.04	90
$P(T_0TT_{16})$				
PDI_2	P+/**PDI_2**−	0.35	0.13	80
PCBM	P+/PCBM−	0.75	0.08	95
$P(T_{12}SeT_{12})$				
PDI_2	$P^+/\mathbf{PDI_2}^-$	0.18	0.15	80
PCBM	-	0.58	0.04	95

a $-\Delta G_{CS}$ estimated as E_S - (IP - EA) where E_S is the energy level of polymer singlet excitons. IP is the Ionisation potential of the polymer and EA is the electron affinity of the electron acceptor. All the energy levels: ΔG_{CS}, E_S, IP and EA are estimated as measured in eV. b Evaluated from the amplitude of the transient absorbance power-law decay phase at 1 μs normalized by the ground state absorbance at the excitation wavelength. c Steady-state PL quenching of the blend film relative to the corresponding pristine polymer film.

Figure 5.15 plots the signal magnitude, corresponding approximately to the yield of dissociated species, versus the relative free-energy difference for charge separation, $-\Delta G_{CS}^{rel}$ (defined as the difference between the singlet exciton energy E_S and the free energy of the

dissociated charges ($IP_{don} - EA_{acc}$). For the polythiophene/PCBM blend films, it is apparent that the yield of charge photogeneration shows a very strong dependence upon ΔG_{CS}^{rel}, with a 300 meV reduction in ΔG_{CS}^{rel} correlating with almost a two orders of magnitude decrease in long-lived polaron yield, in agreement with our previous observations of 19:1 blend films.[55] We note the polymers employed and blend composition used are distinct from those employed in Ref. 55; these data therefore provide further evidence for the generality of the strong ΔG_{CS}^{rel} dependence of charge generation observed for polymer / PCBM films in Ref. 55. In contrast, it is apparent that for the polythiophene/PDI2 films, the yield of dissociated photogenerated charges is essentially independent of ΔG_{CS}^{rel}, at least for the polymer series studied here.

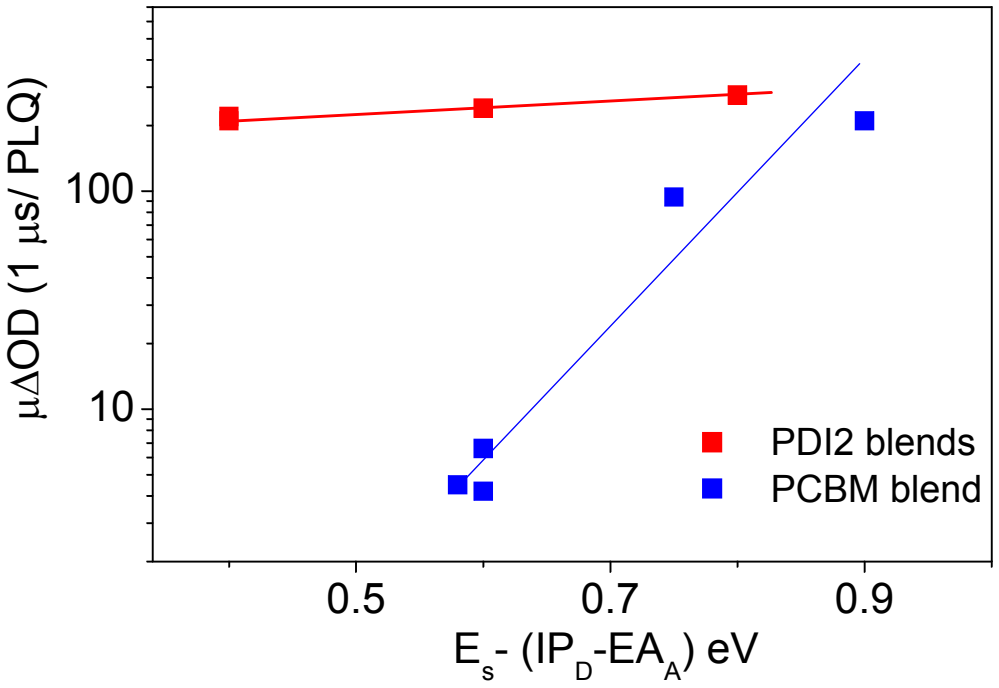


Figure 5.15 Plot of the relative yield of long-lived, dissociated polarons in polythiophene/PDI_2 (filled squares) and polythiophene/PCBM (open squares) blend films, as measured by the amplitude of the transient absorption at 850 and 1000 nm respectively, at 1μs, against estimated driving force for charge separation, $-\Delta G_{CS}$. PDI_2's E.A. normalised to that of PCBM's (-3.7 eV).

We have previously proposed that the strong dependence of charge photogeneration yield upon $-\Delta G_{CS}^{rel}$ for polythiophene/ PCBM blend films originates from the requirement of the CT state to overcome their Coulombic attraction, with a large $-\Delta G_{CS}^{rel}$ providing the polaron pairs with enough thermal energy to overcome this electrostatic attraction.[55] The data

presented here clearly indicates that this requirement for excess thermal energy is less severe when PCBM is replaced by PDI_2 as the electron acceptor. One possibility is that it originates from a difference in domain sizes, with the polythiophene/PDI_2 films exhibiting larger domain sizes, potentially facilitating charge dissociation away from the donor/acceptor interface.[125] Countering this argument, we note that our studies of charge photogeneration as a function of polymer crystallinity, blend composition and annealing[55,126] indicate that the dependence of photogeneration yield upon domain size is probably insufficiently strong to account for the trends in the data reported herein. Alternatively, and of particular interest, this difference may originate from the higher electron mobility of PDI_2 relative to PCBM (1.3 vs. 8×10^{-4} $cm^2V^{-1}s^{-1}$). The higher electron mobility, and the observed increase in polaron yield, may originate microscopically from increased intermolecular delocalisation arising within liquid crystalline π-stacks of the PDI. The previous study by Ohkita indicated that polymer hole mobility was not a key indicator of charge dissociation yield.[55] However, charge separation in these blend films is primarily based upon LUMO to LUMO electron transfer, and as such the electron mobility of the acceptor material might be expected to have a more important influence on the efficiency of polaron pair dissociation. This possibility suggests that a potentially important, but hitherto little considered, strategy for the optimisation of the efficiency of polymer/small molecule solar cells might be to focus on the use of higher electron mobility acceptor materials in order to facilitate the efficiency of photogeneration in such blend films.

The transient absorption measurements described above are indicators of the *yield* rather than the *rate* of charge dissociation. This yield is dependent upon competition between the underlying processes of charge dissociation, geminate recombination and / or thermalisation. We have previously shown,[55] and confirmed herein, that this competition can be influenced by ΔG_{CS}^{rel}. It is shown elsewhere that this yield is enhanced (for equivalent ΔG_{CS}^{rel}) by the use a charge transfer polymer PCPDTBT (poly[2,6-(4,4-bis(2-ethylhexyl)-4H-cyclopenta[2,1-b;3,4-b']dithiophene)-alt-4,7-(2,1,3-benzothiadiazole]).[127]

5.8 Conclusion

The data reported herein suggest that the morphology of the PDI_2 films is very delicate. From ground state absorption and emission spectroscopy, AFM micrographs and PLM data, we conclude that the blend films of P3HT:PDI_2 are sensitive to concentration, solvent and spin rate in addition to thermal annealing. The results found the grain size is dependent on all these parameters. This was confirmed by variation in emission quenching of the blend films, which affects charge photogeneration.

The photophysics of the data conducted for this chapter implies that the yield of charge dissociation can be influenced by the domain morphology and/or electron mobility of the acceptor molecules and implies that, at least in terms of charge photogeneration, PDIs can be more effective electron acceptors than PCBM. As such, if blend morphology limitations upon charge transport can be addressed, PDIs will be promising acceptors for bulk heterojunction solar cells.

Reference

(1) Schmidt-Mende, L. F., A.; Müllen, K.; Moons, E.; Friend, R. H.; MacKenzie, J. D.; *Science* **2001**, *293*, 1119.

(2) Malenfant, P. R. L.; Dimitrakopoulos, C. D.; Gelorme, J. D.; Kosbar, L. L.; Graham, T. O.; Curioni, A.; Andreoni, W.; *Appl. Phys. Lett.* **2002**, *80*, 2517.

(3) Chesterfield, R. J.; McKeen, J. C.; Newman, C. R.; Frisbie, C. D.; *J. Appl. Phys.* **2004**, *95*, 6396.

(4) Rost, C.; Gundlach, D. J.; Karg, S.; Riess, W.; *J. Appl. Phys.* **2004**, *95*, 5782.

(5) Ego, C.; Marsitzky, D.; Becker, S.; Zhang, J.; Grimsdale, A. C.; Müllen, K.; Mackenzie, J. D.; Silva, C.; Friend, R. H. *J. Am. Chem. Soc.* **2003**, *125*, 437.

(6) Meyer, J.-P.; Schlettwein, D.; Wohrle, D.; Jaeger, N. I. *Thin Solid Films* **2005**, *258*, 317-324.

(7) Horowitz, G.; Kouki, F.; Spearman, P.; Fichou, D.; Nogues, C.; Pan, X.; Garnier, F. *Adv. Mater.* **1996**, *8*, 242.

(8) Truijk, C. W.; Sieval, A. B.; Dakhorst, J. E. J.; van Dijk, M.; Kimkes, P.; Koehorst, R. B. M.; Donker, H.; Schaafsma, T. J.; Picken, S. J.; van de Craats, A. M.; Warman, J. M.; Zuilhof, H.; Sudholter, E. J. R. *J. Am. Chem. Soc.* **2000**, *112*, 11057.

(9) Dimitrakopoulos, C. D. ; Malenfant, P. R. L. *Adv. Mater.* **2002**, *14*, 99.

(10) Tang, C. W. **1986**, *48*, 183-185.

(11) Gregg, B. A.; Fox, M. A.; Bard, A. J.; *J. Am. Chem. Soc.* **1989**, *111*, 3024.

(12) Gregg, B. A. *Chem. Phys. Lett.* **1996**, *258*, 376.

(13) Neuteboom, E. E; Meskers, S. C. J; Van Hal, P. A; Van Duren, J. K. J; Meijer, E. W; Janssen, R. A. J; Dupin, H; Pourtois, G; Cornil, J; Lazzaroni, R; Bredas, J. L; Beljonne, D; *J. Am. Chem. Soc.* **2003**, *15*, 8625.

(14) An, Z.; Yu, J.; Jones, S. C.; Barlow, S.; Yoo, S.; Domercq, B.; Prins, P.; Siebbeles, L. D. A.; Kippelen, B.; Marder, S. R. *Adv. Mater.* **2005**, *17*, 2580-2583.

(15) Boom, T.; Hayes, R. T; Zhao, Y; Bushard, P. J; Weiss, E. A; Wasielewski, M. R. J. Am. Chem. Soc. 2002 124, 9582, Liu, S; Sui, G; Cormier, R. A; Leblanc, R. M; Gregg, B. A; *J. Phys. Chem.* **2002**, *106*, 1307.

(16) Meyer, J. P.; Schlettwein, D; Wohrle, D; Jaeger, N. I; *Thin Solid Films* **1995**, *317*, 314.

(17) Cormier, R. A.; Gregg, B. A.; *Chem. Mater.* **1998**, *10*, 1309.

(18) An, Z. **2005**.

(19) Würthner, F.; Thalacker, C.; Diele, S.; Tschierske, C. *Chem. Eur. J.* **2001**, *7*, 2245-2253.

(20) Würthner, F.; Chen, Z.; Dehm, V.; Stepanenko, V. *Chem. Comm.* **2006**, 1188-1190.

(21) Struijk, C. W.; Sieval, A. B.; Dakhorst, J. E. J.; van Dijk, M.; Kimkes, P.; Koehorst, R. B. M.; Donker, H.; Schaafsma, T. J.; Picken, S. J.; van de Craats, A. M.; Warman, J. M.; Zuilhof, H.; Sudholter, E. J. R.; *J. Am. Chem. Soc.* **2000**, *122*, 11057.

(22) Ferrere, S.; Gregg, B. A; *New J. Chem.* **2002**, *26*, 1155.

(23) Takahashi, K.; Nakajima, I.; Imoto, K.; Yamaguchi, T.; Komura, T.; Murata, K.; *Sol. Energy Mater. Sol. Cells* **2003**, *76*, 115.

(24) Signerski, R. *J. Non-Cryst. Solids* **2006**, *352*, 4319.

(25) Nakamura, J.; Yokoe, C.; Mruata, K.; Takahashi, K.; *J. Appl. Phys.* **2004**, *96*, 6878.

(26) Danziger, J.; Dodelet, J.-P.; Lee, P.; Nebesny, K. W.; Armstrong, N. R. *Chem. Mater.* **1991**, *3*, 821.

(27) Pandey, A. K.; Nunzi, J.-M. *Appl. Phys. Lett.* **2006**, *89*, 213506.

(28) Schmidtke, J. P.; Friend, R. H.; Kastler, M.; Mullen, K.; *J. Chem. Phys.* **2006**, *124*, 174704.

(29) Dittmer, J. J.; Marseglia, E. A.; Friend, R. H. *Adv. Mater* **2000**, *12*, 1270.

(30) Shin, W. S.; Jeong, H.-H.; Kim, M.-K.; Jin, S.-H.; Kim, M.-R.; Lee, J.-K.; Leec, J. W.; Gal, Y.-S. *J. Mater. Chem.* **2006**, *16*, 384.

(31) Dittmer, J. J.; Petritsch, K.; Marseglia, E. A.; Friend, R. H.; Rost, H.; Holmes, A. B; *Synth. Mets* **1999**, *102*, 879.

(32) Li, J.; Dierschke, F.; Wu, J.; Grimsdale, A. C.; Mullen, K.; *J. Mater. Chem.* **2006**, *16*, 96.

(33) Gregg, B. A. *J. Phys. Chem.* **1996**, *100*, 852.

(34) Conboy, J. C. O., E. J. C.; Adams, D. M.; Kerimo, J.; Zaban, A.; Gregg, B. A.; Barbara, P.; F. *J. Phys. Chem. B* **1998**, *102*, 4516.

(35) Adams, D. M;. Kerimo, J.; Olson, E. J. C.; Zaban, A.; Gregg, B. A.; Barbara, P. F. *J. Am. Chem. Soc.* **1997**, *119*, 10608.

(36) Keivanidis, P. E.; Howard, I. A.; Friend, R. H. *Advanced Functional Materials* **2008**, *18*, 3189-3202.

(37) Foster, S.; Finlayson, C. E.; Keivanidis, P. E.; Huang, Y. S.; Hwang, I.; Friend, R. H.; Otten, M. B. J.; Lu, L. P.; Schwartz, E.; Nolte, R. J. M.; Rowan, A. E. *Macromolecules* **2009**, *42*, 2023-2030.

(38) Park, S. H.; Roy, A.; Beaupré, S.; Cho, S.; Coates, N.; Moon, J. S.; Moses, D.; Leclerc, M.; Lee, K.; Heeger, A. J., *Nature Photonics* **2009**, *3*, 297 - 302.

(39) Chasteen, S.; V. Sholin, V.; Carter, S. A.; Rumbles, G. *Energy Mater. Sol. Cells* **2008**, *92*, 651-659.

(40) Müller, C.; Ferenczi, T.; Campoy-Quiles, M.; Frost, J.; Bradley, D.; Smith, P.; Stingelin-Stutzmann, N.; Nelson, J.; *Adv. Mater.* **2008**, *20*, 3510.

(41) Mihailetchi, V. D.; Koster, L. J. A.; Blom, P. W. M.; Melzer, C.; de Boer, B.; van Duren, J. K. J.; Janssen, R. A. J.; *Adv. Funct. Mater.* **2005**, *15*, 795.

(42) Chirvase, D., Parisi, J., Hummelen, J. C. & Dyakonov, V. *Nanotech,* **2004**, *15*, 1317.

(43) Shaheen, S. E.; Brabec, C. J.; Sariciftci, N. S.; Padinger, F.; Fromherz, T.; Hummelen, J. C. *Appl. Phys. Lett.* **2001**, *78*, 841.

(44) Martens, T.; D'Haen, J.; Munters, T.; Beelen, Z.; Goris, L.; Manca, J.; D'Olieslaeger, M.; Vanderzande, D.; Schepper, L. D.; Andriessen, R.; *Synth. Met.* **2003**, *138*, 243.

(45) Hoppe, H.; Sariciftci, N. S.; *J. Mater. Res.* **2004**, *19*, 1924.

(46) Chirvase, D., Parisi, J., Hummelen, J. C. & Dyakonov, V. *Nanotechnology* **2004**, 1317-1323.

(47) Yu, G.; Hegger, A. J. *J. Appl. Phys.* **1995**, *78*, 4510.

(48) Yu, G.; Gao, J.; Hummelen, J. C.; Wudl, F.; Heeger, A. J. *Science* **1995**, 270.

(49) Halls, J. J. M. *Nature* **1995**, *376*, 498.

(50) Shaheen, S. E.; Brabec,, C. J.; Sariciftci, N. S.; Padinger, F.; Fromherz, F.; Hummelen, J. C.; *Appl. Phys. Lett.* **2001**, *78*, 841.

(51) Swinnen, A. H., I.; vande Ven, M.; D'Haen, J.; Vanhoyland, G.; Aresu, S.; D'Olieslaeger, M.; Manca, J.; *Adv. Funct. Mater.* **2006**, *16*, 760.

(52) Granström, M. P., K.; Arias, A. C.; Lux, A.; Andersson, M. R. Friend, R. H.; *Nature* **1998**, *395*, 257.

(53) Dittmer, J. J.; Lazzaroni, R.; Marseglia, E.A.; Friend, R.H. *Sol. Energy Mater. Sol. Cells* **2000**, *61*, 53.

(54) Mende, L. S.; Fechtenkotter, A.; Mullen, K.; Moons, E.; Friend, R.H.; Mackenzie, J.D. *Science* **2001**, *293*, 1119.

(55) Ohkita, H.; Cook, S.; Astuti, Y.; Duffy, W.; Tierney, S.; Zhang, W.; Heeney, M.; McCulloch, I.; Nelson, J.; Bradley, D. D. C.; Durrant, J. R.; *J. Am. Chem. Soc.* **2008**, *130*, 3030-3042.

(56) Veldman, D.; Bastiaansen, J. J. A. M.; Langeveld-Voss, B. M. W.; Sweelssen, J.; Koetse, M. M.; Meskers, S. C. J.; Janssen, R. A. *Thin Solid Films* **2006**, *511-512*, 581.

(57) McCulloch, I.; Bailey, C.; Giles, M.; Heeney, M.; Love, I.; Shkunov, M.; Sparrowe, D.; Tierney, S. *Chem. Mater.* **2005**, *17*, 1381.

(58) Tierney, S.; Heeney, M.; McCulloch, I. *Synth. Met.* **2005**, *148*, 195-198.

(59) Attard, P. *Mol. Phys.* **1996**, *89*, 691.

(60) Kasha, M. R., H. R.; El-Bayoumi, M. A. *Pure Appl. Chem.* **1965**, *11*, 371.

(61) Kazmaier, P. M. H., R. *J. Am. Chem. Soc.* **1994**, *116*, 684.

(62) Wang, W. H., J. J.; Wang, L.-Q.; Li, L.-S.; Shaw, W. J.; Li, A. D. Q. *Nano Lett.* **2003**, *3*, 455.

(63) Iverson, I. K. C., S. M.; Seo, W.; Tam-Chang, S.-W.; Pindzola, B. A. *Langmuir* **2002**, *18*, 3510.

(64) Van der Boom, T.; Hayes, R. T.; Zhao, Y.; Bushard, P. J.; Weiss, E. A.; Wasielewski, M. R. *J. Am. Chem. Soc.* **2002**, *124*, 9582.

(65) Langhals, H. K., J.; Johansson, L. B.-A. *J. Chem. Soc., Faraday Trans.* **1998**, *94*, 2919.

(66) Wang, W. L., L.-S.; Helms, G.; Zhou, H.-H.; Li, A. D. Q. *J. Am.Chem. Soc.* **2003**, *125*, 1120.

(67) Neuteboom, E. E.; Meskers, S. C. J.; Meijer, E. W.; Janssen, R. A. J. *Macromol. Chem. Phys.* **2004**, *205*, 217.

(68) Ahrens, M. J.; Sinks, L. E.; Rybtchinski, B.; Liu, W.; Jones, B. A.; Giaimo, J. M.; Gusev, A. V.; Goshe, A. J.; Tiede, D. M.; Wasielewski, M. R. *J. Am. Chem. Soc.* **2004**, *126*, 8284.

(69) Langhals, H.; Demmig, S.; Huber, H. *Spectrochim. Acta* **1988**, *44A*, 1189.

(70) Gvishi, R.; Reisfeld, R.; Burshtein, Z. Chem. *Phys. Lett.* **1993**, *213*, 338.

(71) Davydov, A. S. Theory of Molecular Excitons, **1971**, Plenum New York.

(72) Harrison, W. J. *J. Phys. Chem.* **1996**, *100*, 2310.

(73) van Duren, J. K. J.; Yang, X.; Loos, J.; Bulle-Lieuwma, C. W. T.; Sieval, A. B.; Hummelen, J. C.; Janssen, R.A.J.; *Adv. Funct. Mater.* **2004**, *14*, 425.

(74) Chasteen, S. V.; Sholin, V.; Carter, S. A.; Rumbles, G. *Solar Energy Materials and Solar Cells* **2008**, *92*, 651.

(75) Quist, P. A. C.; Martens, T.; Manca, J. V.; Savenije, T. J.; Siebbeles, L. D. A. *Solar Energy Materials and Solar Cells* **2006**, *90*, 362.

(76) Yang, X.; van Duren, J. K. J.; Janssen, R. A. J.; Michels, M. A. J.; Loos, J. *Macromolecules* **2004**, *37*, 2151.

(77) Martens, T.; D'Haen, J.; Munters, T.; Beelen, Z.; Goris, L.; Manca, J.; D'Olieslaeger, M.; Vanderzande, D.; De Schepper, L.; Andriessen, R. *Synthetic Metals* **2003**, *138*, 243.

(78) Dittmer, J. J. Marseglia, E. A.; Friend, R.H.; *Adv. Mater.* **2000**, *12*, 1270.

(79) Kanna, B. C., K.; Majumdar, A.; , Nano Lett. 2003, 3, 1729. *Nano Lett.* **2003**, *3*, 1729.

(80) Haugeneder, A.; Neges, M.; Kallinger, C.; Spirkl, W.; Lemmer, U.; Feldmann, J.; Scherf, U.; Harth, E.; Gugel, A.; Mullen, K. *Phys. Rev. B.* **1999**, *59*, 15346.

(81) De Cupere, V. ; Tant, J; Viville, P; Lazzaroni, R; Osikowicz, W; Salaneck, R. W; Geerts, H. Y, *Langmuir* **2006**, *22* 7798.

(82) Liu, S. G.; Sui, G.; Cormier, R. A.; Leblanc, R. M.; Gregg, B. A.; *J. Phys. Chem. B,* **2002**, *106*, 1307.

(83) Yang, W.; Lambeth, D.E.; Tang, L.; Laughlin, D. N.; *J. Appl. Phys.* **1997**, *81*, 4370.

(84) Shim, J. B.; Yoshimoto, N.; Yoshizawa, M.; Yoon, D. H.; *J. Cryst. Res. Technol.* **2001**, *36*, 1209.

(85) Nguyen, L. H.; Hoppe, H.; Erb, T.; Günes, S.; Gobsch, G.; Sariciftci, N. S. *Adv Func Mater* **2007**, *17*, 1071.

(86) Campoy-Quiles, M.; Ferenczi, T.; Agostinelli, T.; Etchegoin, P. G.; Kim, Y.; Anthopoulos, T. D.; Stavrinou, P. N.; Bradley, D. D. C.; Nelson, J. *Nat Mater* **2008**, *7*, 158.

(87) Savenije, T. J., Kroeze, J. E., Yang, X. & Loos, J. *Adv. Funct. Mater.* **2005**, *15*, 1260.

(88) Yamanari, T. T., T.; Hara, K.; Saito, K. J. *Photochem. Photobio. A Chem.* **2006**, *182*, 269.

(89) Erb, T. Z., U.; Gobsch, G.; Raleva, S.; Stuhn, B.; Schilinsky, P.; Waldauf, C.; Brabec, C. J.; *Adv. Funct. Mater.* **2005**, *15*, 1193.

(90) Hoppe, H.; Sariciftci, N. S. *J. Mater. Chem.* **2006**, *16*, 45.

(91) Li, G.; Shrotriya, V.; Yao, Y.; Yang, Y. *J. App. Phys.* **2005**, *98*, 043704.

(92) Mihailetchi, V. D.; Xie, H. X.; de Boer, B.; Koster, L. J. A.; Blom, P. W. M. *Adv. Funct. Mater.* **2006**, *16*, 699.

(93) Reyes-Reyes, M.; Kim, K.; Carroll, D. L. *App. Phys. Lett.* **2005**, *87*, 083506.

(94) Yamanari, T.; Taima, T.; Hara, K.; Saito, K. *J. Photochemistry and Photobiology A: Chem.* **2006**, *182*, 269.

(95) Clarke, T. M.; Ballantyne, A. M.; Nelson, J.; Bradley, D. D. C.; Durrant, J. R. *Adv. Funct. Mater.***2008**, *18*, 4029.

(96) McNeill, C. R.; Westenhoff, S.; Groves, C.; Friend, R. H.; Greenham, N. C. *J. Phys. Chem. C* **2007**, *111*, 19153.

(97) Blom, P. W. M.; Mihailetchi, V. D.; Koster, L. J. A.; Markov, D. E. *Adv.Mater.* **2007**, *19*, 1551.

(98) Yazawa, K.; Inoue, Y.; Yamamoto, T.; Asakawa, N. *Physical Rev. B* **2006**, *74*.

(99) Causin, V.; Marega, C.; Marigo, A.; Valentini, L.; Kenny, J. M. *Macromolecules* **2005**, *38*, 409.

(100) Huang, Y. C.; Liao, Y. C.; Li, S. S.; Wu, M. C.; Chen, C. W.; Su, W. F. *Solar Energy Materials and Solar Cells* **2009**, *93*, 888.

(101) Kim, Y. C., S.; Tuladhar, S. M.; Choulis, S. A.; Nelson, J.; Durrant, J. R.; Bradley, D. D. C.; Giles, M.; McCulloch, I.; Ha, C.-S.; Ree, M.; *Nat. Mater.* **2006**, *5*, 197.

(102) Sirringhaus, H. *Nature* **1999**, *401*, 685.

(103) Osterbacka, R. A., C. P.; Jiang, X. M.; Vardeny, Z. V.; *Science* **2000**, *287,*, 839–842.

(104) Jiang, X. *Adv. Func. Mater* **2002**, *12*, 587.

(105) Zhokhavets, V. E., T.; Gobsch, G.; Al-Ibrahim, M.; Ambacher, O. *Chem. Phys. Lett.* **2006**, *418*, 347.

(106) Kim, H. S.; W-W.; Moon, S-J.; *J. Korean Phys. Soc.* **2006**, *48*, 441.

(107) Kim, Y.

(108) Clarke, T. M.; Ballantyne, A.; Nelson, J.; Bradley, D. D. C.; Durrant, J. R. *Adv. Func. Mater.* **2008**, *18*, 4029.

(109) Mihailetchi, V. D. X., H.; de Boer, B.; Koster, L. J. A.; Blom, P. W. M.; *Adv. Funct. Mater.* **2006**, *16*, 699.

(110) Ma, W. W. Y., C.; Gong, X.; Lee, K.; Heeger, A. J.; *Adv. Func. Mater.* **2005**, *15*, 1617.

(111) Raita, S. K., S.; Bhatnagara, P. K.; Mathura, P. C.; Senguptab, S. K.; Kumarb, J.; *Sol. Energy Mater. Sol. Cells* **2007**, *91*, 757.

(112) Vanlaeke, P. e. a. *Sol. Energy Mater. Sol. Cells* **2006**, *90*, 2150.

(113) Klimov, E., Li, W., Yang, X., Hoffmann, G. G. & Loos, J.. *Macromolecules* **2006**, *39*, 4493.

(114) Shuttle, C. G.; O'Regan, B.; Ballantyne, A. M.; Nelson, J.; Bradley, D. D. C.; de Mello, J.; Durrant, J. R. *App. Phys. Lett.* **2008**, *92*, 3.

(115) Mihailetchi, V. D.; Blom, P. W. M.; Hummelen, J. C.; Rispens, M. T. *J. App. Phys.* **2003**, *94*, 6849.

(116) Akaike, K. K., K.; Yoshida, H.; Tsutsumi, J.; Nishi, T.; Sato, N.; Ouchi, Y.; Seki, K., *J. Appl. Phys.* **2008**, *104*, 023710.

(117) Kooistra, F. B. K., J.; Kastenberg, F.; Popescu, L. M.; Verhees, W. J. H.; Kron, J. M.; Hummelen, J. C.; *Org. Lett.* **2007**, *9*, 551.

(118) Shibano, Y.; Umeyama, T.; Matano, Y.; Tkachenko, N. V.; Lemmetyinen, H.; Imahori, H. *Org. Lett.* **2006**, *8*, 4425.

(119) Goldi, D. M. *J. Phys. Chem.,* **1993**, *97*, 11258.

(120) Giaimo, J. M. G., A. V.; Wasielewski, M. R. *J. Am. Chem. Soc.* **2002**, *124*, 8530.

(121) Korovyanko, O. J.; Österbacka, R.; Jiang, X. M.; Vardeny, Z. V.; Janssen, R. A. J. *Physical Rev. B* **2001**, *64*, 235122.

(122) Österbacka, R.; An, C. P.; Jiang, X. M.; Vardeny, Z. V. *Science* **2000**, *287*, 839.

(123) Westerling, M.; Österbacka, R.; Stubb, H. *Physical Rev. B* **2002**, *66*, 165220.

(124) Kircher, T.; Lohmannsroben, H. G. *Phys. Chem. Chem. Phys.* **1999**, *1*, 3987.

(125) Veldman, D.; Ipek, O.; Meskers, S. C. J.; Sweelssen, J.; Koetse, M. M.; Veenstra, S. C.; Kroon, J. M.; van Bavel, S. S.; Loos, J.; Janssen, R. A. J. *J.Am. Chem. Soc.* **2008**, *130*, 7721.

(126) Clarke, T. M.; Ballantyne, A.; Nelson, J.; Bradley, D. D. C.; Durrant, J. R. *Adv. Funt. Mater* **2008**, *18*, 1.

(127) Clarke, T. M. ; Ballantyne, A.; Jamieson, F.; Brabec, C.; Nelson, J.; Durrant, J. R. *Chem. Commun.* **2009**, 89.

VI. Charge photogeneration in P3HT:PDI_X films and devices.

The observation of clear materials structure / charge photogeneration function relationships depends critically upon the selection of suitable materials series. In this chapter we focus upon role of the acceptor electron affinity in determining the efficiency of charge photogeneration, and specifically dissociation of charge transfer state. In particular we study charge photogeneration in films comprising 1:1 blends of poly(3-hexylthiophene) with a series of different perylene diimide derivatives with varying electron affinities in order to investigate the role of the electron acceptor on ΔG_{CS} and thus charge separation.

6.1 Acceptor energy level control of charge photogeneration in organic donor:acceptor blends.

6.1.1 Introduction

The function of organic donor /acceptor blend devices is based on photoinduced charge separation at the donor /acceptor interface. There is increasing evidence that the efficiency of this charge separation process can be determined by the presence of coulombically bound charge transfer (CT) states at the donor / acceptor interface.[1-11] In this chapter we focus upon the role of interfacial energetics in influencing the separation of these CT states into dissociated charge carriers. In particular, we undertake transient optical studies of films comprising regioregular poly(3-hexylthiophene) (P3HT) blended with a series of perylene diimide (PDI) electron acceptors. For this film series, we observe a close correlation between the PDI electron affinity and the efficiency of charge separation. This correlation is then analysed in the context of studies of charge photogeneration for other organic donor / acceptor blend films, including other polymers, blend compositions and the widely used electron acceptor 1-(3-methoxy carbonyl)propyl-1-phenyl-[6,6]C61 (PCBM).

The efficiency of charge photogeneration in organic donor / acceptor blend films (as discussed in chapter 1) has been reported to depend on a range of factors, including film nanomorphology,[11-18] the presence of macroscopic electric fields,[8,10,19] the dielectric constant of the blend,[11,20,21] charge carrier mobilities,[11,14,22-26] the energy difference driving charge separation (ΔG_{CS})[1,2,26] and the strength of electronic interactions at the donor / acceptor interface.[27] Such studies have typically concluded that the efficiency of dissociation of the CT state into free charge carriers, as illustrated as $\eta_{DISS(CT)}$ in Figure 6.1, is a crucial factor determining the charge photogeneration yield, and thus device photocurrent densities. At present there is little consensus over the relative importance of the different factors potentially influencing charge photogeneration, and in particular over how the efficiency of charge photogeneration can be related to or predicted from specific materials properties.

The observation of clear materials structure / charge photogeneration function relationships depends critically upon the selection of suitable materials series. In particular, the observation of a correlation between charge photogeneration and a specific materials property is only possible if other materials properties potentially influencing charge photogeneration are

relatively invariant for the series studied. As discussed in Chapter 5, previous studies have been conducted on the yield of the charge separation process for a series of polythiophenes blended with PCBM.[1] In this materials series (see Chapter 5, Figure 5.15), a correlation was observed between the energy levels of the polythiophene donors and the yield of dissociated charge carriers, as quantified by the magnitude of photoinduced absorption of these charges (ΔOD measured at a time delay of 1 μs) determined by high sensitivity transient absorption spectroscopy. It was proposed that this correlation was consistent with a model in which efficient charge separation was dependent upon the initially generated charge transfer state possessing sufficient excess thermal energy to overcome its Coulombic attraction, with a large ΔG_{CS} providing the initial formed CT states with enough thermal energy to overcome their electrostatic attraction, resulting in a high value for $\eta_{DISS(CT)}$. This model is analogous to Onsager's Theory of charge separation (see Chapter 1.6), which is based upon the concept that the efficiency of separation of photogenerated geminate charge pairs is dependent upon the relative magnitudes of their thermalisation length versus their coulomb capture radius. It has been previously suggested that a large LUMO-LUMO offset (~ ΔG_{CS}) will produce a greater thermalisation length,[28] which, in turn, would increase the probability of separation of the bound radical pairs into the fully dissociated charge carriers. The dependence of charge separation upon ΔG_{CS} observed by Okhita *et al*. had important implications for materials design, as it suggested, at least for the polythiophene / PCBM series studied, that a relatively large free energy loss (0.9 eV) was required to drive efficient charge separation.

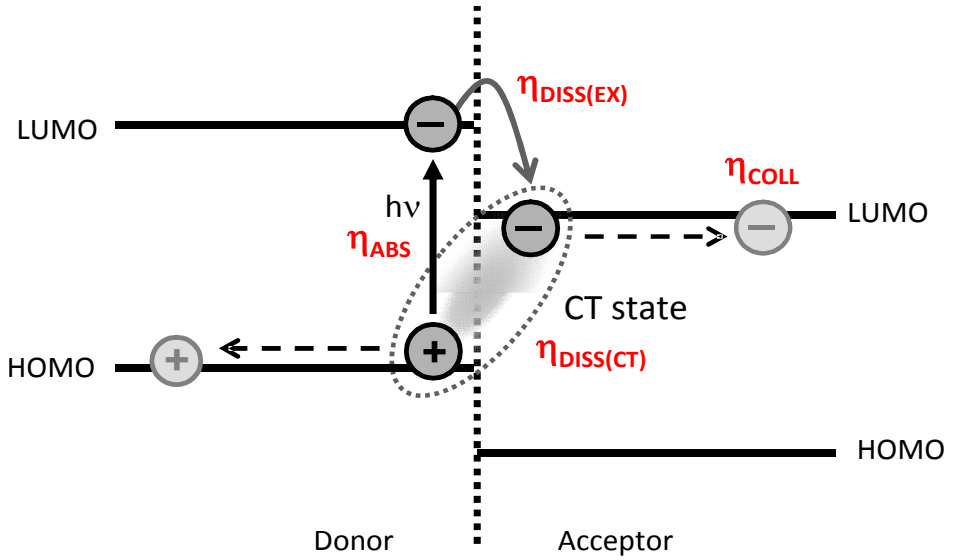
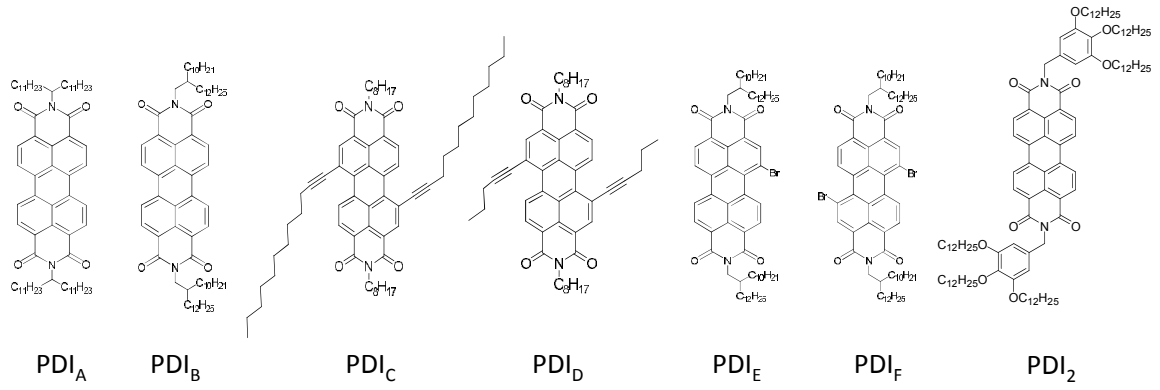


Figure 6.1 Energy level diagram of a donor/acceptor interface showing a simplified viewpoint of photoexcitation of an electron into the donor LUMO (with efficiency η_{ABS}), followed by exciton dissociation via electron transfer into the acceptor LUMO ($\eta_{DISS(EX)}$) and migration of the separated charges away from the interface (η_{COLL}). Also illustrated is the potential for the electron transfer initially to generate a Coulombically bound charge transfer (CT) state that also requires dissociation ($\eta_{DISS(CT)}$) before the free charge carriers can be collected.

Previous work has subsequently extended studies of charge photogeneration to other donor polymers,[3,29] blend compositions[4,30] the effect of thermal annealing[2] and different electron acceptor (Chapter 5). In all three studies, further correlations between ΔG_{CS} and charge photogeneration were observed, as well as additional effects attributed to the influence of film nanomorphology and the charge transfer character of the polymer exciton. In Chapter 5 we reported on comparison of charge photogeneration between polythiophene:PCBM blend films and the same polythiophenes blended with one perylene diimide electron acceptor (PDI_2 in Scheme 6) and observed that for equivalent values of ΔG_{CS}, the PDI_2 acceptor achieved higher charge generation efficiency than PCBM (it should be noted that the presence of noise in the correlation observed can be primarily attributed to the variation of the polymer polaron absorption). The higher charge generation efficiency in PDI_2 was tentatively assigned to result from the higher electron mobility of this PDI relative to PCBM,[26] and indicates that, if charge collection limitations can be addressed, such PDI's may be an attractive alternative to PCBM in organic blend solar cells.

In this chapter we focus upon role of the acceptor electron affinity in determining the efficiency of charge photogeneration, and specifically $\eta_{DISS(CT)}$. In particular we study charge photogeneration in films comprising 1:1 blends of P3HT with a series of different perylene diimide derivatives (PDI_x, Scheme 6) with varying electron affinities in order to investigate the role of the electron acceptor on ΔG_{CS} and thus charge separation.

An advantage of perylene diimide is their characteristic of a well defined and high oscillator strength anion absorption band and that they can have their energetics readily modified by chemical substituents. In this chapter, the results from Chapter 5 are extended to a series of PDI's with electron affinities ranging between 3.5 and 3.64 eV, (The relevant properties of the blends are summarised in Table 6.1) and demonstrate a remarkably close correlation between ΔG_{CS} and charge photogeneration efficiency for this materials series.



Scheme 6. Molecular structure of **PDI_X** derivatives. X = A - F starting from left, and PDI_2 , as employed in Chapter 5, at the far right.

Table 6.1. Properties of the P3HT:PDI_x blends

Blend (P3HT:PDI_x)	[a]EA (eV)	[b]E_S (eV)	[c]ΔG_{rel}^{CS} (eV)	[d]ΔOD	[e]PLQ (%)	ΔOD/PLQ
PDI_A	3.52	2.0	0.72	4.2×10^{-4}	0.86	4.8×10^{-4}
PDI_B	3.55	2.0	0.72	5.1×10^{-4}	0.92	4.7×10^{-4}
PDI_C	3.55	2.0	0.75	3.7×10^{-4}	0.70	5.3×10^{-4}
PDI_D	3.56	2.0	0.76	5.0×10^{-4}	0.90	5.6×10^{-4}
PDI_E	3.59	2.0	0.79	5.1×10^{-4}	0.83	6.2×10^{-4}
PDI_F	3.64	2.0	0.84	3.1×10^{-4}	0.88	4.5×10^{-4}
PDI2	3.5	2.0	0.70	2.9×10^{-4}	0.70	4.1×10^{-4}

a. Estimated electron affinities evaluated by cyclic voltammetry from the peak value. b. Singlet exciton energy of the donor, measured from the intercept of the normalised absorption and emission spectra. c. ΔG_{CS} estimated as E_S - (IP - EA), where IP is the ionisation potential of the polymer evaluated by an ambient ultraviolet photoelectron spectroscopy technique (4.8 eV for P3HT). d. ΔOD evaluated from the amplitude of the transient absorbance power-law decay phase at 1 μs (λ_{probe} = 700 nm), after correction for the ground state absorbance at the excitation wavelength. e. Steady-state PL quenching of the blend film relative to the corresponding pristine polymer film.

6.1.2 Sample Preparation

The general procedures for film fabrication are described in chapter 2.The perylene diimides were kindly supplied by Georgia Tech and were prepared essentially as described in the literature.[31,32] Rieke P3HT was employed as electron donor. Chloroform was used as the solvent in PDI films. All materials were used as received. Solutions were prepared as follows. To the P3HT solution (~20 mg mL^{-1} in chloroform), solutions of PDIx were added at a concentration of ~20 mg mL^{-1}, such that the total concentration was fixed at ~ 20 mg mL^{-1} Pristine P3HT film was spun from solution onto glass substrates at a spin rate of 3000 rpm for 90 s under N_2 atmosphere. The weight concentration of PDIx in the final P3HT blend solutions was fixed at 50 wt %. Solid blend films of P3HT / PDI_X were prepared by spin-coating blend solutions at 500 rpm and 1100 rpm for 60s respectively.

6.1.3 Results and discussion

The relative electron affinities of the PDI_X series of electron acceptors were determined by cyclic voltammetry. In all cases, reversible reduction waves were observed. The resultant effective electron affinities of the acceptors are detailed in Table 6.1, and indicate electron affinity varies by 140 meV between these electron acceptors. The PDI's were all found to blend readily with P3HT, resulting in high optical quality films.

Typical absorption spectra of the pristine materials and blend films are presented in Figure 6.2. It is apparent that the PDI spectra overlap significantly with that of P3HT, implying that photoexcitation of the blends will produce both P3HT and PDI excitons. Photoluminescence (PL) data were collected to evaluate the efficiency of exciton quenching for all blend films. Typical PL data observed for the P3HT:PDI_X blends, represented by PDI_D are shown in Figure 6.2, as well as the corresponding pristine films. Consideration of such absorption spectra and emission spectra indicated that for all P3HT:PDI_X blends, the lowest singlet exciton is that of P3HT. Consistent with this observation, for all blend films (with the exception of PDI_2, see Chapter 5) the PDI emission was very strongly quenched (>99%) relative to pristine PDI films – assigned to rapid energy transfer from PDI to P3HT. As such, charge photogeneration most likely occurs via LUMO-LUMO (rather than HOMO-HOMO) electron transfer from the P3HT singlet excitons, as we discuss further below. Weak residual P3HT PL was observed in the blend films, corresponding to 70 - 92% PL quenching compared to the corresponding pristine P3HT films (determined by integration over the emission band), as detailed in Table 6.1.

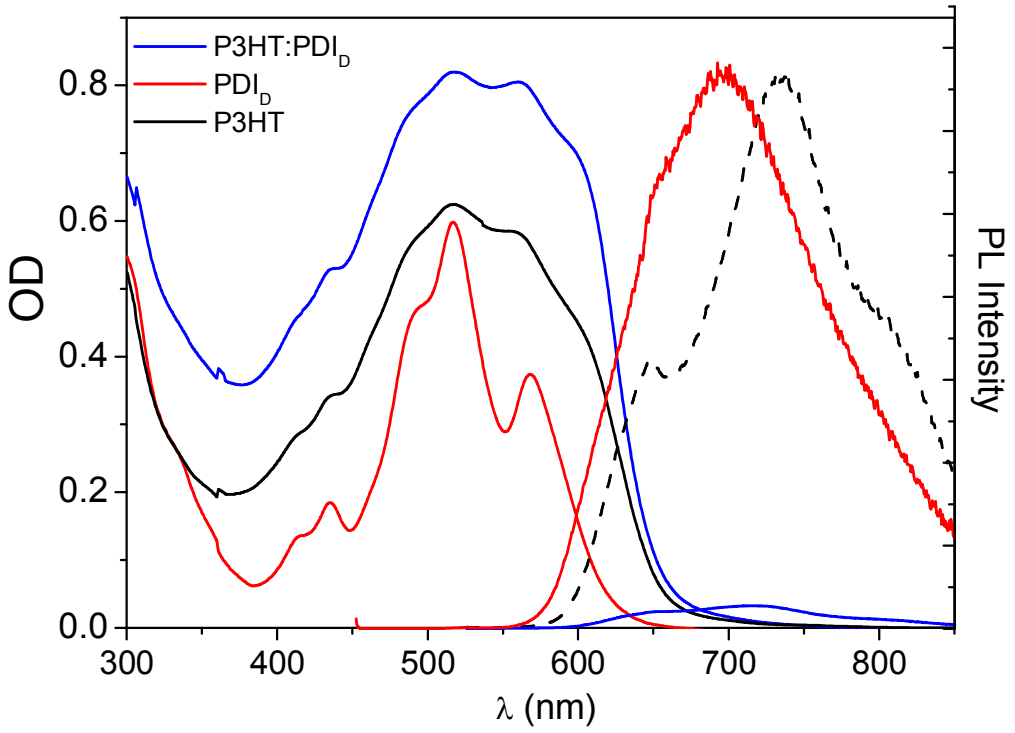


Figure 6.2 Absorption and photoluminescence spectra measured for the following pristine and blend films: PDI_D, P3HT and P3HT:PDI_D. The PL spectra were measured using 500 nm excitation.

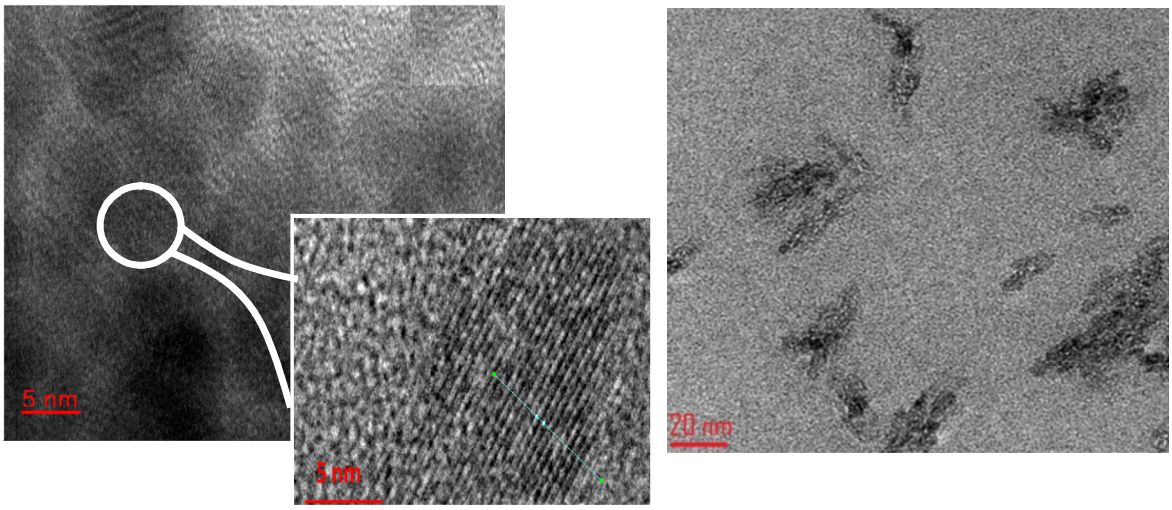


Figure 6.3 TEM micrographs of P3HT:PDI_D (left) film (expanded region, centre: crystallisation of PDI_D lattice) and P3HT:PDI_2 (right).

We turn to morphology studies of these blends. Both atomic force microscopy (AFM) (Figure 6.3) and transmission electronmicroscopy (TEM) (Figure 6.3) data indicate that, P3HT:PDI_D blends show small PDI features on the order of tens of nanometers, which are well dispersed within the P3HT phase. Similar data were obtained for other P3HT:PDI_x films with the exception of films employing PDI_2, consistent with our observation of efficient PDI PL quenching and reasonably efficient P3HT PL quenching. The TEM data of the P3HT:PDI_D films show clear evidence for the crystallinity of the PDI domains, consistent with the absorption spectra, and the well established tendency of PDI's to undergo π stacking, with a lattice spacing of 0.6 nm, typical of that observed for PDI crystallites.[33] The morphology of the PDI_D blend is consistent with those observed by Friend's group[34] where the polymer:PDI blends studied show small features of the order of tens of nanometre and some evidence of perylene aggregation in the case of the PDI/P3HT blend.

Morphology studies of P3HT:PDI_2 blend films show the formation of large PDI_2 aggregates, with phase segregation on the scale of few hundreds of nanometers and roughness sometimes rising 500 - 600 nm out of the plane of the film (Figure 6.3). The greater phase segregation observed for P3HT:PDI_2 is consistent with the less efficient PDI PL quenching we observe in these blend films (70% relative to pristine PDI_2 films). The formation of these larger domains may be attributed to the presence of the tri-alkoxy phenyl groups which also stack in addition to the stacking from the PDI cores.

As discussed earlier on, PL quenching is only an indicator of the efficiency of exciton quenching at the donor / acceptor interface, and is not a reliable indicator of the yield of fully dissociated charges. In particular it is insensitive to the potential for geminate recombination of charge transfer states (initially generated polaron pairs) prior to their dissociation into separated charges. As such PL quenching can only provide an indication of an upper limit to the charge photogeneration yield. Transient absorption spectroscopy (TAS) was therefore employed to monitor the yield of long-lived, dissociated charges observed on the microsecond timescale in each blend film. Consistent with previous reports, the transient spectrum of all P3HT:PDI_X film exhibited a well defined absorption maximum at approximately 700 nm indicative of the formation of PDI anions[35,36] as well as a weaker, broad absorption between 900 and 1000 nm assigned to P3HT cations[2,37-40] (shown for the P3HT:PDI_D blend film in the inset of Figure 6.4). The transient absorption data exhibited

micro- to millisecond power law, oxygen-independent decay dynamics, as illustrated in Figure 3. Control data on pristine P3HT and PDI films gave negligible transient signals on the timescales studied. As it has been discussed previously,[26] such dynamics allow us to assign these absorption transients to the bimolecular recombination of dissociated polarons.

Power law absorption transients similar to those shown in Figure 6.4 were observed for all P3HT:PDI_X films. Whilst similar dynamics were observed for all films, the amplitude of these absorption transients varied significantly. For convenience, we quantify these different signal intensities by the magnitude of the PDI anion absorption at 700 nm at a time delay of 1 μs (corresponding to the time delay used in our previous studies of polymer: PCBM blend films,[1] and approximating to the typical timescale for charge collection in such donor / acceptor blend devices). These ΔOD signal intensities are summarized in Table 6.1, normalized for variations (< ± 35%) in the density of absorbed photons due to variations in film optical density at the excitation wavelength). It is apparent that these changes in ΔOD signal intensities, and therefore yield of dissociated polarons, are much larger than (and do not correlate with) the variation in PL quenching observed between the blend films. As such, these variations in polaron yields cannot be assigned primarily to changes in the efficiency exciton dissociation $\eta_{DISS(EXC)}$. Rather, as it has been concluded previously for other materials systems,[1-4] the observation variation in polaron yield is more reasonably primarily assigned to variations in the geminate recombination losses on the pico-nanosecond timescales and thus to the variations in the efficiency of dissociation of interfacial CT states into free charges $\eta_{DISS(CT)}$.

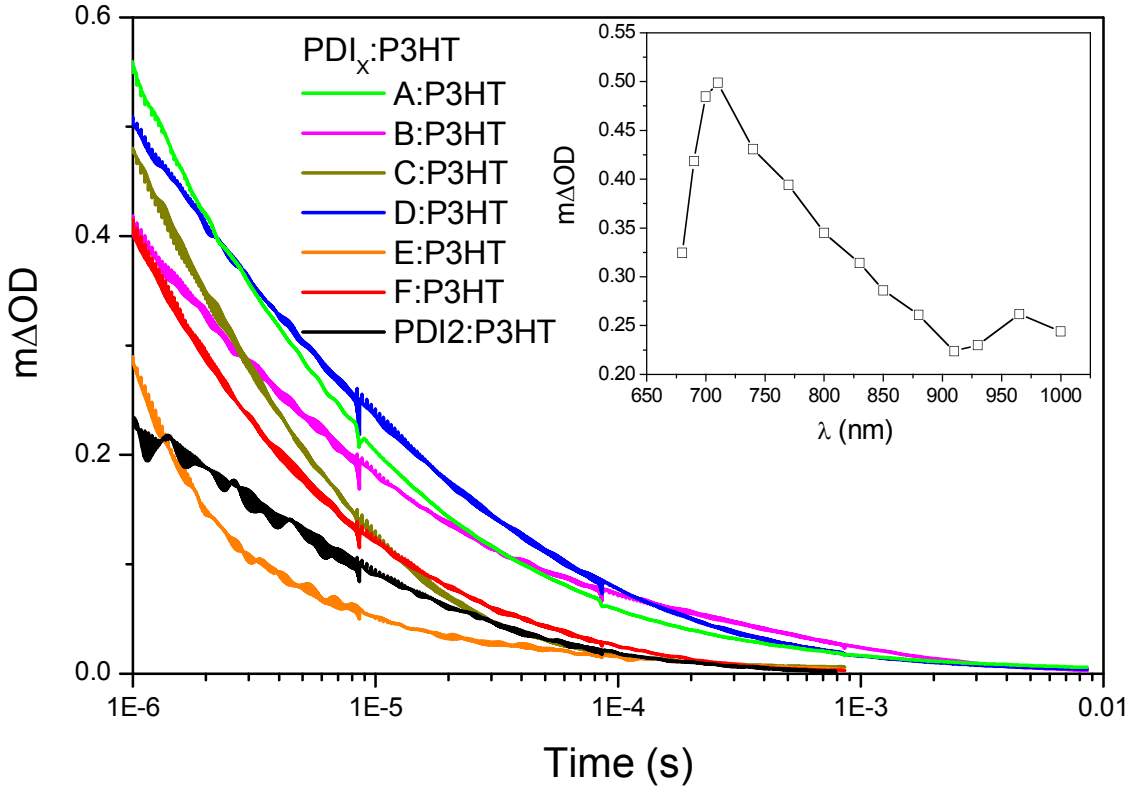


Figure 6.4 Typical transient absorption data for P3HT:PDI$_X$ (1:1) blend film in a N_2 environment, monitored at 700 nm, with λ_{exc} = 520 nm at 50 μJcm^{-2}. Inset: spectrum of P3HT:PDI$_D$ at 1 μs under N_2 using λ_{exc} = 520 nm at 50 μJcm^{-2}.

We turn now to consideration of the extent to which the observed variation in polaron yield can be correlated with variations in interfacial energetics. In this regard, we normalized the ΔOD data to take account of the small variations in PL quenching, and thus $\eta_{DISS(EXC)}$, observed between the blend films, as detailed in Table 6.1 as *ΔOD/PLQ*. As such, *ΔOD/PLQ* should be a direct indicator of the efficiency of dissociation of initially generated interfacial polarons into dissociated charges, $\eta_{DISS(CT)}$. Figure 4 shows a plot of the correlation between this assay of charge transfer state dissociation and the energetic driving force for charge separation $\Delta G_{CS} = E_S - (IP_D - EA_A)$. Calculations were done using either the P3HT or PDI$_x$ singlet energies for E_S. Employing the PDI$_x$ singlet energies, no correlation was observed between ΔG_{CS} and the *ΔOD/PLQ* signal magnitude, indicating that charge separation does not proceed from PDI singlet excitons, consistent with our discussion above of absorption and PL emission spectra. However, employing the P3HT S_1 singlet exciton energy for Es, a

remarkably good correlation is observed between ΔG_{CS} and $\Delta OD/PLQ$. With the exception of PDI_F (discussed below), the polaron yield, and thus $\eta_{DISS(CT)}$, is observed to show a linear dependent upon ΔG_{CS}, increasing by ~ 40 % for a 0.1 eV increase in driving force. The variation in ΔG_{CS} between the different blend films results solely from variations the PDI electron affinities, as both E_S and IP_D correspond to the P3HT, which is invariant for this film series. We thus conclude that for this materials series there is an excellent correlation between the LUMO energy level of the acceptor and the yield of dissociated polarons.

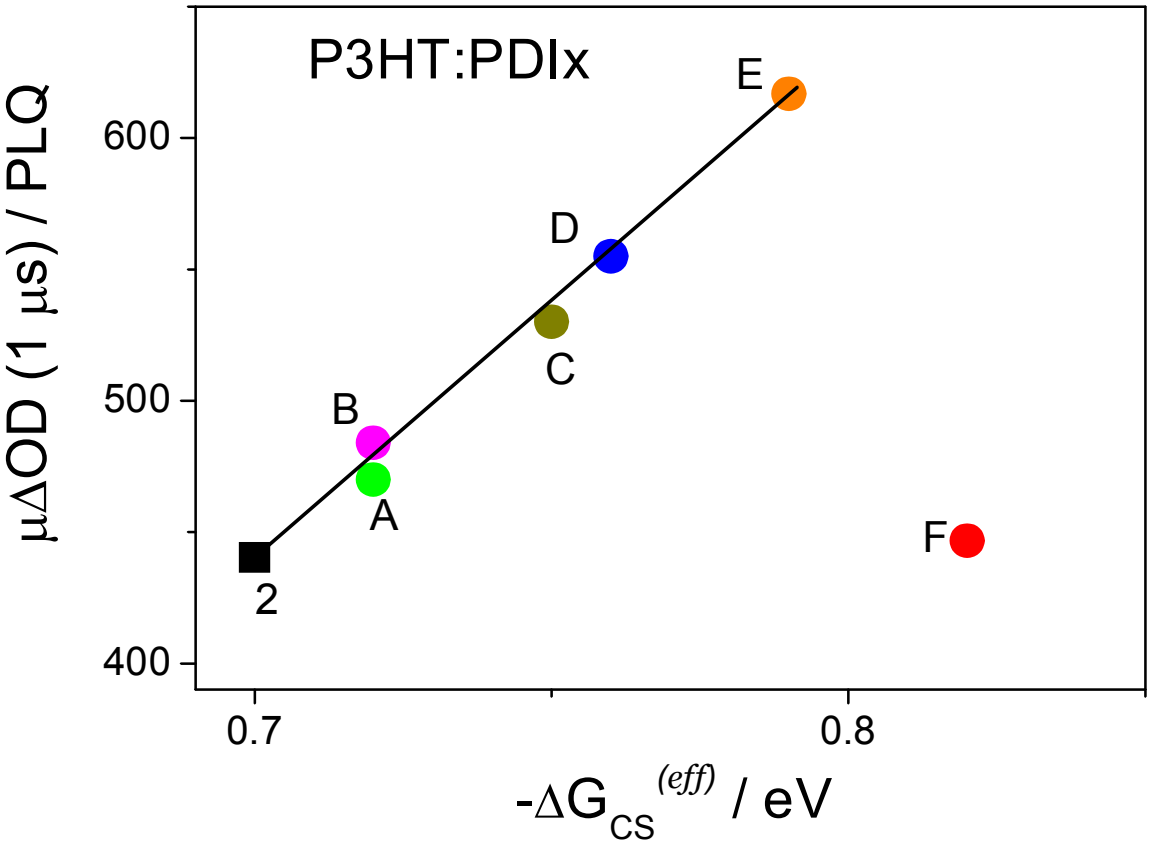


Figure 6.5 Transient absorbance signal measured at 1 μs of various P3HT:PDI_x (1:1) blend films with P3HT plotted against $-\Delta G_{CS}$, estimated as $E_s - (IP_D - EA_A)$. The transient signal has been corrected for variation in the optical absorbance at the excitation wavelength (500 nm) and the PL quenching. λ_{prb} = 700 nm at 50 μJcm^{-2}.

It is striking that, compared to our previous studies of the correlation between polaron yield and ΔG_{CS} as a function of donor polymer (Chapter 5), the correlation observed in Figure 6.5 shows remarkably little deviation from a direct linear dependence. The lack of noise in this correlation can be primarily attributed to the use of the well defined, and relatively invariant, PDI anion absorption band (in contrast to our previous studies based upon polymer polaron absorption) and to our correction for small variations in PL quenching (and thus $\eta_{DISS(EXC)}$) between blend films studied. In this regard, we extended the study of polythiophene : PDI_2 blend films in chapter 5 to polythiophene : PDI_D blend films, monitoring the ΔOD signal at the PDI anion absorption maximum, and normalizing for variations in PL quenching as above, as shown in Figure 6.6. Again a correlation between ΔG_{CS} and $\Delta OD/PLQ$ is observed, although in this case, the correlation is less well defined than that observed in Figure 6.5 presumably due to other factors varying between the polymers to influence charge dissociation in addition to ΔG_{CS}.

It is apparent that the P3HT:PDI_F blend film shows an anomalously low polaron yield considering its relatively large value for ΔG_{CS} In this regard, it is interesting to note that previous studies of this PDI have reported that steric hindrance due to the presence of the two bromine substituents prevents strong crystal stacking of this PDI, resulting in an anomalously low electron mobility relative to the other PDI's studied herein.[41] As proposed in chapter 5 that the relatively high polaron yields observed for polythiophene : PDI_2 blend films relative to polythiophene : PCBM blend films could result from the higher electron mobility of PDI_2 relative to PCBM.[30] As such, the lower polaron yield observed for PDI_F provides further support from this proposition, with its lower charge dissociation efficiency being consistent with its lower electron mobility.

Figure 1.13 summarizes a kinetic model for charge photogeneration in donor/acceptor systems, proceeding via the formation of an interfacial bound polaron pair or 'charge transfer' state, as has been proposed previously.[1,2,42] The model is based upon our experimental observation that whilst polymer excitons are efficiently quenched at the donor / acceptor for all the blend films considered herein, the final yield of dissociated charges is dependent upon the exciton energy E_S relative to the energy of the dissociated polaron pairs (as defined by $IP_D - EA_A$). Following this model, the initial charge separation of the exciton

results in the formation of a vibrationally excited ('hot') CT state, analogous to the 'crossing point' in Marcus electron transfer theory. The coulombic attraction of these CT states results in a significant potential energy barrier to their dissociation, as discussed in detail elsewhere in terms of a charge transfer state binding energy.[43] The model is based upon the concept that the excess thermal energy of the initially formed hot CT can enable the dissociation of the CT state into free charges. As such, the magnitude of the excess vibrational energy (which can be expected to be proportional to ΔG_{CS}) can be expected to correlate with the efficiency of CT dissociation $\boldsymbol{\eta}_{DISS(CT)}$, consistent with the correlation we observe experimentally in Figure 6.5. Within this model, geminate recombination of CT states competes is the primary loss pathway limiting charge photogeneration.

The model detailed in Figure 1.13 is analogous to Onsager's theory of charge photogeneration applied to a donor / acceptor interface (see Chapter 1.4). Onsager theory can be translated directly to charge photogeneration at the donor/acceptor interfaces studied herein. In general, the exciton will undergo vibrational relaxation prior to charge separation at the donor / acceptor interface (except for direct photoexcitation at the interface). However, due to the offset of donor and acceptor LUMO levels, the electron injected in the acceptor will initially be thermally hot. It is therefore plausible that the same consideration of the electron's thermalisation length versus coulomb capture radius r_c can be applied to determine the yield of charge photogeneration at donor/acceptor interfaces. We note that in this context, calculation of r_c should take account of the polaronic nature of the charge carriers, and the energetic disorder present in such materials. As such, a reasonable estimate for r_c is likely to be of the order of 5 nm, as discussed in detail elsewhere.[43]

In this context, the correlation between ΔG_{CS} and polaron photogeneration efficiency, and thus $\eta_{DISS(CT)}$, we observe herein can be understood in terms of the influence of ΔG_{CS} upon the excess thermal energy of the injected electron and thus the electron thermalisation length a. This concept of the energy level offset at the interface influencing the thermalisation length has been proposed previously[44,28] (see Chapter 1.6). Furthermore, recent ultrafast transient vibrational spectroscopic data reported by Pensack and Asbury[44] on a polymer/PCBM blend system indicate barrier-less free charge carrier formation, suggesting

that it is the excess vibrational energy in the CT that enables it to overcome its Coulombic interaction. This is consistent with the energetic model proposed in Figure 1.13.

We turn now to comparison of the results reported in this chapter for the P3HT:PDIx series against those observed previously for polymer:PCBM blend films. Figure 6.6 presents an overview of these data, plotting the charge generation yield, as measured by transient absorption spectroscopy, versus ΔG_{CS} for all the materials series that have been studied in our group to date. These include not only studies of the 1:1 polythiophene : PDI films as detailed herein[26] (see Chapter 5), but also studies of 19:1[1] and 1:1[2] polythiophene: PCBM blend films and PCPDTBT : $PC_{70}BM$ blend films as a function of dithiol.[3] As detailed above, the series employing PDI acceptors have been corrected for differences in PL quenching; this correction was not necessary for the PCBM data series due to the consistently higher PL quenching observed for these series. The data in this figure have also been normalised to account for the higher PDI anion extinction coefficient compared to that of the polymer polaron absorption monitored in our previous studies. Two points are most obviously apparent from this figure. First of all, it is apparent for all the materials series studied, there are clear correlations between ΔG_{CS} and ΔOD. Secondly it is apparent that quantitative strength of these correlations and the absolute magnitudes of ΔOD for a given ΔG_{CS} vary substantially between materials series. The first observation, of the correlation between ΔG_{CS} and ΔOD within each data series, confirms the generality of the hot CT state model we propose above, as summarized in Figure 1.13. The second observation, of the differences between materials series, requires further discussion.

In general, the Onsager based charge separation model detailed in Figure 1.13 suggests that charge photogeneration should be dependent upon range of parameters. The electron thermalisation length a can be expected to depend not only the amount of excess thermal energy (and therefore ΔG_{CS}) but also the electron mobility and thermalisation timescale.[45.] The coulomb capture radius can be expected to depend upon the local dielectric constant. Furthermore the dissociation yield is likely to be dependent upon the molecular structure of the interface, and in particular the spatial separation of the initially generated CT state, the physical size of the donor and acceptor domains (particular if these are less than r_c), the potential presence of macroscopic electric fields and the rate constant for geminate

recombination. In this context, it is remarkable that it is possible to observe such clear correlations between polaron yield and ΔG_{CS} within each materials series shown in Figure 6.6. This observation implies that within each such materials series, the key parameter changing within the series is ΔG_{CS}, and that all the other parameters likely to influence $\eta_{DISS(CT)}$ are relatively invariant within the data spread ('noise') apparent within each series. In this regard it is interesting to note that previous studies have shown that variations in charge photogeneration following annealing of P3HT:PCBM blend films and the use of a dithiol co-solvent in PCPDTBT: $PC_{70}BM$ blend films both correlate with changes in ΔG_{CS}. In both cases, the increase in charge (and current) photogeneration was assigned to a reduction in IP resulting from increased polymer crystallisation. Two recent studies have also reported reductions in P3HT IP upon thermal annealing,[10,48] consistent with these observations. As such it appears clear that ΔG_{CS} is a key parameter determining charge photogeneration yield in such blend films.

Turning now to consideration of the differences between materials series plotted in Figure 6.6, these can be assigned to the other factors influencing $\eta_{DISS(CT)}$ in addition to ΔG_{CS}. We have previously proposed that the significant increase in the yield of dissociated charges in polymer : PDI blend films relative to polymer : PCBM blends with equivalent ΔG_{CS} may result from the higher electron mobility of the PDI's employed,[26] which can be expected to increase the electron thermalisation length.[46] This highlights the potential importance of the charge carrier mobility not only in transport but also to facilitate charge photogeneration. Interestingly, it was previously noted that the charge photogeneration yield did not show a significant correlation with polymer hole mobility.[1] This distinction most probably derives from charge separation in these blends primarily involving LUMO to LUMO electron transfer; with acceptor electron mobility thus being critical parameter. Turning to comparisons of the other materials series, the high charge photogeneration yields for the charge transfer polymer PCPDTBT is indicative of the charge transfer character of this polymer facilitating dissociation of the CT state, either by the effective introduction of a redox cascade at the donor / acceptor interface or modulation of the local dielectric constant.[3] The higher charge photogeneration yields observed for 1:1 compared to 19:1 polythiophene:PCBM blends is consistent with the larger PCBM domains in the 1:1 blends facilitating charge dissociation.[2] Clearly these comparisons are limited in their scope, and

provide only partial insights into the range of parameters which influence charge photogeneration in polymer : small molecule blend films. Nevertheless they do provide some insights into the key materials properties influencing charge photogeneration in such blend films.

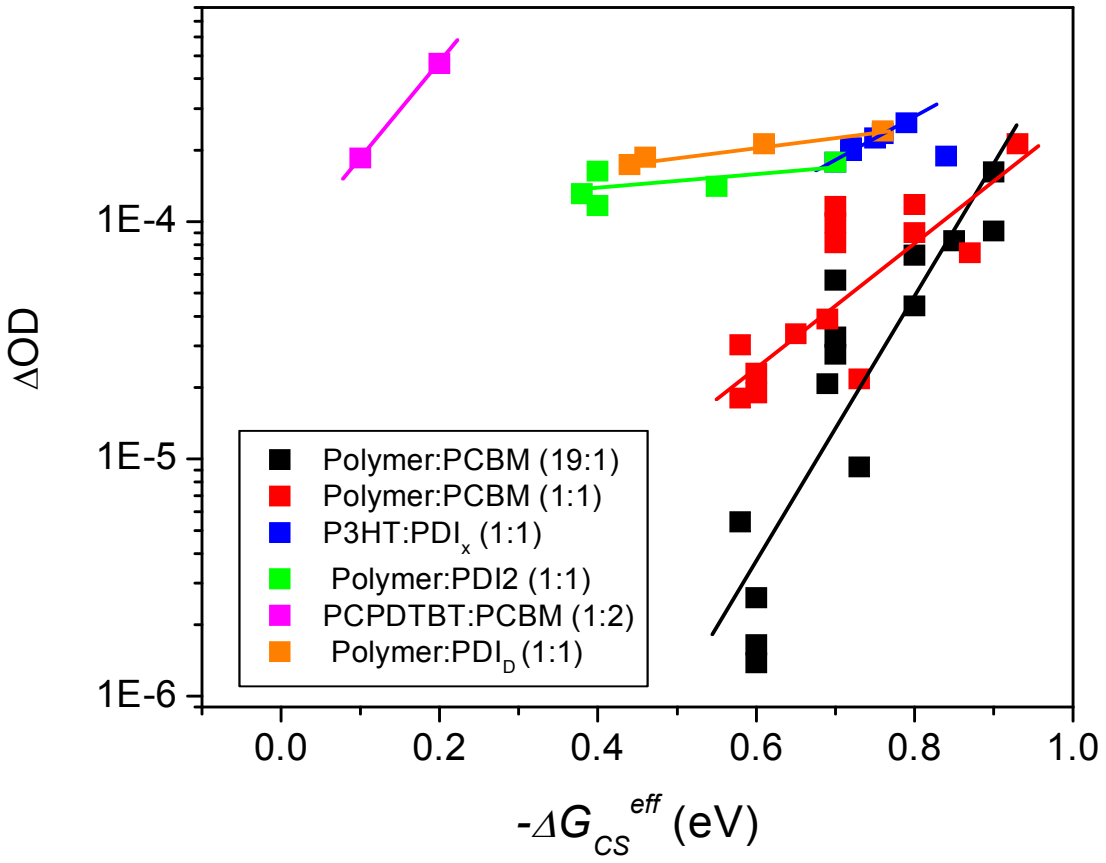


Figure 6.6 Transient absorbance signal measured at 1 μs of various polythiophene : PCBM and polythiophene : PDI_X blend films plotted against $-\Delta G_{CS}$, using an excitation wavelength of 500 nm, a probe wavelengths 700 nm, 850 nm and 970 nm. However, the ΔOD yields have all been normalised for 970 nm probe wavelength. The PDIX data have been all corrected for PL quenching.

These results demonstrate that in comparisons of charge (or photocurrent) photogeneration between materials, several factors may potentially influence charge photogeneration in addition to ΔG_{CS}. In this regard, it is interesting to note that efficient photocurrent generation, and higher open circuit voltages, has been reported for polymer / fullerene blend solar cells employing fullerenes with lower electron affinities than PCBM. The lower electron affinities results in a lower ΔG_{CS} and thus might be expected to result in lower photocurrent generation.

However, the observation of efficient photocurrent generation suggests that an additional factor is enhancing photocurrent generation – such as for example interface molecular structure – although at present the details of what this factor is are unclear.

The study herein has focused upon the charge photogeneration process in blend films, rather than the overall process of photocurrent generation. In particular, it does not include consideration of the charge collection efficiency η_{COLL}. Previously it has been shown for both P3HT:PCBM and PCPDTBT:$PC_{70}BM$ blend films that there is a good correlation between our transient absorption assay of charge photogeneration and photocurrent density, suggesting that charge photogeneration rather than collection is the key determinant of photocurrent density in these devices.[2,47,48] However, for polymer / PDI based devices, it has previously been reported that charge collection is the dominant factor limiting device performance, attributed to unfavourable blend nanomorphologies preventing efficient polaron collection at the device electrodes.[49-53] It is interesting to note that P3HT:PDI_D based devices exhibited substantially higher photocurrent densities than P3HT:PDI2 based devices (see section 6.4), consistent with the differences in film nanomorphologies shown in Figure 6.3. Nevertheless, the photovoltaic device performance for devices based upon P3HT:PDI_X blends films exhibited only modest device performance, consistent with previous studies of polymer / PDI based devices. In this regard, we note that the high charge photogeneration efficiencies we observe for polymer / PDI blend films, coupled with the strong light absorption and excellent stability of PDI's, suggest that if the collection limitations imposed by unfavourable nanomorphology can be addressed, then PDI's may indeed be attractive alternatives to PCBM in organic bulk heterojunction solar cells.

6.1.4 Conclusions

Comparison of charge photogeneration in films comprising of blends of P3HT and a series of different PDI derivatives with varying electron affinities reveals a strong correlation between ΔG_{CS} and charge generation. This correlation results from Onsager model: the exciton will undergo vibrational relaxation prior to charge separation at the donor / acceptor interface. However, due to the offset of donor and acceptor LUMO levels, the electron injected in the acceptor will initially be thermally hot. In this context, the correlation between ΔG_{CS} and polaron photogeneration efficiency, and thus $\eta_{DISS(CT)}$, we observe can be understood in terms

of the influence of ΔG_{CS} upon the excess thermal energy of the injected electron and thus the electron thermalisation length a.

Furthermore, it is clear from an examination of the ΔG_{CS} plot that each polaron yield dependence only exists within each series. The correlations observed between ΔG_{CS} and charge photogeneration yield within each polymer:acceptor series are suggestive of the generality of this relationship, although further work is required. Furthermore, the energetic model proposed to account for these results is consistent with the well-established Onsager and Marcus theories. It can therefore be concluded that the yield of photogenerated charges in polymer/acceptor systems is likely to be dependent upon the excess vibrational energy of the bound radical pair, such that the key kinetic competition in the photogeneration process is between vibrational relaxation and dissociation of this species.

6.2 Organic photovoltaic devices

6.2.1 Introduction

Many materials have been known and studied for decades. Of these, only a small fraction has been used with success in OPV devices because of various electrical, optical and stability requirements. As discussed in Chapter 1, the function of organic solar cells is based upon charge photogeneration at donor/acceptor heterojunctions, which is greatly influenced by crystallinity, packing structures, morphology and frontier energy levels. In this section we focus on device performance based on perylene diimide blend films. In particular, we focus and investigate correlation between our photophysics results from Chapter 5 and 6 (an assay of charge photogeneration yield determined in blend films) and nanomorphology as probed by AFM and TEM with device performance.

The requirements for the most basic architecture of polymer/small molecule OPV devices include a transparent substrate and electrode, a light-absorbing organic active layer, and a back electrode (see Chapter 2).

The most frequently employed OPV substrate is glass for a variety of reasons. It is cheap and it provides a good barrier against oxygen and water diffusion into the device. On top of the glass substrate a transparent electrode, most commonly tin-doped indium oxide (ITO) is deposited. ITO is readily available commercially as a film on glass. The conductivity of ITO on glass lies between ~ 3000–6000 S/cm.[54] The ITO work function is in the range of 3.7–5.1 eV, frequently taken as ~4.7 eV, with variation in this value dependent on the surface pre-treatment method used for cleaning.[55-57]

Various metals are employed for the back electrode. The energetics of the metal is an important consideration for several reasons. The built-in electric field which facilitates the separation of photoinduced charges at the donor/acceptor interface is dependent upon the work function differential of the device electrodes. If the work function, φ_f, of ITO is taken as ~4.7 eV, a metal with a raised work function (closer to vacuum), would generate a field that aids hole collection at the anode and electron collection at the metal cathode. Table 4.2 gives the work function for some commonly used metals. Relative to aluminium (Al), silver (Ag)

with a deeper work function and calcium (Ca) with a raised work function, in theory creates a smaller and larger electric field, respectively. Utilizing a metal with a φ_f deeper than that of ITO, reverses the field entirely, supporting charge flow in the opposite direction. The strategy of using a gold electrode in devices with inverse architecture is therefore frequently employed.

Table 6.2: Workfunction of some common back electrodes utilised in organic PVs.

Metal	Workfunction/ eV
Aluminium	4.2
Calcium	2.9
Silver	4.3-4.7
Gold	5.1

A second consideration in the choice of back electrode material is the alignment of the metal work function with respect to the active layer energy levels. In order to form a desired Ohmic contact and effectively collect electrons at the cathode, the metal φ_f must be approximately equal to the acceptor LUMO energy. If the φ_f is significantly farther from vacuum, the built-in electric field is less than ideal.

A diagram showing the constituent energy levels (the values of which are found as varying in the literature) of a typical P3HT:PDI device is given in Figure 6.7.

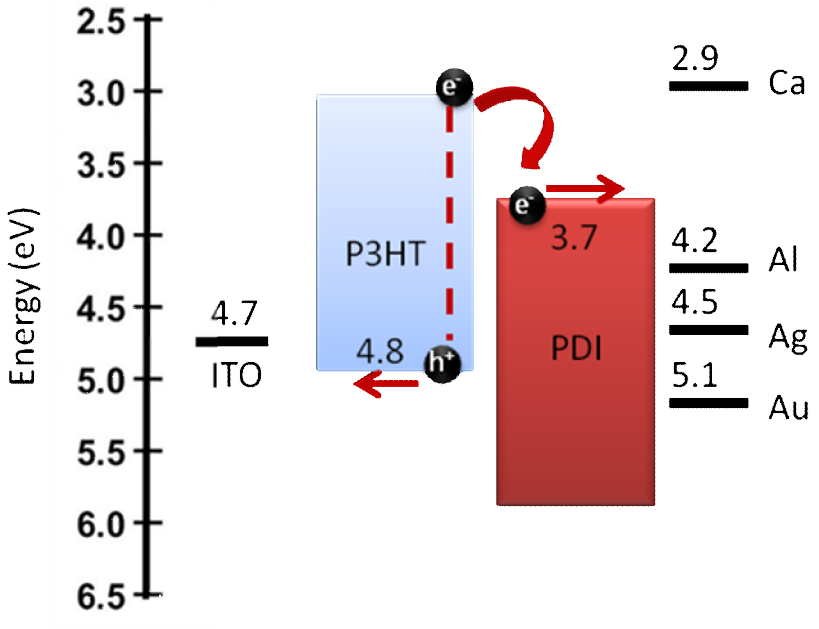


Figure 6.7 Energy level diagram detailing the relevant energy levels of P3HT and PCBM along with back electrodes: calcium (Ca), aluminium (Al), silver (Ag) and gold (Au).

Extensive attempts are underway to achieve advances in OPV device performance, including both the development of new materials[58,59] and the optimization of device processing, fabrication conditions [60-62] and the nature of the constituent materials, such as the polymer regioregularity[63] and molecular weight.[64] As such, systematic device optimization is critically dependent upon a clear understanding of the factors determining device performance. For the P3HT:PCBM blend system, thermal annealing significantly improves the efficiencies of the solar cells by up to an order of magnitude,[65] mostly through increasing the short-circuit current (J_{SC}) and the fill factor (FF).[60,66] The higher device characteristics as a result of the enhanced morphology upon thermal annealing (see Chapter 5) have most often been either assigned to an increase in charge carrier mobility[62,67-70] or a reduction in geminate recombination losses, thereby increasing the efficiency of CT state dissociation into the free charge carriers.[71]

6.2.2 Material and methods

Devices were fabricated as described in Chapter 2.

Active layers were prepared and spun as detailed in sections 5.2 and 6.1.2. The composition ratio and the back electrode for each device are stated in Table 6.3.

6.2.3 Results and discussion

Initial devices fabricated from P3HT:PDI_2 lend films resulted in poor devices. In order to investigate the effect of energetics, photophysical and morphological properties of polythiophene: PDI blend films on their photovoltaic performances, solar cells based on blends given in Table 6.3 spun from chloroform solution were fabricated.

Table 6.3: Active layer, component ratio, back electrode and annealing treatment used for each device

Blend	Ratio	Back electrode	Annealing temperature
P3HT:PDI_2	1:1, 1:2, 1:4, 2:1	Al, Ca, Au	Non-annealed
P3HT:PDI_2	1:1, 1:2, 1:4	Al	140 ^oC
P3HS:PDI_2	1:1	Al	Non-annealed
PBTTT:PDI_2	1:1	Al	Non-annealed and annealed at140 ^oC
P3HT:PDI_X	1:1, 1:2, 1:3,	Al	Non-annealed and annealed at 140 ^oC
P3HT:PDI_D	1:1, 1:2, 1:3, 1:4, 1:5	Al, Ca + Al	75, 140, 175, 185 ^oC
SP220:PDI_D	1:1	Al	Non-annealed and annealed at 140 ^oC
P($T_{10}T_{10}TT_0$):PDI_D	1:1	Al	Non-annealed and annealed at 140 ^oC

Figure 6.8a shows a J-V curve characteristics of ITO/PEDOT:PSS/P3HT:PDI_2/Al (1:1) device, typical for all PDI_2 blends, under white light illumination with an intensity of 100 $mWcm^{-2}$. The first noticeable feature is the shape of the J-V curve, which shows a very small photocurrent, with somewhat symmetrical charge migration. This behaviour suggests poor percolation pathways and collection at the electrodes. This characteristic appears to be present in all PDI_2 devices fabricated, regardless of the electrodes evaporated, thermal annealing, or any other varying parameters. The devices appear to be more resistive (series resistance as recognised by the low rectification).

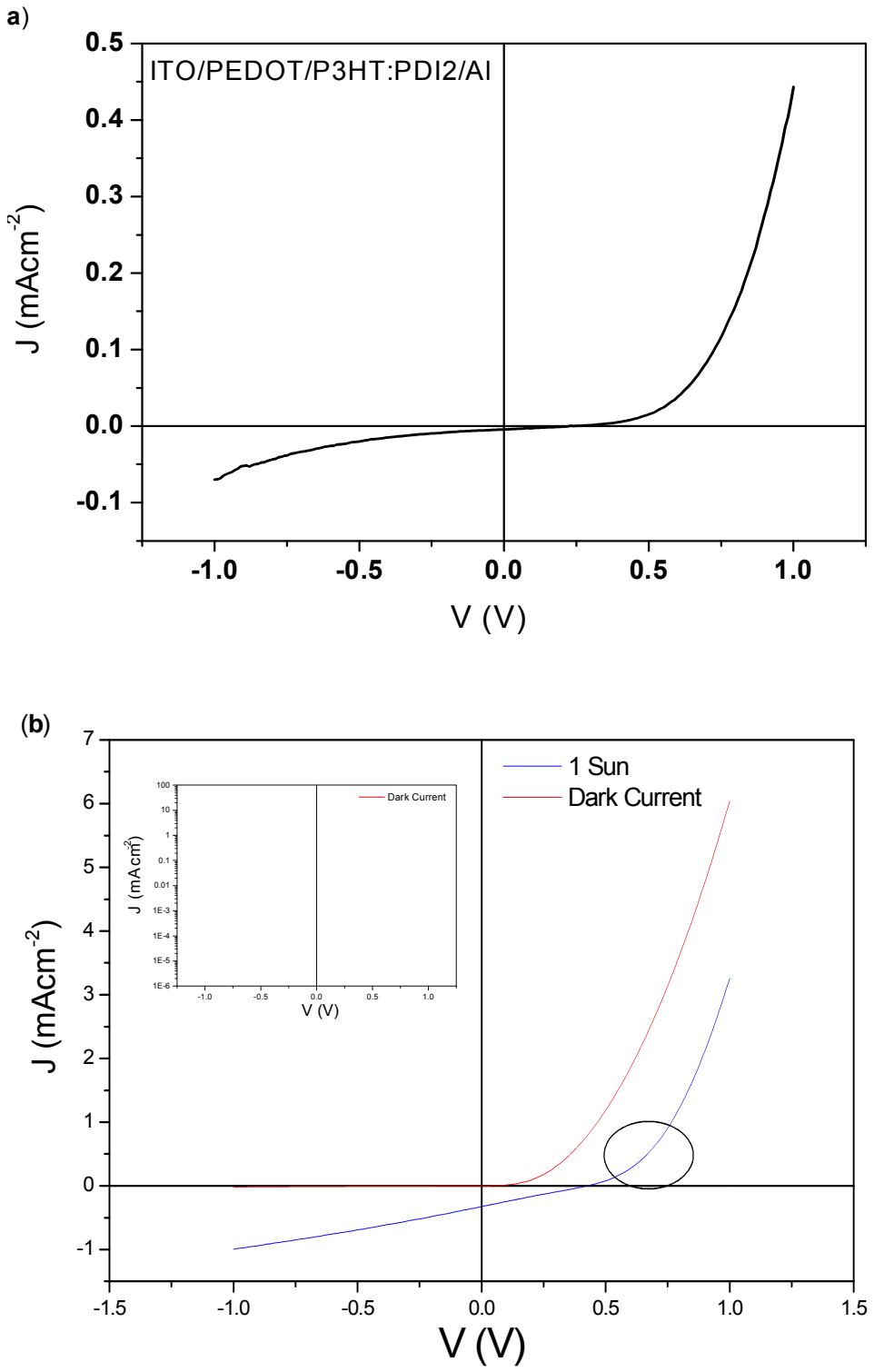


Figure 6.8 J-V curves for devices of (top) P3HT:PDI_2 and (bottom) P3HT:PDI_D 1:1 blends measured under constant illumination with 100 mW.cm^{-2} AM1.5 simulated light at room temperature.

For the other PDI derivatives, however, a more typical J-V curve, with higher photocurrent is observed (Figure 6.8 b). In general, the diodes have a low turn on current and the devices under light show good series resistance (low leakage current). However, morphology is an issue which needs to be addressed as confirmed by the low rectification values and field dependence of the devices (as indicated by the almost linear J increase with V). Furthermore, despite the various electrodes used, the contacts are not the most energetically suited ones as suggested by the raised curve over the voltage axis, indicated with a circle on the J-V curve in Figure 6.9. In a standard device the curving of the J-V occurs in the fourth quadrant rather than first quadrant as seen for these PDI devices.

A typical device characteristic presented by ITO/PEDOT:PSS/P3HT:PDI_D/Al (1:1), with ITO/PEDOT:PSS/P3HT:PDI2/Al (1:1) overlaid is depicted in Figure 6.9. The P3HT:PDI_D blend PV cell shows a short-circuit current (Jsc) of 0.33 mA/cm^2 and an open-circuit voltage (Voc) of 0.43 V, both parameters much higher than that observed for the P3HT:PDI_2 PV cell (0.004 mA/cm^2 and 0.23 V). The low Voc and Jsc of the P3HT:PDI_2 blend PV cell may be attributed to the significant phase separation and consequent formation of large PDI_2 aggregates. Firstly, the rough P3HT:PDI_2 layer may form some shunt paths after top electrode deposition, thereby resulting in a low Voc. Secondly, previous studies of polycrystalline perylene diimide films have demonstrated exciton diffusion lengths of up to 2.5 μm,[10b] compared to only ~10 nm for conjugated polymers.[72] Therefore, the large phase separation of P3HT:PDI_2 blend in PV cells may cause inefficient dissociation of P3HT excitons due to its short diffusion range, thus resulting in a small Jsc. Conversely, the finer phase separation and larger interfacial area of P3HT:PDI_D blends results in greater exciton dissociation as well as potentially better charge percolation pathways, allowing a higher charge photogeneration yield (as observed in the TAS data Figure 6.5) and a greater Jsc. From above, this is another factor, in addition to the effect of ΔG_{CS} that allows a higher charge photogeneration yield (as observed in the TAS data) and a greater Jsc.

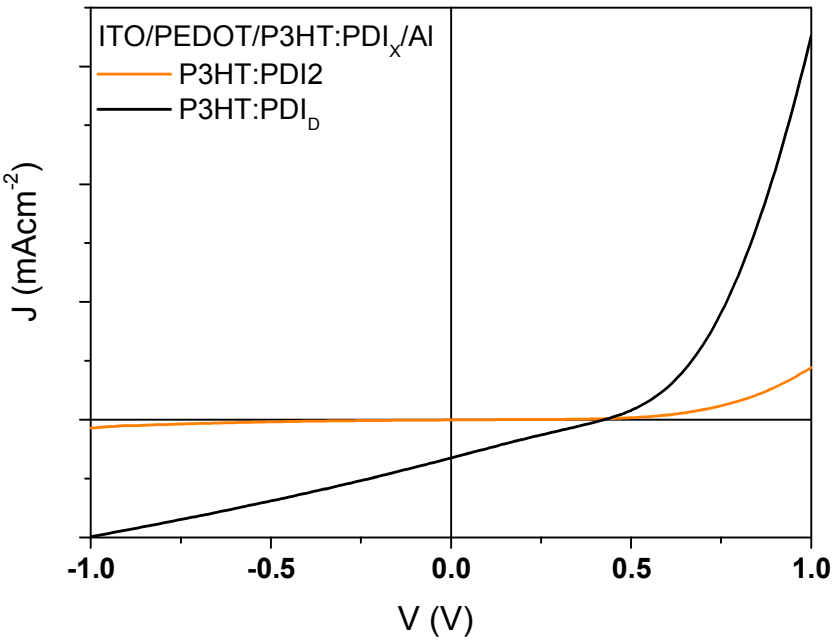


Figure 6.9 The J-V curves for devices of annealed P3HT:PDI$_D$ and P3HT:PDI2 1:1 blends measured under constant illumination with 50 mW.cm^{-2} AM1.5 simulated light at room temperature.

The generally low Jsc and power conversion efficiencies are attributed to poor morphology and alignment of these PDI devices (as mentioned in section 6.1). A key feature involved in obtaining high power conversion efficiencies is thermal annealing. Annealing is known to significantly improve the efficiencies of P3HT:PCBM devices,[65] with observed increases in both the Jsc and the fill factor,[73] through both nanomorphology and charge photogeneration yield (Chapter 5.5). Friend's group studied a blend of P3HT and N, N'-bis(1-ethylpropyl)-3,4,9,10-perylene bis(tetracarboxyl diimide), EP-PTC, and found thermal annealing can improve the morphology and crystal growth of the PDIs and effectively reduce electron trapping.[51]

The device *J-V* curves shown in Figure 6.10 reveal an initial J_{SC} of 0.1 mA.cm^{-2} that increases by a factor of 3 after annealing at 150°C for 20 minutes.

For the unannealed P3HT:PDI$_X$ system, an emission quenching of > 99% is observed from the pristine to the blend film – indicative of efficient exciton splitting at the P3HT:PDI

interface for this unannealed film. As shown in Figure 6.11a, annealing of the P3HT:PDI_X film increases the fluorescence (by a factor dependent upon the crystallinity of the original film); that is, the polymer emission quenching relative to the pristine film is reduced by annealing. This is consistent with TEM morphology studies (Figure 6.11b) that indicate annealing enhances the phase segregation between P3HT and PDI_X, increasing the mean distance between electron donor and acceptor and thereby reducing the efficiency of exciton transfer to the interface.[74,75] It can thus be concluded that the enhanced J_{SC} after annealing does not originate from enhanced exciton quenching at the P3HT:PDI_X interface. This observation is consistent with P3HT:PCBM devices.

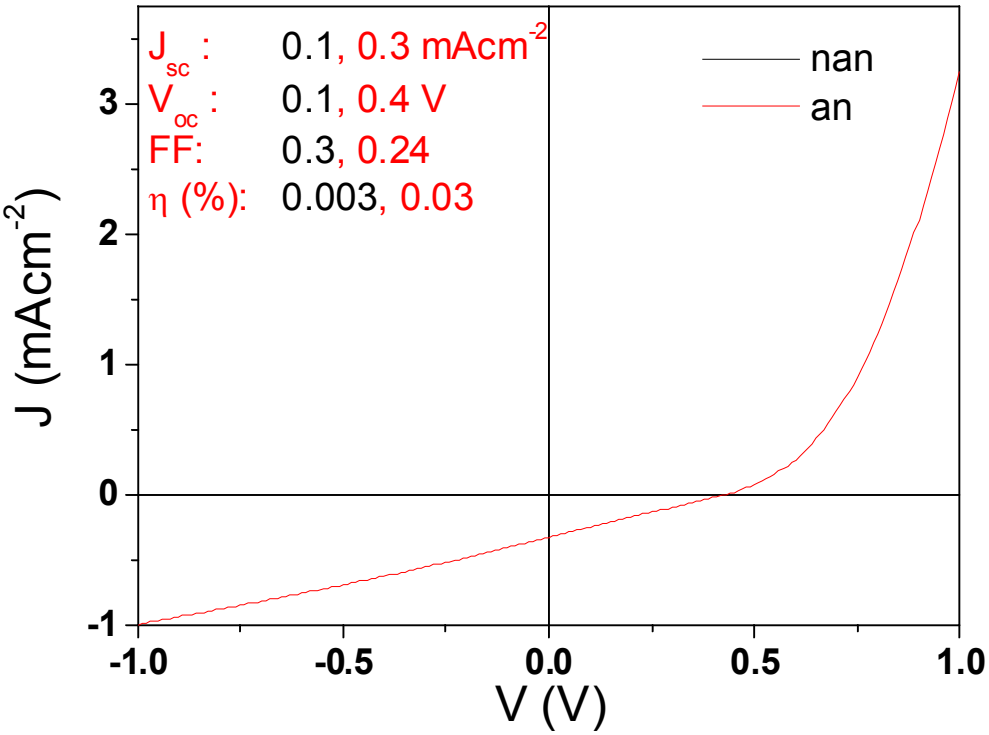
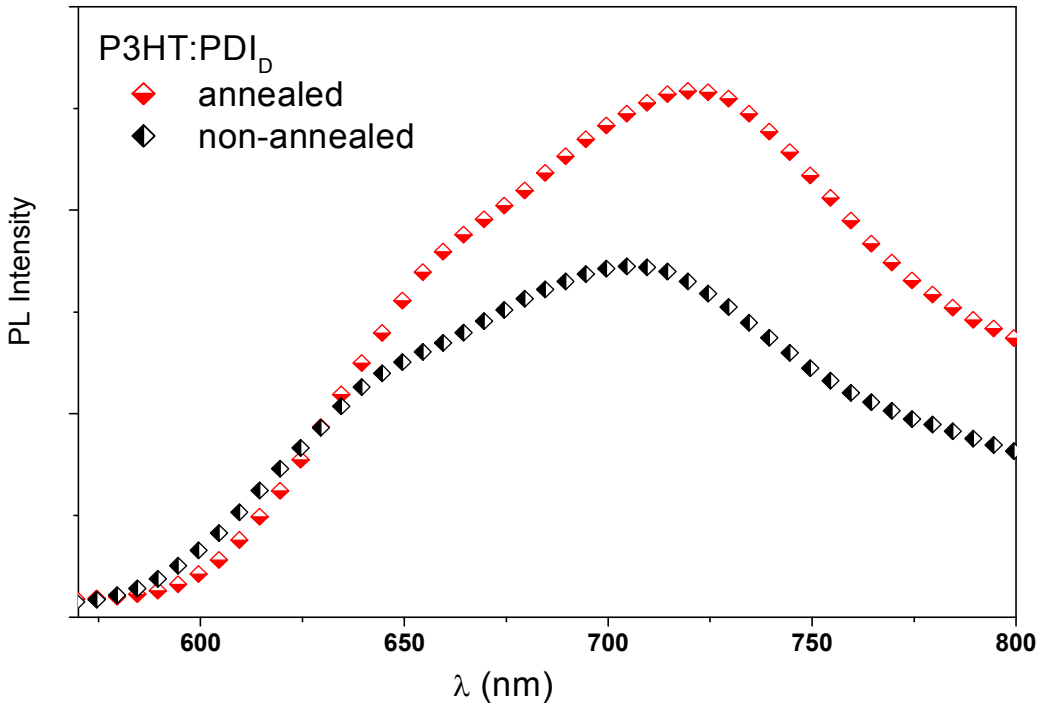


Figure 6.10 J-V of annealed (red) at 150 °C and non-annealed (black) P3HT:PDI_D (1:1) devices.



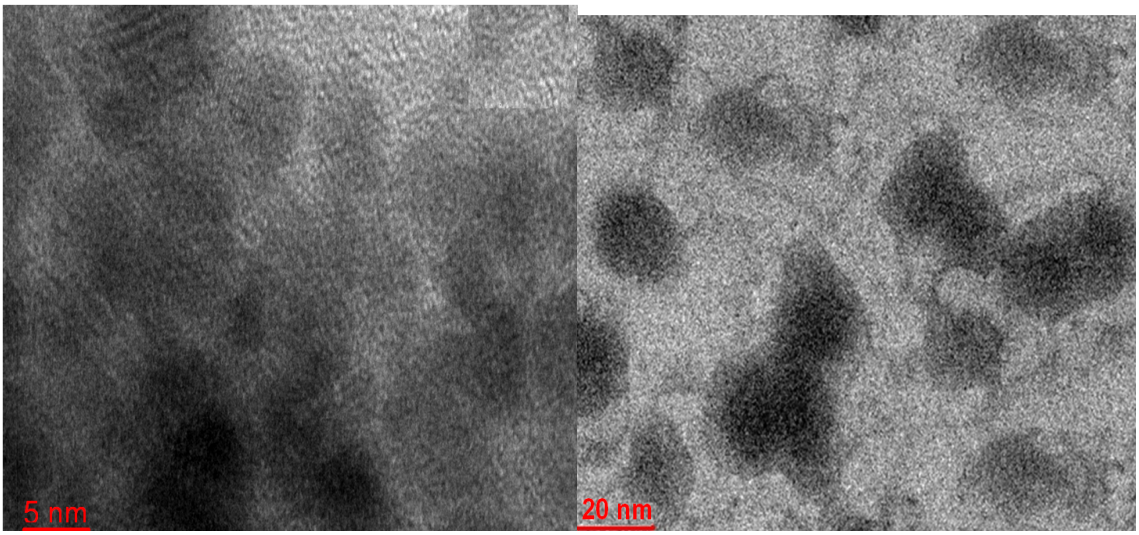


Figure 6.11 a) Emission spectra of P3HT:PDI$_D$ before (black) and after (red) annealing at 150°C for 20 minutes. b) TEM images of P3HT:PDI$_D$ film before and after thermal annealing at 150°C for 20 minutes.

If we turn now to consideration of the influence of annealing upon the yield and recombination dynamics of dissociated charges, consistent with improved percolation pathways observed from TEM morphology data (Figure 6.11b), annealing of the P3HT:PDI_D blend at 150 ^oC for 20 minutes improves the charge collection (three fold) and the power conversion efficiency of the devices by an order of magnitude in agreement with TAS data. Figure 6.12 illustrates the corresponding decay dynamics of the photoinduced absorption signals for the two films, monitored at 700 nm (the $PDI^{\bullet-}$ absorption maximum). These dynamics can be well fit by power law decays, characteristic of bimolecular recombination of dissociated polarons. Thermal annealing results in an increase in the value of the power law exponent and the lifetime, attributed to increased crystallinity of the film. We therefore conclude that the observed increase in ΔOD signal amplitude derives from an enhancement in charge generation yield and tentatively assign the greater phase segregation to better percolation pathways for charge collection. This improvement may also be correlated with increased crystallinity of P3HT upon thermal treatment[66,70,74,76] resulting in stronger interchain interactions[77] and enhanced hole mobility[78] and leading to more defined and increased phase segregation of P3HT phases and PDI crystals. This observation is consistent with thermal annealing studies of P3HT:PCBM blend film[71] by microsecond transient absorption spectroscopy of the yield of dissociated polarons, where thermal annealing of the blend film resulted in an almost two-fold increase in the yield of photogenerated charges. The magnitude of this enhancement in charge photogeneration upon annealing was sufficient for it to be a significant contributor to the improvement in photocurrent.

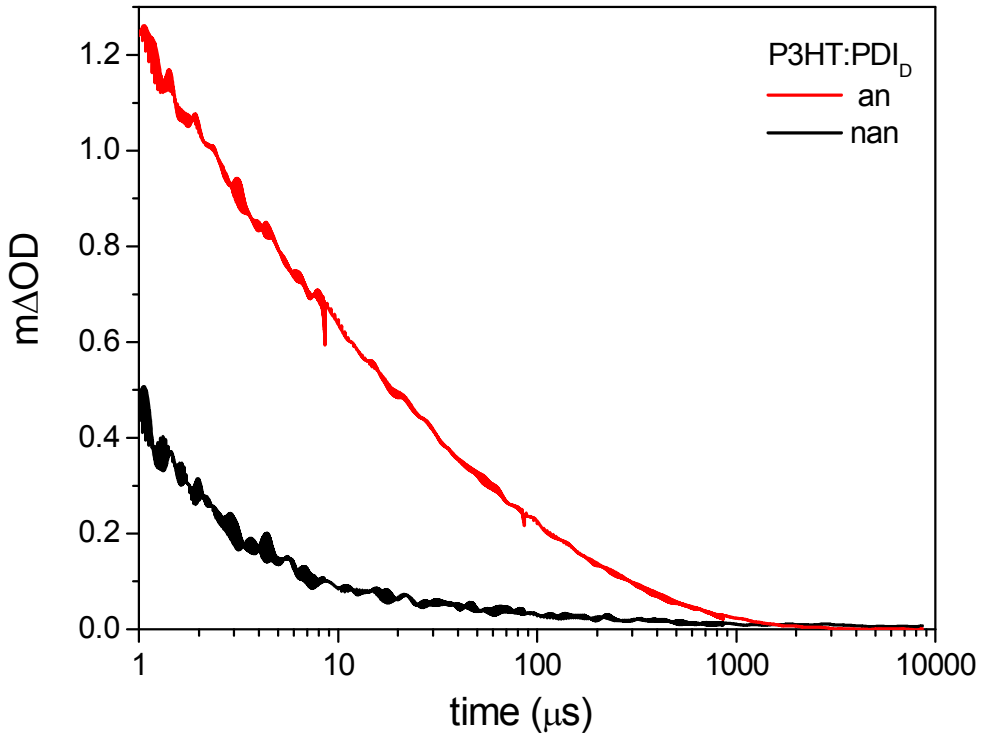


Figure 6.12 TAS of annealed (red) at 150 °C and non-annealed (black) P3HT:PDI$_D$ (1:1) films.

However, even after post-annealing, the devices still suffer from inefficient charge collection. The same issue can be also observed in other polythiophene:PDI devices, where efficient charge photogeneration is observed (Figure 6.13), however small photocurrent suggest that the charge collection is poor. To further confirm the importance of charge collection in these devices, we looked at different composition ratios of P3HT:PDI$_D$ devices. As shown in Figure 6.14 a, with increasing PDI$_D$ loading we observe an improved J_{SC} leading to higher power conversion efficiency. Complementing this observation is our TAS data on this blend for the measured weight ratios of 1:1, 1:2, 1:4 and 1:5, (Figure 6.14 panel b) where the yield of charge photogeneration does not change with ratio. However, the decays appear longer-lived going from the 1:1 to 1:5 ratio, implying better nanomorphology and percolation pathways, hence a higher short circuit current (and more efficient charge collection).

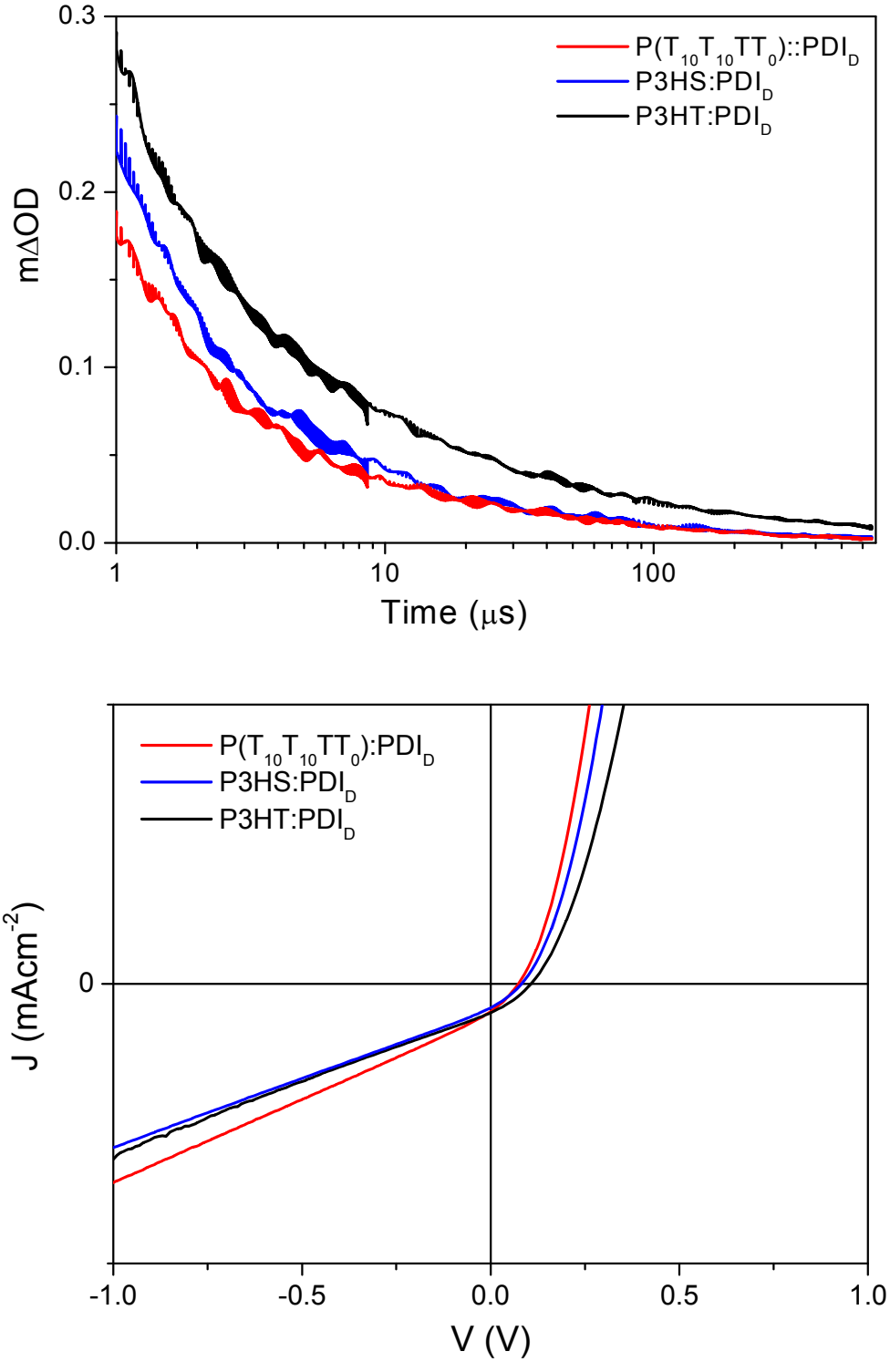


Figure 6.13 Transient absorption decays of P3HT:PDI_D (black), P3HT:PDI_D (blue) and SP220:PDI_D (red) measured under 40 μJcm^{-2} energy at 500 nm. and corresponding J-V curves (bottom) for devices of P3HT:PDI_D (black), P3HT:PDI_D (blue) and p($T_{10}T_{10}TT_0$):PDI_D (red) 1:1 blends measured under constant illumination with 100 mW.cm^{-2} AM1.5 simulated light at room temperature.

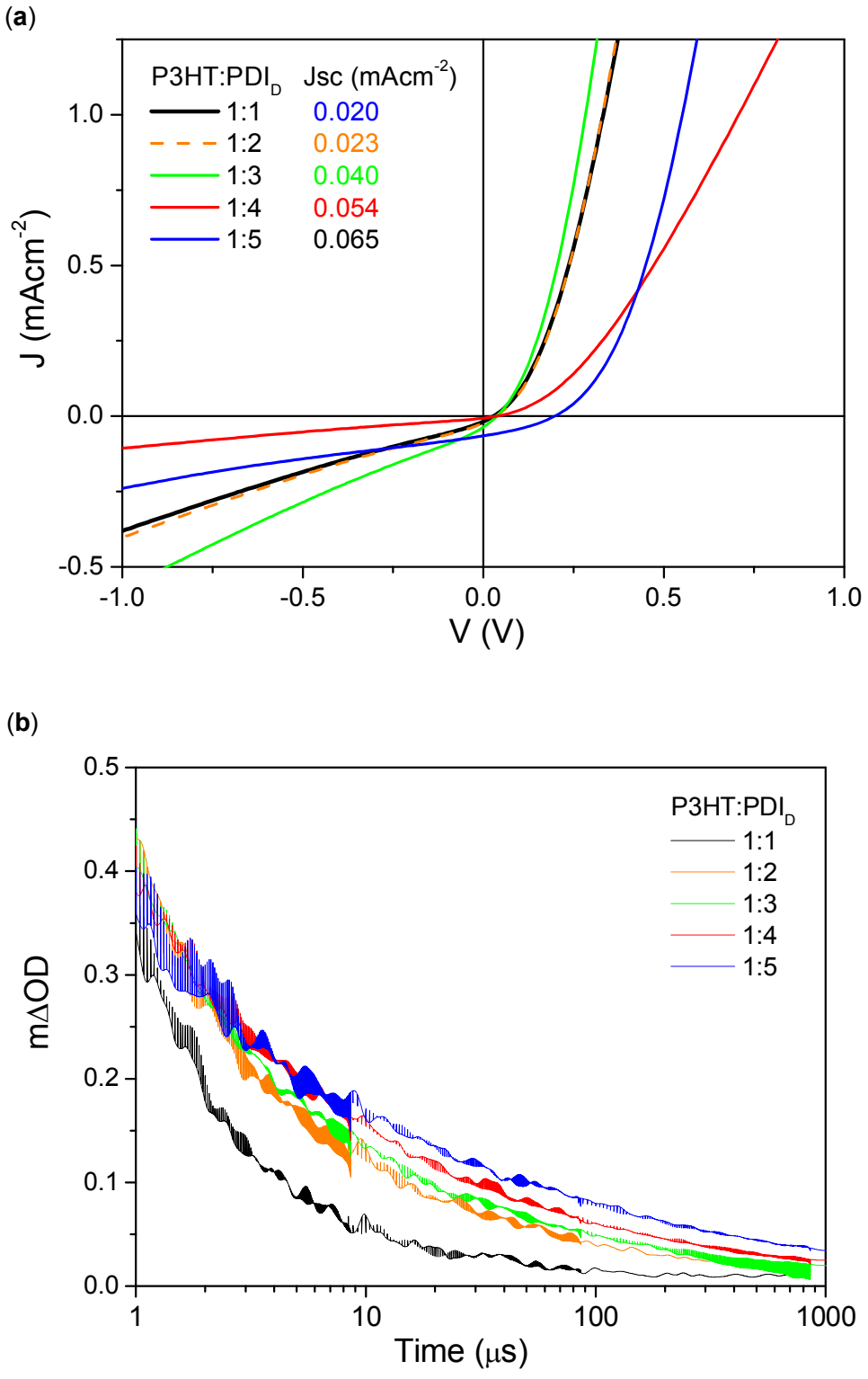


Figure 6.14 (a) The J-V curves for devices of P3HT:PDI$_D$ blend at different composition ratios measured under constant illumination with 100 mW.cm^{-2} AM1.5 simulated light at room temperature. (b) Corresponding transient absorption decays excited at 500 nm with excitation energy of 40 μJcm^{-2} and probed at 700 nm.

As such, all our results presented herein along with other studies,[34,53] indicate that in these PDI devices, nanomorphology strongly dictates the performance metrics of the corresponding solar cell. The efficient and balanced extraction of the photoinduced charge carriers via the electrodes of the device demands the formation of sufficient percolation pathways that will minimize charge carrier trapping, and the consequent carrier recombination events in the active layer. Unfortunately, the constraints placed on the morphology by charge generation, which is favoured by fine phase segregation, are counter to those of charge transport. Thus a better understanding and control over the morphology is the central issue that needs to be addressed in order to resolve the poor charge collection of dissociated polarons to the electrodes. One approach is by using additives such as block co-polymers in polymer/PDI blends. Large-scale phase segregation often occurs within blends of semiconducting polymers and PDI. A diblock-copolymer as a compatibilizer has been used by Frechet *et al*. to demonstrate the role of diblock-copolymer in controlling the phase segregation of a P3HT:PDI blend for enhancing device efficiencies.[52]

6.2.4 Conclusions

Our results here imply despite high and efficient charge photogeneration yields, PDI blends do not fabricate efficient photovoltaic devices. The studies we have undertaken suggest that several factors can favour efficiency of P3HT:PDI_X devices. We have demonstrated, through the use of transient absorption spectroscopy, that thermal annealing results in an increase in the yield of dissociated charges in P3HT:PDI blend films, whilst increase in PDI composition results in longer lived carriers. These are likely to be significant contributors to the improvement in short circuit current and photovoltaic device efficiency observed. However, the favoured nanomorphology in these blend films appears to limit the device performance.

Reference:

(1) Ohkita, H.; Cook, S.; Astuti, Y.; Duffy, W.; Tierney, S.; Zhang, W.; Heeney, M.; McCulloch, I.; Nelson, J.; Bradley, D. D. C.; Durrant, J. R. *Journal of the American Chemical Society* **2008**, *130*, 3030-3042.

(2) Clarke, T. M.; Ballantyne, A. M.; Nelson, J.; Bradley, D. D. C.; Durrant, J. R. *Advanced Functional Materials* **2008**, *18*, 4029 - 4035.

(3) Clarke, T.; Ballantyne, A.; Jamieson, F.; Brabec, C.; Nelson, J.; Durrant, J. *Chemical Communications* **2009**, 89-91.

(4) Keivanidis, P. E.; Clarke, T. M.; Durrant, J. R.; Bradley, D. D. C.; Nelson, J. *in preparation* **2009**.

(5) Tvingstedt, K.; Vandewal, K.; Gadisa, A.; Zhang, F.; Manca, J.; InganaÌˆs, O. *Journal of the American Chemical Society* **2009**, *131*, 11819-11824.

(6) Clarke, T. M.; Ballantyne, A. M.; Tierney, S.; Heeney, M.; Duffy, W.; McCulloch, I.; Nelson, J.; Durrant, J. R. **2009**, *submitted for publication*.

(7) Yin, C.; Kietzke, T.; Neher, D.; Horhold, H.-H. *Applied Physics Letters* **2007**, *90*, 092117.

(8) Offermans, T.; Hal, P. A. v.; Meskers, S. C. J.; Koetse, M. M.; Janssen, R. A. J. *Physical Review B (Condensed Matter and Materials Physics)* **2005**, *72*, 045213.

(9) Hertel, D.; Soh, E. V.; Bässler, H.; Rothberg, L. J. *Chemical Physics Letters* **2002**, *361*, 99-105.

(10) Veldman, D.; Opek, O.; Meskers, S. C. J.; Sweelssen, J.; Koetse, M. M.; Veenstra, S. C.; Kroon, J. M.; Bavel, S. S. v.; Loos, J.; Janssen, R. A. J. *Journal of the American Chemical Society* **2008**, *130*, 7721-7735.

(11) Mihailetchi, V. D.; Koster, L. J. A.; Blom, P. W. M.; Melzer, C.; de Boer, B.; van Duren, J. K. J.; Janssen, R. A. J. *Advanced Functional Materials* **2005**, *15*, 795-801.

(12) Chasteen, S. V.; Sholin, V.; Carter, S. A.; Rumbles, G. *Solar energy materials and solar cells* **2008**, *92*, 651-659.

(13) Hoppe, H.; Glatzel, T.; Niggemann, M.; Schwinger, W.; Schaeffler, F.; Hinsch, A.; Lux-Steiner, M. C.; Sariciftci, N. S. *Thin Solid Films* **2006**, *511-512*, 587-592.

(14) Quist, P. A. C.; Martens, T.; Manca, J. V.; Savenije, T. J.; Siebbeles, L. D. A. *Solar energy materials and solar cells* **2006**, *90*, 362-378.

(15) Zhang, F.; Jespersen, K. G.; Björström, C.; Svensson, M.; Andersson, M. R.; Sundström, V.; Magnusson, K.; Moons, E.; Yartsev, A.; Inganäs, O. *Advanced Functional Materials* **2006**, *16*, 667-674.

(16) Müller, J. G.; Lupton, J. M.; Feldmann, J.; Lemmer, U.; Scharber, M. C.; Sariciftci, N. S.; Brabec, C. J.; Scherf, U. *Physical Review B* **2005**, *72*, 195208-195217.

(17) Shaheen, S. E.; Brabec, C. J.; Sariciftci, N. S.; Padinger, F.; Fromherz, T.; Hummelen, J. C. *Applied Physics Letters* **2001**, *78*, 841.

(18) Blom, P. W. M.; Mihailetchi, V. D.; Koster, L. J. A.; Markov, D. E. *Advanced Materials* **2007**, *19*, 1551-1566.

(19) Mihailetchi, V. D.; Koster, L. J. A.; Hummelen, J. C.; Blom, P. W. M. *Physical Review Letters* **2004**, *93*, 216601.

(20) Mandoc, M. M.; Veurman, W.; Sweelssen, J.; Koetse, M. M. *Applied Physics Letters* **2007**, *91*, 073518.

(21) Lenes, M.; Kooistra, F. B.; Hummelen, J. C.; Severen, I. V.; Lutsen, L.; Vanderzande, D.; Cleij, T. J.; Blom, P. W. M. *Journal of Applied Physics* **2008**, *104*, 114517.

(22) Hoppe, H.; Sariciftci, N. S. *Journal of Materials Chemistry* **2006**, *16*, 45-61.

(23) Reyes-Reyes, M.; Kim, K.; Carroll, D. L. *Applied Physics Letters* **2005**, *87*, 083506.

(24) Li, G.; Shrotriya, V.; Yao, Y.; Yang, Y. *Journal of Applied Physics* **2005**, *98*, 043704.

(25) McNeill, C. R.; Halls, J. J. M.; Wilson, R.; Whiting, G. L.; Berkebile, S.; Ramsey, M. G.; Friend, R. H.; Greenham, N. C. *Advanced Functional Materials* **2008**, *18*, 2309-2321.

(26) Shoaee, S.; An, Z.; Zhang, X.; Barlow, S.; Marder, S. R.; Duffy, W.; Heeney, M.; McCulloch, I.; Durrant, J. R. *Chemical Communications* **2009**, 5445 - 5447.

(27) Nelson, J.; Kirkpatrick, J.; Ravirajan, P. *Physical Review B* **2004**, *69*, 035337.

(28) Peumans, P.; Forrest, S. R. *Chemical Physics Letters* **2004**, *398*, 27-31.

(29) Clarke, T. M.; Jamieson, F. C.; Durrant, J. R. *The Journal of Physical Chemistry C* **2009**.

(30) Benson-Smith, J. J.; Goris, L.; Vandewal, K.; Haenen, K.; Manca, J. V.; Vanderzande, D.; Bradley, D. D. C.; Nelson, J. *Advanced Functional Materials* **2007**, *17*, 451-457.

(31) Würthner, F. T., C.; Diele, S.; Tschierske, C. *Chem. Eur. J.* **2001**, *7*, 2245-2253.

(32) van Herrikhuyzen, J. S., A.; Schenning, A. P. H. H.; Meijer, E.W. *J. Am. Chem. Soc.* **2004**, *126*, 10021.

(33) J. Mizuguchi *J. Appl. Phys.* **1998**, *84*, 8.

(34) Foster, S.; Finlayson, C. E.; Keivanidis, P. E.; Huang, Y. S.; Hwang, I.; Friend, R. H.; Otten, M. B. J.; Lu, L. P.; Schwartz, E.; Nolte, R. J. M.; Rowan, A. E. *Macromolecules* **2009**, *42*, 2023-2030.

(35) Giaimo, J. M. G., A. V.; Wasielewski, M. R. *J. Am. Chem. Soc.* **2002**, *124*, 8530.

(36) van der Boom, T.; Hayes, R. T.; Zhao, Y.; Bushard, P. J.; Weiss, E. A.; Wasielewski, M. R. *J. Am. Chem. Soc.* **2002**, *124*, 9582.

(37) Korovyanko, O. J.; Österbacka, R.; Jiang, X. M.; Vardeny, Z. V.; Janssen, R. A. J. *Physical Review B* **2001**, *64*, 235122.

(38) Österbacka, R.; An, C. P.; Jiang, X. M.; Vardeny, Z. V. *Science* **2000**, *287*, 839-842.

(39) Riedel, I. v. H., E.; Parisi, J.; Martín, N.; Giacalone, F.; Dyakonov, V. *Adv. Func. Mater.* **2005**, *15*, 1979-1987.

(40) Westerling, M.; Österbacka, R.; Stubb, H. *Physical Review B* **2002**, *66*, 165220.

(41) Jones, B. A.; Facchetti, A.; Wasielewski, M. R.; Marks, T. J. *Journal of the American Chemical Society* **2007**, *129*, 15259-15278.

(42) Westenhoff, S.; Howard, I. A.; Hodgkiss, J. M.; Kirov, K. R.; Bronstein, H. A.; Williams, C. K.; Greenham, N. C.; Friend, R. H. *Journal of the American Chemical Society* **2008**, *130*, 13653-13658.

(43) Clarke, T. D., J. *Chem. Rev.* **2009**, *in press*.

(44) Pensack, R. D.; Asbury, J. B. *Journal of the American Chemical Society* **2009**.

(45) Brédas, J.-L.; Norton, J. E.; Cornil, J.; Coropceanu, V. *Accounts of Chemical Research* **2009**, *accepted for publication*.

(46) Peng, Y.-Q.; Lu, F.-P. *Applied Surface Science* **2006**, *252*, 6275-6279.

(47) Keivanidis, P. Clarke, T.; Lilliu, S.; Agostinelli, T.; Macdonald, J; Durrant, J.; Bradley, D.; Nelson, J. *J Phys Chem Lett*, *in press*.

(48) Clarke, T. B., A.; Shoaee, S.; Soona, Y.; McCulloch, I.; Nelson, J. Durrant, J *In preparation* **2010**.

(49) Conboy, J. C. O., E. J. C.; Adams, D. M.; Kerimo, J.; Zaban, A.; Gregg, B. A.; Barbara, P.; F. *J. Phys. Chem. B* **1998**, *102*, 4516.

(50) Adams, D. M. K., J.; Olson, E. J. C.; Zaban, A.; Gregg, B. A.; Barbara, P. F. *J. Am. Chem. Soc.* **1997**, *119*, 10608.

(51) Dittmer, J. J.; Marseglia, E. A.; Friend, R. H.; *Adv. Mater* **2000**, *12*, 1270.

(52) Rajaram, S. A., P. B.; Kim, B. J.; Fréchet, J. M. *J. Chem. Mater.* **2009**, *21*, 1775.

(53) Keivanidis, P.; Howard, I.; Friend, H. R. *Adv. Func. Mater.* **2008**, *18*, 1-14.

(54) Yang, Y. H., Q.; Metz, A. W.; Ni, J.; Jin, S.; Marks, T. J.; Madsen, M. E.; DiVenere, A.; Ho, S.-T., *Adv. Func. Mater.* **2004**, *16*, 321.

(55) Chen, C.-P. T., T.-C.; Ko, B.-T.; Chen, Y.-D.; Ting, C. *ACS Appl. Mater. Interfaces* **2009**, *1*, 741.

(56) Brumbach, M. V., P. A.; Marrikar, F. S.; Schulmeyer, T.; Simmonds, A.; Xia, W.; Lee, P.; Armstrong, N. R. *Langmuir* **2007**, *23*, 11089.

(57) Xue, J. F., S. R. *J. Appl. Phys.* **2004**, *95*, 1869.

(58) Muhlbacher, D. S., M.; Morana, M.; Zhu, Z. G.; Waller, D.; Gaudiana, R.; Brabec, C. *Adv. Mater.* **2006**, *18*, 2884.

(59) Peet, J. K., J. Y.; Coates, N. E.; Ma, W. L.; Moses, D.; Heeger, A. J.; Bazan, G. C. *Nat. Mater* **2007**, *6*, 497.

(60) Kim, y. C., S. A.; Nelson, J.; Bradley, D. D. C.; Cook, S.; Durrant, J. R. *Appl. Phys. Lett.* **2005**, *86*, 063502.

(61) Al-Ibrahim, M. A., O.; Sensfuss, S.; Gobsch, G. *Appl. Phys. Lett.* **2005**, *86*, 201120.

(62) Hoppe, H. S., N. S.; *J. Mater. Chem.* **2006**, *16*, 45.

(63) Kim, Y. C., S.; Tuladhar, S. M.; Choulis, S. A.; Nelson, J.; Durrant, J. R.; Bradley, D. D. C.; Giles, M.; McCulloch, I.; Ha, C.-S.; Ree, M.; *Nat. Mater.* **2006**, *5*, 197.

(64) Schilinsky, P. A., U.; Scherf, U.; Biele, M.; Brabec, C. J.; *Chem. Mater. B.* **2005**, *17*, 2175.

(65) Raita, S. K., S.; Bhatnagar, P. K.; Mathur, P. C.; Sengupta, S. K.; Kumar, J.; *Sol. Energy Mater. Sol. Cells* **2007**, *91*, 757.

(66) Nguyen, L. H. H., H.; Erb, T.; Gunes, S.; Gobsch, G.; Sariciftci, N. S. *Adv. Func. Mater.* **2007**, *17*, 1071.

(67) Mihailetchi, V. D. X., H. X.; de Boer, B.; Koster, L. J. A.; Blom, P. W. M. *Adv. Func. Mater.* **2006**, *16*, 699.

(68) Reyes-Reyes, M. K., K.; Carroll, D. L. *Appl. Phys. Lett.* **2005**, *87*, 083506.

(69) Li, G. S., V.; Yao, Y.; Yang, Y. *J. Appl. Phys.* **2005**, *98*, 043704.

(70) Yamanari, T. T., T.; Hara, K.; Saito, K.; *J. Photochem. Photobiol. A* **2006**, *182*, 269.

(71) Clarke, T. M. B., A.; Nelson, J.; Bradley, D. D. C.; Durrant, J. R. *Adv. Func. Mater.* **2008**, *18*, 4029.

(72) Shaw, P. E.; Ruseckas, A.; Samuel, I. D. W. *Advanced Materials* **2008**, *20*, 3516.

(73) Clarke, T. M. Ballantyne, A.; Jamieson, F.; Brabec, C.; Nelson, J.; Durrant, J. R. *Chem. Commun.* **2009**, 89.

(74) Campoy-Quiles, M. F., T.; Agostinelli, T.; Etchegoin, P. B.; Kim, Y.; Anthopoulos, T. D.; Stavrinou, P. N.; Bradley, D. D. C. ; Nelson, J.; *Nat. Mater.* **2008**, *7*, 158.

(75) Zhokhavets, U.; Erb, T.; Hoppe, H.; Gobsch, G.; Sariciftci, N. S. *Thin Solid Films* **2006**, *496*, 679-682.

(76) Savenije, T. J. K., J. E.; Yang, X. N.; Loos, J. *Adv. Func. Mater.* **2005**, *15*, 1260.

(77) Chirvase, D. P., J.; Hummelen, J. C.; Dyakonov, V. *Nanotechnology* **2004**, *15*, 1317.

(78) Erb, T. Z., U.; Gobsch, G.; Raleva, S.; Stuhn, B.; Schilinsky, P.; Waldauf, C.; Brabec, C. J. *Adv. Func. Mater.* **2005**, *15*, 1193.

VII. Conclusions

The research described in this thesis was focused largely upon on perylene-based materials. The objective of the research was to recognize and address the parameters influencing charge photogeneration in organic donor / acceptor solar cells. The research can be divided into the following:

The primary focus of this PhD thesis was to study charge photogeneration in donor: acceptor blends and donor-acceptor molecules, focusing in particular on polythiophene:perylene diimide (PDI) films for application to photovoltaic devices and obtain a photophysical model to describe their transient absorption decay dynamic signals. In order to gain understanding of the relationship between structural properties and charge photogeneration, we examined the effect of the side groups, bay substitution and electron affinity of perylene diimide on charge generation yields. This was done by examining a range of perylene diimides compared with PCBM system to study the physical parameters which are influential on charge separation and subsequently the photocurrent.

Charge photogeneration in polythiophene:perylene diimide films

A basic outline of the mechanisms leading to charge photogeneration in polythiophene:perylene diimide films can be drawn.

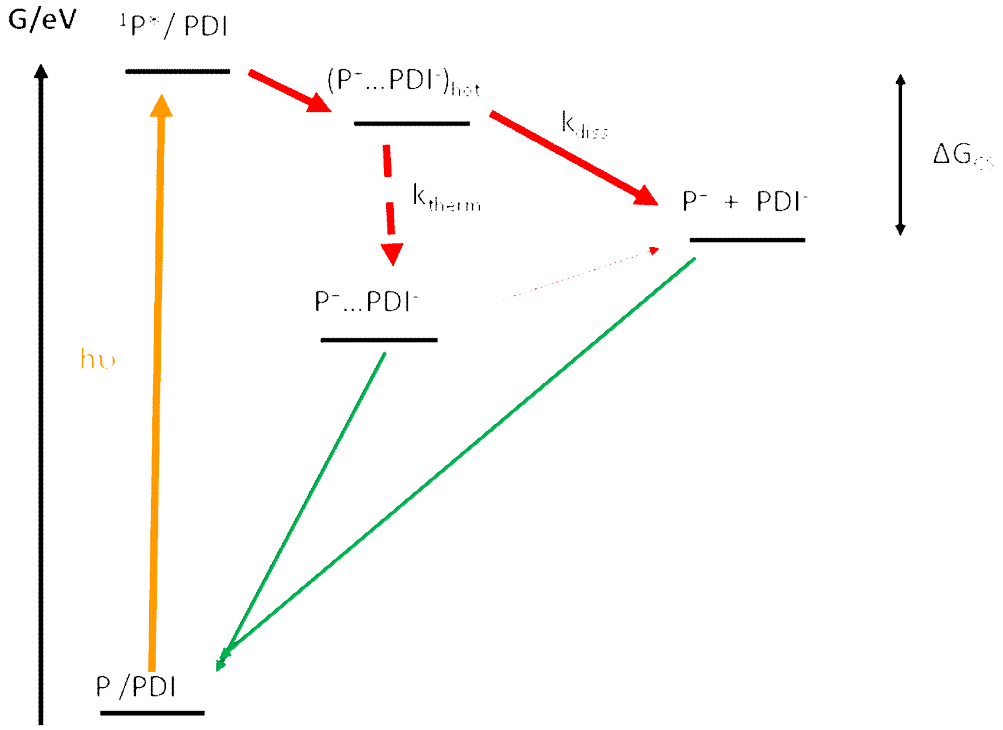


Figure 7.1 charge photogeneration and recombination in polythiophene:perylene diimide (PDI) films. The orange arrow is the excitation process, green arrows are recombination loss mechanisms and red arrows present internal changes.

As was suggested from the results chapter 5 and 6, our results is consistent with a model where a hot charge transfer state is formed after charge transfer and this is assumed to be the primary product formed at the interface. There is much debate in the literature over the parameters influencing or mechanism by which charge transfer states at the interface overcome their strong Coulomb attraction to become free charges. The transient absorption measurements described are indicators of the yield rather than the rate of

charge dissociation. This yield is dependent upon competition between the underlying processes of charge dissociation, geminate recombination and / or thermalisation. In PDI systems, we speculate that the hot charge transfer state has a similar or higher energy to that of the free charges and therefore facilitates the dissociation of charges. The yields of charge dissociation of the charge transfer state, to form separated species, are shown to be dependent on the domain size and or mobility of the acceptor material. Higher electron mobility, and the observed increase in polaron yield, may originate microscopically from increased intermolecular delocalisation arising within liquid crystalline π-stacks of the PDI.

In systems with PDI_2 rather than PCBM as the electron acceptor, we revealed a greater yield of dissociated charges with a smaller ΔG when the same polymer is utilised, this is proposed to be a result of PDI_2's higher electron mobility. Further comparison of charge photogeneration in films comprising of blends of P3HT and a series of different PDI derivatives with varying electron affinities reveals a strong correlation between ΔG_{CS} and charge generation. This correlation results from Onsager model: the exciton will undergo vibrational relaxation prior to charge separation at the donor / acceptor interface. However, due to the offset of donor and acceptor LUMO levels, the electron injected in the acceptor will initially be thermally hot. The higher electron mobility of PDIs compared to PCBM facilitates the separation of the hot charge transfer state into the fully dissociated charges. In this context, the correlation between ΔG_{CS} and polaron photogeneration efficiency, and thus $\eta_{DISS(CT)}$, we observe can be understood in terms of the influence of ΔG_{CS} upon the excess thermal energy of the injected electron and thus the electron thermalisation length *a*.

It is clear from an examination of the ΔG_{CS} plot of different donor / acceptor systems (Figure 6.6) that each polaron yield dependence only exists within each series. The correlations observed between ΔG_{CS} and charge photogeneration yield within each polymer / acceptor series are suggestive of the generality of this relationship, although further work is required. Furthermore, the energetic model proposed to account for these results is consistent with the well-established Onsager and Marcus theories. The results presented in this thesis therefore provides further evidence to support the validity of the

previous model: the yield of photogenerated charges in polymer / acceptor blend systems is likely to be dependent upon the excess vibrational energy of the bound radical pair, such that the key kinetic competition in the photogeneration process is between vibrational relaxation and dissociation of this species. More specifically, the results presented in this thesis demonstrate the effect of acceptor's LUMO energy level in this model.

Another important consideration in the charge separation process is the nanomorphology of the blend films. We find that replacing PCBM with two pyrazolinofullerenes appears to greatly increase geminate recombination losses. As we have argued in chapter 3, this transition appears to be the result of the pronounced change in nanomorphology between the blend films. More specifically, the modified fullerene blend films exhibit much smoother blend films indicative of a finer blend nanomorphology, reducing the blend domain size, and thus impeding the dissociation of the initially generated polaron pairs to dissociate into spatially uncorrelated charges. Whilst clearly this is not promising for device studies, it highlights the importance of the domain size in the bulk heterojunction on achieving efficient charge dissociation.

It can be concluded from our donor-acceptor molecules, that long-lived charges observed in film is due to intermolecular charge separation. However, strong coupling between the donor and acceptor moieties in the D-A molecule, means that the intramolecular charge separation functions to accelerate non-radiative decay to ground. As a result, the system is shorter lived with a lower yield.

The application of molecular donor–acceptor structures to photovoltaic energy conversion requires a detailed understanding of the correlations between molecular structure, electron-transfer dynamics and device function. Whilst solution studies are essential to develop an understanding of the intramolecular photochemistry of molecular donor-acceptor systems, such studies are not adequate and not a reliable indicator of photochemical function of these molecular systems in solid films and the application of

such structures to solid-state solar energy conversion requires careful consideration of interplay between intra- and intermolecular charge-transfer processes.

The work in this thesis has demonstrated (to some degree) some of the current state of knowledge of charge photogeneration in organic bulk heterojunction solar cells. A frequent theme in the current literature is the function of interfacial charge transfer states, with geminate recombination of these charge-transfer states being suggested in many studies to be a key loss mechanism (chapter 3). Evidence for the functional importance of these charge transfer states in limiting charge photogeneration remains rather indirect. However, the experimental and theoretical evidence is steadily accumulating that these charge transfer states do indeed play a significant role in determining the efficiency of charge photogeneration in organic solar cells, and that optimization of charge photogeneration is an important challenge for achieving further advances in photovoltaic device efficiencies.

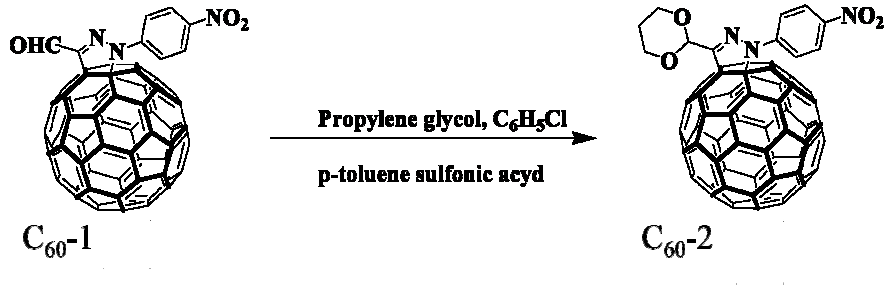
Future work

Blend nanomorphology can have a substantial role in minimizing geminate recombination in the organic polymer / PDI blend films. Our studies have demonstrated that nanomorphology is key not only to determining the efficiency of exciton quenching and charge transport in organic bulk heterojunction solar cells, but is furthermore important in enabling the dissociation of the initially generated polaron pairs. Both geminate and bimolecular recombinations of charges, are mechanisms which place limits on film / device charge generation and efficiency. Direct geminate recombination of charges was inferred in chapter 3 demonstrating effect of nanomorphology. Also from chapters 5 and 6 we observe the effect of aggregates, domain size and other morphology data on charge generation and collection. Thus, further studies are required to establish if improved morphology can lead to improved percolation pathways, thereby reducing recombination and enhancing charge collection. One approach is through application of surfactants to these polmer:PDI binary systems. This will potentially improve the donor-acceptor interface and miscibility between the two components, perhaps achieving more homogenous blends.

Appendix

Experimental Details for Synthesis of pyrazolinofullerene C_{60}-2 from C_{60}-1

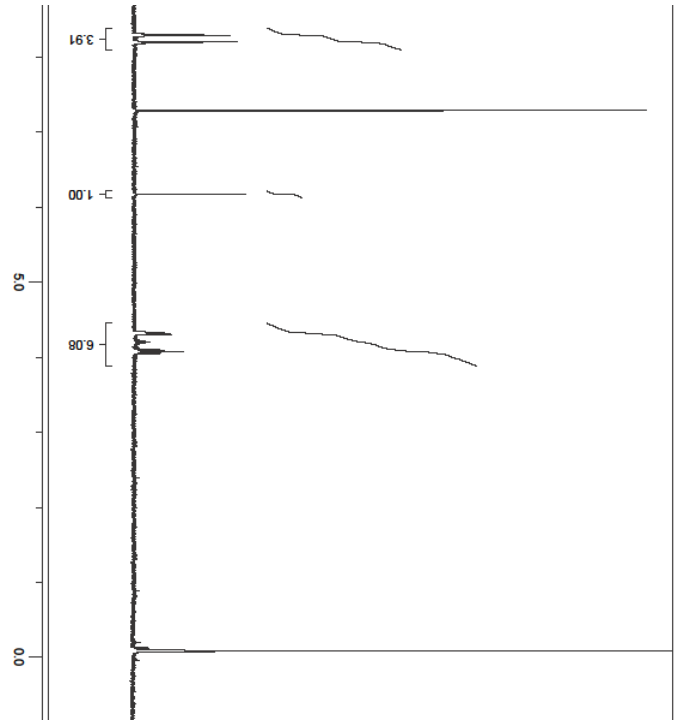
The synthesis of **C_{60}-1** has been published previously.[1]



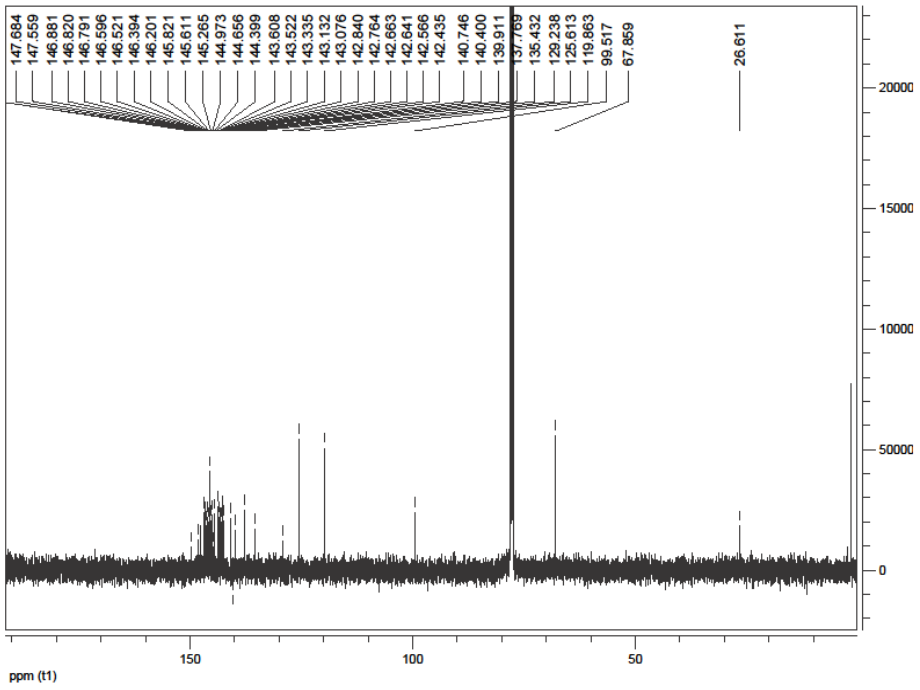
Scheme A1 structures of **C_{60}-1** and **C_{60}-2** molecules.

A solution of **C_{60}-1** (150 mg, 0.164 mmol), propylene glycol (19 mg, 0.243 mmol) and p-toluenesulfonic acid (1 drop) in cholorobenzene (150 mL) was heated at reflux under argon atmosphere for 24 h. The solvent was removed in vacuo and the residue was purified by flash chromatography on silica gel using toluene to elute compound **C_{60}-2.** The solvent was removed in vacuo and further purification of the solid was achieved by centrifuging with methanol and hexane.

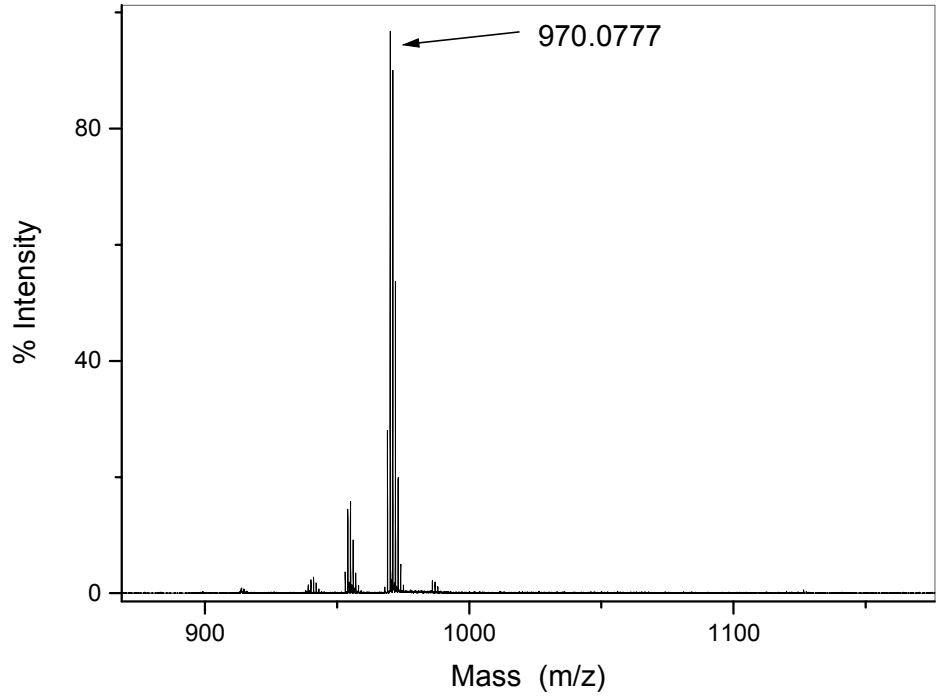
Yield: 127 mg were obtained 80%. ^{1}H NMR ($CDCl_3/CS_2$) δ 8.27 (d, *J*=9.2 Hz, 2H), 8.17 (d, *J*=9.2 Hz, 2H), 6.14 (s, 1H), 4.0-4.3 (m, 6H). ^{13}C NMR ($CDCl_3/CS_2$) δ 149.65, 148.04, 147.68, 147.55, 146.88, 146.82, 146.79, 146.59, 146.52, 146.39, 146.20, 145.82, 145.61, 145.26, 144.97, 144.65, 144.39, 143.60, 143.52, 143.33, 143.13, 143.07, 142.84, 142.76, 142.66, 142.64, 142.56, 142.43, 140.74, 140.40, 139.91, 137.76, 135.43, 129.23, 125.61, 119.86, 99.51, 67.85, 26.61. FT-IR (KBr): 2922, 1591, 1508, 1324, 527 cm^{-1}. UV-vis (Toluene) λ 284, 332, 428. MS *m/z* 970.07 (M+1). Calculated for $C_{71}H_{11}N_3O_4$: 969.07.



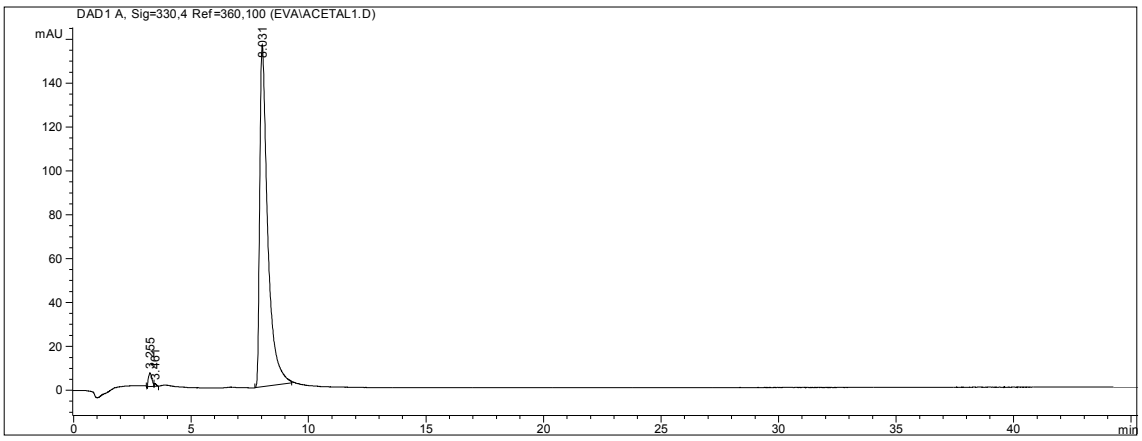
^{1}H-NMR of **2** $CDCl_3/CS_2$



^{13}C-NMR of **C_{60}-2** $CDCl_3/CS_2$



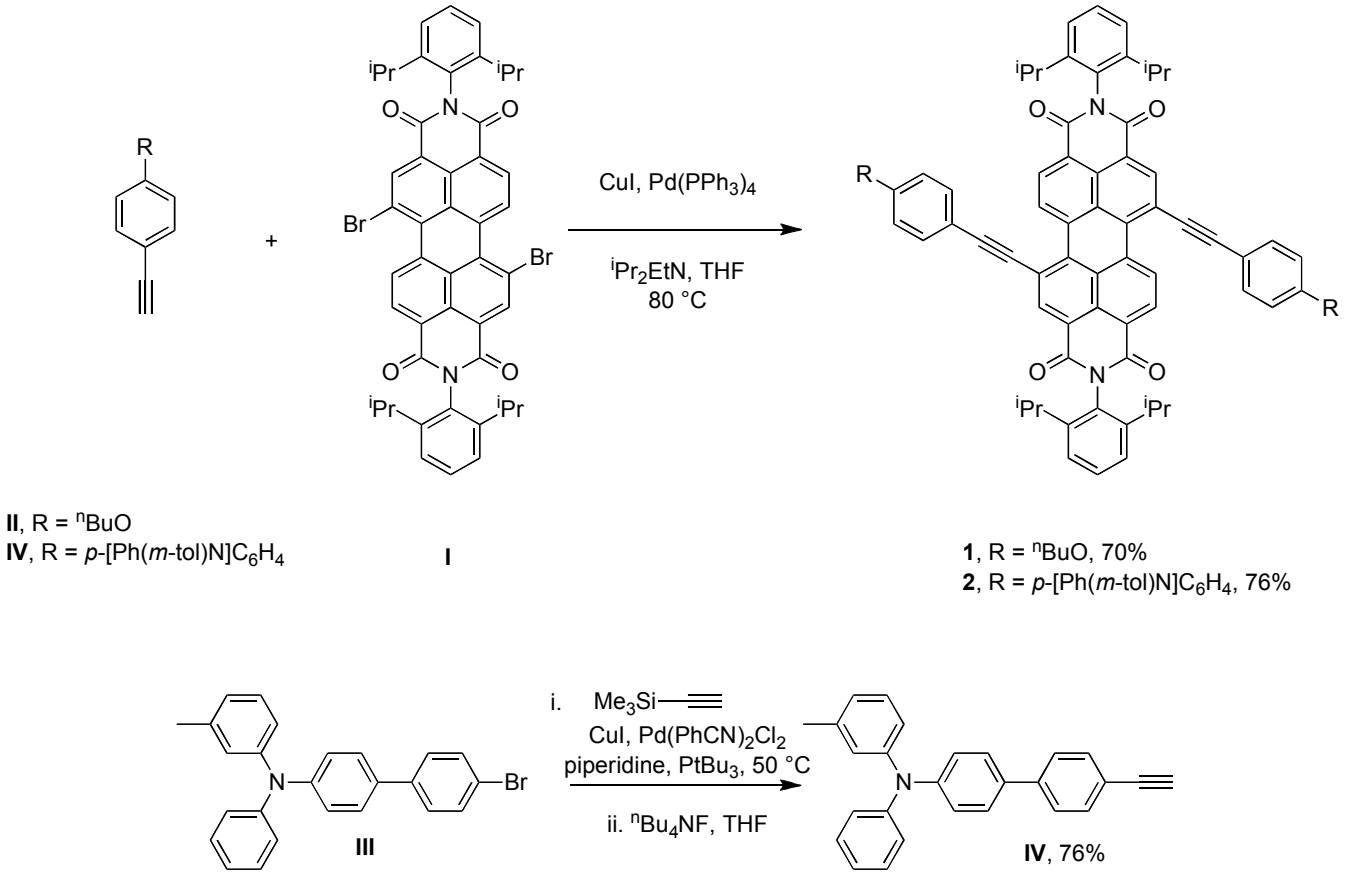
Mass Spectroscopy of **C_{60}-2**



HPLC of **C_{60}-2** Toluene 1mL/min.

Experimental Details for Synthesis of TTF-PDI and PDI control

Compounds TTF-PDI (**1)** and control PDI (**2)** were synthesized as shown in Scheme A2.



Scheme A2. Synthesis of **1**, **2**, and the intermediate, **IV**.

1. CuI (0.008 g, 0.042 mmol) and $Pd(PPh_3)_4$ (0.02 g, 0.02 mmol) were added to a deoxygenated solution of **I**[1] (0.20 g, 0.23 mmol) in THF (10 mL) and $^{i}Pr_2EtN$ (20 mL). After the resultant solution was further deoxygenated for 10 minutes, **II** (0.11 g, 0.63 mmol) was added. The reaction was heated at 80 °C under argon for 15 h. After cooling to room temperature, the reaction mixture was poured into 2 M HCl (150 ml) solution and extracted with CH_2Cl_2. The organic phase was dried over $MgSO_4$ and was filtered. The solvents were removed under reduced pressure and the residue was purified by flash chromatography eluting with 1:1 CH_2Cl_2 / hexane to give 1 (0.17 g, 70%). ^{1}H NMR (300 MHz, $CDCl_3$) δ 10.26 (d, J = 8.4 Hz, 2H), 9.05 (s, 2H), 8.83 (d, J = 8.1 Hz, 2H), 7.66 (d, J = 9.0 Hz, 4H), 7.55 (t, J = 7.5 Hz, 2H), 7.41 (d, J = 7.5 Hz, 4H), 6.97 (d, J = 7.5 Hz, 4H), 4.05 (t, J = 6.5 Hz, 4H), 2.80 (septet, J = 6.6 Hz, 4H), 1.75 (m, 4H), 1.60-1.52 (m, 4H), 1.20 (d, J = 6.9 Hz, 24H), 0.90 (t, J = 7.2 Hz, 6H). $^{13}C\{^1H\}$ NMR (125 MHz, $CDCl_3$) δ 163.9, 163.7, 160.9, 146.1, 138.6, 135.2, 134.3, 134.0, 131.3, 130.9, 130.2, 128.6, 127.9, 124.6, 123.4, 122.5, 121.4, 115.5, 114.2 (two peaks separated by ca. 3.7 Hz), 100.12, 90.3, 68.4, 31.6, 29.7, 24.5, 19.6, 14.3. HRMS (MALDI): calcd. for $C_{72}H_{66}N_2O_6$: 1054.4921; found: 1054.5165. Elemental analysis: calcd. for $C_{72}H_{66}N_2O_6$, C 81.95, H 6.30, N 2.65; found C 81.45, H 6.56, N 2.61.

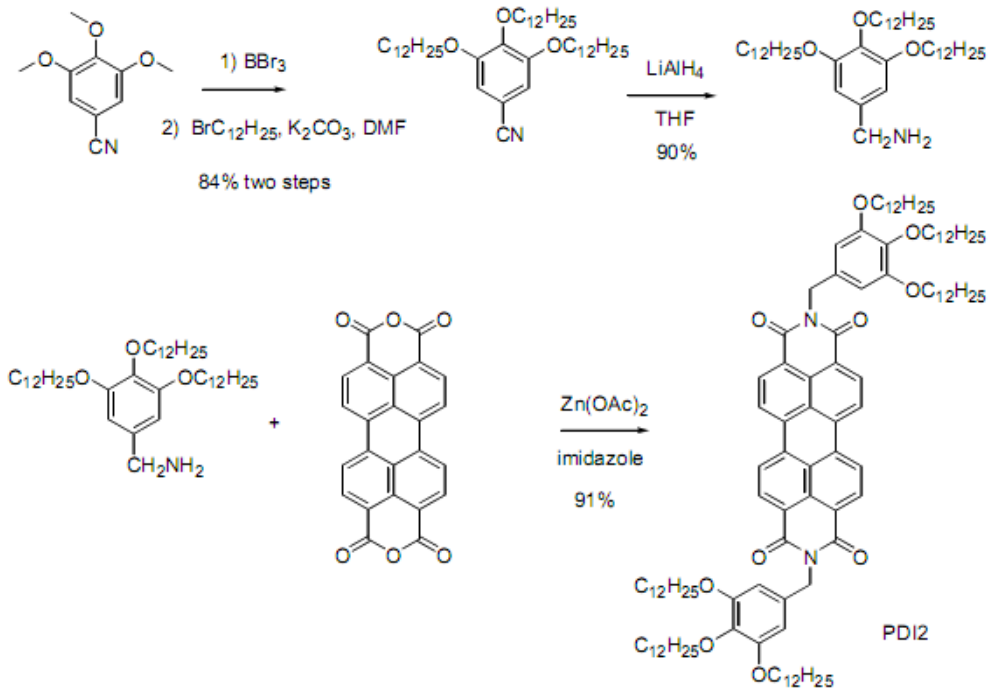
IV. $Pd(PhCN)_2Cl_2$ (0.06 g, 0.15 mmol), CuI (0.06 g, 0.30 mmol) and piperidine (15 mL) were added to an ampoule containing **III**[2] (2.02 g, 4.86 mmol) and the mixture was deoxygenated for 10 min. P^tBu_3 (0.59 g of 10% wt. solution in hexane, ca. 0.30 mmol) was added and the mixture was further deoxygenated for 15 min. $Me_3SiC{\equiv}CH$ (1.0 mL, 7.1 mmol) was added and the reaction mixture was heated to 50 °C for 5 h. The mixture was then poured into 2 M aqueous hydrochloric acid (75 mL) and was extracted with ethyl acetate. The combined organic extracts were washed with 2 M aqueous hydrochloric acid (50 mL) and water (100 mL), dried over anhydrous magnesium sulfate and filtered. After removal of solvent, the residue was purified by column chromatography, eluting with hexane. After removal of solvent, the resulting solid (1.90 g) was dissolved in THF (10 mL) and 1.0 M $^nBu_4NF$ THF solution (10 mL) was added. The resulting mixture was stirred at room temperature under nitrogen for 3 h. After 2 M aqueous hydrochloric acid (5 mL) was added, the mixture was further stirred for 10 min and was extracted with CH_2Cl_2. The organic extracts were dried over anhydrous magnesium sulfate and filtered; the solvent was removed under reduced pressure and the residue was recrystallized from ethyl acetate. 1.26 g (76%) of

a brown solid was obtained. ^{1}H NMR (500 MHz, $CDCl_3$) δ 7.52 (s, 4H), 7.44 (d, J = 8.5 Hz, 2H), 7.25 (t, J =8.0 Hz, 2H), 7.15 (t, J = 8.0 Hz, 1H), 7.10 (m, 4 H), 7.02 (t, J = 7.5 Hz), 6.94 (s, 1H), 6.91 (d, J = 8.0 Hz, 1H), 6.85 (d, J = 7.5 Hz, 1H), 3.09 (s, 1H), 2.26 (s, 3H). ^{13}C NMR (125 MHz, $CDCl_3$) δ 147.6, 147.4, 147.3, 140.9, 139.1, 133.4, 132.4, 129.2, 129.0, 127.5, 126.2, 125.3, 124.4, 124.0, 122.9, 121.8, 120.2, 83.7, 77.6, 21.5 (one peak missing from the aromatic region, presumably due to overlap). HRMS (EI): calcd. for $C_{27}H_{21}N$ m/z: 359.1674; found 359.1661. Elemental analysis: calcd. for $C_{27}H_{21}N$, C 90.21, H 5.89, N 3.90; found C 89.94, H 5.88, N 3.90.

2. Compound **2** was synthesized in an analogous fashion to **1** using the following quantities of reagents: **I** (0.22 g, 0.25 mmol), **IV** (0.22 g, 0.61 mmol), toluene (10 mL), dioxane (5 mL), $^{i}Pr_2EtN$ (10 mL), $Pd(PhCN)_2Cl_2$ (0.02 g, 0.05 mmol), CuI (0.01 g, 0.05 mmol), $P^{t}Bu_3$ (0.21 g, 10% wt. solution in hexane, ca. 0.10 mmol). Yield: 0.27 g (76%). ^{1}H NMR (500 MHz, $CDCl_3$): δ 10.25 (d, J = 8.0 Hz, 2H), 9.03 (s, 2H), 8.85 (d, J = 8.5 Hz, 2H), 7.73 (d, J = 8.5 Hz, 4H), 7.68 (d, J = 8.5 Hz, 4H), 7.52 (m, 6H), 7.37 (d, J = 8.0 Hz, 4H), 7.27 (m, 4H), 7.15 (m, 10H), 7.04 (t, J = 8.0 Hz, 2H), 6.96 (s, 2H), 6.93 (d, J = 8.5 Hz, 2H), 6.87 (d, J = 7.5 Hz, 2H), 2.79 (septet, J = 6.5 Hz, 4H), 2.27 (s, 6H), 1.20 (d, J = 6.5 Hz, 24H). ^{13}C{^{1}H} NMR (125 MHz, $CDCl_3$):δ 163.9, 163.6, 148.5, 147.9, 147.8, 146.1, 142.5, 139.7, 138.7, 135.2, 134.6, 133.5, 132.8, 131.5, 130.9, 130.2, 129.7, 129.6, 128.8, 128.6, 128.1, 127.3, 126.0, 125.1, 124.8, 124.6, 123.7, 123.6, 122.7, 122.4, 121.1, 120.5, 99.7, 91.8, 29.7, 24.4, 21.8, (four peaks missing from aromatic region, presumably due to overlap). HRMS (MALDI): *m/z* calcd. for $C_{102}H_{80}N_4O_4$: 1424.6180; found: 1424.6104. Elemental Analysis: calcd. for $C_{102}H_{80}N_4O_4$, C 85.93, H 5.66, N 3.93; found C 85.88, H 5.66 N 3.91.

Perylene diimide small molecules:

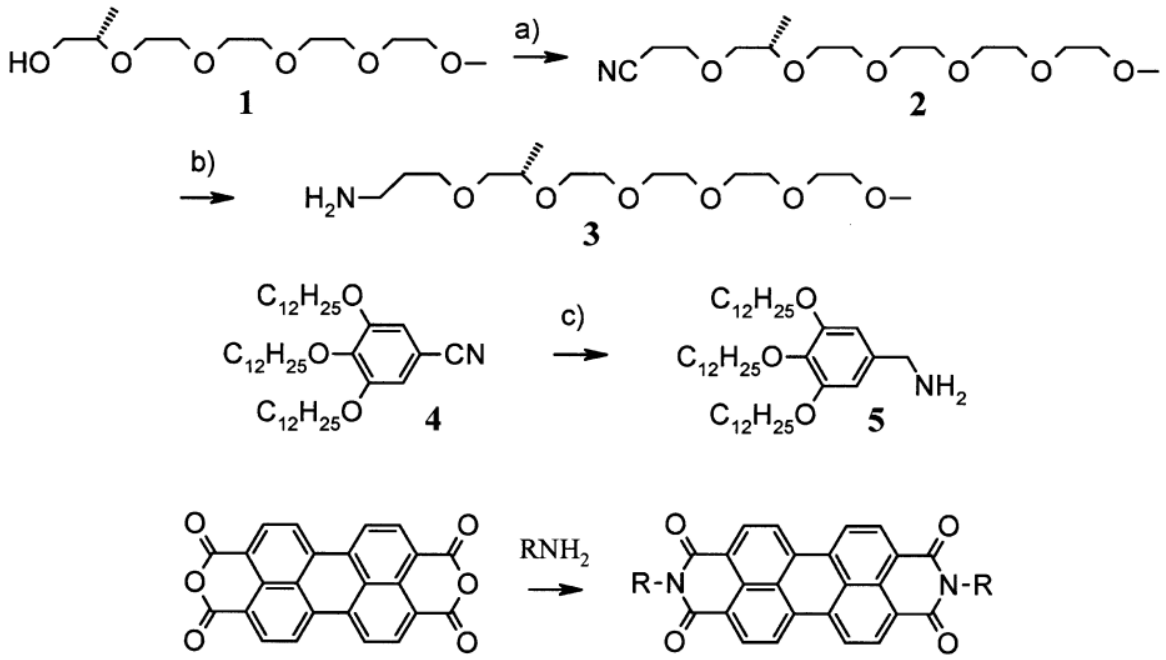
The perylene diimide derivatives were synthesized by condensation of the corresponding amines with perylene dianhydride under basic conditions. **PDI2** was synthesized with tridodecyloxybenzyl amine in melted imidazole (Scheme 2.2), the synthesis of which was also recently reported



Scheme A3 Schematic synthesis of PDI_2

PDI2 was synthesized from the corresponding amine-terminated chains (Scheme 1, Figure 1) with 3,4,9,10-perylenetetracarboxy anhydrides at 160 °C in imidazole in the presence of zinc acetate. Ethyleneoxide derivative **3** was synthesized from alcohol **1** followed by a Michael addition of acrylonitril and subsequent reduction with BH3. Benzylamine derivative **5** was obtained after a reduction of benzonitrile derivative **4** with H2 in the presence of PtO2.

The liquid crystalline behavior of PDI2 was investigated by optical polarization microscopy (OPM) and differential scanning calorimetry (DSC) (Figure 2 and Experimental Section in the Supporting Information). DSC measurements showed that **PD1** is liquid crystalline between -46 °C (ΔH) 0.95 kJ/mol) and 219 °C (ΔH) 17.8 kJ/mol). By OPM, a hexagonal columnar mesophase could be detected for perylene bisimide **PDI2**.[12c]



Scheme A4 Intermediates for PDIs

Most organic and inorganic chemicals were obtained from TCI, Aldrich, and Alfa Aesar while palladium-based catalysts were purchased from Strem Chemicals and used without further purification. PDI_A,[1] PDI_B,[2] PDI_C,[3] and PDI_F,[4] were synthesized as described in literature (same as PDI_2 - see above). PDI_D was prepared following a modification of a procedure described in literature.[4]

PDI_D : *N,N′*-Bis(*n*-octyl)-1,7-dibromo-3,4,9,10-perylene diimide[6] (0.50 g, 0.65 mmol), CuI (10 mg, 0.052 mmol), and $Pd(PPh_3)_2Cl_2$ (38 mg, 0.052 mmol) were charged to a two-neck round-bottomed flask equipped with a condenser. After evacuating and refilling with nitrogen three times, pent-1-yne (0.14 g, 2.8 mmol), toluene (10.0 mL), and triethylamine (3.0 mL) were added by syringe. The mixture was then heated at 80 °C under N_2 for 12 h. After the mixture was cooled to room temperature, it was passed throught a short silica-gel plug, eluting with $CHCl_3$. After the solvent was removed under reduced pressure, the resulting solid was heated to reflux in $CHCl_3$ / MeOH (1 : 4, 50 mL) for 2 h. After the mixture was cooled to

room temperature, PDI_D was collected by filtration as a red solid (0.38 g, 74%). ^{1}H NMR (500 MHz, $CDCl_3$): δ 10.00 (m, 2H), 8.67 (s, 1.66H), 8.62 (s, 0.36H), 8.59 (d, J = 8.5 Hz, 0.39H) 8.54 (d, J = 8.5 Hz, 1.75H), 4.13 (t, J = 7.5 Hz, 4H), 4.04 (t, J = 7.0 Hz, 4H), 1.82-1.71 (m, 8H), 1.49-1.23 (m, 18H) 1.17 (t, J = 7.0 Hz, 6H), 0.88 (t, J = 7.0 Hz, 6H), (the aryl proton resonances in the ^{1}H NMR spectrum indicate that the minor 1,6-dibromo isomer is also present[6]). $^{13}C\{^1H\}$ NMR (125 MHz, $CDCl_3$): δ 163.1, 162.9, 162.6, 162.4, 137.7, 133.4, 133.2, 133.1, 132.9, 130.0, 126.8, 122.7, 122.4, 121.5, 121.2, 121.1, 120.5, 101.8, 101.7, 82.5, 40.6, 31.8, 29.4, 29.3, 28.0, 27.2, 22.7, 22.3, 21.8, 14.1, 13.9 (The observation of four carbonyl carbon resonances and one more aromatic carbon is attributed to the presence of both 1,6 and 1,7 isomers[4,6]). HRMS (FAB) calcd for $C_{50}H_{54}N_2O_4$ (M^+) 746.4083, found: 747.4200 (M + H). Anal. Calcd for $C_{50}H_{54}N_2O_4$: C, 80.40; H, 7.29; N, 3.75. Found : C, 80.14; H, 7.29; N, 3.77.

PDI_E : PDI_B[2] (6.0 g, 5.6 mmol), K_2CO_3 (4.0 g, 29 mmol) and chlorobenzene (80 mL) were mixed in a 200 mL round-bottomed flask equipped with a condenser. Bromine (4.8 mL, 93 mmol) in chlorobenzene (10 mL) was then added dropwise. The reaction mixture was then heated to 60 ^{o}C overnight, before being cooled to room temperature and poured into saturated $Na_2S_2O_3$ solution (500 mL). The mixture was then extracted with $CHCl_3$ (2 × 200 mL); the organic phase was washed with water (2 × 100 mL) and dried over Na_2SO_4. After the solvent was removed, the residue was purified using column chromatography on silica gel, with $CHCl_3$ / hexane (1 : 1) as the eluent. After the solvent was removed under reduced pressure, PDI_E was obtained as a red solid (2.7 g, 42 %). ^{1}H NMR (500 MHz, $CDCl_3$): δ 9.62 (d, J = 8.0 Hz, 1H), 8.72 (s, 1H), 8.51 (m, 3H), 8.36 (m, 2H), 4.09 (d, J = 7.0 Hz, 2H), 4.06 (d, J = 7.0 Hz, 2H), 1.95 (m, 2H), 1.5-1.1 (m, 80H), 0.82 (m, 12H). $^{13}C\{^1H\}$ NMR (125 MHz, $CDCl_3$): δ 163.5, 163.2, 163.1, 162.3, 138.9, 133.5, 133.1, 133.0, 130.8, 130.3, 128.5, 128.3, 127.9, 127.6, 126.6, 123.5, 123.4, 123.3, 122.92, 122.7, 122.5, 120.9, 44.79, 44.72, 36.63, 36.58,

31.9, 31.7, 30.1, 30.0, 29.7, 29.6 (2 close peaks), 29.6, 29.4, 26.5 (2 close peaks), 22.7, 14.1 (Two aryl carbon peaks and 31 alkyl carbon peaks were not observed, presumably due to overlap). HRMS (MALDI) calcd for $C_{72}H_{105}BrN_2O$ (M^+): 1140.728, found: 1140.734. Anal. Calcd for $C_{72}H_{105}BrN_2O$: C, 75.69; H, 9.26; N, 2.45. Found : C, 75.77; H, 9.26; N, 2.50.

Quantum Chemical calculation

The calculations were performed using the Gaussian 03 suite at the B3LYP/6-31G(d) level of theory. Both the TPA-PDI-TPA triad (**2**) and the PDI reference compound (**1**) were geometry optimized with C_2 symmetry constraints. The optimized structures were used for frequency calculations, which confirmed a full optimization (i.e. no virtual frequencies). TD-DFT calculations revealed that for the lowest excited state, for both systems, the dominant singly excited configuration is HOMO → LUMO. Thus, the lowest transition in **2** has a much larger donor-to-acceptor charge-transfer character than that of the reference compound (**1**). According to Hush-theory the relatively high oscillator strength and energy of the transition suggest a considerable electronic coupling between the donor (TPA) and acceptor (PDI). This is most probably due to the triple bond attached to the PDI core, which allows for an efficient extension of the core orbitals towards the donor. Design criteria to consider when improving the charge dissociation in films of TPA-PDA-TPA could involve inserting a phenyl instead of the triple bond and removing some bulky substituents. This would potentially balance the intra and intermolecular electronic coupling for more efficient dissociation.